Department of Electronic and Electrical Engineering
Communication Research Group

Multifunctional Reconfigurable Millimeter Wave Loop Antenna Array for 5G and B5G Applications

By:

Rawad W Shada Asfour

Supervisor's Name:
Dr. Salam Khamas & Mr. Edward A Ball

A thesis submitted in partial fulfilment of the requirements for the degree of Doctor of Philosophy

December 2023

Acknowledgments

I would like to begin by expressing my deepest gratitude to God for granting me the strength, courage, and persistence to undertake and complete this thesis.

I extend my sincere appreciation to my supervisory committee, Dr. Salam Khamas and Mr. Edward A Ball, for their invaluable guidance and unwavering support throughout my academic journey. Their mentorship, encouragement, and insightful feedback have played a pivotal role in shaping my thesis. Their wealth of experience and perspectives have been a tremendous asset to my work.

I would also like to acknowledge the University of Sheffield and the EEE staff for their continuous support during my studies.

I wish to convey my gratitude to my family for their unwavering support and motivation. I also dedicate my success to my children, Miral and Walid.

Last but not least, I want to express my deep gratitude to my wife for her unwavering love, support, and understanding during this challenging yet exhilarating journey we've embarked on together. Thank you for always believing in me, lifting me up when I needed it, and granting me the room to come this far.

With sincere gratitude,

Rawad Asfour

Abstract

Antennas serve as pivotal components within communication systems, facilitating the transmission and reception of signals through electromagnetic radiation. Traditional antenna designs prioritize optimization for fixed frequencies, radiation patterns, and polarisations. In contrast, contemporary electronic and wireless communication technologies demand antennas that are both compact and multifunctional, capable of adapting to dynamic operating scenarios. Reconfigurable antennas (RAs) emerge as a compelling alternative, offering dynamic adaptability to varying conditions and thereby enhancing system functionality and operational flexibility. The distinctive advantage of reconfigurability positions an RA as the equivalent of several non-reconfigurable antennas, resulting in compactness, cost reduction, and simplified system integration.

This research focuses on the development of compact and low-profile RAs through streamlined control mechanisms. The objective is to achieve multiple reconfigurability functionality while maintaining uniform performance across all states. The proposed reconfigurable antenna concepts aim to circumvent complex feeding structures and biasing arrangements, ultimately enhancing antenna performance. The thesis presents a comprehensive exploration of novel antenna designs, each addressing specific challenges and requirements within the realm of wireless communication. The research contributes five distinct advancements to antenna technology, spanning various frequency bands and applications.

Initially, a cost-effective circular polarisation open-loop antenna is designed at 6 GHz. An in-depth analysis of parameters such as size, shape, substrate thickness, and loop gap size yield valuable insights, enabling tailored optimization for specific applications. To expand the CP bandwidth, the design incorporates concentric parasitic open-loop antennas. This is followed by designing a similar loop antenna that is customized to operate at 27.5 GHz. Subsequently, the millimetre-wave loop has been utilised to design a phased array featuring 4-elements. The precise control of the main beam steering has been achieved through the implementation of a corporate feed network and four-phase shifters employing transmission line time delay techniques. Experimental findings confirm the configuration's ability to facilitate left-hand circular polarisation (LHCP) radiation over a scanning angle of 50°, explicitly ranging from -25° to +25°. This accomplishment aligns with the stringent criteria for maintaining a radiation pattern with an axial ratio (AR) of less than 3 dB across a broad frequency spectrum. Additionally, the design achieves a peak gain of approximately 11 dBic in combination of a total efficiency surpassing 85% throughout the CP bandwidth. Besides, the proposed design offers the advantages of compact size and low cost.

Leveraging coplanar stripline (CPS) structure and photonic bandgap (PBG), a singly fed reconfigurable circular loop antenna is proposed for millimetre-wave communication systems. This

antenna's distinctive feature lies in its capacity to adjust polarisation and bandwidth characteristics owing to the strategic integration of two PIN diodes. These diodes are engineered to function in various modes, allowing for three distinct polarisation states and accommodating two distinct bandwidths. A meticulous alignment of these PIN diodes enables a single DC bias network to be used as a highly effective RF choke, which simplifies the design and reduces the associated losses. The simple and totally planar configuration offers a choice of RHCP or LHCP radiation at 28 GHz. This is accompanied by impedance matching and axial ratio bandwidths of 12.9% and 8%, respectively, over the same frequency range with a gain of 7.5 dBic. Moreover, when the PIN diodes are unbiased, the antenna offers linear polarisation (LP) over two narrow bandwidths at 27 GHz and 29 GHz, featuring a maximum gain of 7.2 dBic. Therefore, the proposed configuration offers three operating modes: wide-band RHCP, wide-band-LHCP, and dual LP narrow-bands.

In pursuit of this objective, a 4-element multifunctional reconfigurability array antenna is designed to operate at 27.5 GHz. By controlling the PIN diodes biasing and using only two CPS lines, an innovative multifunctional reconfigurable array effortlessly generates a scanning beam at angles spanning up to ±25° across three distinct polarisations, RHCP, LHCP, and LP. Furthermore, the system achieves a reconfigurable frequency interface between circular and linear polarisations. This comprehensive study showcases a commendable array gain of approximately 10 dBic, coupled with a remarkable radiation efficiency surpassing 74%. This represents the first attempt to design a millimetre-wave multifunctional reconfigurable array. Furthermore, the proposed array offers simplicity and outperforms published counterparts that operate at lower frequencies.

Finally, a comprehensive assessment of the performance of on-chip CP circular loop antennas that have been designed and fabricated to operate in the Q/V frequency band. The study utilizes Gallium Arsenide (GaAs) and Silicon Carbide (4H-SiC) semiconductor wafer substrates. The measured results highlight the achievement of impedance matching at 40 GHz and 44 GHz for the 4H-SiC and GaAs substrates, respectively. Moreover, the outcomes confirm the generation of a left-hand circularly polarized wave in the case of the 4H-SiC substrate. As a result, a 4-element circularly polarised loop array antenna has been fabricated for operation at 40 GHz, employing the 4H-SiC wafer as a low-loss substrate. The results underscore the antenna's remarkable performance, exemplified by a broadside gain of approximately 9.7 dBic. Additionally, the proposed design showcases an impressive radiation efficiency of 92% emphasizing its efficacy and suitability for prospective applications.

List of publications

Journal Papers

1. R. **Asfour,** S.K. Khamas and E.A. Ball, (**2023**), “Cost-Effective Design of Polarization and Bandwidth Reconfigurable Millimeter-Wave Loop Antenna,” Sensors, 23(24), 9628.
2. **R. Asfour**, S. K. Khamas and E. A. Ball, (**2023**), “Design and Measurements of Circularly Polarized Millimeter-Wave Phased Array Antenna Using Time Delay Transmission Lines,” IEEE Access, vol. 11, pp. 122016-122028.
3. **Asfour, R**, Khamas, S.K., Ball, E.A., Ng, J.S., Huang, G., Allanic, R., Le Berre, D., Quendo, C., Leuliet, A. and Merlet, T., (**2024)**. On-Chip Circularly Polarized Circular Loop Antennas Utilizing 4H-SiC and GaAs Substrates in the Q/V Band. Sensors, 24(2), p.321.
4. **R. Asfour**, S. K. Khamas, and E. A. Ball, (**2021**), “Performance Evaluation of a Millimeter-Wave Phased Array Antenna Using Circularly Polarized Elements,” International Journal of Electronics and Communication Engineering, 15(12), pp. 398-401.
5. Albakosh, W., **Asfour, R**., Abdou, T.S., Khalil, Y. and Khamas, S.K., **2024**. Wideband Millimeter-Wave Perforated Cylindrical Dielectric Resonator Antenna Configuration. Magnetism, 4(1), pp.73-90.
6. **R. Asfour,** S. K. Khamas and E. A. Ball, **(2024)** "Multifunctional Reconfigurable Array Antenna for Millimeter-wave Applications" submitted to the IEEE Transaction on Antenna and Propagation.
7. W. Al Bakosh, **R. Asfour**, Y. Khalil, and S. Khamas, **(2024)** "Wideband millimetre-wave Hemispherical Dielectric Resonator Antenna with a Perforated Top Layer," Accepted to Electronics journal, MPDI with Manuscript ID: electronics-2953895.
8. A. Soltan, **R. Asfour**, and S. K. Khamas, **(2024)** "Frequency Reconfigurable Millimeter-Wave Rectangular Dielectric Resonator Antenna," to be submitted soon to **Sensors**.

Conference Papers

1. **R. Asfour**, S. K. Khamas, and E. A. Ball, **(2023)**, "Performance Evaluation of a Circularly Polarized Circular Loop Antenna Printed on GaAs, InP, and 4H-SIC Substrates in the Q/V band Frequencies," 17th European Conference on Antennas and Propagation (EuCAP), Florence, Italy, pp. 1-5.
2. **R. Asfour**, S.K. Khamas, and E.A. Ball, **(2021)**. “Performance Evaluation of a Millimeter-Wave Phased Array Antenna Using Circularly Polarized Elements,” International Journal of Electronics and Communication Engineering, 15(12), pp. 398-401.

3. **R. Asfour**, W. Albakosh, and S. Khamas, Edward A Ball, **(2024)** "A Low-Profile Fully Planar Loop Antenna for Polarization Reconfigurability" has been accepted at the 2024 IEEE International Symposium on Antennas and Propagation
4. W. Albakosh, **R. Asfour**, and S. Khamas, **(2024)**. '‘60 GHz Wideband Circularly Polarized Layered Hemispherical DRA" has been accepted at the 2024 IEEE International Symposium on Antennas and Propagation
5. W. Al Bakosh, **R. Asfour**, and S. Khamas, **(2024).** ‘’Wideband Millimeter-Wave Layered Cylindrical Dielectric Resonator Antenna’' has been accepted at the 2024 IEEE International Symposium on Antennas and Propagation.
6. Waled Albakosh, **Rawad Asfour**, and Salam K Khamas. "Measurements of Slot-Fed Circularly Polarized Layered Cylindrical DRA for X-Band Applications" has been submitted to **2024** Advanced Topics on Measurement and Simulation (ATOMS). Paper number 1571012749.
7. Akrem Soltan, **Rawad Asfour**, and Salam K Khamas " Dual Band Frequency Reconfigurable X-Band Rectangular Dielectric Resonator Antenna" has been submitted to **2024** Advanced Topics on Measurement and Simulation (ATOMS). Paper number 1571013024.
8. Tarek S. Abdou, **Rawad Asfour**, and Salam K Khamas 'Omnidirectional Hemispherical Dielectric Resonator Antenna for On Body Applications" has been submitted to **2024** Advanced Topics on Measurement and Simulation (ATOMS). Paper number 1571012752.

Teaching Papers

1. **R. Asfour** and S. K. Khamas, (2023), “Antenna Education for Junior-Level Undergraduate Students: A Case Study of an Effective Teaching Approach”, in International Conference on Studies in Engineering, Science, and Technology (ICSEST). Antalya, Turkey.
2. **R. Asfour**, R. Saad, and S. K. Khamas, " Hybrid Methodologies Approach for Enhanced Technology-Based Antennas Teaching" to be submitted to the IEEE Transactions on Education.
3. **Rawad Asfour**, Salam K Khamas, and Rola Saad **(2024).** "Bridging the Gap Between Theory and Practice in Antenna Teaching for Graduate Students" has been submitted to the SEFI Educating Responsible Engineers Conference.

Table of Contents

List of Figures

List of Tables

List of Abbreviations

2D	Two Dimensional
3D	Three Dimensional
5G	Fifth Generation
AC	Alternating current
AR	Array Factor
AUT	Antenna Under Test
BS	Base Station
BFN	Beamforming Network
BW	Bandwidth
CP	Circular Polarization
CPS	Coplanar Stripline
CPW	Coplanar Waveguide
CPWG	Grounded Coplanar Waveguide
CST	Computer Simulation Technology
dB	Decibel
DC	direct current
DRA	Dielectric Resonator Antenna
EM	Electromagnetic
FOM	Figure of Merit
FOV	Field of View
FR-4	Flame Retardant and 4 means Fibre Glass Epoxy
GaAs	Gallium Arsenide
GSG	Ground-Signal-Ground
HPBW	Half Power Beamwidth
4H-SiC	4H-silicon carbide
IF	Intermediate Frequency
IoT	Internet of Thing
LHCP	Left Hand Circular Polarization
LP	Linear Polarization
MS	Macro Station
MIMO	Multiple-in Multiple-out
MRAA	Multifunctional Reconfigurable Antenna Array
PBG	Photonic Bandgap

PCB	printed Circuit Board
PIN-diode	Positive Intrinsic Negative diode
RA	Reconfigurable Antenna
RF	Radio Frequency
RFID	Radio Frequency Identification
RHCP	Right Hand Circular Polarization
SLL	Side Lobe Levels
TTD	Time True Delay
UHF	Ultra High Frequency
UHDV	Ultra-High-Definition Video
ULA	Uniform Linear Array
VNA	Vector Network Analyser

Chapter 1

Introduction

1.1 Millimeter-wave communications

In an era marked by an insatiable demand for high-speed data transmission and ever-evolving wireless technologies, millimeter-wave (mmWave) communication has emerged as a ground-breaking solution. Operating in the frequency range of 30 GHz to 300 GHz, mmWave communication offers unprecedented data rates, minimal interference, and the potential to revolutionize the way we connect and communicate.

With the remarkable surge in data traffic and the continual emergence of new applications such as wearable devices, autonomous systems, drones, and the Internet of Things (IoT), there is a growing demand for diverse sets of requirements [1-2].

As a result, the pressing need for increased bandwidth and faster wireless communication is placing significant pressure on the current spectrum, especially the sub-6 GHz bands. This urgency has driven research into harnessing the potential of the mmWave frequency band to meet these substantial demands [3].

While mmWave communication systems have found successful applications in indoor scenarios [4], their use in outdoor environments for mobile communication systems is hindered by various external factors. Notably, there are fundamental distinctions between mmWave communications and lower-frequency existing communication systems, primarily due to the sensitivity of mmWave signals to attenuation. Factors like high propagation loss, rain attenuation, atmospheric absorption, foliage loss, and susceptibility to blockage from buildings and humans are key challenges. These losses and attenuations significantly impact mmWave systems, limiting their full potential [5]. This limitation is primarily because electromagnetic waves at very high frequencies experience substantial attenuation during their journey between different nodes. This can be justified since at very high frequencies the electromagnetic waves in the very frequencies are significantly attenuated during the travel between different nodes. To this end, the free field attenuation can be determined by Friis formula given as [6]

$$P_{r,dB} = P_{t,dB} + G_{t,dB} + G_{r,dB} + 20log_{10}\left(\frac{\lambda}{4\pi R}\right), \tag{1.1}$$

where $P_{r,dB}$ and , $P_{t,dB}$ denote the received and the transmitted powers in dB, respectively. Parameters $G_{r,dB}$ and $G_{t,dB}$ represent the gains of the receiving and transmitting antennas, respectively, and, R is the distance between the transmitter and receiver.

The small wavelengths of mmWave frequencies, ranging from 10mm to 1mm, enable the deployment of numerous antenna elements in compact arrays. The use of a large number of elements at the transmitter provides high spatial processing gains and directivity, compensating for path loss [7].

Millimeter-wave phased arrays are central to the next generation of wireless communication systems. Specifically, phased arrays allow for beam steering in various angular directions to achieve high directivity. Furthermore, phased arrays enhance the capacity of cellular networks by improving the signal-to-interference ratio (SIR), targeting desired users, and mitigating interference from other users [8]. However, the reliance on highly directional transmissions will necessitate specific design changes to the next-generation wireless communication systems.

1.2 Characteristics of Millimeter-Wave Communications

1.2.1 Wireless Channel Properties

The utilization of higher frequencies, such as those in the millimeter-wave bands, introduces distinct effects on link quality. Notably, factors like molecular elements (e.g., rain and dust) and atmospheric conditions (e.g., air density) contribute to signal attenuation. However, it's worth noting that the propagation losses due to rain attenuation and atmospheric absorption become negligible when the distances between the transmitter and receiver are on the order of approximately 200 meters [9].

1.2.2 Enhanced Directivity

Millimeter-wave links offer crucial directivity, essential for ensuring reliable communications. Electromagnetic antenna arrays, which can be steered electronically, effectively function as patterns on the circuit board. By manipulating the phase of each antenna during transmission, the array steering generates a focused beam directed toward the desired location, resulting in high-performance gains in the intended direction while minimizing losses in other directions [10].

1.2.3 Sensitivity to Signal Obstruction

Electromagnetic waves, in general, have limited diffraction capabilities when encountering obstacles, especially when those obstacles are significantly larger than the wavelength. At mmWave frequencies, common obstructions like humans and furniture are primary sources of signal blockage. Human blockage, for instance, can lead to signal loss in the range of 20-30 dB. According to measurement results, with 1-5 people present, the channel is blocked in approximately 1% to 2% of cases [11]. Additionally, in conventional wireless communication systems, non-line-of-sight (NLoS) communications result in higher losses compared to line-of-sight (LoS) propagation.

1.3 Millimeter-Wave Communications Applications

1.3.1 Leveraging Millimeter-Wave for Small Cell Access

In response to the exponential surge in mobile users and device proliferation, the escalating demands for data rates, network capacity, and coverage have spurred the development of small-cell access solutions. This approach aims to achieve a remarkable 10,000-fold enhancement in network efficiency and affordability [12]. Within this context, mmWave communication in tandem with small cells has emerged as a powerful means to deliver multi-gigabit data rates and facilitate a wide array of bandwidth-intensive multimedia applications, including high-definition television. Moreover, the strategic integration of mmWave and small cell technologies presents a viable strategy for augmenting network coverage, enhancing capacity, and mitigating interference issues. Figure 1.1 depicts a block diagram illustrating the application of mmWaves in conjunction with small cells.

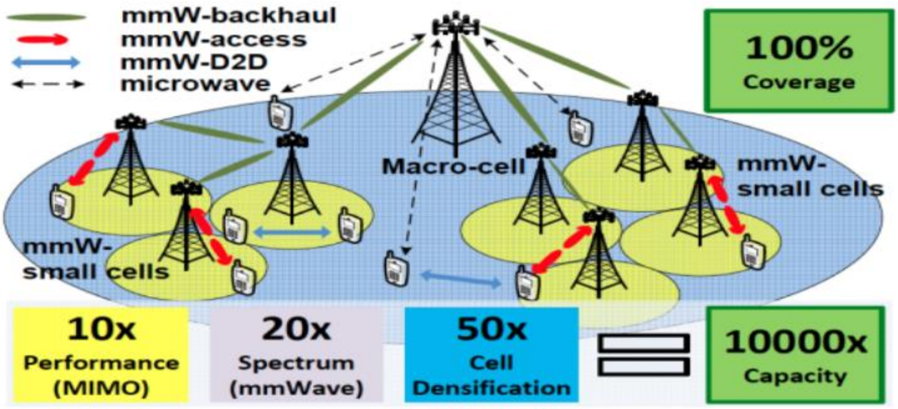

Figure 1.1: illustration of mmWave small cell access [2].

1.3.2 Beamforming Networks (BFN)

Wireless communication systems face various challenges, such as signal attenuation, which can compromise link capacity and reliability. To address these issues and pave the way for high data throughput rates, mmWave and massive multiple-input multiple-output (massive-MIMO) systems have emerged as pivotal technologies in next-generation communication systems. By harnessing mmWave frequencies and employing extensive antenna arrays, these systems focus transmitted beams on intended recipients, enhancing capacity, communication reliability, and coverage. This signal-shaping technique is commonly referred to as beamforming. Beamforming directs transmitted energy precisely while minimizing interference in other directions.

Phased array networks represent a paradigm shift in wireless communication, offering unprecedented flexibility, adaptability, and signal control. As technology continues to evolve, these networks are expected to play an increasingly pivotal role in shaping the way we connect and communicate in an ever-connected world. Nevertheless, mobile device mobility and various outdoor and indoor propagation conditions can introduce significant signal attenuation, impacting system performance. Therefore, meticulous design of base station (BS) and mobile station (MS) antennas is imperative in mmWave cellular communication systems [13]. Achieving improved link quality necessitates the application of beam steering at both BSs and MSs, as illustrated in Figure 1.2.

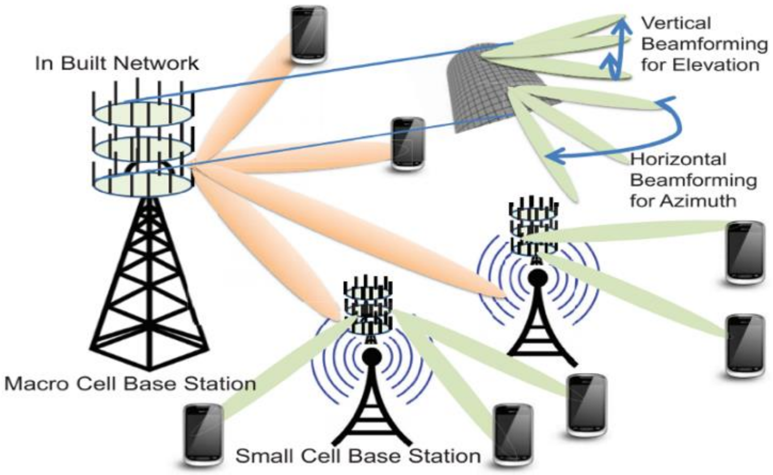

Figure 1.2: Massive MIMO and beamforming scenario at BS and MS [13].

1.4 Aims of the Research and Motivation

In the context of this research endeavor, the author embarked on a comprehensive investigation into the design of a cost-effective, circularly polarized circular loop antenna. This undertaking was motivated to confront the formidable challenge of pioneering an innovative antenna array that utilizes a true-time-delay transmission line. The envisioned outcome was a system capable of achieving precise beam steering while preserving circular polarization.

Furthermore, the author aimed to investigate the development of a singly fed reconfigurable circular loop antenna designed for millimeter-wave (mmWave) communication systems. A distinguishing feature of this antenna lies in its ability to adjust both polarization and bandwidth characteristics. This capability is made possible through the strategic integration of two PIN diodes, engineered to function in various modes, enabling three distinct polarization states and accommodating two distinct bandwidths. A meticulous alignment of these PIN diodes enables the utilization of a single DC bias network as a highly effective RF choke, which simplifies the design and reduces the associated losses.

Additionally, the author of this thesis aimed to address the challenge of realizing a reconfigurable antenna that will serve as an element from which a multifunctional reconfigurable array can be designed, offering both polarization and pattern reconfigurability. The ultimate goal was to mitigate circuit-level losses and create an antenna structure distinguished by both elegance and efficiency.

Moreover, the author aimed at the significance of on-chip implementation, contemplating the utilization of substrates such as 4H-SIC and GaAs. This aspect of the research marked a crucial endeavor in extending the practical utility of the proposed antenna system, with potential implications for cutting-edge applications in integrated circuit design.

1.5 Original Contributions

To achieve the objectives set forth in this thesis, several concepts have been developed and the designs are validated accordingly. As an outcome of this research, the following original contributions are carried out in this thesis:

CP circular loop antenna using coplanar waveguide feed: The first contribution of this research revolves around the design of a cost-effective CP open-loop antenna fed by a coplanar waveguide port (CPW). The design is specifically tailored for operation at 6 GHz, offering a low-profile solution that is both efficient and economically viable. Furthermore, this contribution entails an extensive analysis of how various parameters influence the performance of the CP antenna. These parameters encompass a range of factors, including the antenna's size, shape, substrate thickness, outer loop gap size, and the effect of the ground plane, among others. By scrutinizing the impact of these parameters, a deeper understanding of the antenna's functionality is gained, enabling optimization for specific applications.

Phased array antenna using time delay transmission lines: A 4-element open-loop array antenna has been meticulously designed and constructed to realize circularly polarized (CP) beam steering, covering a substantial range of ±25°. This achievement is made possible through the successful implementation of four-phase shifters, leveraging the time delay technique within transmission lines. An analysis of the results demonstrates that this cost-effective design not only offers a high gain but also achieves this performance with a significantly reduced number of elements. This reduction in the number of elements translates to the use of a simpler and more efficient feeding network, which further enhances the overall efficiency of the system. Moreover, the integration of beam steering capabilities significantly extends the antenna's operational range and efficiency, making it a valuable advancement in the field of antenna technology.

Cost-Effective Polarisation Reconfigurable Planar Loop Antenna: A low-profile, cost-effective circularly polarized single-loop antenna designed for mmWave frequencies is presented. This innovative design incorporates two strategically placed gaps, enabling polarization reconfigurability. The antenna utilizes a coplanar stripline (CPS) structure featuring a photonic bandgap (PBG), which simplifies the biasing of the PIN diodes without the need for lumped RF chokes or capacitors. This elimination of additional elements minimizes associated losses, resulting in higher overall efficiency. Moreover, by biasing the PIN diodes within the antenna design, the system can generate different circular polarization senses, including LHCP, RHCP, and LP waves. This adaptability enhances the antenna's versatility, making it well-suited for a range of communication needs and scenarios.

Multifunctional reconfigurable mmWave array with polarization, frequency and pattern control: The contribution is the design of a 4-element phased array system with the goal of creating a versatile and reconfigurable mmWave array. This multifunctional array can modify both its polarization, frequency, and pattern. In each of the array elements, two gaps are designed to house PIN diodes, which act as flexible switches, allowing for the selection of the desired polarization by toggling between forward-bias and reverse-bias states. Additionally, strategically positioned PIN diodes within the phase shifter gaps provide precise control over beam steering in the desired directions. To achieve this, CPS lines are employed to bias the PIN diodes in both the antenna elements and the phase shifters through vias. This comprehensive approach not only demonstrates the adaptability and versatility of the mmWave array but also makes a significant contribution to the advancement of reconfigurable antenna technology.

On-chip CP loop antenna using 4H-SIC and GaAs substrates within the Q/V band: In a comparative study, two different dielectric substrates (4H-SIC and GaAs) have been utilized for a CP circular loop antenna operating within the Q/V frequency band for the first time in the final contribution of this research. Furthermore, GaAs antennas will be designed and generate diverse circular polarizations, achieved by strategically altering gap positions in the antenna design, resulting in both LHCP and RHCP circular polarizations. This adaptability enhances the antenna's versatility, making it well-suited for various communication needs. Additionally, a 4-element open-loop array antenna will utilize the 4H-SIC substrate. This design incorporates a parallel feed network, significantly optimizing the antenna's performance, particularly enhancing signal transmission and reception efficiency, marking a notable advancement in on-chip antenna technology.

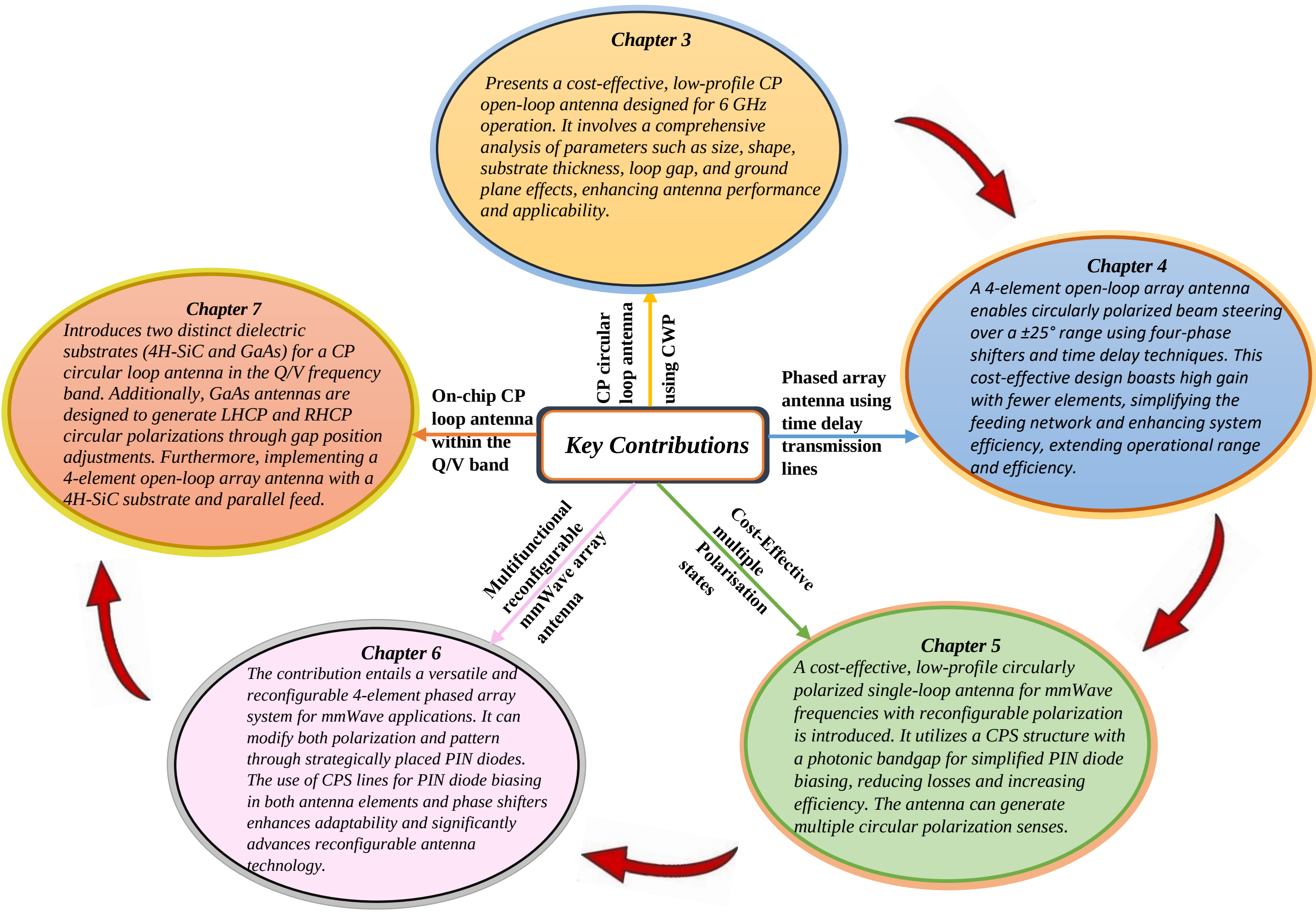

Figure 1.1: Summary of the key contributions per each technical chapter

1.6 Thesis Outline

This thesis is structured into eight chapters; a key summary of each chapter's development is provided below:

- Chapter 1 presents a brief introduction to mmWave communication and its characteristics and applications. The aims for this thesis and the research motivation are then provided. The areas of novelty and originality of research contributions are also detailed. Finally, some useful definitions are outlined at the end of this chapter.
- In Chapter 2, a foundational context is provided for the current research, offering insights into essential concepts such as different polarization types, loop antennas, array antennas, and the principles of reconfigurable antennas. This chapter lays the groundwork by explaining the fundamental concepts and terminology that are central to the research, ensuring a solid understanding of the key elements relevant to the study.
- Chapter 3 begins a comprehensive introduction to the configuration and fundamental design principles governing the Circularly Polarized (CP) loop antenna. It then proceeds to delve deeply into an extensive examination of the various parameters like substrate thickness, ground plane sizes, and outer loop gap size. Moreover, the chapter encompasses a detailed comparative analysis of the antenna with and without the incorporation of a parasitic loop, elucidating the significant impact of this addition. To provide a holistic understanding, this chapter meticulously outlines the process of creating prototypes, simulations, fabrication, and the precise measurements conducted on the proposed CP loop antenna, offering valuable insights into its practical application and performance. This multifaceted exploration equips readers with a profound grasp of the intricate nuances of the CP loop antenna and its underlying design principles.

- Chapter 4 serves as an in-depth exploration of the design configuration of the circularly polarized (CP) single-loop element using a CPW port at mmWave frequency. The chapter delves into the implementation of a 1 × 4 beam steering linear array antenna, specifically focusing on left-hand circular polarization (LHCP). This array is constructed using the proposed circular loop element. Additionally, the chapter elucidates the methodology of employing true time delay techniques to facilitate CP beam steering, ensuring that the antenna system can precisely direct beams toward desired directions.
- Chapter 5 commences by presenting an in-depth exploration of the configuration and design principles governing the CP reconfigurable loop antenna, while also delving into the pertinent parameters that shape its functionality. Notably, it delves into the innovative use of PIN diodes for efficient antenna switching in RF applications, highlighting their crucial role in achieving versatility. Additionally, it focuses on the isolation of RF current from the biasing coplanar stripline through the integration of a photonic Bandgap Structure, enabling the implementation of different circular polarization senses. Furthermore, Chapter 5 offers a comprehensive examination of the practical aspects of the research, detailing the prototypes, simulation methodologies, fabrication processes, and the precise measurements conducted on the proposed CP reconfigurable loop antenna. These experiments are conducted at both 6 GHz and the challenging mmWave frequency of 28 GHz, providing valuable insights into the antenna's performance across different operational ranges.
- Chapter 6 of this research will address a critical gap in existing literature, which lacks the presence of multifunctional reconfigurable antennas (MRAs) designed for mmWave applications. The upcoming chapter will be dedicated to the comprehensive exploration of the design, fabrication, and measurements of such a unique antenna

system. Building upon the phased array design introduced in Chapter 4, we will further enhance it to achieve a multifunctional reconfigurable mmWave array, a groundbreaking innovation not previously reported.

This multifunctional reconfigurability will be achieved through the implementation of a reconfigurable element and a reconfigurable feed network. In the preceding chapter, we introduced a low-cost planar antenna concept aimed at achieving polarization reconfigurability at mmWave frequencies. This reconfigurable antenna will serve as a foundational element from which we will craft a multifunctional reconfigurable array. This advanced array will offer not only polarization reconfigurability but also pattern reconfigurability, signifying a significant advancement in the field of antenna technology.

- Chapter 7 begins by presenting the configuration and design principles of a circularly polarized antenna. It goes on to provide a thorough examination of measurements conducted on an on-chip antenna situated on a GaAs substrate, with a specific focus on the options for circular polarization (CP) radiation. This GaAs-based prototype serves as a reference point for evaluating the performance of a 4H-SiC-based antenna, with comparative analysis involving fabrication and measurement. In addition, Chapter 6 outlines the methodology for designing the proposed on-chip array antenna, using a 4H-SiC substrate and covers the prototype development, simulation, fabrication, and measurement of the proposed antenna array.
- Chapter 8 culminates the research journey by summarizing the key findings and drawing meaningful conclusions. Moreover, this chapter extends its scope by offering valuable recommendations that point the way toward future research directions and potential areas of exploration.

Chapter 2

Background

2.1 Antenna Polarization

The antenna polarization represents an essential factor for selecting and installing antennas. The concept of antenna polarization refers to the orientation of the electric field in the electromagnetic wave radiated by an antenna. Antenna polarization plays a fundamental role in determining how effectively an antenna can transmit and receive signals in a given communication system. The two primary types of antenna polarization are linear polarization and circular polarization. The following subsections discuss the two types briefly.

2.1.1 Linear Polarization (LP)

Linear polarization involves the electric field oscillating in a single plane, either vertically or horizontally. This type of polarization is commonly used in various wireless communication systems, such as cellular networks, where the antennas on both the transmitting and receiving ends are aligned with the same linear polarization to maximize signal strength. Linear polarization can be further classified into two subtypes: vertical polarization and horizontal polarization. A schematic of linearly polarized waves is illustrated in Figure 2.1.

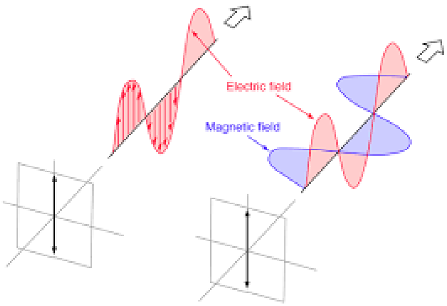

Figure 2.1: Linearly polarized waves.

Mathematically, linear polarization can be described by the following equations for the electric field vector, E(t):

Vertical and horizontal LP:

$$E(t) = E_0 \times \sin(\omega t) \times \hat{J} \tag{2.1}$$

$$E(t) = E_0 \times \cos(\omega t) \times \hat{I} \tag{2.2}$$

Here, E_0 represents the maximum amplitude of the electric field, ω is the angular frequency, t is time, ˆJ denotes the unit vector in the vertical direction, and ˆI is the unit vector in the horizontal direction.

Linear polarization antennas are easy to fabricate but have a negative effect in terms of polarization mismatch, reflectivity, inclement weather, absorption, and Faraday rotation [14]. Therefore, the circularly polarized antenna provides more advantages as compared to the linear-polarized antenna.

2.1.2 Circular Polarization and its Important Role in mmWave Communications

Circularly polarized (CP) antennas have received much attention in recent years compared to linearly polarized counterparts. CP has the potential to achieve radiation to reduce multi-path effects. CP can also allow more flexible orientation of the receiver and transmitter antennas [15]. CP describes a unique polarization state where the electric field vector rotates in a circular pattern as the wave propagates. This property allows CP signals to maintain their integrity in the face of signal polarization mismatches and multipath interference, making them highly resilient and suitable for numerous applications. From satellite communication and global positioning systems to radar technology and wireless communication, CP plays a pivotal role in ensuring reliable and robust signal transmission. The design and deployment of circularly polarized antennas, coupled with a deep understanding of CP principles, are fundamental in achieving superior signal quality and performance in today's complex and challenging communication environments. Circular polarization2 can be obtained if two orthogonal modes with equal amplitudes and 90-degree time phase differences as illustrated in Figure 2.2. This can be achieved by adjusting the physical dimensions of the antenna or by various feed arrangements [15].

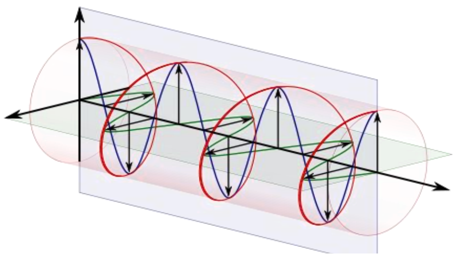

Figure 2.2: Circular polarized waves.

The significance of employing circular polarization, as opposed to linear polarization, in the next generation of millimetre-wave applications is underscored by several key factors. Firstly, the issue of reflectivity comes into play, as microwave signals interact with materials they encounter. This interaction can result in signal reflection from the ground or other objects, potentially causing a polarization reversal – for instance, a right-hand circularly polarized (RHCP) wave may become left-hand circularly polarized (LHCP) [16]. By utilizing RHCP antennas at the receiver, it becomes possible to reject LHCP reflected signals, effectively mitigating multipath interferences stemming from these reflections.

Furthermore, CP also provides immunity against the Faraday rotation effect caused by the ionosphere, a phenomenon that can result in significant signal loss, often exceeding 3dB [17]. Lastly, CP antennas offer the benefit of not requiring strict alignment between the transmitting and receiving antennas, in contrast to linearly polarized antennas, which are susceptible to polarization mismatch if misalignment occurs [18]. This feature proves especially valuable in mobile satellite communications, where maintaining a constant antenna orientation can be challenging. As a result, received CP signals remain robust and consistent regardless of antenna orientation, ensuring a reliable communication link.

When a plane radio wave propagates over an extensive distance, it lacks field components in the direction of its travel (referred to as the z-direction), thereby assuming the form of a transverse electromagnetic (TEM) plane wave. The instantaneous field of such a plane wave may be described as follows:

$$E = E_x + E_y \tag{2.3}$$

where the E_x and E_y components are specified as:

$$E_x = E_{xm} \cos(wt + k_{oz} + \Phi_x) \tag{2.4}$$

$$E_y = E_{ym} \cos(wt + k_{oz} + \Phi_y) \tag{2.5}$$

In this context, E_{xm} and E_{ym} represent the maximum values, and k_{oz} denotes the free-space wavenumber, which is defined as $k_{oz} = 2\pi/\lambda$. The radiated wave's polarisation can be categorized as linear, circular, or elliptical, depending on the orientation of its electric field vector E. When z = 0, the equation above can be streamlined as [19]:

$$E_x = E_{xm} \cos (wt + \Phi_x) \tag{2.6}$$

$$E_y = E_{ym} \cos (wt + \Phi_y) \tag{2.7}$$

The polarization is circular only when both E_x and E_y field components have the same magnitude and in quadrature, i.e.,

$$E_{xm} = E_{ym} = E_m \tag{2.8}$$

$$\Delta\Phi = \Phi_y - \Phi_x = \pm\frac{\pi}{2} + 2n\pi, \; n = 0,1,2, \ldots \tag{2.9}$$

When $\Phi_y - \Phi_x = \frac{\pi}{2}$, Equations (2.8) and (2.9) can be expressed as:

$$E_x = E_m \cos (wt + \Phi_x) \tag{2.10}$$

$$E_y = E_m \cos\left(wt + \Phi_x + \frac{\pi}{2}\right) = -E_m \sin(wt + \Phi_x) \tag{2.11}$$

It is a well-established principle that the magnitude of the electric field vector remains constant, while its orientation changes over time. This results in the electric field vector undergoing circular rotation within the xy plane, aligning with the propagation direction as shown in Figure 2.3. Furthermore, when we talk about circular polarization, if the electric field vector rotates clockwise, it is referred to as RHCP, as demonstrated in Figure 2.3a. Conversely, if the electric field vector rotates counterclockwise, it is defined as LHCP, as depicted in Figure 2.3b.

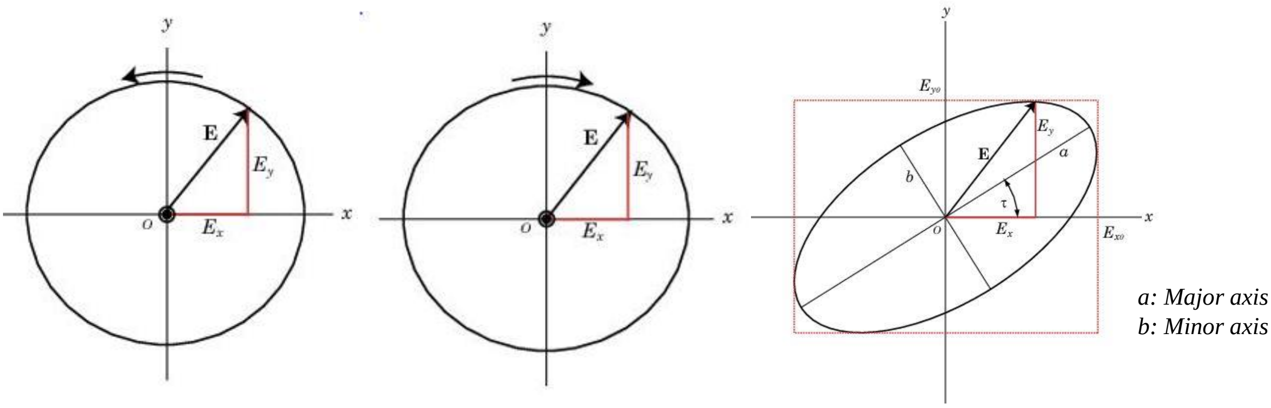

(a) (b) (c)

Figure 2.3: E-field vector of (a) Right-hand circular polarisation and (b) Left-hand circular polarisation (c) Elliptical polarisation.

Circular polarization quality was evaluated by employing the axial ratio (AR) parameter, determined by dividing the maximum electric field strength, associated with the maximum radius of the ellipse, by the minimum electric field strength, corresponding to the minimum radius of the ellipse, as depicted in Figure 2.3c. Therefore, the mathematical representation of the axial ratio can be expressed as follows:

$$AR = 20log_{10}\left(\frac{E_{max}}{E_{min}}\right) \tag{2.12}$$

where $|E|\left(\frac{max}{min}\right) = \sqrt{\frac{1}{2}(E_x^2 + E_y^2) \pm \sqrt{(E_x^4 + E_y^4 + 2E_x^2E_y^2cos2\Delta\Phi)}}.$

From the equation presented above, when the magnitudes of Ex and Ey are equal, and their phase difference is precisely 90º, the axial ratio $AR = 0\,dB$, which means the wave's polarisation is circular. In practical terms, when AR is at or below 3 dB, it signifies that circular polarization has been achieved. Conversely, if AR exceeds 3 dB, it indicates the presence of linear polarization. This 3 dB threshold serves as a crucial criterion for assessing polarisation characteristics.

2.2 Loop Antenna

In recent years, the loop antenna has received much research attention due to its simplicity, cost-effective implementation, fabrication simplicity, and versatility for many applications [27]. The loop antenna, renowned for its versatility, has found a newfound significance in the realm of mmWave applications, showcasing its adaptability and effectiveness in harnessing the power of these exceptionally high-frequency radio waves. With mmWave frequencies typically ranging from 30 to 300 gigahertz, the challenges of efficient signal reception and transmission become increasingly demanding. The loop antenna rises to this challenge with its inherent qualities, making it an invaluable tool for various cutting-edge applications. In mmWave communication systems, the loop antenna's compact form factor and its ability to resonate at these elevated frequencies are crucial. Its size is particularly advantageous, as mmWaves require smaller antenna elements to maintain the necessary gain. Loop antennas can be conveniently integrated into compact electronic devices, making them suitable for applications like 5G and beyond, wireless communication systems, and high-speed data transmission. Moreover, loop antennas excel in their capacity to minimize interference and cross-polarization, ensuring that the signal remains pure and highly directional. This is essential in applications like automotive radar systems. The loop antenna's resilience in harsh environmental conditions, low noise characteristics, and ability to maintain high gain at mmWave frequencies have made it indispensable in a range of scientific and research applications. These include spectroscopy, remote sensing, and even security scanning technologies, where precision and reliability are non-negotiable. The loop antenna is typically classified as either an electrically small or electrically large loop antenna.

2.2.1 Electrically Small Loop Antenna

The electrically small loop antenna is characterized by its overall length (circumference) typically being less than one-tenth of a wavelength (C < λ/10). When these antennas radiate, the nulls are perpendicular to the antenna axis, while the major lobe is along the antenna axis. An electrically small loop of a single turn has low radiation resistances compared to their ohmic loss resistances. Therefore, they are usually classified as poor radiators, which are not suitable for transmission in radio communication while it is typically in the receiving mode, where the efficiency of the antenna is not as crucial as the signal-to-noise ratio (SNR) [20]. These antennas, whether circular or of any shape, display field patterns and resistance curves closely resembling those of infinitesimal dipole antennas. The electrically small loop antenna primarily demonstrates inductive characteristics, in contrast to the predominantly conductive nature of a short dipole antenna [21]. The current distribution across an electrically small loop remains constant throughout the loop, maintaining a uniform phase and amplitude. It is worth noting that the electrically small loop's radiation resistance can be significantly enhanced by adding more turns, bringing it closer to the characteristic impedance of practical transmission lines.

Radiation resistance of small circular loop antenna in free space R_r can be calculated as [20]

$$R_r = 20\pi^2 \left(\frac{C}{\lambda}\right)^4, \tag{2.13}$$

where c is the circumference and λ is a wavelength. Equation (2.13) provides the radiation resistance for a single loop, but when the loop antenna has an N turn, then the radiation resistance would be increased with a factor of N^2

$$R_r = 20\pi^2 \left(\frac{C}{\lambda}\right)^4 N^2. \tag{2.14}$$

2.2.2 Electrically Large Loop Antenna

The electrically large loop antenna is distinguished by its overall length (circumference), which approximates a free-space wavelength (C ~ λ). When compared to its smaller counterpart, the large loops radiate the nulls in the direction of the antenna's axis, while the major lobes extend perpendicularly to the antenna axis. Notably, the current distribution within an electrically large loop is no longer uniform, exhibiting varying phases and amplitudes throughout the loop. This variance results in distinct characteristics when compared to smaller loops. In the case of the electrically large loop antenna, its radiation resistance is substantially higher, leading to enhanced radiation efficiency compared to electrically small loop antennas. This difference in size and current behavior underscores the pivotal role played by electrically large loop antennas in addressing unique challenges and opportunities within the field of electromagnetic engineering. The radiation resistance of large circular loop antenna in free space can be given as [21].

$$R_r = 60\pi^2 \left(\frac{C}{\lambda}\right), \tag{2.15}$$

Loss resistance of small & large circular loop antenna in free space (one turn) is given as

$$R_L = \frac{C}{2\pi b}\sqrt{\frac{\omega\mu_0}{2\sigma}}, \tag{2.16}$$

where μ_0 is the permeability of free space, and σ is the metal conductivity.

2.3 Array Antenna

An antenna array refers to groups of antennas, which work together as a single antenna to transmit or receive radio waves albeit with desired directional characteristics of a particular shape. Besides, the array antennas achieve a performance improvement that can produce radiation patterns that are not produced by a single antenna [22].

As mentioned earlier, high directivity is often required in the mmWave frequency range, while the radiation patterns of an individual antenna are relatively wide with low gain. It should be noted that high directivity of a single antenna can be achieved by enlarging the dimensions of the radiating aperture to be much larger than λ, but multiple side lobes will appear. However, an array antenna with small size represents an effective way to increase the electrical size with a minimum of side lobes Thus, the interference of partial fields generated by individual elements will be constructive in the desired direction and destructive in the remaining space [22]. To control the overall antenna pattern, there are fundamental characteristics that need to be optimized. For example,

- The geometrical configuration of the overall array.
- The relative distance between adjacent elements.
- The excitation amplitude and phase of each element.
- The far-field pattern of the individual elements.

Therefore, the array antenna can be used to increase the overall of gain and directivity. In addition, arrays facilitate steering the main beam in a particular direction. Besides, arrays can reduce power wastage. As well as cancel out interference from other directions. This is in addition to important applications in determining the direction of arrival of an incoming signal as well as achieving a high signal-to-noise ratio (SNR).

Array antenna has several geometric configurations which can group as follows:

- Linear arrays: the radiation elements arranged in a single line (vertically or horizontally).
- Planar arrays: the radiating elements arranged in a two-dimensional grid.
- Circular arrays: the radiation elements arranged in a circular pattern.
- Conformal arrays: In this type, the radiating elements are arranged in a 3D surface plane.

2.4 Grounded Coplanar Waveguide (CPWG)

Figure 2.4a illustrates a coplanar waveguide (CPW) port accompanied by a ground plane, which serves as a pivotal element in the field of microwave and radio frequency engineering. Its primary purpose is to facilitate the efficient transmission and reception of electromagnetic signals while preserving a coplanar structure, where both the signal trace and the ground plane are placed on the same layer. This configuration offers several advantages, including reduced signal radiation, controlled impedance, and improved isolation between neighboring components on a circuit board. The presence of the ground plane beneath the CPW helps maintain signal integrity and minimizes electromagnetic interference, making it a versatile and indispensable tool for high-frequency applications in modern electronics and communication systems. Figure 2.4b provides an illustration of the approximate dimensions that are essential for implementing the CPW port.

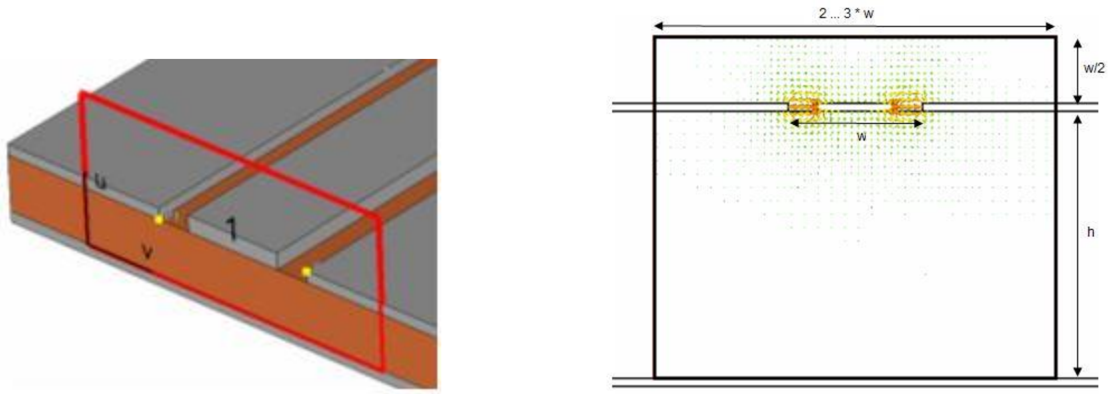

Figure 2.4: Illustrate a coplanar waveguide port.

2.5 Overview of the Reconfigurable Antenna Systems.

The IEEE Standard Definitions of Antenna Terms released in 2014 [23] provided a definition for a 'reconfigurable antenna' as an antenna capable of altering its operational characteristics, including resonant frequency, radiation pattern, and polarization, through mechanical or electrical adjustments to its architecture. The reconfiguration process typically involves direct interaction with the antenna's fundamental operating mechanism, influencing the surface current or electric field distribution to achieve reversible changes in its output characteristics [24, 26]. As a result, antennas that lack an integrated reconfiguration mechanism and instead rely on external reconfiguration circuits or feeding/matching networks are appropriately classified outside the category of 'reconfigurable antennas.' For example, a phased array antenna's performance is primarily controlled by external phase shifters manipulated from the outside, while the fundamental functioning of the antenna remains unaltered.

2.5.1 Categories of Antenna Reconfigurability

The concept of antenna reconfigurability primarily pertains to the deliberate modification of its core attributes. In essence, an antenna's performance is primarily governed by three fundamental characteristics. Depending on which property is intentionally adjusted or fine-tuned, the reconfigurability of antennas can be classified into four distinct groups, as illustrated in Figure 2.5.

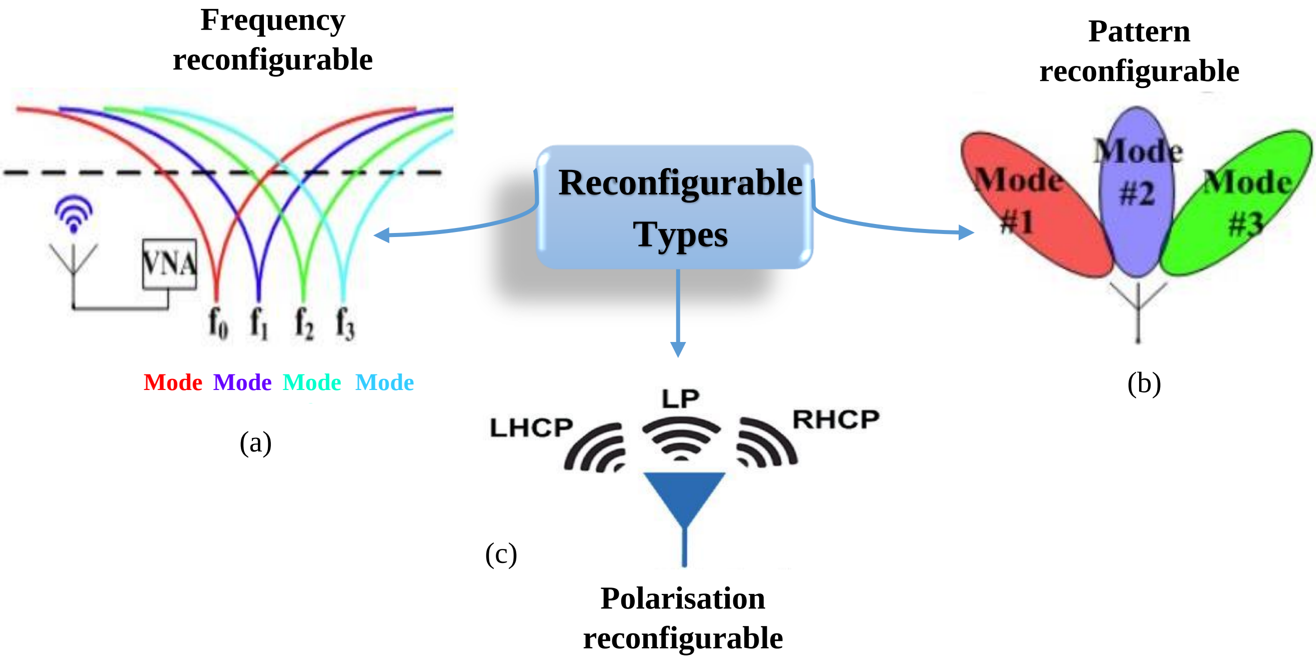

Figure 2.5: Three types of reconfigurable antennas: Polarization, Pattern and Frequency.

2.5.1.1 Frequency Reconfigurability

Among the many attributes of antennas, operational frequency stands out as the most pivotal. Frequency reconfigurability in the context of antennas pertains to the antenna system's capacity to modify or adapt its operating frequency. This remarkable capability empowers the antenna to seamlessly shift between various frequency bands or fine-tune its resonant frequency to align with the prerequisites of a specific communication system or application. Figure 2.1(a) provides a conceptual illustration of the process of adjusting the operating frequency of an antenna.

Frequency reconfigurability can be accomplished through a diverse array of techniques, including the integration of tunable components like PIN diodes or switched capacitors. These components enable the antenna to change its electrical characteristics, such as the resonant frequency, impedance, or bandwidth, in response to the desired frequency range.

Due to its dynamic frequency-regulating behavior, this category of antenna exhibits a notable trait known as frequency selectivity, rendering it exceptionally useful for interference filtering. Consequently, frequency-reconfigurable antennas hold great promise as cost-effective and efficient alternatives to multiple Fixed-Parameter Antennas (FPAs) in various scenarios. This offers a significant advantage over the current practice of using either separate single-band antennas or a single wideband antenna to cover the distinct operational requirements of multiple frequency bands.

2.5.1.2 Pattern Reconfigurability

Pattern reconfigurability represents another valuable attribute of reconfigurable antennas. In the domain of antennas and electromagnetic systems, a reconfigurable antenna refers to an antenna's capacity to alter or adapt its radiation pattern to accommodate diverse operational demands. The radiation pattern of an antenna defines how it radiates or receives electromagnetic waves in three-dimensional space, and it plays a crucial role in determining the antenna's coverage, directionality, and performance in various applications. A conceptual representation of pattern reconfigurability is provided in Figure 2.1(b).

Typically, pattern reconfigurable antennas find application in tasks such as beam steering and interference nulling. By dynamically adjusting the antenna's maximum radiation, these antennas can maximize gain in the desired direction, ensuring a dependable connection with mobile devices and effectively mitigating interference.

2.5.1.3 Polarisation Reconfigurability

Polarization reconfigurability is a notable attribute in the realm of antennas and electromagnetic systems. It refers to an antenna's capability to adjust or adapt its polarization state to align with specific operational requirements. Polarization in the context of antennas describes the orientation of the electric field vector within the electromagnetic wave radiated by the antenna. This characteristic plays a critical role in various applications, as it determines how effectively the antenna can transmit or receive signals and mitigate interference. In Figure 1.1(c), the concept of polarization reconfigurability is depicted.

Polarization reconfigurability can be attained through deliberate alterations in the antenna's configuration, feed arrangement, or through the application of PIN diodes. This capability of polarization reconfiguration serves to reduce polarization mismatch losses, enhance resistance to interference signals, and guarantee robust signal reception for portable devices.

2.5.1.4 Compound Reconfigurability

Compound reconfigurability represents the final category of reconfigurable antennas, notable for its ability to demonstrate multiple forms of adaptability within a single antenna structure, employing various control methods. These antennas have the potential to alter their operating frequency, polarization, scan the radiation pattern, and fine-tune the resonant frequency. Independently managing an antenna's diverse attributes, including resonance, radiation, and polarization, is indeed a challenging task, as it risks interference between these features. Nevertheless, the control over multiple parameters makes the antenna remarkably versatile and effective in diverse operating environments [27] ,[28].

For instance, compound reconfigurability provides a practical solution to simplify the complexity of diversity techniques used in communication systems. However, it necessitates careful design strategies to ensure that the multiple reconfigurability functions within a single antenna configuration do not interfere with one another during antenna operation.

2.6 CST (Computer Simulation Technology)

CST Simulation is a leading provider of electromagnetic simulation software, widely used for the design and analysis of various electromagnetic devices, including antennas.

Designing antennas using CST simulation is a crucial and highly efficient process in the field of electromagnetic engineering. CST Simulation provides a comprehensive platform for modeling, analyzing, and optimizing antenna designs. With CST simulation, engineers and researchers can create detailed 3D models of antenna structures, enabling them to explore a wide range of design possibilities. This software is instrumental in assessing critical antenna characteristics, including radiation patterns, impedance matching, gain, and polarization.

In this research, CST Simulation was utilized as a pivotal tool for the simulation and analysis of various antenna designs and configurations. CST Simulation provided a robust and versatile platform to model the complex electromagnetic behaviors of our antennas. The software's high fidelity in capturing real-world electromagnetic phenomena ensured the accuracy of our results. CST Simulation also enabled us to explore the effects of different materials, substrates, and structural modifications, helping us make informed design choices. Figure 2.6 presents an overview of the CST Simulation interface.

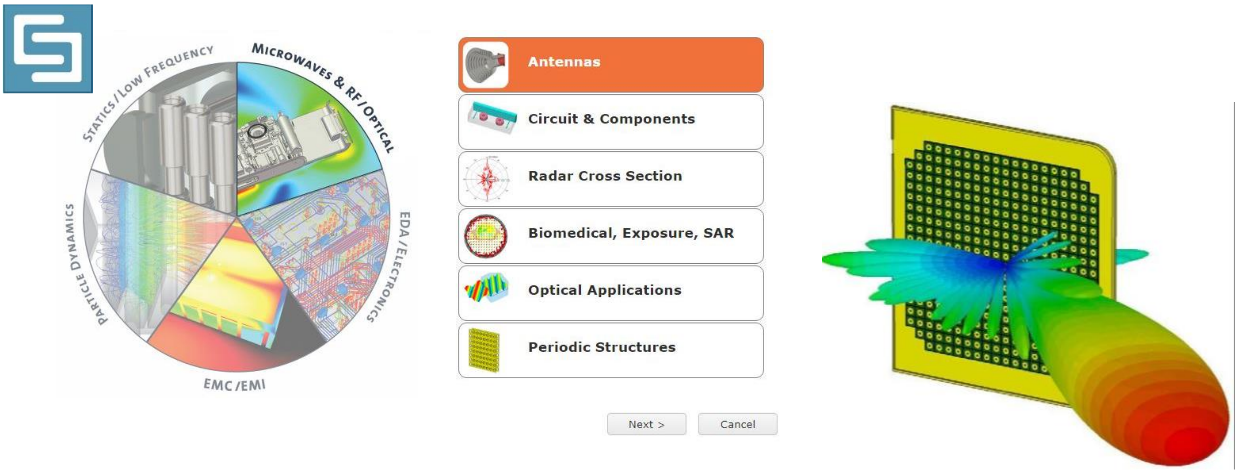

Figure 2.6: Depicts a CST microwave studio.

2.7 Antenna Design through Simulation

The design and simulation processes are carried out within CST, while the physical or manufactured antenna is subject to testing and quantification of the S11 parameter using a Vector Network Analyzer (VNA). Additional evaluation of the antenna's radiation pattern, circular polarization bandwidth, and gain is performed using a spherical near-field measurement apparatus. Figure 2.7 illustrates the flowchart outlining the proposed methodology.

The proposed antenna design was implemented using CST version 2020, involving the configuration of various parameters, including the frequency spectrum, port designation, mesh cells, and simulation modality. A hexahedral mesh, discretizing the computational volume via rectangular cuboids (x, y, z), was utilized.

The S11 results provide insights into the antenna's performance characteristics, encompassing impedance bandwidth and resonance frequency. To account for radiation losses in the antenna and its feed network, the loss tangent was incorporated into the material properties.

The purpose of measuring antenna gain is to quantify the ability of an antenna to concentrate its radiated power in a specific direction in comparison to an isotropic radiator. As a key performance parameter, the gain of an antenna is instrumental in understanding various aspects including directionality, efficiency, and suitability for specific applications. For instance, while a point-to-point communication system might necessitate a high-gain directional antenna, an indoor Wi-Fi system could benefit more from a lower-gain omnidirectional antenna. Typically, antenna gain is measured in dBi, which stands for decibels relative to an isotropic radiator, but when dealing with antennas that have circular polarization, the gain is measured in dBic.

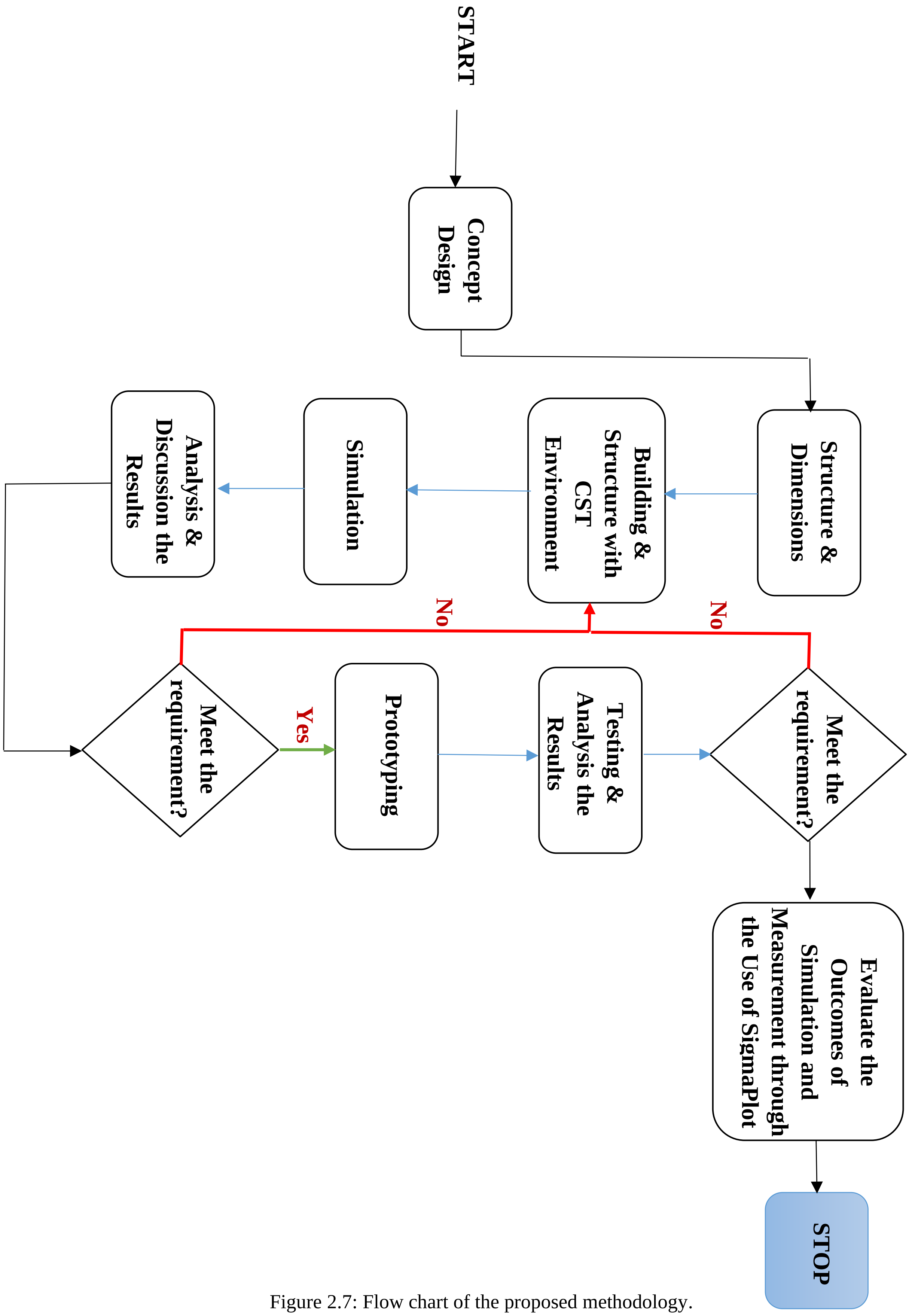

Figure 2.7: Flow chart of the proposed methodology.

2.8 Procedures for Antenna Measurement

To corroborate the findings of the CST Microwave Studio, it is necessary to construct an actual antenna and subject it to testing. After calibrating the connection cable, measuring the S11 parameter is relatively simple once the antenna is linked to the network analyser. Nevertheless, far-field evaluations such as the axial ratio and gain are not as straightforward.

The electric field's azimuthal component, represented by E_{Φ}, and the polar component, denoted by E_{Θ}, can be experimentally ascertained. To accomplish this, the E_{Φ} component can be procured by stationing the receiving horn antenna unidirectionally at ϕ = 0° within the anechoic chamber, while concurrently rotating the transmitting antenna at various elevation angles θ (θ = 0º, 45º, 90º, and 360°). The disparity in received power must not surpass 3 dB, which is equivalent to the axial ratio. This methodology is reiterated for the quantification of the E_{Θ} component by orienting the horn antenna at ϕ = 90°.

When the complex voltage constituents in horizontal and vertical planes exhibit equal amplitude and are in phase quadrature (±90°), these elements can be amalgamated to delineate either the left-handed circular polarization or right-handed circular polarization wave components [9]. The extraction of RHCP and LHCP field components from the assessed radiation pattern has been executed in accordance with the following procedure:

$$E_{RHCP} = \frac{1}{\sqrt{2}}(E_H + JE_V) \tag{2.17}$$

$$E_{LHCP} = \frac{1}{\sqrt{2}}(E_H - JE_V) \tag{2.18}$$

where

$$E_H = H_a \cos(H_p) + V_a \sin(V_p) \tag{2.19}$$

$$E_v = H_a \cos(H_p) - V_a \sin(V_p) \tag{2.20}$$

and

$$AR = 10\log\left(\frac{|E_{RHCP}|+|E_{LHCP}|}{|E_{RHCP}|-|E_{LHCP}|}\right) \tag{2.21}$$

H_a and $V_a$signify the amplitude of horizontal and vertical constituents, whereas H_p and V_p denote the phase components ascertained in the far field for each respective orientation. To assess the antenna gain, a comparative technique has been employed, utilizing an additional horn antenna at the receiving terminus. The gain of the antenna can be derived from the known gain of the reference horn through the application of equations (1-7) [107].

$$G_{ant}\ in\ dB = G_{Horn}\ in\ dB + 10log_{10}\left(\frac{P_{ant}}{P_{Horn}}\right) \tag{2.22}$$

Chapter 3

Circularly Polarized Circular Loop Antenna Using Coplanar Waveguide Feed

3.1 Circularly Polarized Loop Antenna Design

3.1.1 Introduction

Circularly polarized (CP) planar antennas have become increasingly popular in wireless communications due to their unique advantages. One key benefit is their ability to minimize multipath effects, as highlighted in [31], thereby enhancing signal reliability. Additionally, CP antennas eliminate the requirement for precise alignment between transmitter and receiver antennas, a distinct advantage over linearly polarised (LP) antennas [32]. Unlike LP antennas, CP antennas effectively address polarization mismatch issues and mitigate interference arising from multipath reflections. This makes them a preferred choice for improving the robustness and efficiency of wireless communication systems.

Several approaches have been suggested for circularly polarized (CP) antenna design, including those employing multi-feed techniques, dual-probe feed methods, and using a perturbation to the antenna shape.

In [33], researchers introduced a compact dual-feed square patch antenna operating at 2.45 GHz. This design incorporated bent slots aligned parallel to the central line of the patch. Circular polarization was achieved by introducing a 90° phase shift between the two ports through a Wilkinson power divider, which records a λ/4 difference between its outputs. However, the adoption of a power divider and dual feeding accesses for generating left-hand circular polarization or right-hand circular polarization introduces signal losses. These losses can have a substantial impact on the overall efficiency of the antenna system. Furthermore, the utilization of such components increases both the complexity and cost of the system, particularly when operating at mmWave frequencies.

Numerous methods have been proposed to design and explore the characteristics of CP open-loop antennas. Researchers have employed a probe-fed CP loop antenna, as evidenced in studies such as [34-37]. For example, in [34], an open-loop antenna featuring circular polarization was introduced, employing a coaxial probe for operation at a frequency of 1.4 GHz. The antenna attained a 12% axial ratio (AR) bandwidth. The study accomplished a traveling-wave current distribution along the loop by incorporating a gap, leading to the generation of circularly polarized radiation. Similarly, in [35], a probe-fed circularly polarized (CP) antenna was demonstrated within X-band frequencies spanning 5.15 GHz to 5.85 GHz, achieving an axial ratio (AR) bandwidth of circa 16%. The study introduced a parasitic loop inside the original loop, enhancing the axial ratio bandwidth without a direct electrical connection to its surroundings. This approach has been adopted in this research design will be electromagnetically excited through the original loop, and thus, the bandwidth of the axial ratio can be increased. In [36], a different investigation centered on crafting a reconfigurable circularly polarized loop antenna intended for operation at 3.8 GHz, showcasing an axial ratio (AR) bandwidth of approximately 12.7%.

However, probe feeding encounters limitations at higher frequencies, particularly in the mmWave range, where fabricating antennas with reduced sizes becomes challenging due to the necessity of drilling holes in the substrate. Hence, the antenna's efficiency will be diminished, impacting the overall system.

This chapter explores the use of a circular open-loop antenna to achieve circular polarization. By introducing a gap perturbation along the loop circumference, the circular open-loop antenna can radiate a circularly polarized wave, whereas loop antennas inherently radiate linearly polarized waves [38]. To address the limited bandwidth issue of CP loop antennas compared to spiral antennas, the addition of a parasitic element inside the original loop significantly enhances the axial ratio (AR) bandwidth [39]. This parasitic element creates an additional resonance, effectively expanding the AR bandwidth without significantly increasing the size or complexity of the antenna structure.

Furthermore, the loop antenna has attracted considerable research interest owing to its uncomplicated design, cost-effective implementation, and adaptability for a range of applications, particularly at mmWave frequencies [40]. Beyond its simplicity, loop antennas are extensively employed in direction-finding applications for radar and UHF transmitters, showcasing their versatility. Moreover, they play a pivotal role in Radio-Frequency Identification (RFID) applications, underlining their significance in diverse technological domains. The appeal of loop antennas lies not only in their technical attributes but also in their broad applicability across various communication and sensing scenarios.

3.1.2 Contribution to this Chapter

The contribution of this chapter encompasses the following key aspects, highlighting its significance in the field of antenna design:

1. Design and Fabrication of a Cost-Effective CP Open-Loop Antenna: The chapter presents the development of a circularly polarized (CP) open-loop antenna fed by a coplanar waveguide port (CPW). This design is specifically tailored for operation at 6 GHz, offering a low-profile solution that is both efficient and economically viable.

2. Enhanced Axial Ratio Bandwidth through Concentric Parasitic Loop: To achieve wider bandwidth performance, the antenna incorporates a concentric parasitic loop within the outer loop structure. This addition effectively enhances the axial ratio bandwidth, allowing for improved circular polarization characteristics.

3. Wideband Matching and Excellent Radiation Efficiency: The proposed antenna design not only achieves wideband matching, covering a substantial frequency range, but also demonstrates radiation efficiency.

4. Facilitating Future mmWave Antenna Design: The overall performance verification of this antenna serves as a stepping stone toward the development and fabrication of antennas that operate in mmWave frequencies. By successfully designing and evaluating this CP open-loop antenna at 6 GHz, valuable insights and knowledge are gained, paving the way for future advancements in higher-frequency designs.

3.1.3 Chapter Organization

This chapter is structured as follows: Section 3.2 begins by introducing the configuration and design principles of the Circularly Polarized (CP) loop antenna. This is followed by Section 3.3, which delves into an in-depth study of the parameters associated with the antenna. In Section 3.4, a comparative analysis between the antenna with and without the parasitic loop is presented. Moving on to Section 3.5, the chapter details the prototypes, simulation, fabrication, and measurements of the proposed CP loop antenna. Subsequently, Section 3.6 offers a comparative performance analysis of the proposed configuration with existing counterparts documented in the literature. Finally, Section 3.7 provides a summary and concluding remarks for the chapter.

3.2 Antenna Configuration

In order to achieve CP radiation, the loop circumference needs to be approximately one wavelength [41]. This is because the traveling wave current is excited along the loop, which is the main cause of generating the circularly polarised wave.

When the circumference of a normal loop antenna is approximately one wavelength, the maximum linear polarization radiation appears in the broadside direction. However, the broadside linear polarization radiation can be changed to a circular polarization wave by perturbing the loop element with the insertion of an air gap along the loop circumference.

As shown in Figure 3.1, the CP antenna consists of two open wire loops placed above the lossy FR-4 substrate, with a size of 27×44×5.6mm and a dielectric constant of εr=4.3. The printed circular loops and substrate are mounted above a square copper plate that acts as a reflecting ground plane with a thickness of 1mm. As mentioned earlier, the antenna has been fed using a coplanar waveguide port (CWP) connected to the outer loop at φ=0, which acts as a driven loop, while the inner loop acts as a parasitic element. The width of the feed l2 and the distance l3 between the feed and grounded rectangular pads are optimized to be 0.93 mm and 0.56 mm for 50Ω matching, respectively. By adjusting the size of the parasitic loop and the positions of the two gaps (φ_1, φ_2), an optimal performance for the on-axis (in the z direction) axial ratio can be achieved.

The circumference of the outer loop can be calculated at the operation frequency of 6 GHz in terms of the effective wavelength, λ_{eff}, [20] by calculating, the effective permittivity as:

$$\varepsilon_{eff} = \frac{\varepsilon_r+1}{2}. \tag{3.1}$$

From this, the effective wavelength can be expressed as

$$\lambda_{eff} = \frac{\lambda_0}{\sqrt{\varepsilon_{eff}}}. \tag{3.2}$$

where λ_0 is the free-space wavelength Finally, the circumference of the outer loop should be approximately equal to λ_{eff} to achieve a CP and main beam in the broadside direction, i.e.

$$2\pi R_1 \simeq \lambda_{eff} \tag{3.3}$$

The antenna has been designed using CST and the optimized geometrical parameters for the wideband CP loop antenna are listed in Table 3.1.

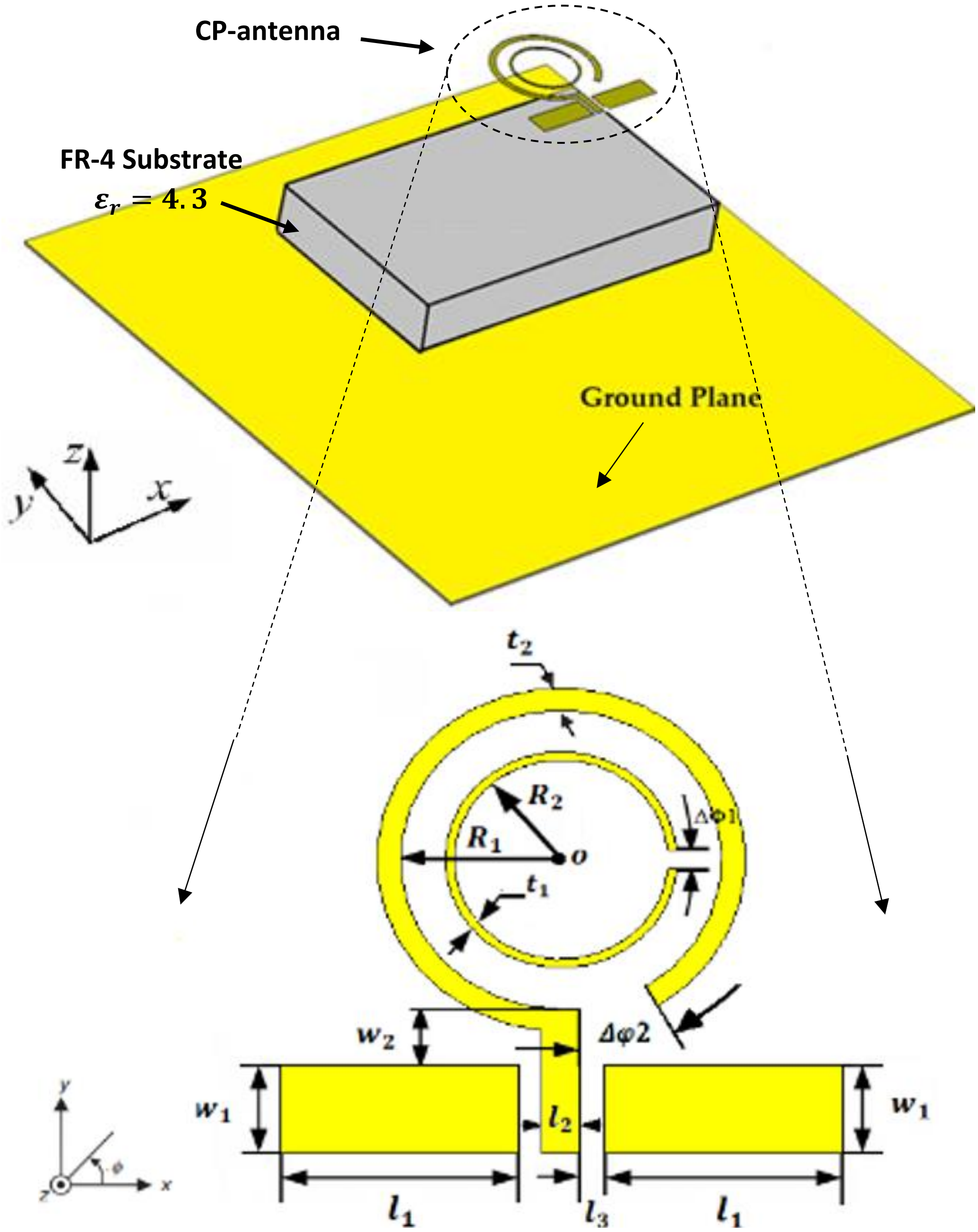

Figure 1.1: Geometry of circular loop antenna.

Table 3.1 Dimensions Parameters of the Antenna

Symbol	***Quantity***	***Value***
R_1	outer loop radius	5.85mm
R_2	parasitic loop radius	3.9 mm
t_1	outer loop width	0.744 mm
t_2	parasitic loop width	0.28 mm
l_1	pads length	7.44 mm
l_2	transmission line width	0.93 mm
l_3	the gap between the transmission line & pads	0.56 mm
w_1	pads width	3 mm
w_2	the width between the pads & outer loop	1.3 mm
a_0	antenna thickness	0.035 mm
h	The thickness of the substrate	5.6 mm
t	reflector thickness	1 mm
Subx	substrate length	44 mm
Suby	substrate width	27 mm
$\Delta\varphi_1$	parasitic loop gap	5^{O}
$\Delta\varphi_2$	outer loop gap	35^{O}

3.2 Parameters Study

This section will provide a thorough analysis of how the various parameters affect the CP antenna results. The term "parameters" refers to the different variables and factors that can influence the antenna's performance. These parameters can include the size and shape of the antenna, the thickness or type of substrate used, the outer loop gap size variation, and the ground plane effect, among others.

By examining the impact of these parameters, we can gain a deeper understanding of how the antenna functions and how it can be optimized for specific applications.

3.2.1 Impact of Varying Substrate Thickness

The antenna parameters were thoroughly investigated through simulations by methodically varying the substrate thickness (h) within a range of 1.6mm to 5.6mm for the circular loop antenna configuration. As a result, it becomes apparent that the resonance frequency demonstrates a slight downward trend as the substrate thickness (h) incrementally increases as shown in Figure 3.1. Simultaneously, Figure 3.3 illustrates a notable enhancement in the axial ratio bandwidth as the substrate thickness increases. This visualization effectively conveys the impact of substrate thickness on the antenna's characteristics, facilitating an in-depth understanding of their relationship and the implications on the overall antenna performance.

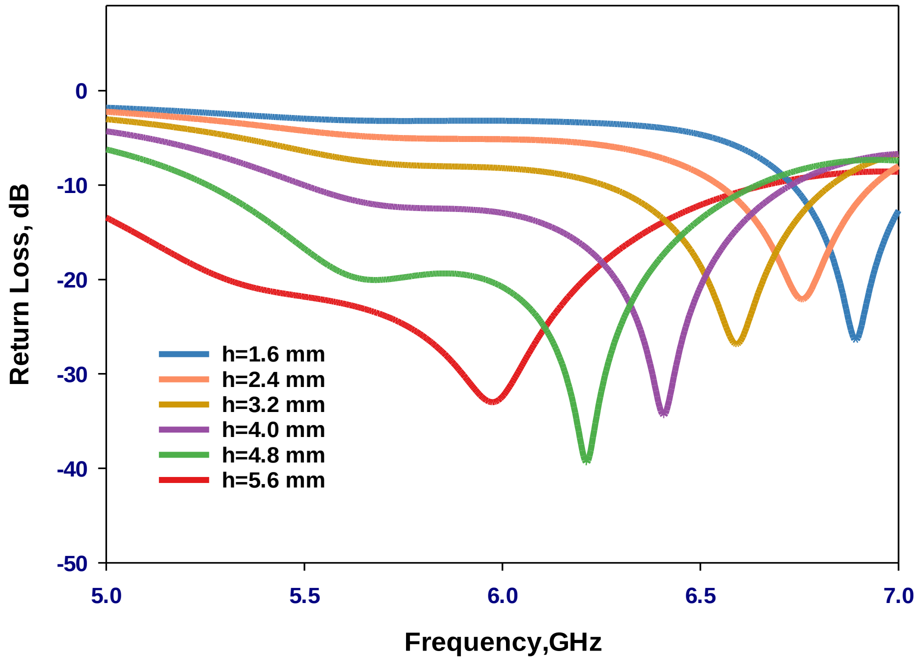

Fig.3.2: Performance of Return Losses Across Various Substrate Thicknesses

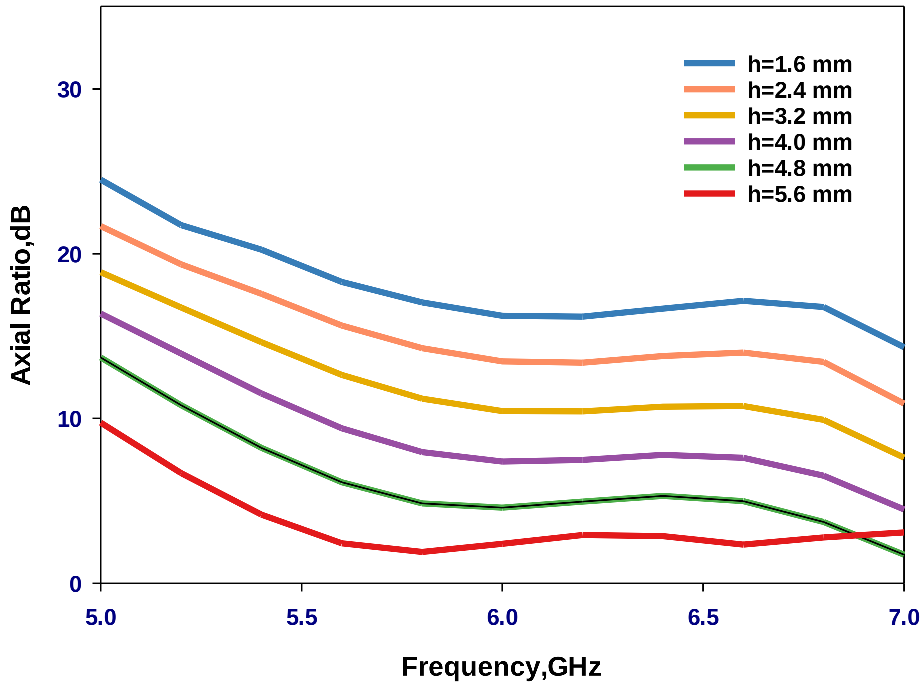

Figure 3.3: Variation of the axial ratio with different substrate thicknesses.

3.2.2 Impact of the Outer Loop Gap Size Variation

The wideband performance of the axial ratio is achieved by introducing a gap in the outer loop. Figure 3.4 shows the AR variation with different values of $\Delta\varphi 1$ between 5-35 deg. 25% of circular polarization bandwidth has been achieved when the gap size is about 35^o.

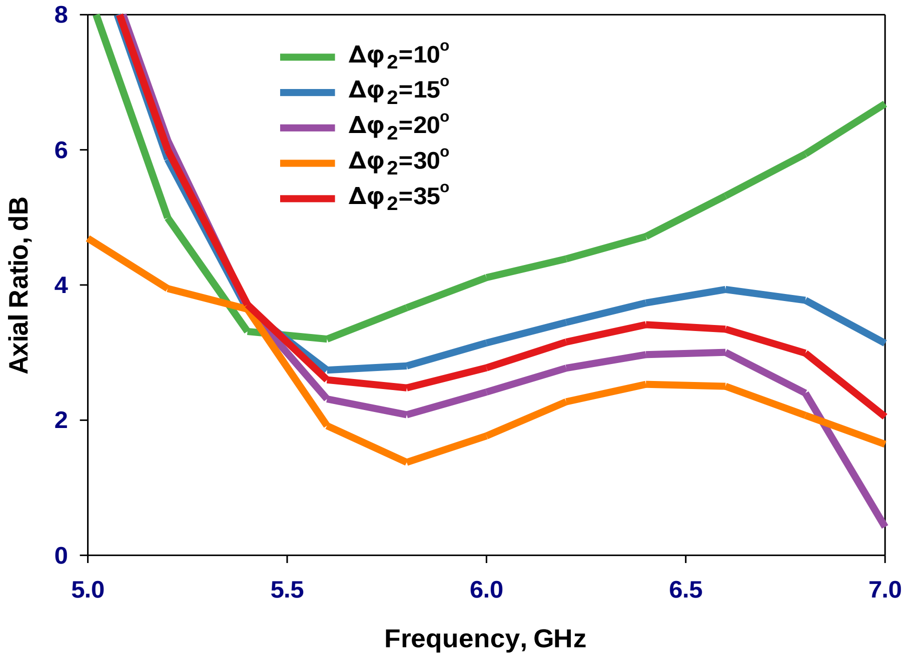

Figure 3.4: Axial ratio variation with different sizes of outer loop gap**.**

3.2.3 Ground Plane Effect on the Antenna Performance

The gain of an antenna is influenced by several factors, one of which is the size of the ground plane. Figure 3.5 presents a detailed comparison of the return loss and axial ratio performance for the antenna when paired with distinct square ground plane dimensions, specifically lengths of 60, 70, 80, 90, and 100 mm. The analysis demonstrates that the return loss maintains a relatively stable pattern across the various ground plane sizes. Additionally, the axial ratio is only slightly influenced by the alterations in the dimensions of the finite ground plane.

In Figure 3.6, the simulated gain corresponding to the differing ground plane dimensions, ranging from 60x60 mm to 100x100 mm, is depicted. The results clearly indicate a positive correlation between the gain and the expansion of the ground plane dimensions. As the size of the ground plane increases, the antenna system experiences a corresponding enhancement in gain, thereby potentially improving its overall performance.

The reason for this is due to several factors, the most important of which are reflections and surface waves. A larger ground plane provides a more extensive reflective surface for the radiating elements of the antenna. This increases the constructive interference of the reflected waves with the direct waves, leading to an enhanced radiation pattern and ultimately, higher gain. It is important to note that the relationship between ground plane size and antenna gain is not always linear, and other factors may also come into play. However, increasing the ground plane size generally results in an enhancement of the antenna's performance, including its gain.

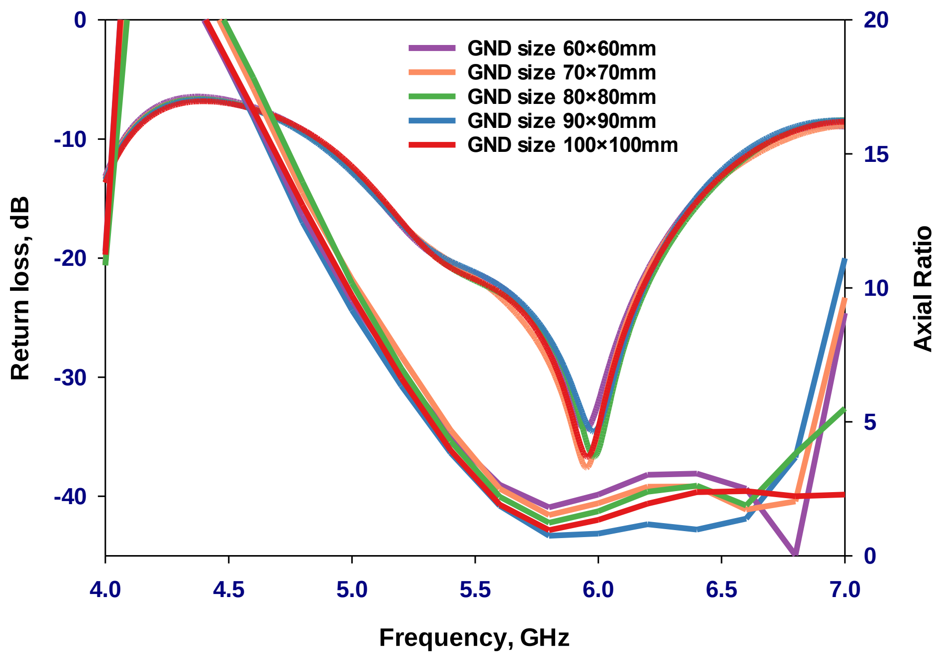

Figure 3.5: Simulated return losses and axial ratio for the antenna with different ground plane sizes.

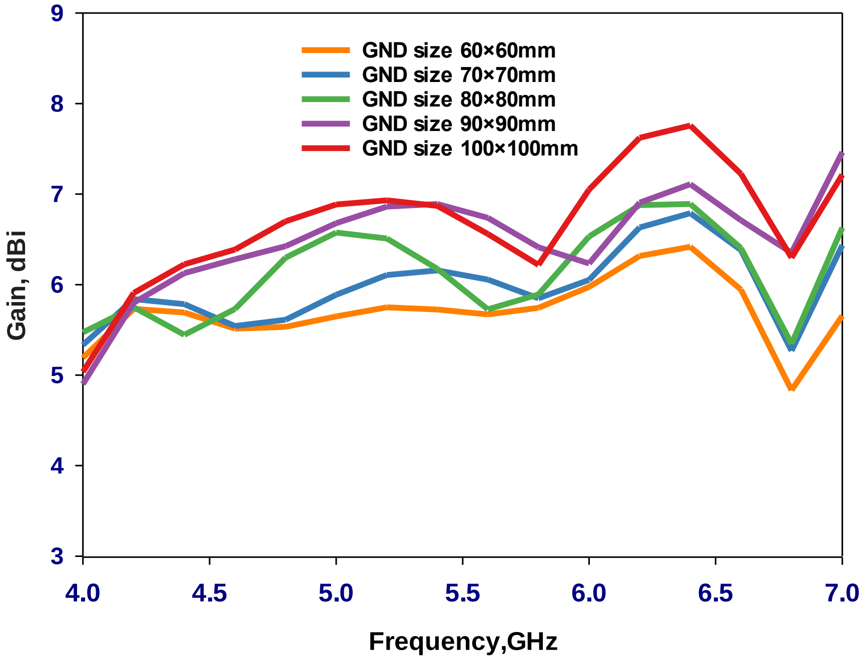

Figure 3.6: Simulated gain for the antenna with different ground plane sizes.

3.2.4 A Comparative Analysis of Configuration Antenna with and Without Parasitic Loop

The assessment of the antenna's performance is conducted by comparing scenarios with and without the inclusion of a parasitic loop. This comparison allows for a deeper understanding of the impact and effectiveness of the parasitic loop on the overall performance of the antenna system.

Figure 3.7 presents the simulated axial ratio and gain, comparing scenarios with and without the inclusion of the parasitic loop. Upon integrating the inner loop, the AR $\leq$ 3 dB bandwidth experiences a notable increase from 6.5% to 33%. Despite this improvement, the gain decreases by approximately 1.1 dBi, attributable to the coupling loss between the two loops. As anticipated, the parasitic loop significantly enhances the AR bandwidth, given that each loop generates an AR minimum. The merging of these two minima ultimately results in the observed bandwidth improvement.

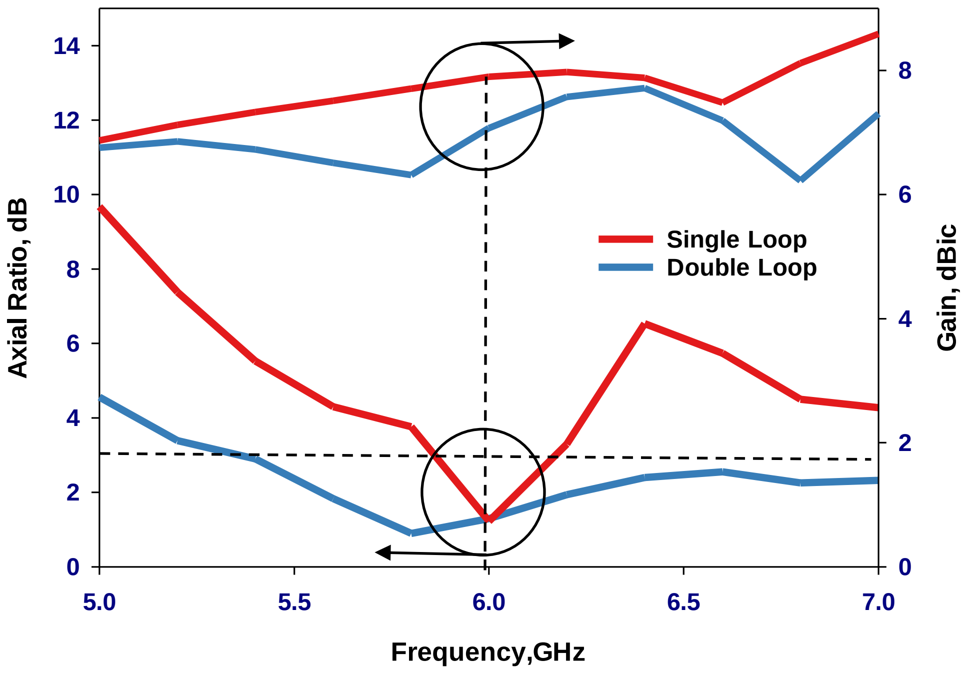

Figure 3.7: Simulated axial ratio and gain of single loop and double loop CP antennas.

3.3 Measurement and Analysis

This section presents the fabrication and measurement results. In the case of the proposed PCB antenna, an anechoic chamber was utilized to measure its radiation pattern and gain characteristics, employing both transmitting and receiving towers for the evaluation process as illustrated in Figure 3.8. The reflection coefficients were measured using a Keysight E5071C vector network analyser.

As illustrated in Figure 3.9, the proposed antenna is capable of providing an extensive impedance-matching bandwidth, approximately 32.3%, encompassing frequencies from 4.8 GHz to 6.67 GHz, for |S11| is less than -10 dB in the simulation. The measurement results, covering a frequency range from 4.9 GHz to 7 GHz.

Within the same figure, a minor discrepancy between the measured S11 results and the simulated values can be observed. This inconsistency might stem from the soldering process of the SMA connector, which could be the cause of the noted misalignment.

Additionally, Figure 3.9 presents the gain performance of the proposed antenna, highlighting the comparison between the simulated and measured results. At the operational frequency of 6 GHz, the antenna demonstrates a high gain, with the simulated outcome achieving approximately 7.05 dBic, while the measured result reaches around 6.7 dBic.

Figure 3.10 depicts a comparison between the measured and simulated axial ratio (AR) bandwidth, where AR is less than 3dB. Upon examination, it is evident that there is a strong correlation between the simulated and measured AR bandwidths, with values of 29% and 33%, respectively. This close agreement signifies the effectiveness and accuracy of the antenna's design and simulation process. The gain and axial ratio measurements are found to be consistent with the simulation results within the frequency range of 5 GHz to 7 GHz. The simulated result of the radiation efficiency is circa 79% at 6 GHz.

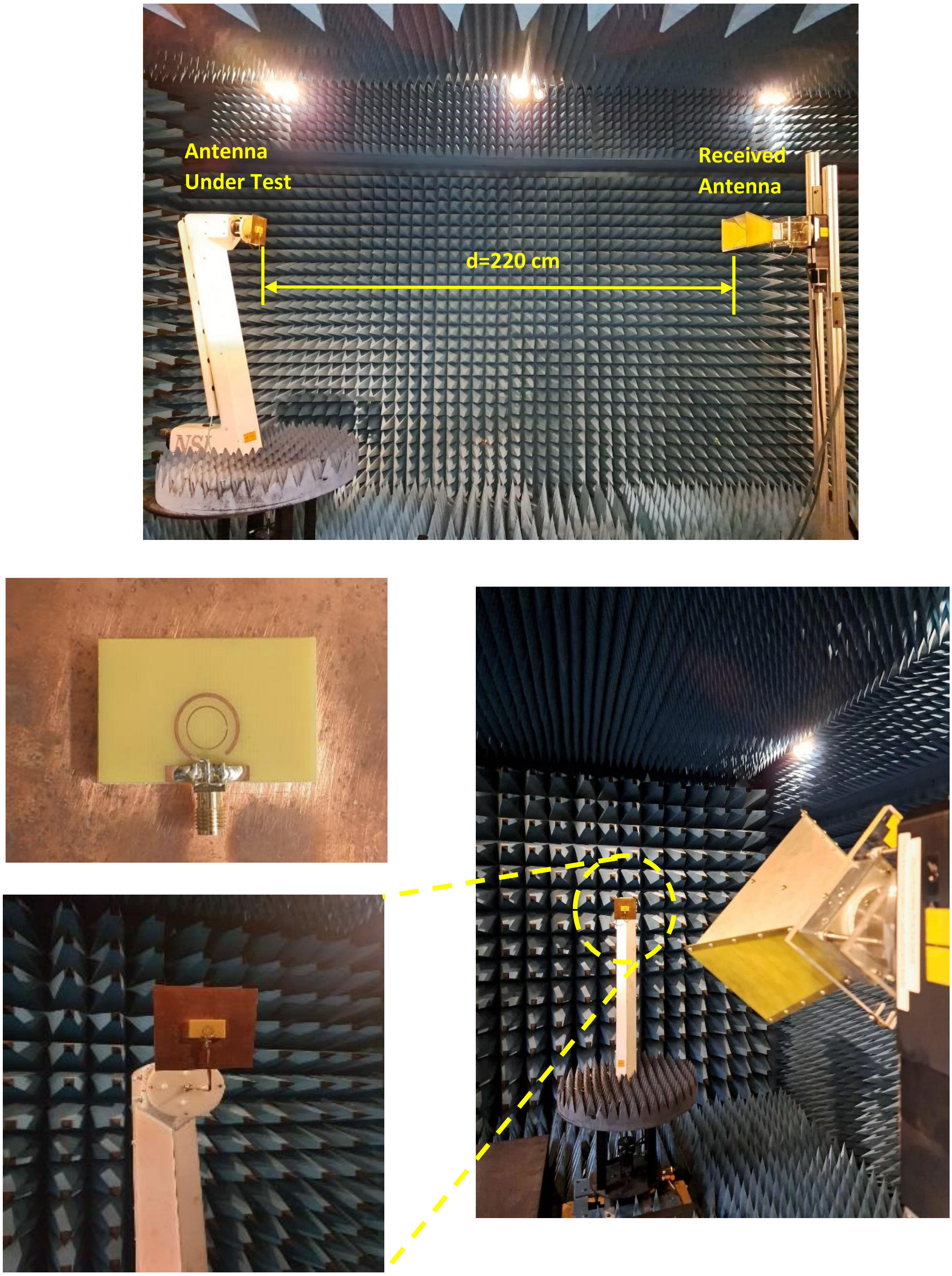

Figure 3.8: Photographs of the proposed antenna in a spherical measurement lab.

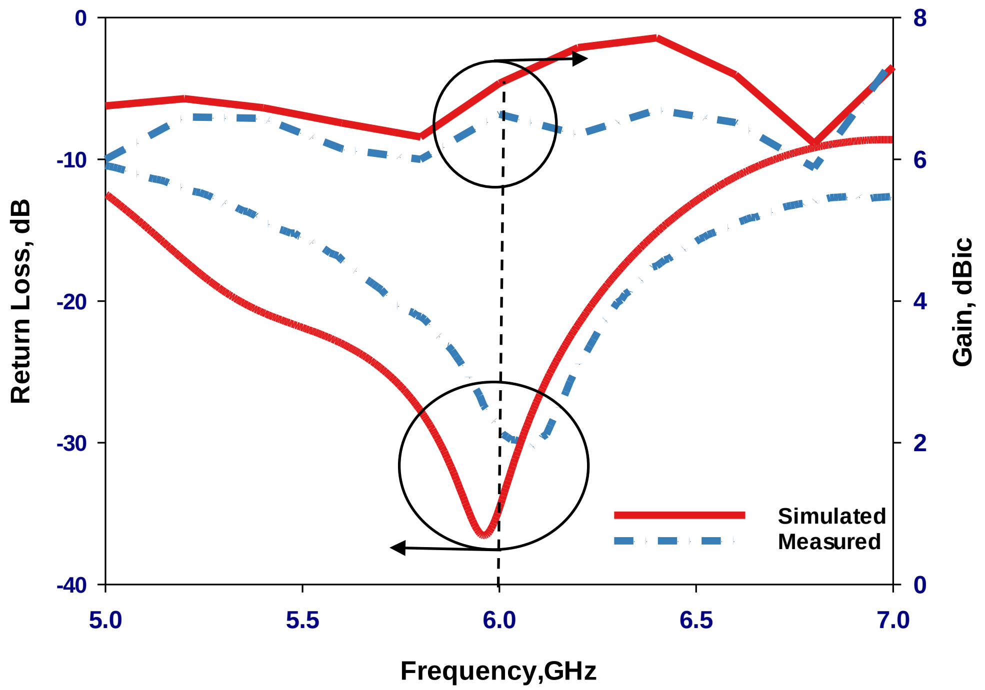

Figure 3.9: Measured and simulated performance return loss and gain of the proposed antenna.

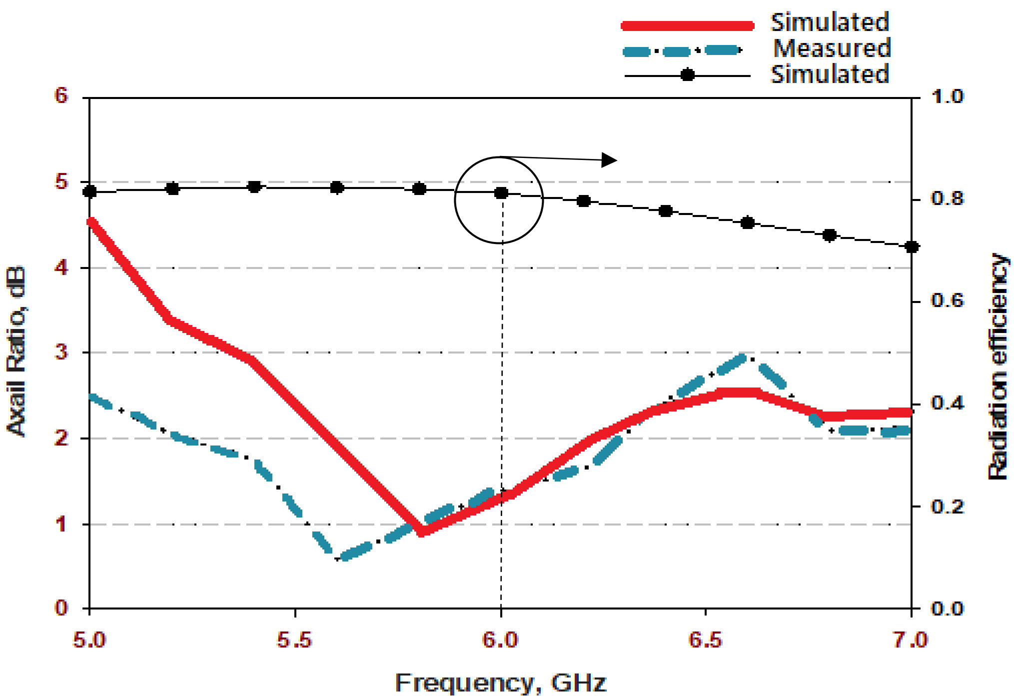

Figure 3.10: Measured and simulated axial ratio and total efficiency of the proposed antenna.

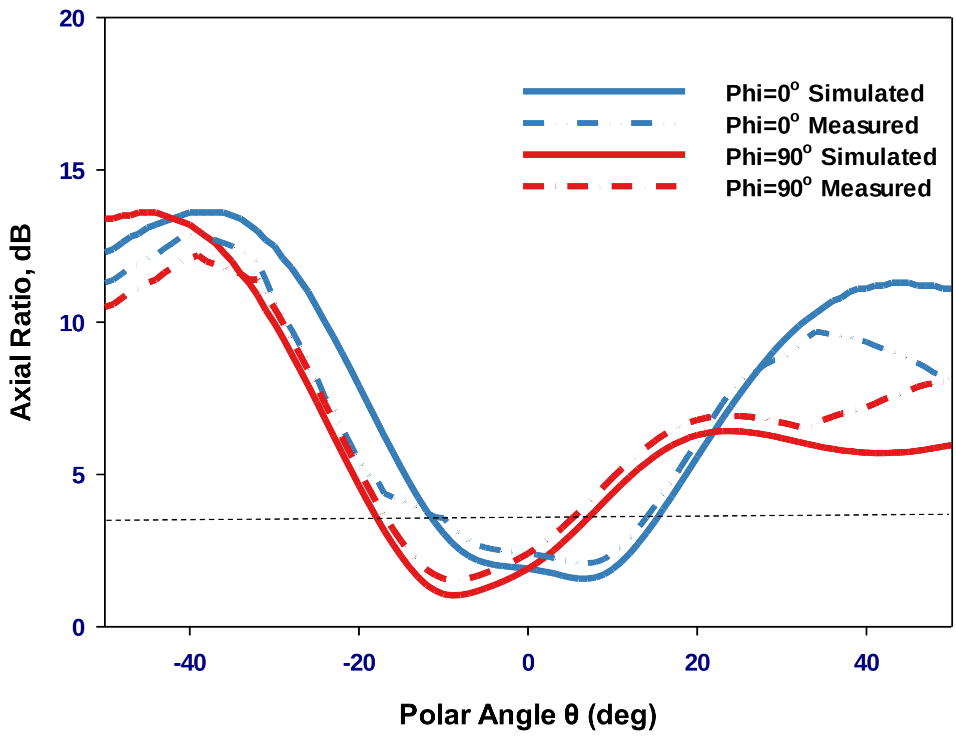

Figure 3.11: AR as a function of polar angle θ at 6GHz.

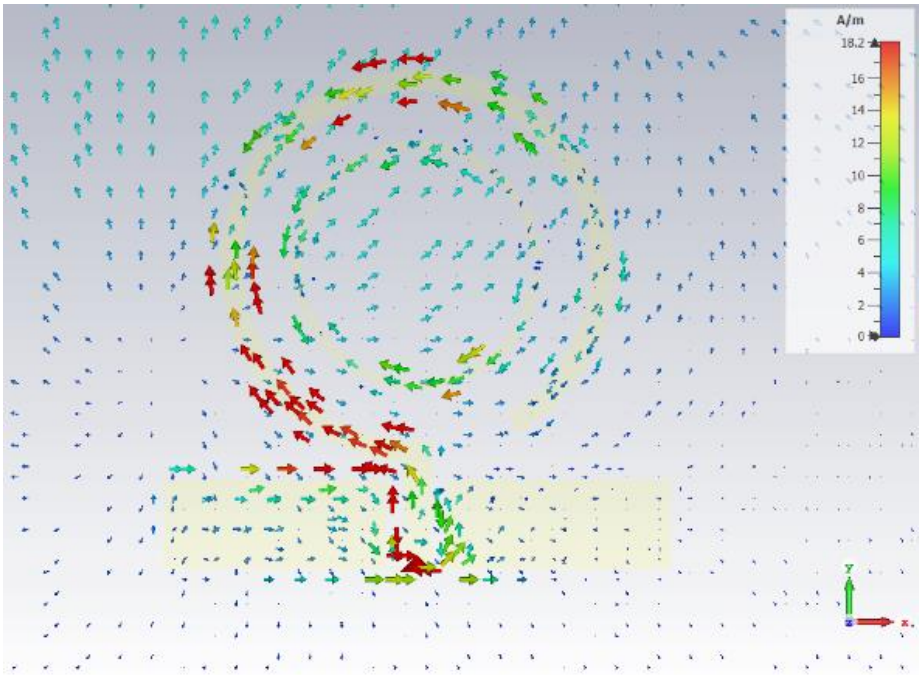

Figure 3.12: Travelling-wave current distribution along the loop.

Furthermore, Figure 3.11 illustrates the 3 dB axial ratio (AR) beamwidth of the proposed design at 6 GHz, showing a reasonable agreement between measurement and simulation. The measured and simulated AR beamwidths at θ=0° are (-9.8° to 13.5°) and (-10.5° to 14.5°), respectively. Similarly, at θ=90°, the measured and simulated AR beamwidths are (-17.5° to 4°) and (-18° to 5°). This alignment between measurement and simulation affirms the accuracy of the experiment, highlighting the significance of this research contribution.

In Figure 3.12, the simulated current distribution along the loop is illustrated, leading to LHCP. Circularly polarized waves display dynamic changes in both magnitude and direction during propagation. The current's amplitude fluctuates along the loop, gradually decreasing and taking on a spiral or helical path as it rotates around the propagation direction. This traveling-wave distribution generates the distinctive circular polarization pattern, with the direction (clockwise or anti-clockwise) determining the polarization sense.

Finally, the far-field radiation pattern for the Antenna Under Test (AUT) has been measured. The horn antenna is used as a reference antenna for this purpose. Both antennas' apertures are parallel to the XY-plane, ensuring that the measurements are made in the same plane. The tests are conducted with the horn antenna at two different positions: 0° and 90°. At 0°, the E-field (electric field) of the horn is in the y-direction, and at 90°, the E-field is in the x-direction.

The E_L & E_R measured and simulated radiation patterns at 6 GHz and phi=0° are presented in Figure 3.13 as evidenced by the fact that the E-field component in the left-hand direction (E_L) is greater than the E-field component in the right-hand direction (E_R) by approximately 8 dB.

Figure 3.14 compares the measured radiation pattern at 5.8 GHz and 6 GHz with the simulated radiation pattern of the proposed antenna. The good agreement between the simulation and measurement results validates the accuracy of the simulation model.

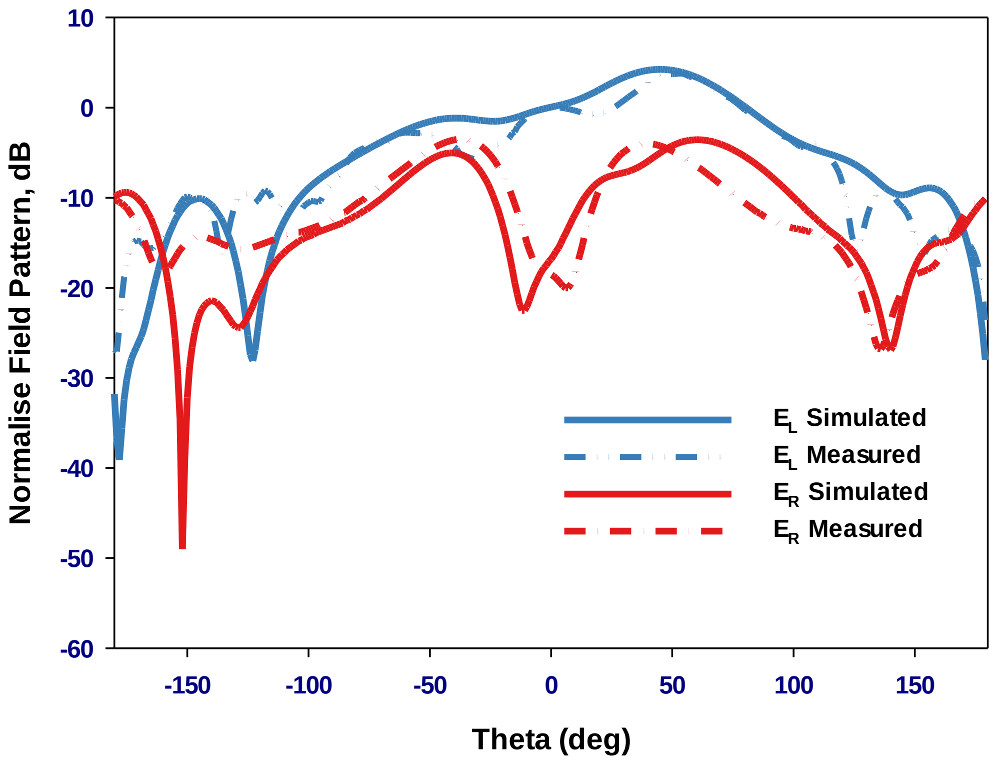

Figure 3.13: EL & ER radiation patterns function at 6GHz and Phi =0°.

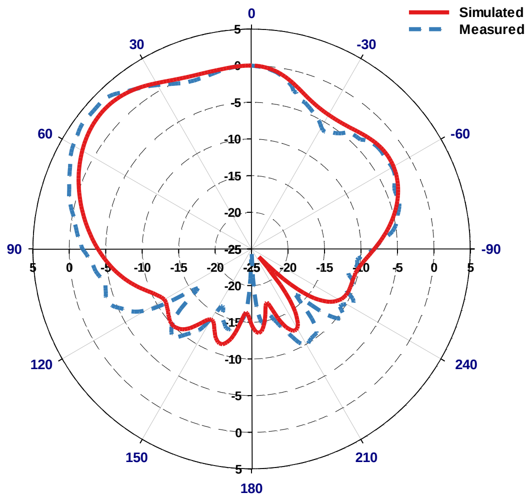

XOZ of 5.8 GHz

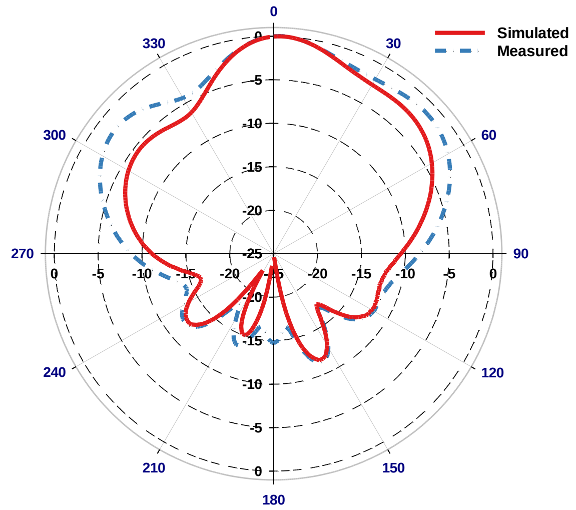

YOZ of 5.8 GHz

(a)

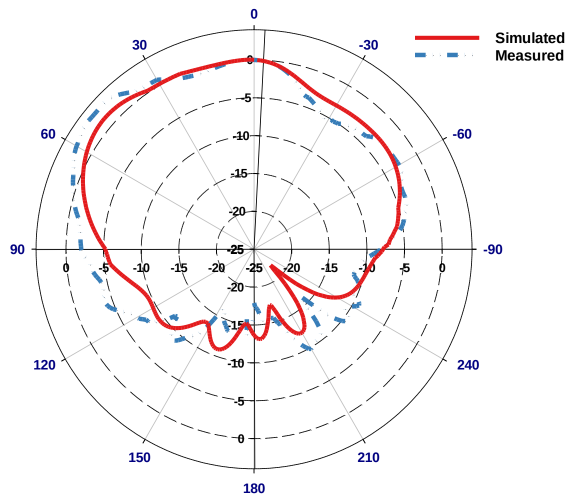

XOZ of 6 GHz

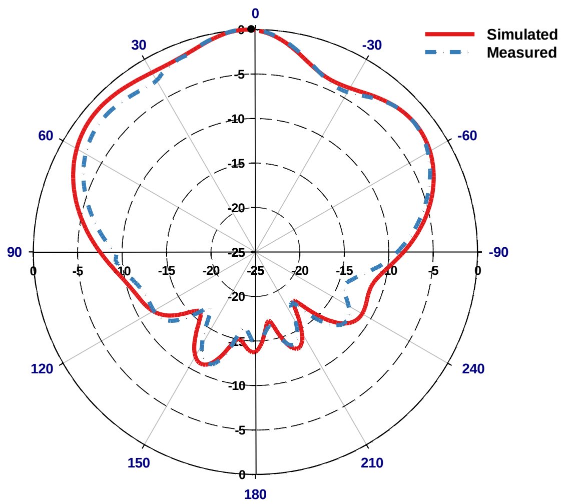

YOZ of 6 GHz

(b)

Figure 3.14: Simulated and measured XOZ-plane and YOZ-plane normalized E-plane radiation patterns (a) at 5.8 GHz, (b) at 6GHz.

Table 3.2 Performance Comparison of the Proposed CP Loop Antenna Those Reported in the Literature

Ref.	**Type of antenna**	**Feeding structure**	**Operating Frequency**	**S_{11} bandwidth**	**AR bandwidth**	**Peak gain (dBic)**	**Antenna efficiency**
[4]	Loop	Probe-fed	1.4 GHz	**	16%	6	**
[5]	Loop	Probe-fed	5.15 GHz to 5.85 GHz	**	16%	6	**
[6]	Loop	Probe-fed	3.8 GHz	**	12.7%	7	**
[7]	Loop	Probe-fed	5 GHz to 6.5 GHz	31%	21%	7	**
This work	**Loop**	**CWP**	**5 GHz to 7 GHz**	**32.3%**	**33%**	**7**	**>79%**

** The values were not supplied.

Table 3.2 presents a comprehensive comparison of the performance between the proposed CP loop antenna and various designs documented in the literature. The findings from this table reveal that the proposed CP loop antenna exhibits commendable impedance and AR bandwidths within the frequency range of 5 GHz to 7 GHz. Notably, our antenna design boasts a low profile and is cost-effective, employing CWP feeding as an alternative to the probe feed structure used in the designs presented in the comparative studies.

The presented design showcases an impressive AR bandwidth of approximately 33%, outperforming the results reported in all the aforementioned comparisons. Furthermore, our design achieves an antenna efficiency surpassing 79%, while the efficiency of the designs in the reported comparisons remains undisclosed.

3.4 Summary

In the 6 GHz UNII band, a wideband CP circular loop antenna has been successfully developed, showcasing an impressive AR bandwidth exceeding 33%. The integration of a parasitic loop has played a crucial role in significantly expanding the AR bandwidth and achieving LHCP radiation. The antenna's structural simplicity and CP sense flexibility, combined with the utilization of CWP feeding instead of the probe feed structure, make it highly suitable for a broad range of wireless communication applications, particularly at mmWave frequencies.

The experimental results highlight that the proposed antenna exhibits exceptional radiation efficiency, reaching circa 79%, accompanied by a gain of ~6.7dBic. These findings underscore the antenna's efficacy and further emphasize its potential for advanced wireless communication systems.

Chapter 4

Circularly Polarized Millimeter-Wave Phased Array Antenna Using Time Delay Transmission Line.

4.1 Circularly Polarized Array Antenna Design

4.1.1 Introduction

Currently, there is an ever-increasing demand for higher data rates to support bandwidth-hungry applications driven by the Internet of Things (IoT) devices [41]. This has motivated researchers to move to higher operational frequencies such as the mmWave bands to meet the requirements of high data rates [42]. However, mmWave signals face several technical challenges such as high propagation attenuation, high directivity requirements, atmospheric absorption, and sensitivity to blockage [43]. Therefore, innovative approaches and insights in the architecture and design of mmWave systems are required to cope with these challenges. To this end, high-gain antennas have been investigated using various configurations, including the Yagi-Uda structure [44], backing cavity [45], superstrate antenna [46], lens antenna [47], metamaterials [48], parasitic elements [49], and arrays [50]-[59]. Among all these design techniques, antenna arrays represent the most widely used approach to increasing the gain. [60]. Besides, beam-scanning antennas are widely used in military and civilian sectors because of their flexibility and agility in beam pointing as well as their ability to seek and track target signals on moving carriers [61]. Due to the advantages of minimizing the impact of polarization mismatch and mitigating multipath interferences, antenna arrays with circularly polarized elements are preferable in comparison to those utilizing linearly polarization. Additionally, a CP phased array antenna has the potential to improve the signal quality in transmission and reception. Therefore, CP beam-scanning represents a key technology for several wireless systems applications such as satellite communications, remote sensing detection, electronic jamming, radar, and navigation.

However, the achieved AR bandwidth depends on the utilized antenna element's CP bandwidth and on the performance of the sequentially phase rotated feeding network. Further, the main beam's AR may deteriorate when the scanning angle is shifted away from the broadside direction. Therefore, achieving CP antenna arrays with wide AR scanning angles represents a challenge. To this end, several methods have been proposed to design and explore various design criteria for CP phased array antennas [62-65]. Specifically, the use of sequentially rotated CP spiral antenna elements operating at X-band frequencies [62]. Additionally, a CP phased array of dielectric resonator antenna (DRA) elements working at 10.5 GHz, has been proposed with a main beam scanning range of 22° [63]. Furthermore, a CP beam-scanning approach has been explored using an air-filled substrate-integrated waveguide in the 12-18 GHz frequency range, with scanning angles between 28° and -13° [64]. Additionally, a space-fed multi-beam reflect array reconfigurable patch array antenna operating at 3.65 GHz has been proposed in [65]. Despite the encouraging outcomes of utilizing circularly polarized beam-scanning antennas, a number of technical challenges persist that must be resolved. One prominent issue is the lack of a low-complexity design that is both feasible and practical for real-world implementation. Addressing this challenge is crucial for the widespread application and adoption of CP beam scanning antennas. As an array element, the loop antenna offers several advantages over other counterparts such as the easiness of fabrication, implementation simplicity, and low cost [66]. These advantages mean the loop antenna can be utilized easily as an array element in many wireless applications. However, most of the reported loop antenna arrays offer linear polarization or dual linear polarizations, which is also the case for patch antennas [67]. On the other hand, there are few papers that are focused on CP arrays, especially with respect to beam steering. For example, an X-band CP-linear array of 10 sub-array elements was proposed with a broadside gain of 17.4 dBic and a CP beam steering range of ±15° [68]. Hence, the work does not address the challenge of operating at the higher frequency, i.e., mmWave, bands and thus, falls short of predicting the system performance in this preferred scenario. In another study, a 2×2 DRAs array was designed to operate in the X-band frequency range, i.e. at 10.5 GHz, and the results demonstrated a monotonic CP beam scanning from −22° to 22° albeit with a lower array gain of ~6.6 dBic [69]. Besides, the antenna is designed for the X-band, hence bulk production is complex and costly at mmWave frequencies due to the required precise alignment and bonding of each DRA. Furthermore, a 1× 8 stacked CP patch elements phased array antenna was designed with a beam scanning range of ±45°at a low-frequency band of 3.5 GHz [70]. In that paper, the importance of achieving AR while steering the beam at the desired angle has been emphasized. However, the variation of the 3 dB AR bandwidth as a function of the scanning angle (θ) has not been presented. In addition, the CP radiation is based on using PIN diodes since a CP patch was designed using reconfigurable 2-bit phase states. Hence, using a large number of PIN diodes may be complicated and costly to manufacture and bias at mmWave frequencies. Moreover, a CP tightly coupled mmWave array with chamfered corners and etched cross-slot patch elements was reported in [71], with a simulated 3 dB AR bandwidth of 15%. Nevertheless, the achieved CP beam steering has not been verified experimentally.

Furthermore, many of the reported CP loop antenna designs are focused on a probe-fed loop antenna [72-74] with usually wider CP bandwidths that are associated with a high antenna's profile. For example, a study focused on designing a CP loop antenna for the C-band frequency range, specifically at 6 GHz, demonstrating an AR bandwidth of around 15.3%

albeit with a voltage standing wave ratio (VSWR) that exceeds 2 over the achieved CP bandwidth [73]. Another wideband probe-fed CP loop antenna, operating at 2.5 GHz, was reported in [74] with an overlap of ~15% between the CP and impedance bandwidths. However, the wide bandwidths of those probe-fed loops were achieved using a high antenna profile of $0.2\lambda_0$-$0.25\lambda_0$, which can be impractical for many applications, especially at mmWave frequencies.

Based on the above literature review, it can be observed that a viable CP antenna array design that is feasible for high operational frequencies is needed. In addition, and to the best of our knowledge, a study of the involved design and measurements of mmWave phased array that can achieve CP beam scanning has not been investigated earlier.

In this study, a low-profile phased array of CP-circular loop elements is designed and fabricated to provide a CP beam steering range of ±25° at 27.5 GHz using a coplanar waveguide port (CWP). This has been achieved based on the wideband CP and wide-angle scanning characteristics of the loop antenna. To this end, a 1 × 4 LHCP linear array antenna based on the proposed circular loop elements is fabricated and measured. Comprehensive simulation and measurement results are presented to demonstrate the effectiveness of the proposed antenna design. Achieving precise control of beam steering across a range of angles involves the utilization of a corporate feed network in conjunction with four-phase shifters that apply advanced transmission line time delay techniques. This approach enables the fine-tuning and adjustment of the main beam direction with high accuracy, ensuring optimal performance. The results demonstrate that the proposed CP phased array achieves promising performance in terms of the respective impedance and AR bandwidths of 10.9% and 8% over the same frequency range in combination with a scanning angle range of ±25°. This is combined with a high gain of up to 11 dBic over the CP beam scanning range. The results demonstrate that the proposed CP phased array antenna could be useful for mmWave applications and practical implementations such as satellite and wireless communications systems.

4.1.2 Contribution to this Chapter

In light of the challenges mentioned above, we outline the following key contributions of the presented work:

1. A cost-effective, low-profile, CP single-loop antenna is designed and fabricated for the millimeter-wave frequency range. The proposed antenna design incorporates two concentric loops, with the outer loop serving as the active element and the inner loop enhances the CP bandwidth. This design delivers commendable performance characteristics in terms of both return losses and axial ratio bandwidths.

2. Four-phase shifters are implemented using the transmission line time delay technique. The phase shifters enable beam steering at various angles by controlling the phase of the electromagnetic wave.

3. A 4-element open loop array antenna is created to achieve CP beam steering over a range of ±25°. In addition, the low-cost design offers a high gain of 11 dBic using a considerably reduced number of elements compared to the designs reported in the literature. The reduced number of elements means a simpler and efficient feeding network can be utilized. Furthermore, the beam steering capability increases the range and efficiency of the antenna.

4.1.3 Chapter Organization

This chapter is organized as follows; Section 4.2 introduces the configuration and design principles as well as the simulation and measurement results of the single-loop element configuration. Sections 4.3 and 3.4 presents the methodology of the proposed phased array antenna design. The prototypes, simulation, fabrication, and measurements of the proposed antenna arrays are presented in Section 4.5. The performance of the proposed configuration is compared to counterparts in the literature in Section 4.6. This chapter is summarized in Section 4.7.

4.2 MmWave Circularly Polarized Antenna Design and Configuration

This section discusses the proposed designs of single and array antennas and configurations with the aim of achieving a CP beam-steering by changing the excitation phase of the individual elements. The simulations were implemented using the Computer Systems Technology (CST) Microwave Studio.

4.2.1 Design of Circularly Polarized Single Element

For the design of a single element, three-layers are used that include the actual antenna, Rogers RT/Duroid 4003C substrate with a dielectric constant of εr=3.55 and a loss tangent of $\tan\delta$=0.0027, as well as a copper ground plane. The substrate size is 37 mm × 40 mm × 0.508 mm and the geometrical parameters of the circularly polarized loop antenna are listed in Table 4.1.

Figure 4.1 illustrates the geometry of the proposed wideband CP antenna element. The printed circular loop and substrate have been mounted above a square copper plate, i.e., the wafer backplane, which acts as a reflecting ground plane. The proposed antenna consists of two concentric loops in which the outer loop represents the active element. Besides, the antenna radius needs to be selected so that the loop's circumference is approximately one effective wavelength, λ_{eff} which has been achieved according to the dimensions in Table 4.1.

The outer loop gap, $\Delta\varphi_2$, is optimized to establish a traveling wave current distribution along the loop, which is essential to achieve the circular polarization. Besides, the inner loop has been chosen with a smaller gap to enhance the CP bandwidth.

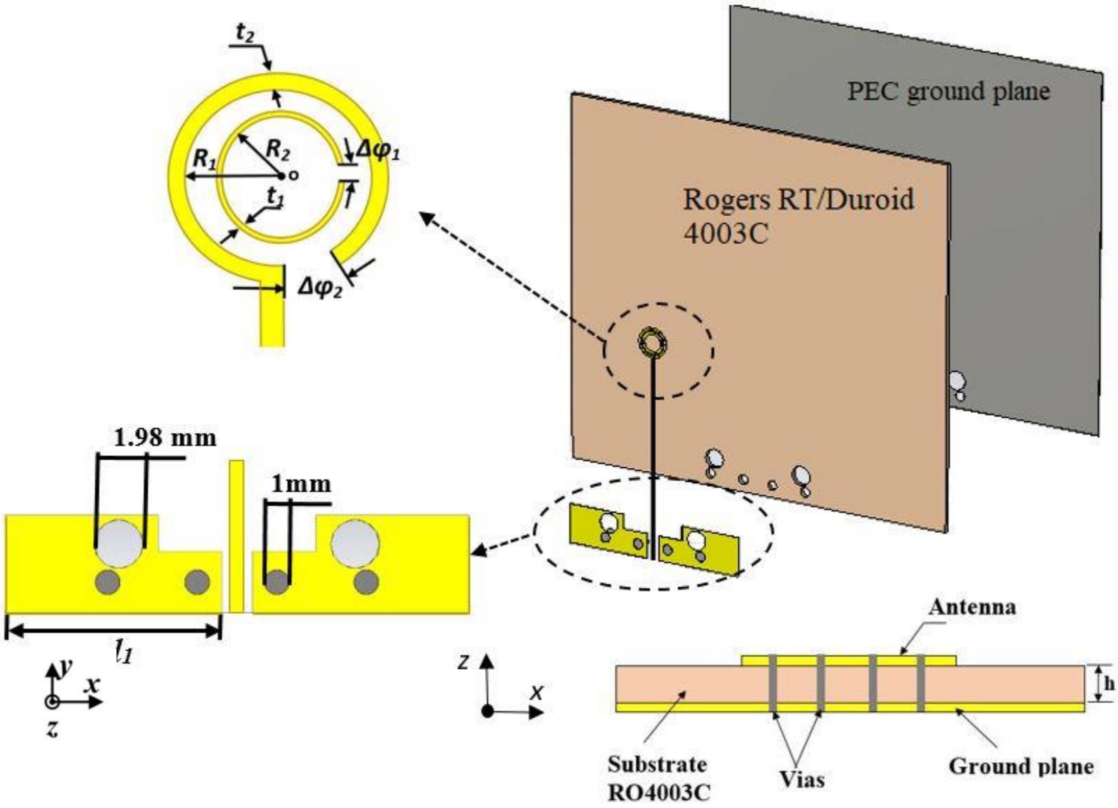

Figure 4.1: The geometry of the proposed wideband CP antenna element.

Figure 4.2(a) illustrates the measured and simulated return losses of the proposed single element, where a reasonable agreement can be observed between the measured and simulated data, indicating the accuracy of the measurements. Furthermore, the results indicate that the proposed element exhibits a relatively wide bandwidth, as evidenced by the recorded measurement results of approximately 8.2% compared to the simulation result of 8.1%, both centered at 27.5 GHz.

In Figure 4.2(b), the antenna performance is evaluated in terms of axial ratio bandwidth and gain. The results indicate that the proposed antenna exhibits relatively wide measured and simulated CP bandwidths of approximately 4.7% and 4.4%, as determined by the 3 dB criteria. This means that the antenna maintains a constant polarization purity over a relatively wide range of frequencies. Furthermore, the measured and simulated single antenna's gains are ~6.1 dBic and 6.7 dBic, respectively.

Table 4.1 The Parameters of the Proposed Antenna

Symbol	Quantity	Value
R_1	Outer loop radius	1.25 mm
R_2	Parasitic loop radius	0.9 mm
t_1	Outer loop width	0.2 mm
t_2	Parasitic loop width	0.24 mm
l_2	Transmission line width	0.24 mm
l_3	Gap between the transmission line & pads	0.28 mm
a_0	Antenna thickness	0.035 mm
t	Reflector thickness	0.035 mm
$\Delta\varphi_2$	Outer loop gap	0.16 mm
$\Delta\varphi_1$	Parasitic loop gap	0.2 mm

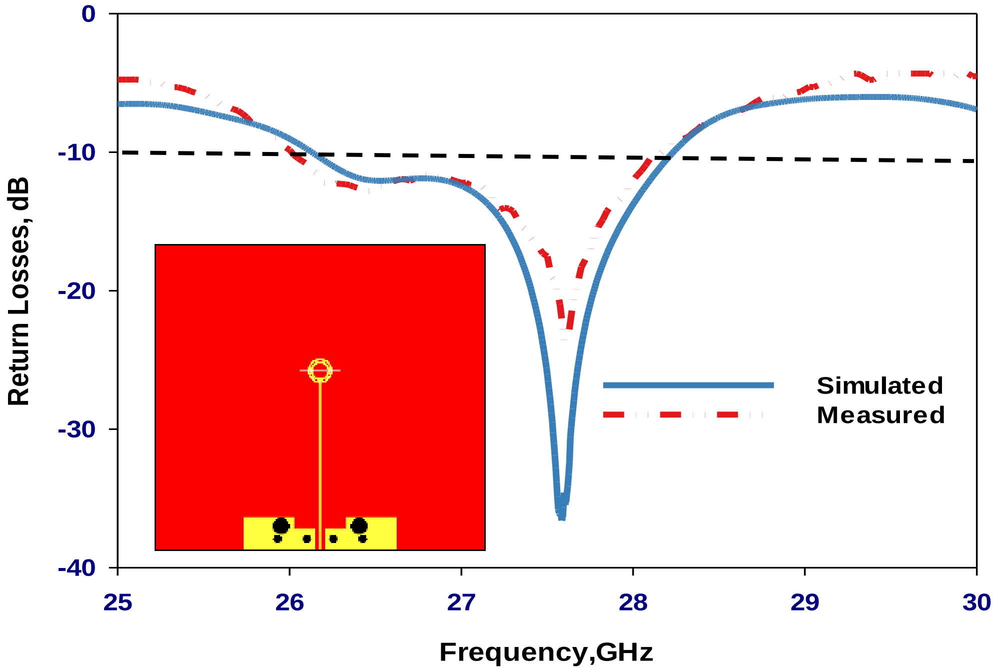

(a)

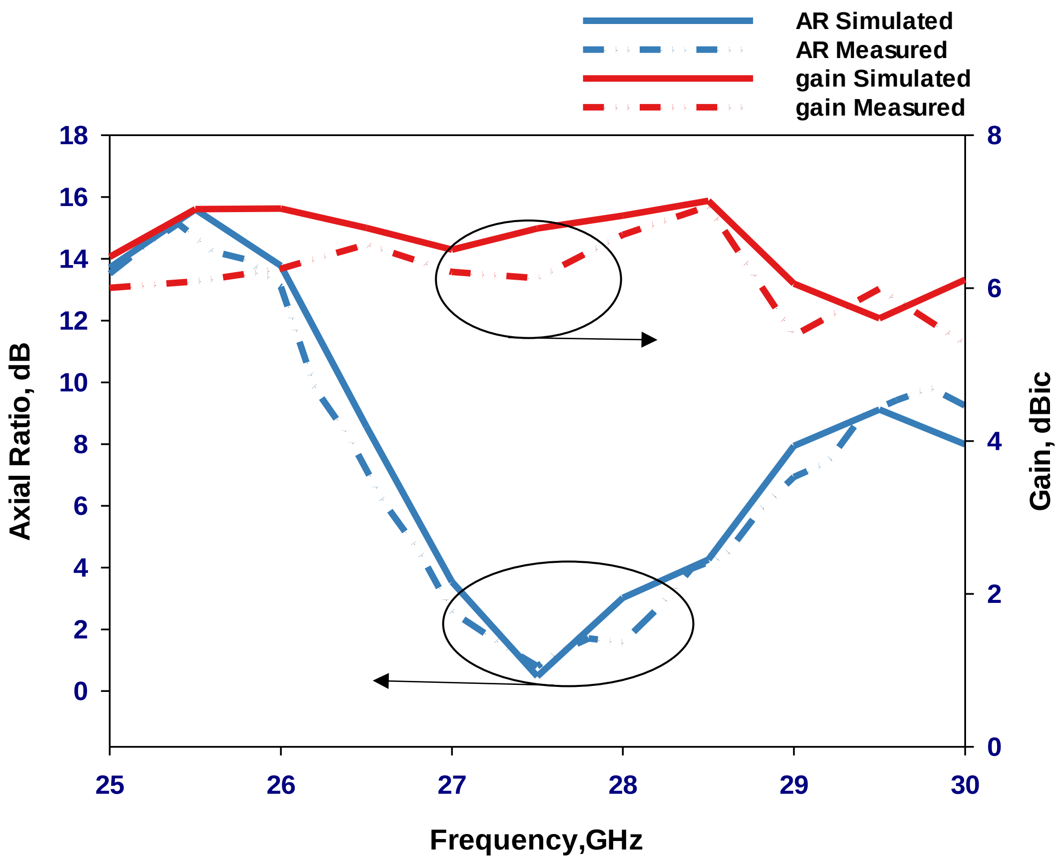

(b)

Figure 4.2: Simulated and measured results of the single loop (a) Return losses (b) AR and gain.

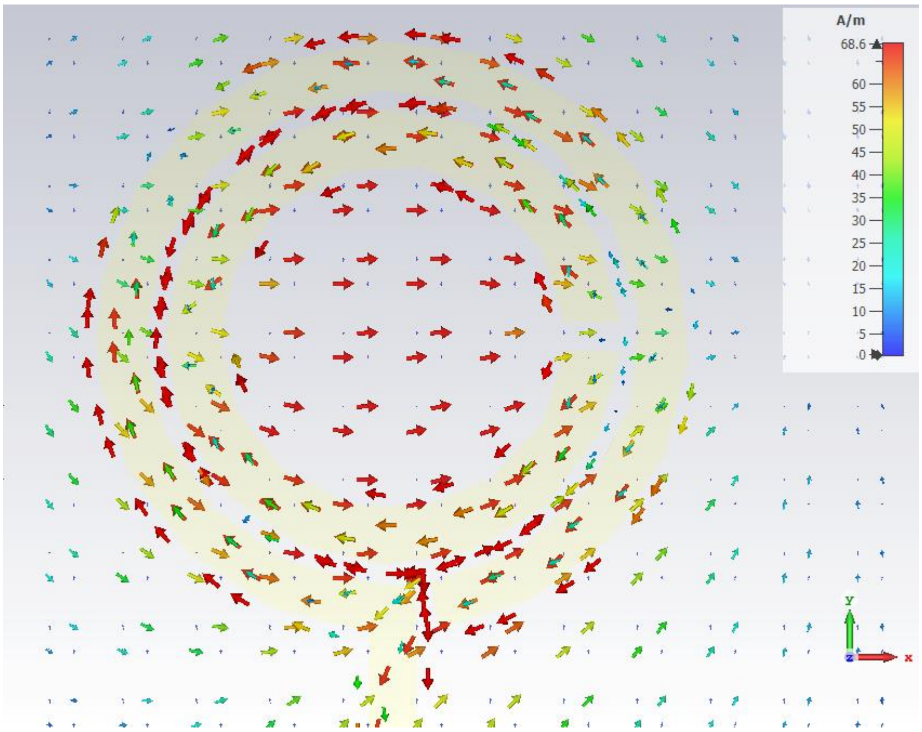

Figure 4.3: Depiction of current distribution within the circular loop.

Figure 4.3 depicts the current distribution within the circular loop. The circularly polarized far-field can be represented in terms of the right-hand, E_R, and left-hand, E_L, field components. At the same time, Figure 4.3 indicates a clockwise traveling-wave current, which results in an LHCP wave in which E_L is greater than E_R by about 13.16 dB. The results demonstrate that the proposed antenna element satisfies the requirements of Ka-band frequencies in terms of return losses, size and bandwidth. Overall, the study suggests that the simulated and measured results are approximately matched. Additionally, the proposed antenna offers favorable outcomes, which has inspired further research into CP beam scanning utilizing 4-element antenna arrays.

4.3 CP Array Design Methodology

4.3.1 Structure of Using True Time Delay for Beam Direction

In the phased antenna array, a time delay is needed for beam steering. However, a time delay can also be emulated with a phase shift, which is quite common and practically implemented in many applications [75]. As illustrated in Figure 4.4(a) phase shift can be achieved using transmission lines with different electrical lengths. If the insertion phase, i.e., the phase of S21, of the two lines are Φ_1 and Φ, respectively, the phase shift can be expressed as $\Delta\Phi = \Phi - \Phi_1$. In the proposed design, a parallel feed network has been preferred and used instead of a series feed network, which is typically simpler to design and implement. Within this parallel feed network, each arm of the feed network can be adjusted to provide the desired phase shift. Furthermore, parallel feed networks can be more efficient in terms of power distribution since they maintain a consistent voltage level across all elements. Conversely, series feed networks can introduce power losses due to impedance mismatches and variations in voltage distribution.

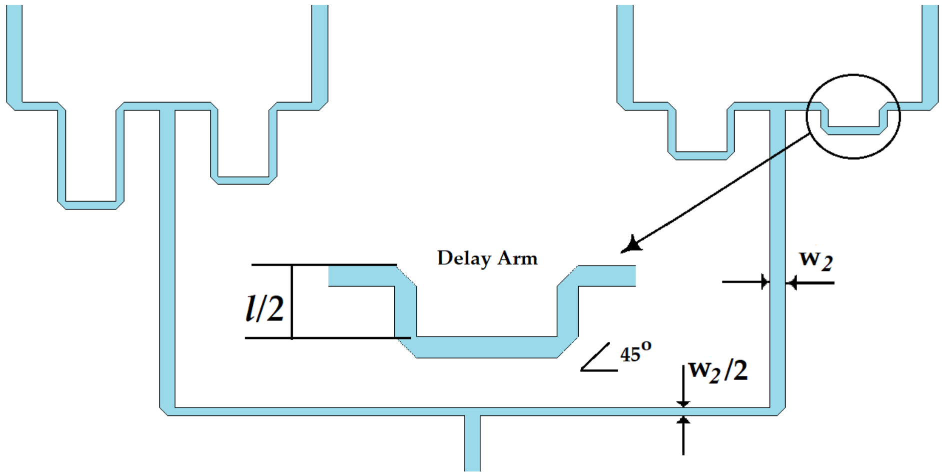

(a)

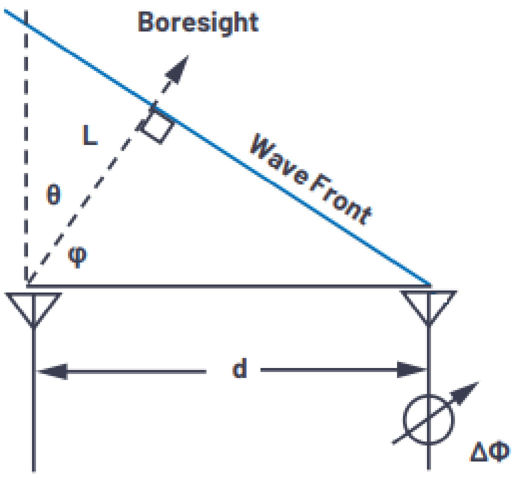

(b)

Figure 4.4: (a) Corporate feed network connected to phase shifters of the proposed antenna. (b) Derivation of phase shift ΔΦ as a function of the required beam steering angle [75].

To achieve noise reduction and improve the performance of the array, 45° angle bends of transmission lines are proposed as shown in Figure 4.4(a) [75]. When a transmission line is bent by ~90˚, small positive and negative charges are built up on the bent surfaces, thereby, causing the capacitance to develop across the line. This results in a change in the impedance of the transmission line, which causes a mismatch at the load, and this could reduce the overall system performance.

The formulation of the phase shift between two adjacent elements can be expressed in terms of Figure 4.4(b) as:

$$\sin\theta = \cos\varphi = \frac{L}{d} \tag{4.1}$$

where θ represents the required main-beam direction, i.e.

$$\Delta\Phi = d\sin\theta,\ \Delta t = \frac{2\pi L}{\lambda} = \frac{2\pi d \sin\theta}{\lambda}. \tag{4.2}$$

where Δt represents the time delay.

Figure 4.4(b) defines the trigonometry between different elements, where d represents the distance between adjacent antennas. The beam is pointed in an off-boresight direction, θ, at an angle, φ, from the horizon. The time delay l is used in beam steering, which is equal to the time that it takes the wavefront to travel over the distance L. Furthermore, L is a fraction of the wavelength, and thus, a phase delay could be substituted for the time delay. Therefore, to determine the phase shift that is needed for beam steering, a phase shift between the adjacent elements of ΔΦ is used, which can be calculated as in equation 4.2. As mentioned earlier, the distance between the elements was chosen to be ~0.5λ, i.e. d=4.65 mm at 27.5 GHz. For instance, should there be a requirement to steer the beam to an angle of 15°, the optimal phase shift, denoted as ΔΦ, between the elements can be determined. By employing MATLAB code for calculations, we find that ΔΦ amounts to 39.5°.

4.3.2 Calculation of the Physical Length of Phase Shifters

Figure 4.5 presents the schematic of four transmission line phase shifters; each section generates a different phase shift determined by its respective transmission line length. The required microstrip line physical length, l, to generate a phase shift (delay) of $\Delta\Phi$ between adjacent elements can be calculated as:

$$\Delta\Phi = k_e\, l = \sqrt{\varepsilon_e} k_0 l \, , \tag{4.3}$$

where k_0 is the free space wavenumber, ε_e is the effective dielectric constant that can be calculated as $\varepsilon_e = \frac{\varepsilon_r + 1}{2}$. By establishing the main beam angle θ as a function of the phase shift between adjacent elements, denoted as ΔΦ, we can express the normalized array factor for a uniform linear array as follows [76]:

$$AF[\Theta, \Delta\Phi] = \frac{sin(N\left[\frac{\pi d \sin(\Theta)}{\lambda} - \frac{\Delta\Phi}{2}\right])}{NSin(\frac{\pi d \sin(\Theta)}{\lambda} - \frac{\Delta\Phi}{2})} \tag{4.4}$$

The array factor incorporates conditions where the elements are evenly spaced along the array axis and separated by a distance d, with a constant phase shift between adjacent elements, and all elements have equal excitation amplitudes.

Therefore, employing MATLAB code, $\Delta\Phi$ has been calculated as the phase difference among elements within the beam steering ±30°. Consequently, the required microstrip physical length to achieve ±15° beam steering has been calculated as l=0.76 mm.

Utilizing the attained physical length, it is possible to execute the anticipated four-phase shift from each segment of the microstrip lines. The four-phase shifters of the transmission lines are designed in CST based on the physical length calculated as 0.38 mm, 0.76 mm, 1.14 mm, and 1.52 mm respectively. As depicted within the blue highlighted regions of Fig. 4.5(a), four-phase shifters have been simulated to accomplish a beam steering angle of +15°.

Figure 4.5(b) exhibits the successful steering of the beam to an angle of +15°, accomplished utilizing the 'combine result' tool in CST. The phase shifter is simulated without the antenna elements.

These lengths correspond to a 38.8° phase shift between adjacent elements at 27.5 GHz, with a marginal difference of around 0.7 between the calculated and simulated results.

The phase shifter's performance met the design expectation, as demonstrated by the phase of reflection coefficient obtained from each arm of the transmission line at the operation frequency of 27.5 GHz, which is shown in Figure 4.5(c).

The phase shifter is designed to fit within the antenna elements' spacing, making the phase shifting particularly useful for antenna arrays in small electronic devices with area constraints.

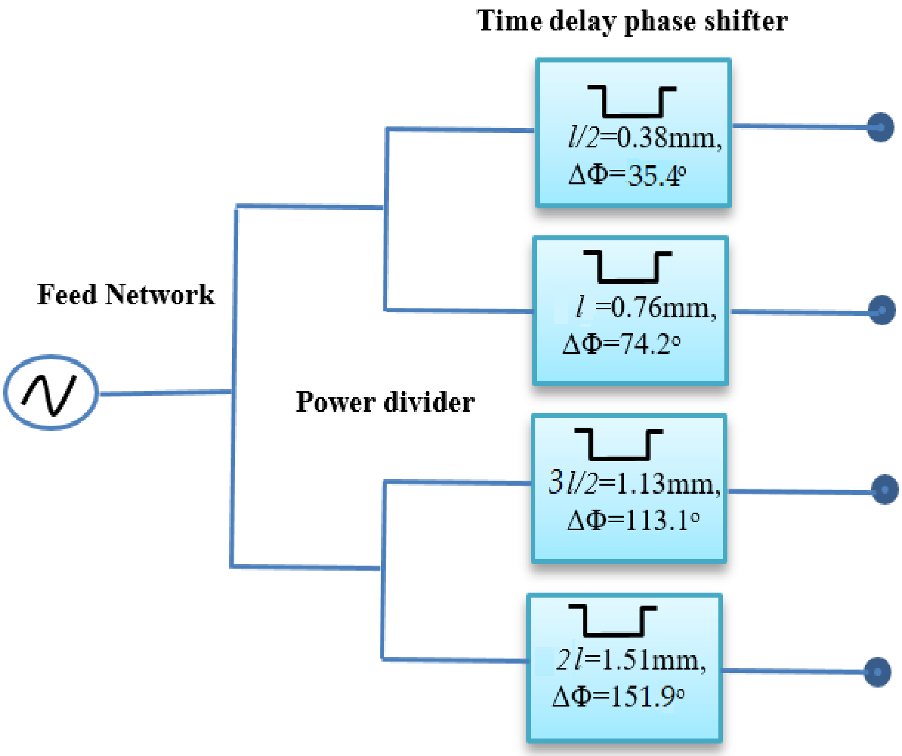
Time delay phase shifter
l/2=0.38mm,
ΔΦ=35.4°
l =0.76mm,
ΔΦ=74.2°
3l/2=1.13mm,
ΔΦ=113.1°
2l=1.51mm,
ΔΦ=151.9°
Feed Network
Power divider

(a)

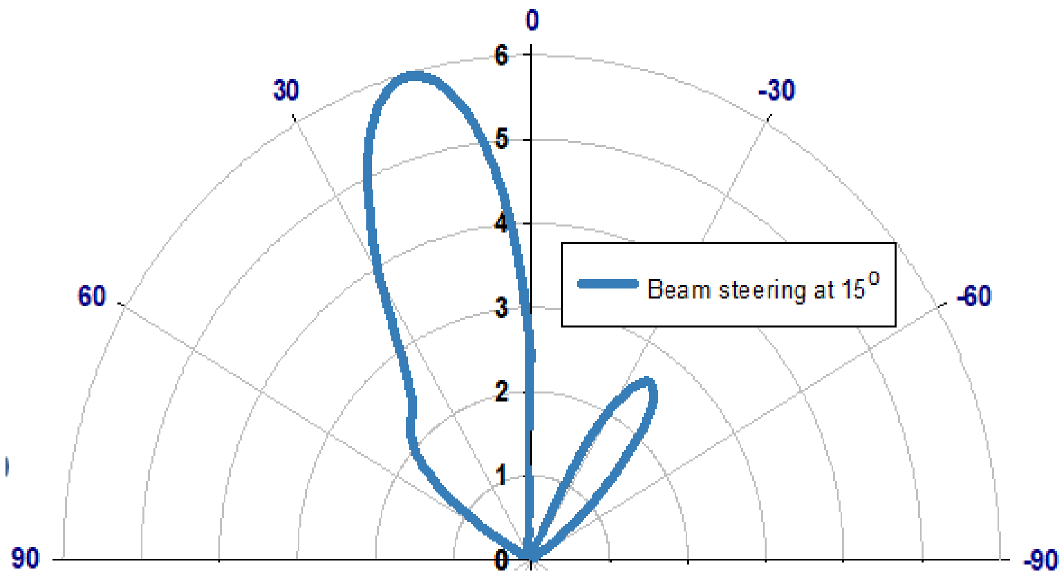
0
6
5
4
3
2
1
0
30
-30
60
-60
90
-90
Beam steering at 15°

(b)

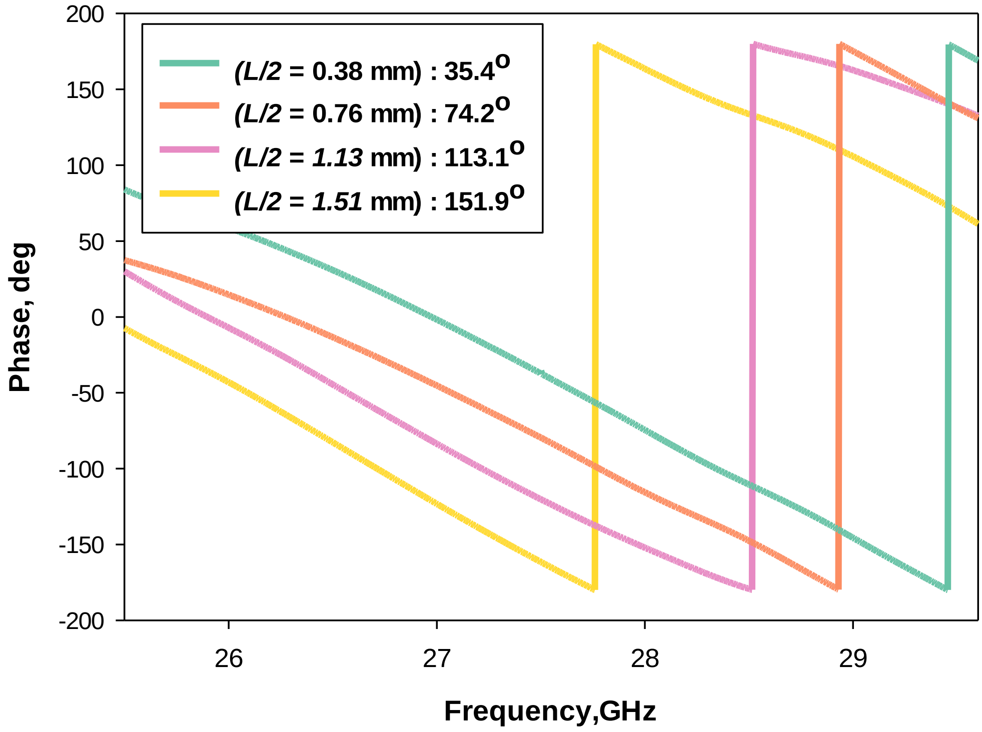

(c)

Figure 4.5: (a) Block diagram of linear phased array concept using true time delay phase shifters. (b) Polar radiation pattern with main beam steering to +15°, (c) Illustration of the phase differences as a function of frequency comparing four transmission lines on a phase shifter.

4.4 Design of Circularly Polarized 4-Elements Antenna Arrays

Now a single element has been tested, 4-element antenna arrays are investigated. Based on the performance of a single antenna, 1×4 uniform linear antenna arrays are designed with a spacing of 4.55 mm (≃λ/2) between adjacent elements, where λ stands for the free space wavelength at 27.5 GHz. The antenna spacing is chosen to achieve maximum gain and minimum side lobe levels (SLL). The antenna arrays are fed using a parallel feed network with a 0.24 mm wide microstrip transmission line. By utilizing power dividers and transmission line phase shifters at the shunt feed of the phased-array antennas, beam steering can be achieved. The incorporation of vias into the design confers several benefits, such as enhanced grounding, minimizing surface waves, and expanding the bandwidth, all of which contribute to superior antenna performance. Accordingly, the proposed antenna array has been equipped with six vias, each with a 1 mm radius and spaced 4 mm apart from center to center.

As per the proposed design, augmenting the number of phase shifters can broaden the scanning range and enhance the precision of beam shaping. Nevertheless, it's essential to bear in mind that the complexity and potential cost of the system may be higher with the increased number of phase shifters, and this relationship often depends on the number of antenna elements in use. Figure 4.6(a) presents the broadside array configuration, where equal length feeding lines are used to feed the elements. This configuration ensures that all elements receive the same signal amplitude and phase, resulting in constructive interference and the formation of a strong main beam at θ=0°. Figure 4.6(b) illustrates a current that travels in a clockwise direction, resulting in a Left-Hand Circular Polarization (LHCP). The maximum magnitude is observed at the input, and it subsequently decreased as it moves along the loop. Figure 4.6(c) presents a photo of the loop array prototype utilized in the study. Figure 4.6(d) illustrates the 2.4 mm connector used in the measurement, demonstrating that the antenna's hole design is compatible with the connector, having a centre-to-centre distance of 9.52 mm.

Figures 4.7(a) and 4.7(b) illustrate the transmission lines that are used to achieve the required phase shift by utilizing different electrical line lengths. This approach is known as a true-time delay [76], which can improve the bandwidth of a phased array with parallel feeding. True-time delay is particularly suitable for broadband applications, as the direction of the main beam remains constant over a range of frequencies. In essence, true-time delay involves introducing delay sections along the transmission lines of the feed network, which correspond to the required phase shift. By adjusting the time delay for each element, the overall phase shift across the array can be controlled, allowing precise beam steering.

This study employs four phase shifters to enable the steering of a CP main beam by adjusting their dimensions. Moreover, the traveling current distribution is maintained as in the case of the designed single-loop antenna Therefore, the main beam steering process achieves an LHCP wave, which is the case in the designed single-loop antenna. The illustrated current distribution of each array structure during the beam steering is depicted in Figures 4.7(c) and 4.7(d) at 27.5 GHz. Figure 4.7(e) provides photographs of the fabricated arrays when a true time delay transmission line is utilized.

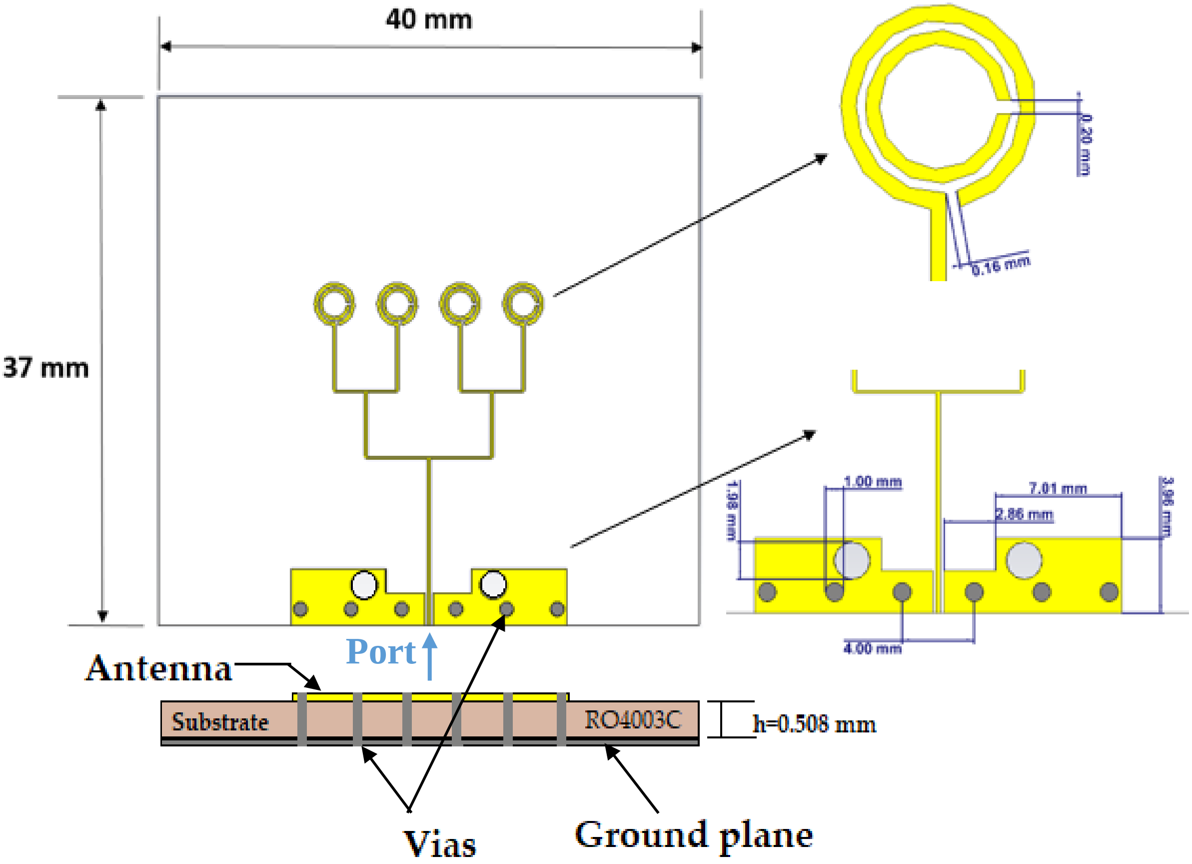
40 mm
37 mm
0.20 mm
0.16 mm
1.00 mm
7.01 mm
2.86 mm
1.98 mm
3.96 mm
4.00 mm
Port
Antenna
Substrate
RO4003C
h=0.508 mm
Vias
Ground plane

(a)

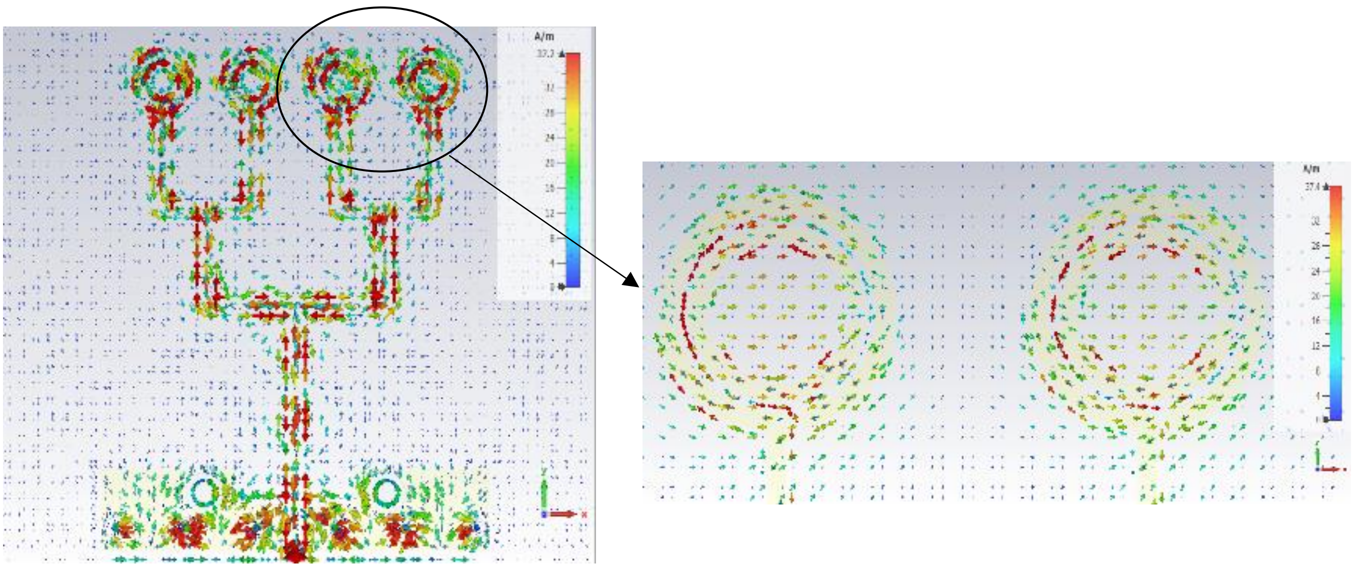

(b)

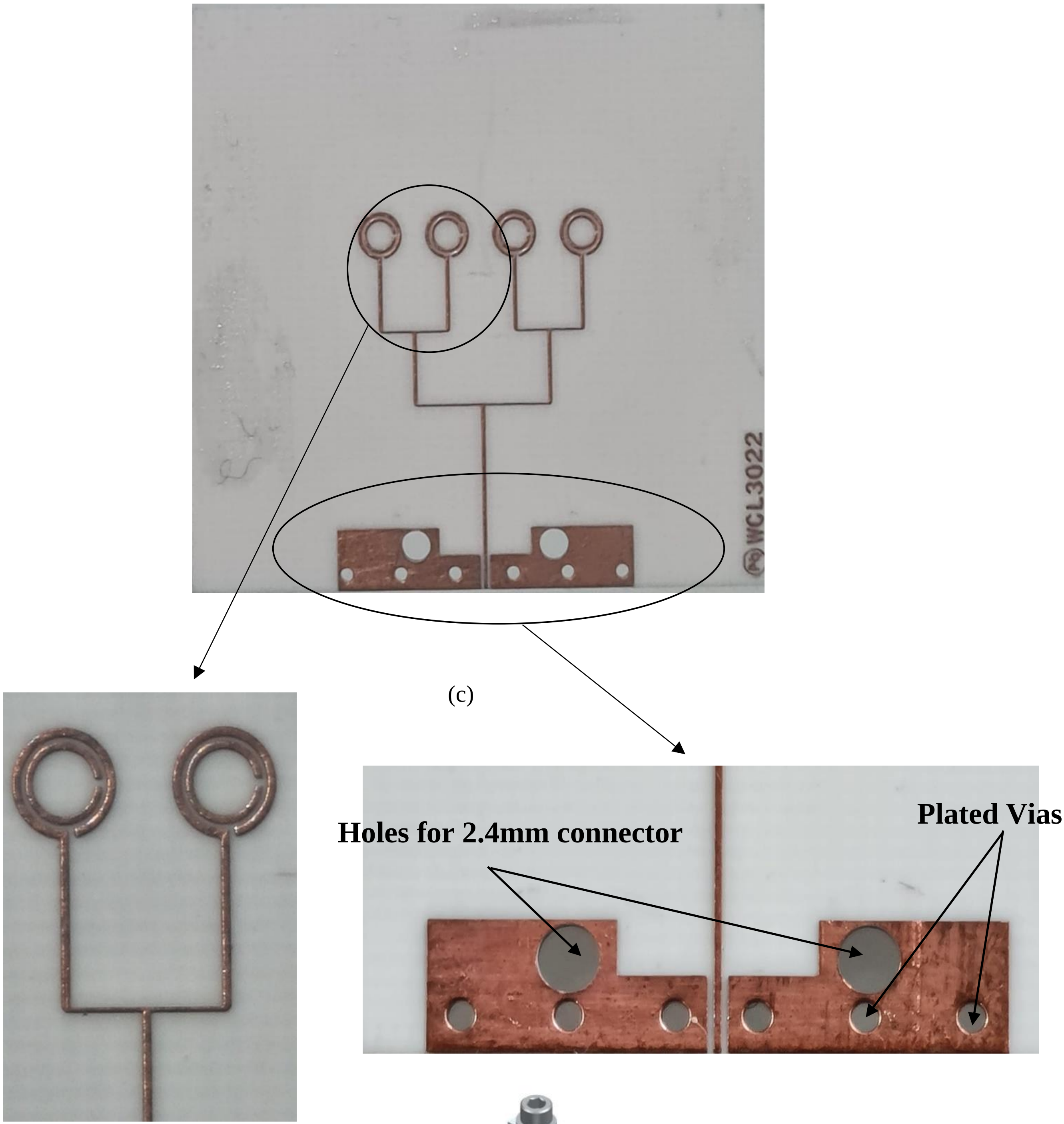

(c)

(d)

Figure 4.6: The configuration of 4 circular loops broadside antennas array. (b) current distribution at 27.5 GHz. (c) Photographs of the prototype (d) ELF50-002 Connector utilized in the measurement process.

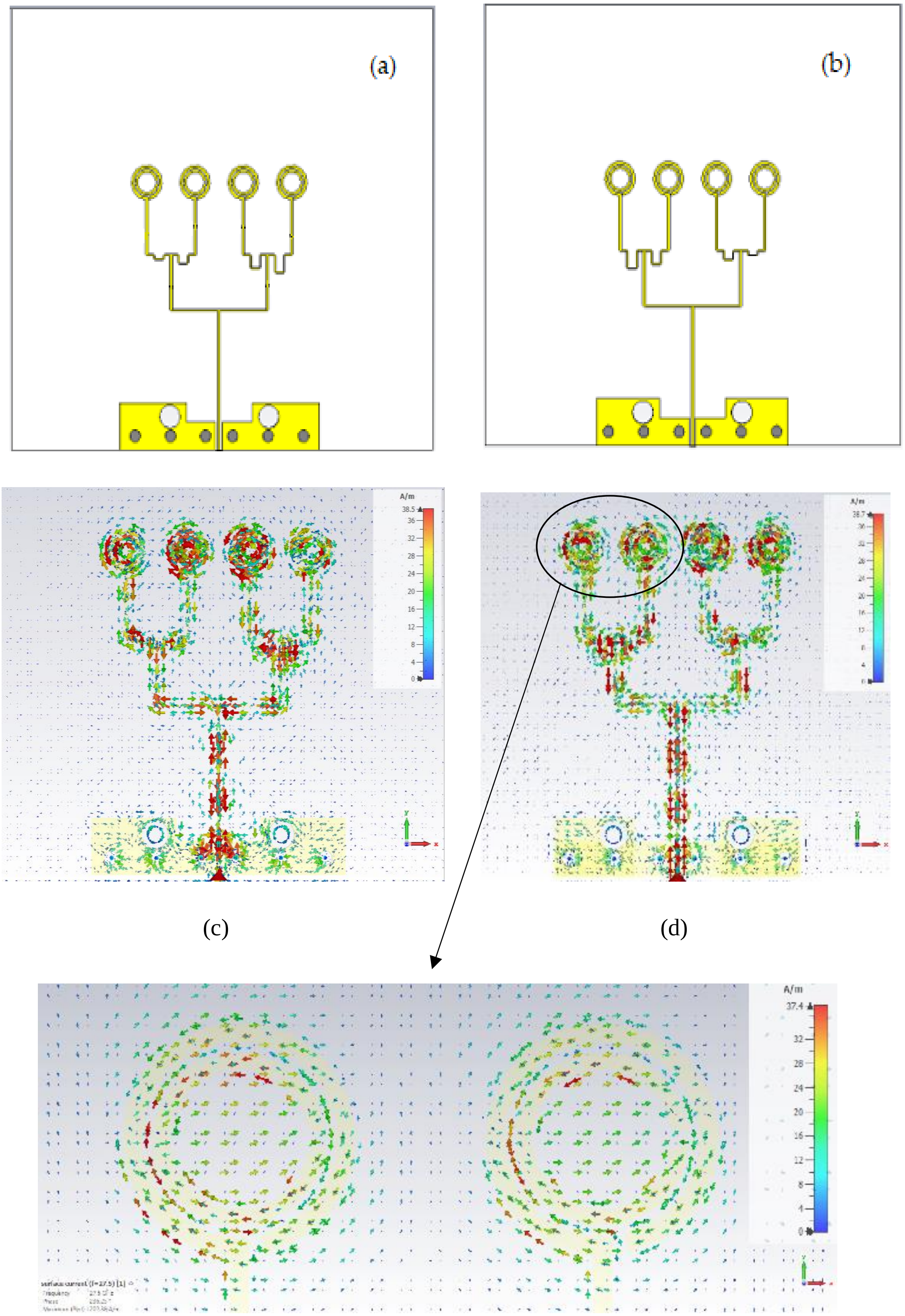
(a)
(b)
A/m
(c)
(d)
A/m
37.4
32
28
24
20
16
12
8
4
0

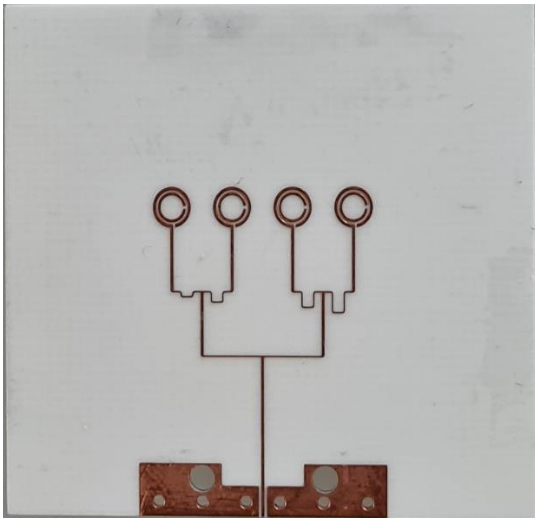

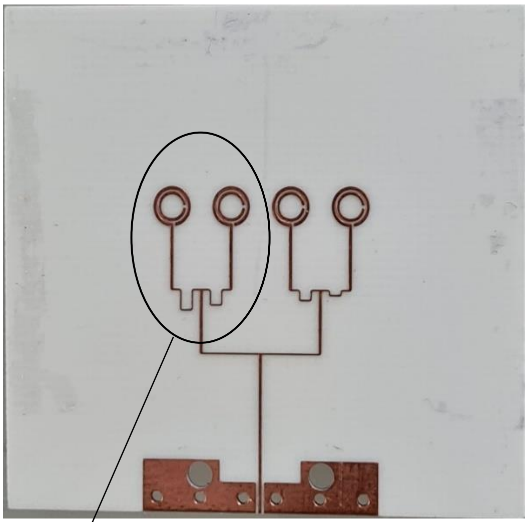

(e) (f)

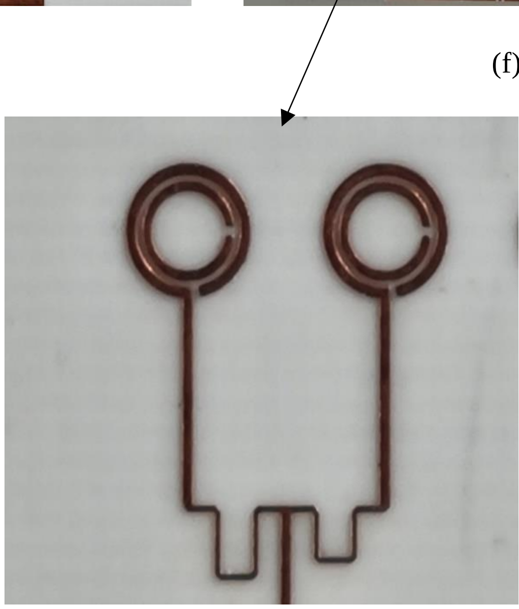

Figure 4.7: The structure of the proposed antenna arrays (a) Array with beam steering to the right-hand side. (b) Array with beam steering to the left-hand side. (c) Current distribution at 27.5 GHz for a +15^{o} beam steering (d) Current distribution at 27.5 GHz for a -15^{o} beam steering. (e) Prototypes of arrays using time delay transmission line with beam steering to the right-hand side. (f) Prototypes of arrays using time delay transmission line with beam steering to the left-hand side.

4.5 Impacts of Beam Steering on Array Performance

Beam steering is an essential capability that provides flexibility in adjusting the main beam direction to meet specific operational requirements. However, this feature, while beneficial, also introduces certain limitations that warrant thoughtful consideration during the design and application of beam-steering systems. Key limitations include the reduction in antenna gain, depending on the beamwidth of the loop element, the influence of mutual coupling, and the narrowing of the axial ratio bandwidth, which must be carefully considered in the design and application of beam-steering systems.

Figure 4.8 illustrates the simulated gain E-plane radiation patterns at 27.5 GHz within a ±30° scanning range in the E-plane. According to the simulation results, the antenna's gain experiences a reduction of approximately 3 dB at angles of ±25°. This reduction can be primarily attributed to the fact that the array factor (AF) depends on the pattern of a point source element and needs to be multiplied by the radiation pattern of a single loop that has a HPBW of 83°. Therefore, it is expected that the array's gain is reduced when the main beam is steered. In addition, as the transmission line length of the phase shifter is augmented, it may contribute to an escalation in the mutual coupling, thereby inducing modifications in the radiation patterns of individual loop elements. Ultimately, this sequence of events leads to a reduction in the overall pattern gain.

The variation of the AR bandwidth during the beam steering of ±30° is presented in Figure 4.9. The findings indicate that as the scanning angle increases, the AR bandwidth in each scanning plane experiences a reduction. For instance, at a scanning angle of 30°, the requirement of AR < 3 dB is met over a narrower frequency range of 27.4 GHz to 27.5 GHz. This reduction in the AR bandwidth can be attributed to the change in the traveling wave current distribution of each element due to mutual coupling caused by an increase in the length of the phase shifter transmission line. (According to Figure 4.9(b), there is no AR that is less than 3 dB at -30°).

Table 4.2 illustrates the phase difference between the two elements, and also reports the physical length of four transmission line phase shifters within a beam steering spectrum that spans ±30 degrees.

Table 4.3 presents a summary of the achieved gains and AR bandwidth results during the beam steering range. From Table 4.3, it can be observed that a useful AR bandwidth of ~200 MHz is achieved when the main beam is steered to ±30°.

Table 3.2 Phase differences and physical lengths of the phase shifters within a beam steering range of ±30°

Scan angle	**The physical length of the transmission line (mm)**				**Phase difference Between two elements**
	Phase shifter 1 (*l*/2)	**Phase shifter 2 (*l*)**	**Phase shifter 3 (3*l*/2)**	**Phase shifter 4 (2*l*)**	
5°	0.135	0.27	0.405	0.54	13.4°
10°	0.27	0.54	0.81	1.08	26.6°
15°	0.38	0.76	1.14	1.52	39.5°
20°	0.53	1.06	1.59	2.12	52.5°
25°	0.655	1.31	1.965	2.62	64.9°
30°	0.775	1.55	2.325	3.1	76.7°

Table 4.3 Gain and AR Bandwidth within a Beam Steering Range of ±30°

Scan angle	AR bandwidth %	Gain dBic	Scan angle	AR bandwidth %	Gain dBic
5°	4.4	10.6	-5°	4.5	9.97
10°	6	10.5	-10°	5	9.43
15°	4.8	10.2	-15°	6	9.23
20°	3.8	9.33	-20°	4	8.61
25°	0.72	8.3	-25°	0.7	7.65
30°	0.25	7.2	-30°	0.2	7.25

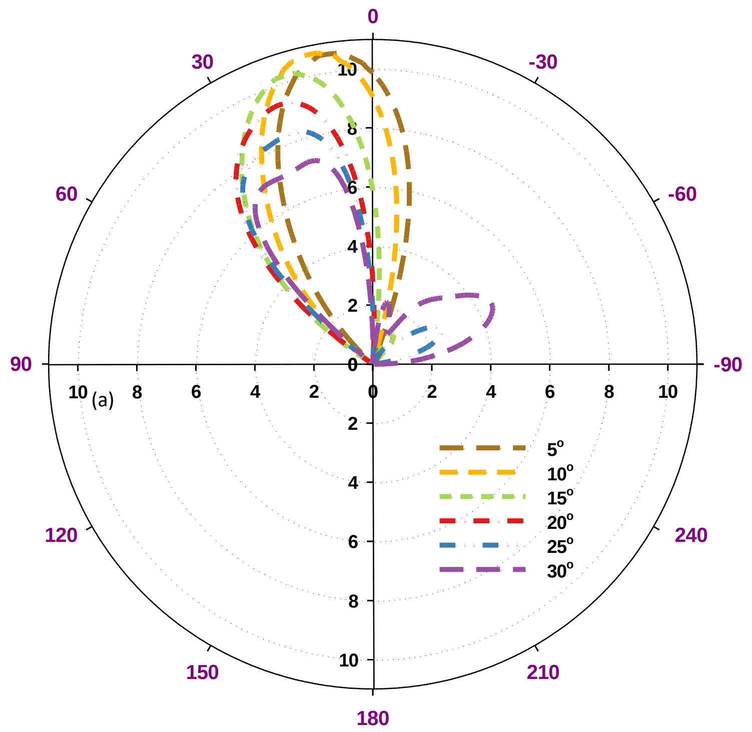

(a)

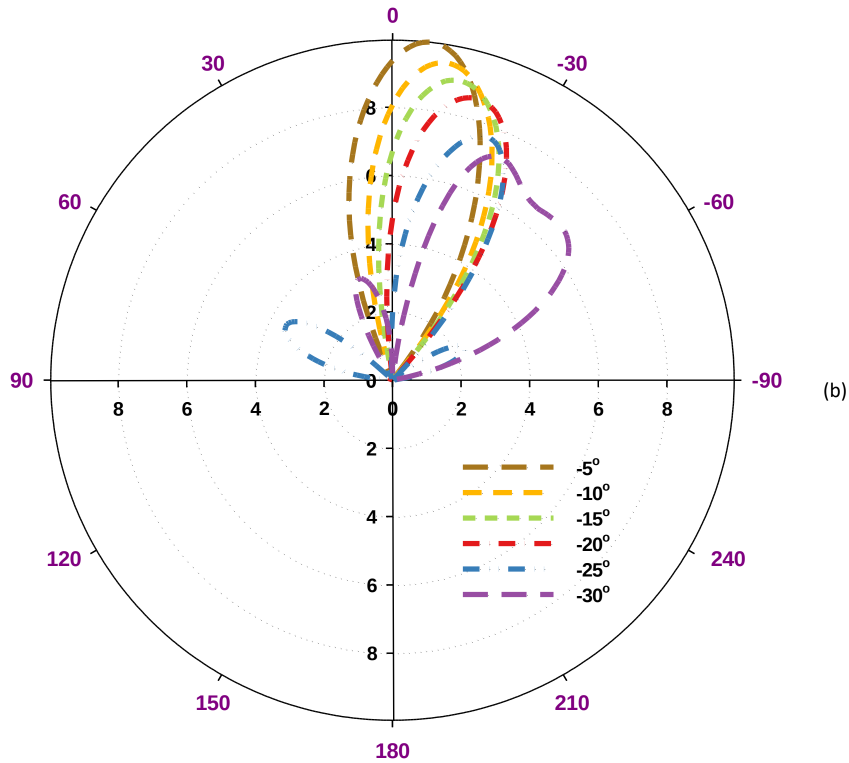

(b)

Figure 4.8: illustrates the simulated gain E-plane radiation patterns at 27.5 GHz within a ±30° scanning range in the E-plane.

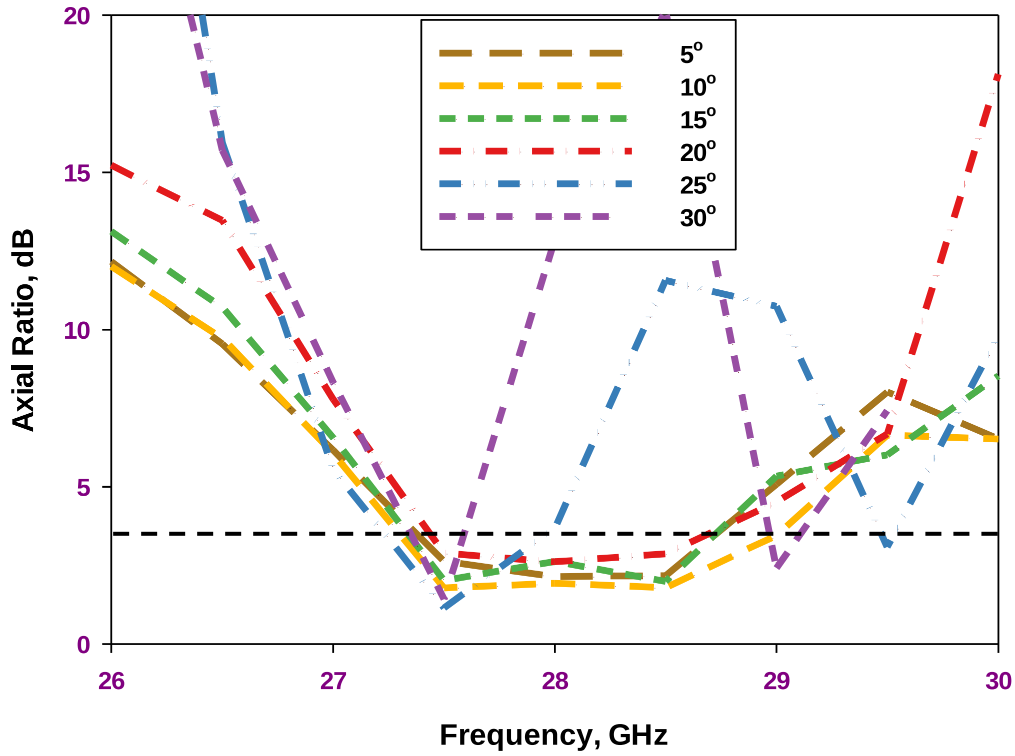

(a)

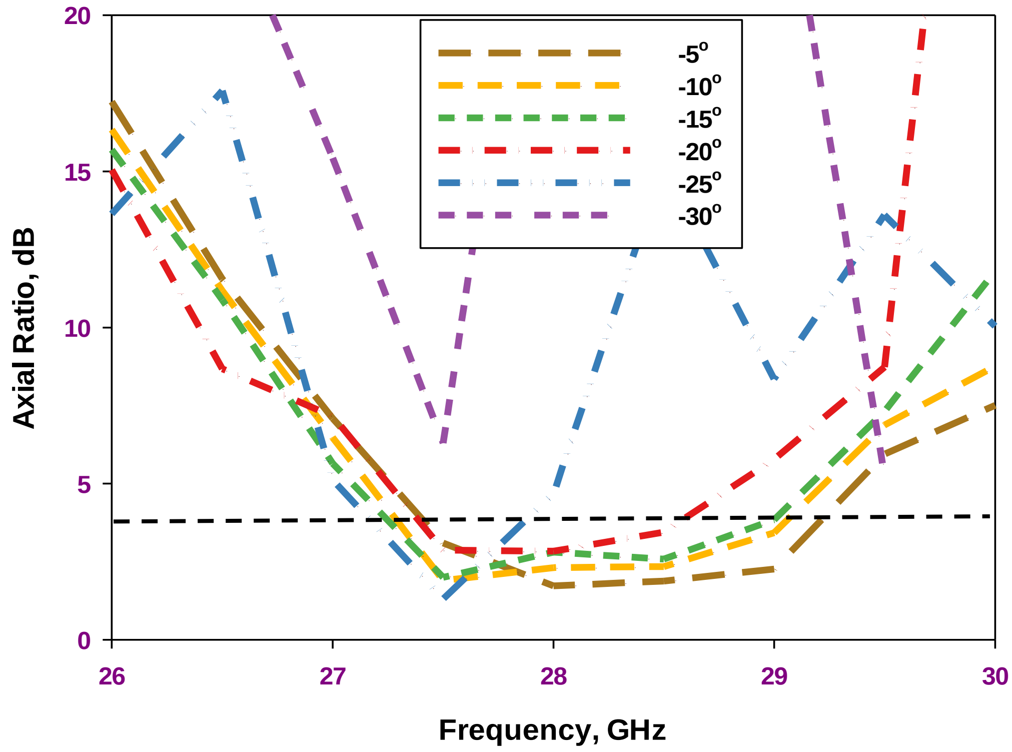

(b)

Figure 4.9: Simulated AR as a function of frequency; (a) Beam steering range of 0° to 30° (b) Beam steering range of -30° to 0°.

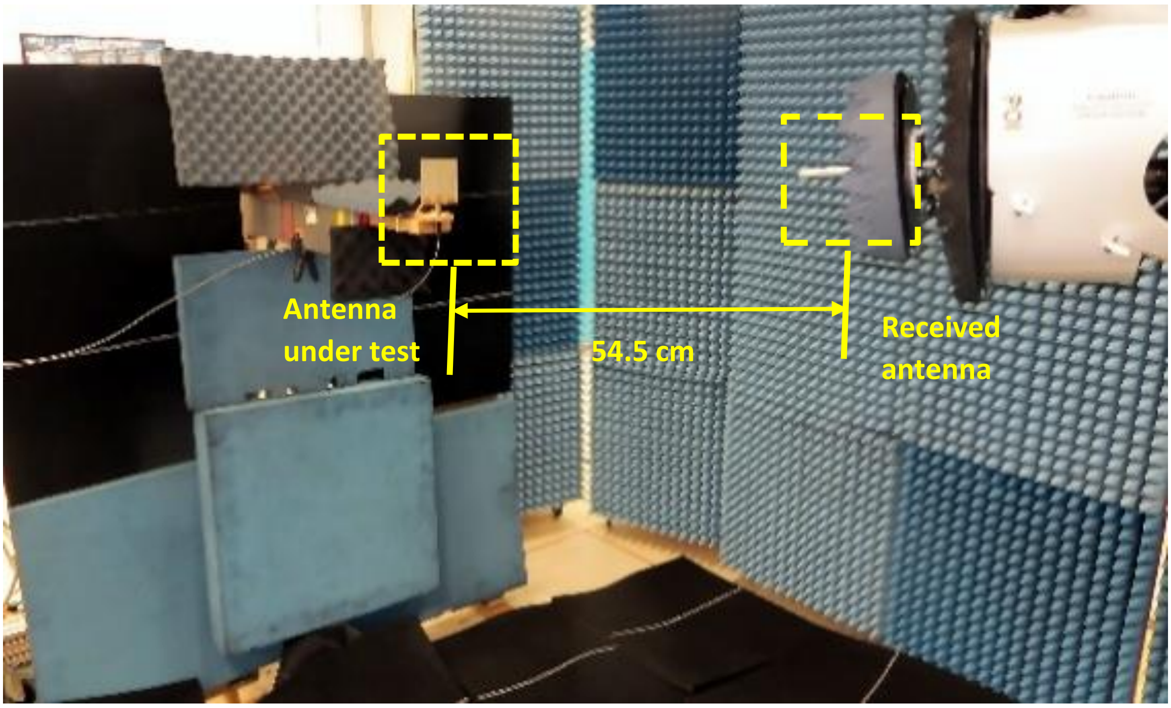
Antenna
under test
54.5 cm
Received
antenna

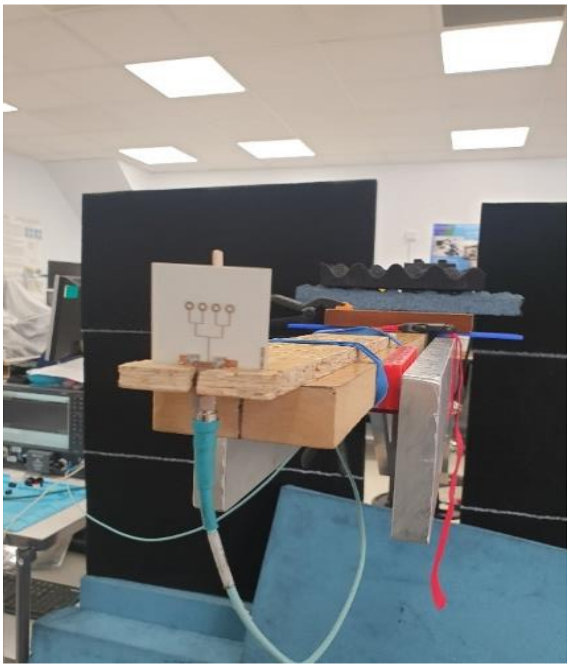

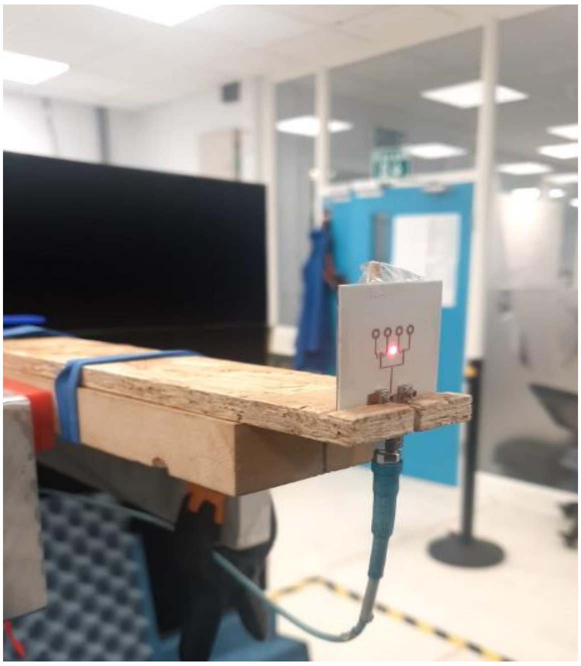

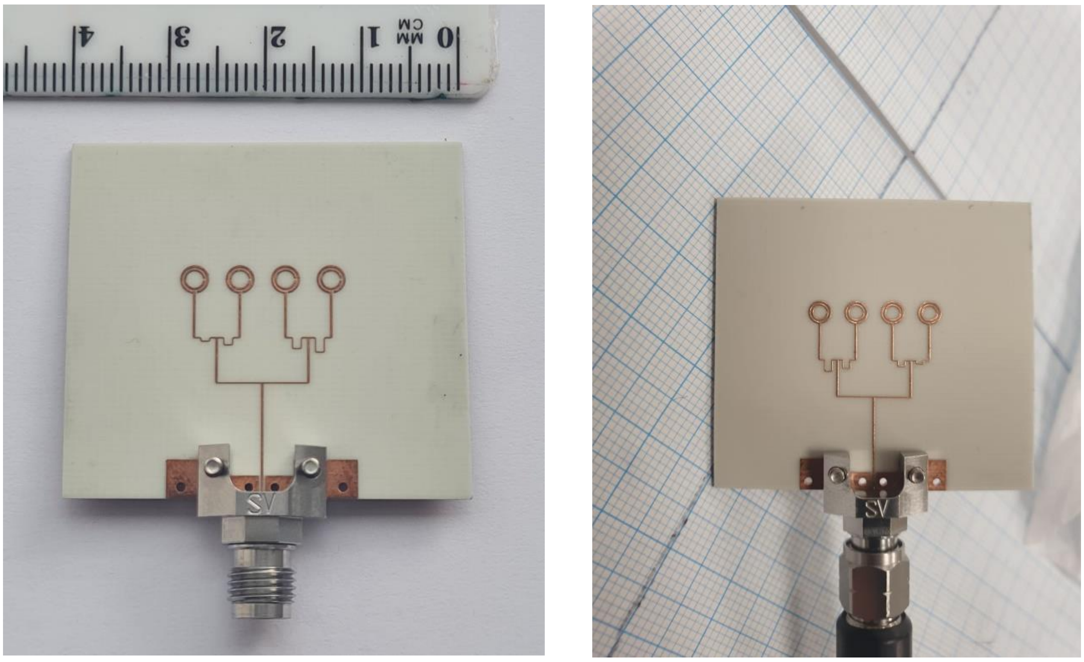

Figure 4.10: Photographs of the array antennas in a spherical measurement lab.

4.6 Fabrication and Measurements

This section presents the fabrication and measurement results. To this end, three prototypes of the proposed CP 4- elements circular loop array are fabricated and tested to verify the design.

The measurements are conducted using the E5071C mmWave vector network analyzer, as well as the National mmWave Measurement Facility (NmmMF) [77]. The reflection coefficient was measured using a 2.4 mm SMA and an N5245B vector network analyzer (VNA). Noting that the (SNF-FIX-1.0) measurement system is suitable for measuring mmWave antenna packaged on chips with frequency ranges from 10 GHz to 110 GHz. Figure 4.10 presents photographs of array antennas in the NmmMF during the measurement process.

It is important for the phased array to maintain good impedance matching at all beam steering angles. To verify this, simulations and measurements of the return losses have been carried out at beam steering angles of -15^o, 0^o, and 15^o degrees and compared as illustrated in Figure 4.11. The results demonstrate an excellent agreement between simulations and measurements. Besides, the results also indicate that particularly good impedance matching is achieved across all the beam steering angles. For each of the evaluated beam steering angles (-15°, 0°, and 15°), the simulated antenna arrays exhibit percentage impedance bandwidths of approximately 13.8%, 17.4%, and 13.8% respectively, while the measured results show bandwidths of around 14.5%, 18.1%, and 14.5% respectively. This indicates that all three antenna arrays operate within the same frequency range during the beam steering process.

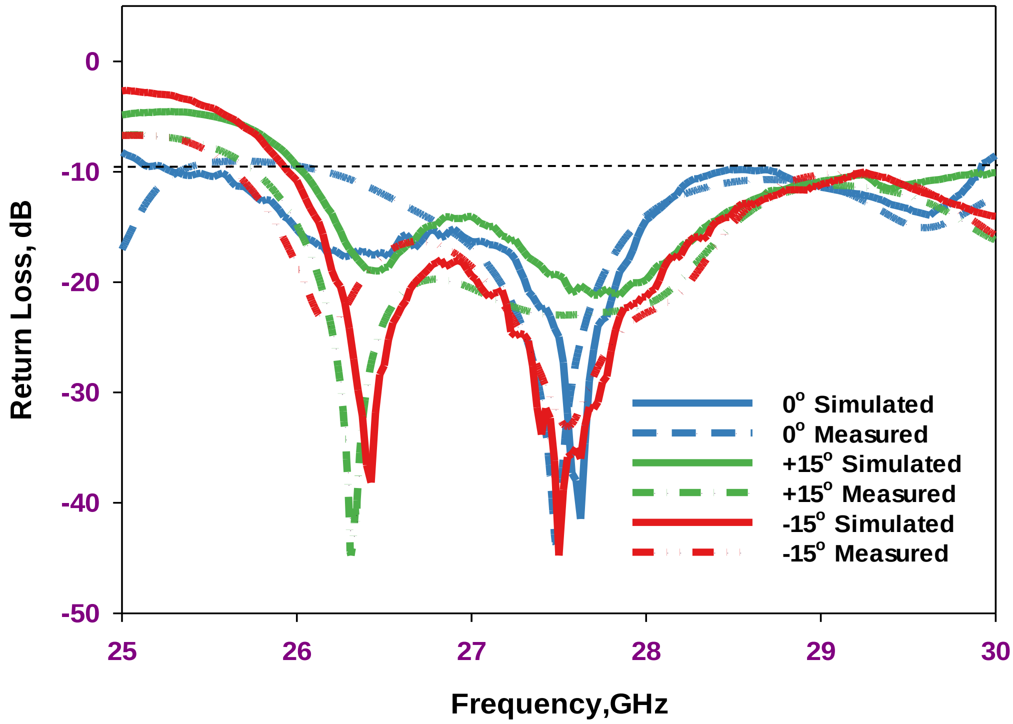

Figure 4.11: Return losses as a function of frequency for different beam steering angles.

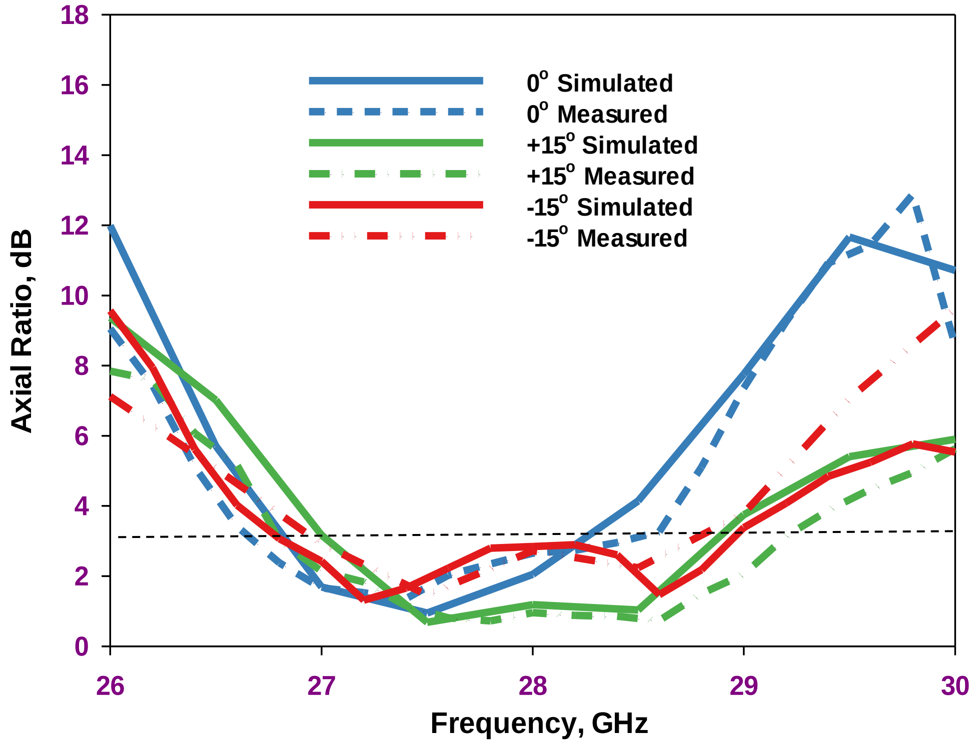

Figure 4.12: AR for three beam steering angles.

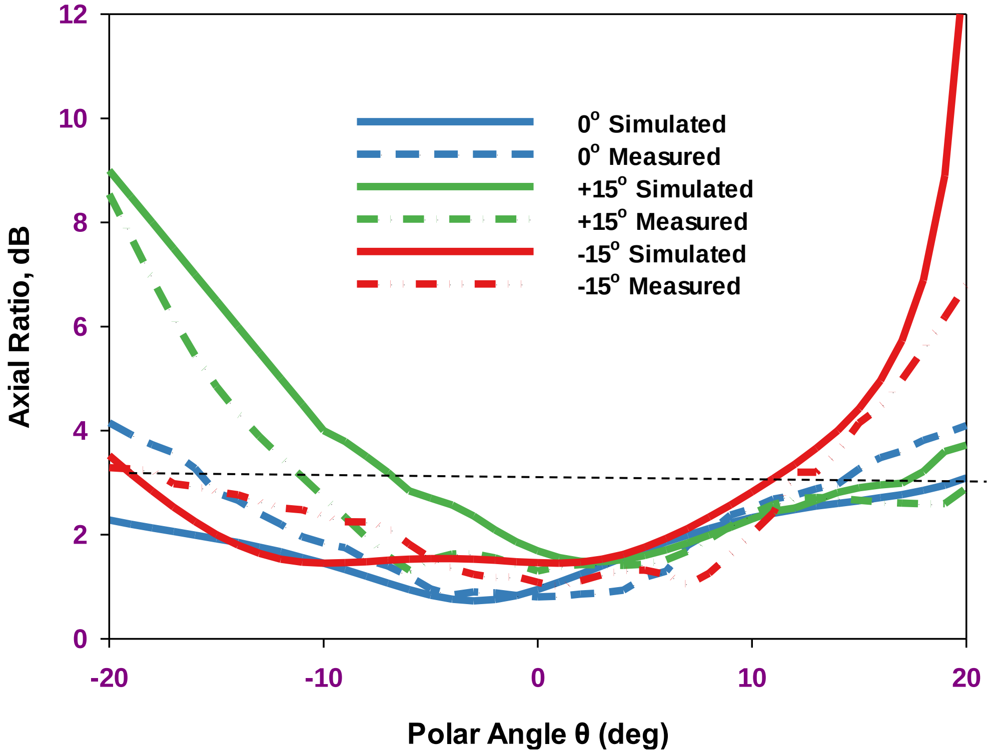

Figure 4.13: AR as a function of polar angle θ at 27.5GHz for three beam steering angles.

The measured and simulated axial ratios of three antenna arrays are presented in Figure 4.12 at three scanning angles. The simulated 3dB AR bandwidths are approximately 8.1%, 6.3%, and 8.4%, which are in close agreement with the measured results of 7.5%, 6.6%, and 8.7%, all centered at 27.5 GHz. In addition, the 3 dB AR beamwidths of the three cases are depicted in Figure 4.13 at 27.5 GHz with reasonable agreement between results and simulations. For example, for a main beam direction of -15°, the respective measured and simulated AR beamwidths are (-18° to 12°) and (-19° to 11°). Similarly, when the main beam is directed at 0°, the respective measured and simulated AR beamwidths are (-16° to 16°) and (-25° to 19°). Finally, for a main beam direction of 15°, the respective measured and simulated AR beamwidths are $(-11^{o}$ to $22^{o})$ and $(-7^{o}$ to $18^{o})$. This validates the correctness of the experiment and underpins the contribution of this research.

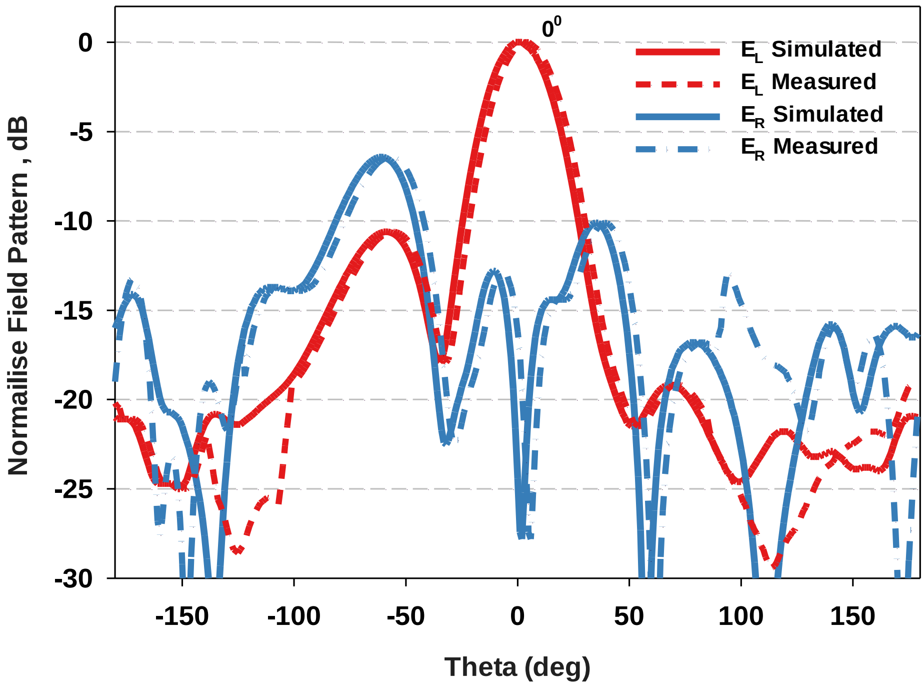

(a)

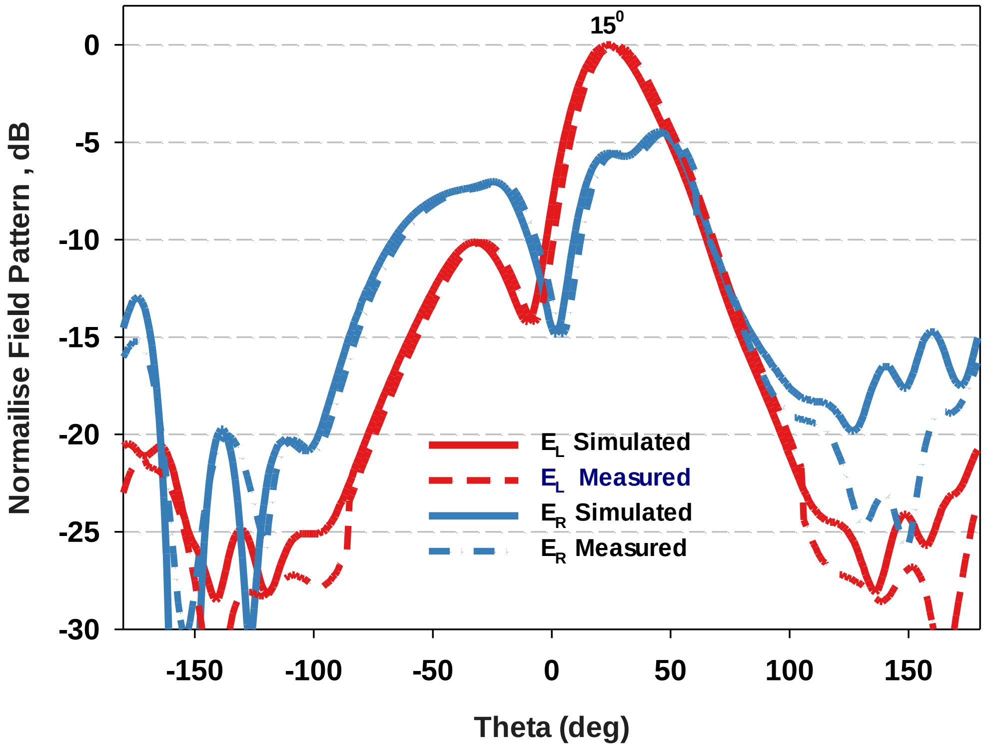

(b)

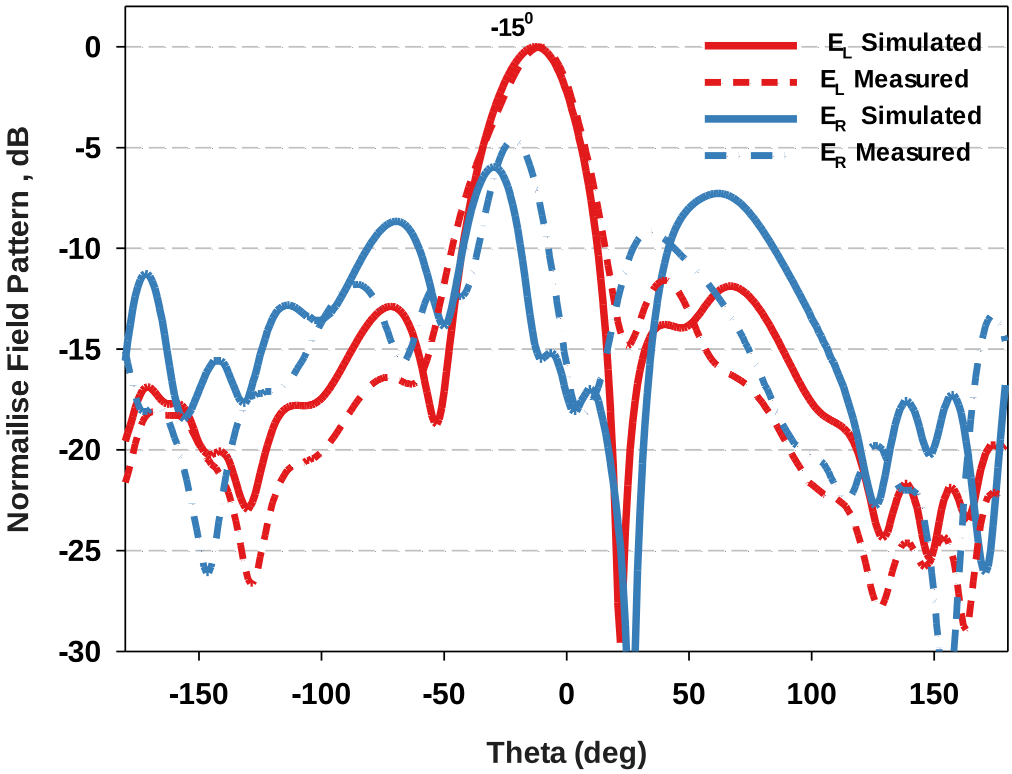

(c)

Figure 4.14: EL & ER radiation patterns function (a) Beam steering angle of 0° (b) Beam steering angle of +15° (c) Beam steering angle of -15°.

The E_L & E_R radiation patterns at phi=0 are presented in Figure 4.14 for the three considered arrays with a close agreement between measurements and simulations. In all cases, E_L is stronger than E_R, which corresponds to an LHCP sense. For example, E_L is greater than E_R by more than 15 dB in the case of broadside radiation. However, the difference between E_L & E_R is reduced as the steered beam angle is increased, which indicates the degrade of the circular polarization level. The maximum gains of three antenna arrays are presented in Figure 4.15, where it can be observed that the measured broadside gain is circa 10.8 dBic. In addition, the antenna gain is gradually reduced when the scanning angle is increased, as has been discussed earlier. For example, when the scanning angle is increased to -15°, and +15°, the antenna gain is reduced to about 9.8 dBic and 10.2 dBic, respectively. Moreover, the results indicate that the side-lobe levels are increased due to the beam steering. Figure 4.16 presents the radiation efficiency for the three antenna arrays. The simulated and measured results depict a high radiation efficiency of circa 86% for the three different beam steering angles considered at 27.5 GHz.

Expanding the number of elements in the antenna array beyond four may yield advantages, including increased gain, enhanced beam steering accuracy, and extended scanning capabilities. However, it also comes with challenges related to increased size, complexity, and cost, which need to be carefully considered in the design and implementation of the antenna system.

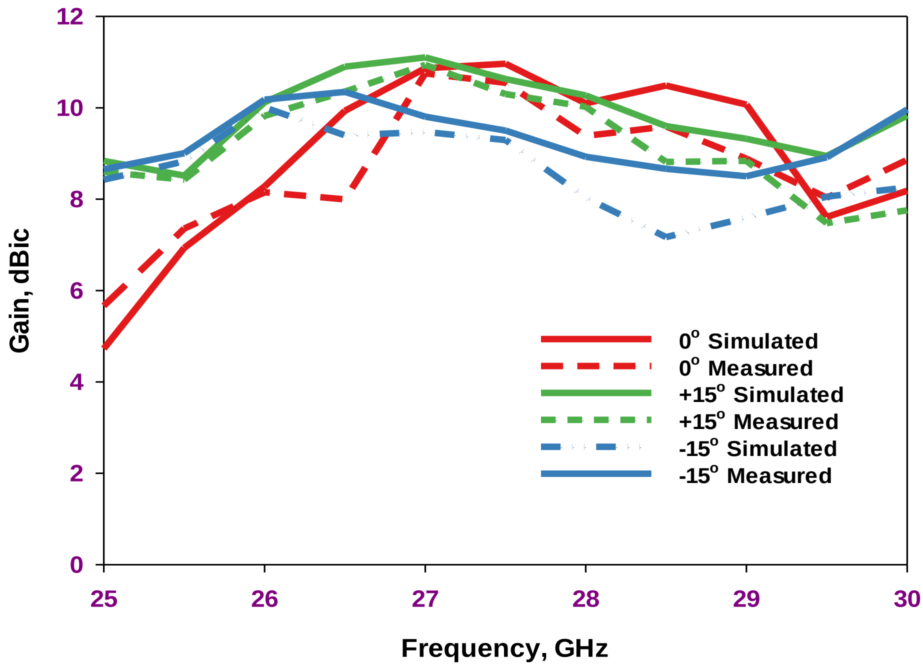

Figure 4.15: Main beam gain for the three beam steering angles.

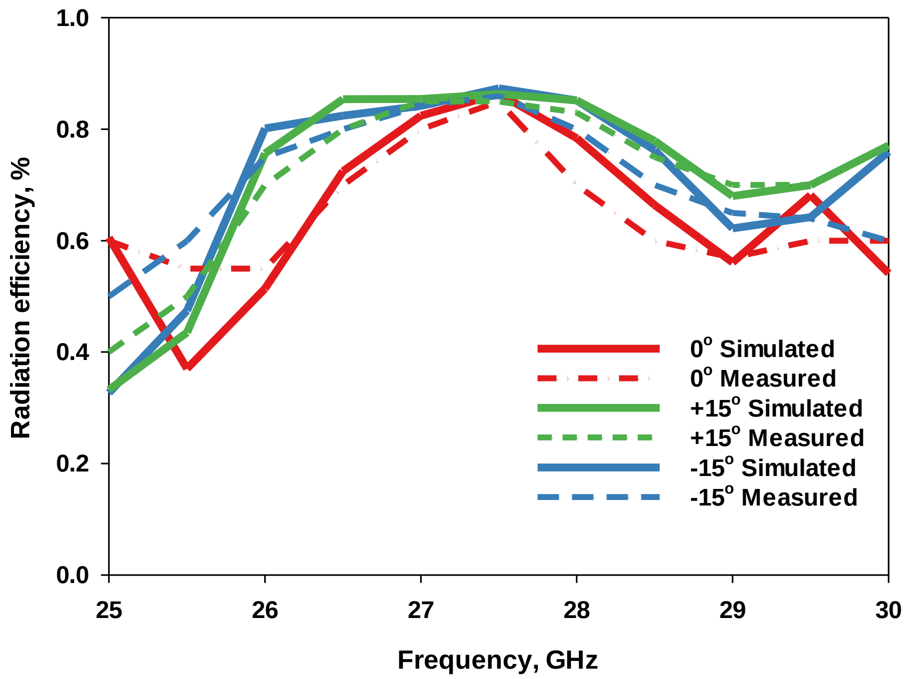

Figure 4.16: Simulated radiation efficiency (η) for three different beam steering angles.

Table 4.4 Performance Comparison of the Proposed CP Phased Array Against Those Reported in the Literature

Ref.	Number of elements	Number of layers	Size mm^2	Operating Frequency	S_{11} bandwidth	AR bandwidth	Scanning angle range	Peak gain (dBic)	Antenna efficiency
[62]	4×4	5	93×97	X-band 8-12GHz	40%	**	±25°	**	**
[64]	1×10	5	**	X-band	40%	18%	-13° to +28°	12.72	⸙ 32%
[69]	2×2	6	45×45	X-band 10.5GHz	4.3%	4.7%	±22°	6.6	**
[71]	4×16	6	**	mmWave	6.6%	**	±40°	**	**
This work	**1×4**	**3**	**37×40**	**mmWave 27.5GHz**	**10.7%**	**8.3%**	**±25°**	**10.8**	**>85%**

** The values were not supplied.
⸙ The exact values were not supplied, and the data were obtained by extrapolating the given information.

4.7 Performance Comparison

Table 4.3. presents a comparison between the performance of the proposed CP phased array antennas and the state-of-the-art designs reported in the literature. From this Table, it can be observed that the proposed CP phased array offers a good impedance and AR bandwidths at the mmWave frequency range. In particular, the array proposed is characterized by a cost-effective and streamlined design, notably featuring a low-profile structure composed of just 3 PCB layers. In contrast, contemporary designs, as evidenced in comparative literature, often rely on 5 or 6 layers. Consequently, the previous designs, with their increased layers count, exhibit heightened complexity and cost when juxtaposed with the proposed design. Furthermore, adopting a time delay transmission line structure to achieve beam steering results in a notable reduction in the overall cost. This approach involves a simplified configuration that contributes to cost saving by avoiding the need for complex and expensive components or

techniques typically associated with beam steering methods.

In addition, a reduced number of elements is utilized in the proposed design to achieve a maximum gain of 10.8 dBic, which is comparable to the published state-of-the-art designs that use more antenna elements. In addition, the sizes of the presented phased arrays are smaller than those published earlier. Furthermore, the proposed antenna arrays demonstrate a CP beam scanning range of ±25 degrees, surpassing the beam scanning capabilities presented in [64], and [68]. Moreover, the antenna efficiency of our design exceeds 85%, which significantly outperforms the efficiencies reported in [62], [64], [68], and [71]. In [68], the authors accomplished a 4.3% (AR) bandwidth, whereas in [81], the AR bandwidth curve has not been provided. In contrast, the presented design attains an AR bandwidth of ~ 8.7%, surpassing the results presented in [68]. Although the proposed antenna can cover an axial ratio over a beam steering range of ±25°, the decision was made to fabricate the design with a scanning angle of ±15° due to the wider AR bandwidth and higher gain at this angle.

4.8 Summery

This study proposed a 4-elements phased array of circular loop antennas to achieve CP radiation. It has been observed that by adjusting the lengths of the transmission line phase shifter, the main beam can be efficiently directed to achieve CP beam at scanning angles of up to ±25°. In addition, this study demonstrated that LHCP radiation can be obtained during the beam steering at 27.5 GHz with a peak gain of circa11 dBic in a combination with a radiation efficiency that exceeds 85%. Another advantage of the proposed phased array configuration is the simpler and lower cost design compared to the published counterparts. The results confirm an excellent agreement between the measured and simulated results, which underpins the contributions of this research. The promising results obtained by the proposed antenna make it useful for practical implementations such as satellite and wireless communications systems.

Chapter 5

Cost-Effective Design of Polarization and Bandwidth Reconfigurable Millimeter-Wave Loop Antenna

5.1 Introduction

In the realm of mmWave applications, the demand for enhanced communication capabilities has fueled the emergence of reconfigurable antennas as a pivotal solution. These antennas offer a crucial degree of flexibility and adaptability, specifically tailored to address the challenges inherent in mmWave frequencies. Given that mmWave frequencies pose unique hurdles in signal propagation and susceptibility to environmental obstacles, reconfigurable antennas play a vital role in mitigating these challenges [78, 80]. Their ability to adjust radiation patterns, polarization, and beamforming characteristics in real-time provides a dynamic response to the intricacies of mmWave communication environments.

Moreover, beyond their technical advantages, reconfigurable antennas significantly contribute to the overall efficiency and cost-effectiveness of mmWave systems. By offering adaptability and versatility, these antennas facilitate streamlined design approaches, diminishing the reliance on complex and specialized hardware components. This, in turn, promotes the development of compact and lightweight mmWave devices, aligning with the escalating demand for miniaturization in contemporary communication systems.

In a parallel development, circularly polarized antennas have garnered substantial interest in the realm of mmWave communication systems. This interest is rooted in well-established advantages, such as their resistance to multipath interference and tolerance to misalignment between transmitting and receiving antennas [81]. As such, the incorporation of circularly polarized antennas into mmWave designs represents a strategic choice to enhance the robustness and reliability of communication systems operating in these high-frequency bands. The synergy between reconfigurable antennas and circularly polarized antennas presents a holistic approach to addressing the multifaceted challenges and optimizing performance in the rapidly evolving landscape of mmWave applications. However, circular polarization can be achieved in one of in two senses: LHCP or RHCP. As a result, it is important to design an antenna that supports the two polarization senses to sustain communications in challenging and demanding environments. Therefore, studies have been published proposing novel mmWave circularly polarized antennas [82]-[89]. However, these approaches share a limitation of providing fixed circular polarization senses, i.e. either LHCP or RHCP, thereby restricting their usage to a single polarization type. In contrast, an array that utilizes LHCP and RHCP has been proposed [90]. Besides, other designs have been reported that incorporate multiple feeding ports to generate the desired circular polarization sense, albeit at the cost of added complexity [91, 92]. In addition, a cost-effective design of a polarization reconfigurable mmWave antenna that is capable of radiating CP and LP waves provides another needed degree of flexibility to any communication system.

Prototypes of polarization reconfigurable mmWave antennas have been reported in a number of studies [89]-[95]. For example, a K-band polarization reconfigurable patch antenna has been proposed in a layered structure using radio-frequency microelectromechanical system (RF-MEMS) to switch between two polarization modes, LHCP and LP, over impedance bandwidths of 11.8% and 3%, respectively, with a peak gain of ~3.9 dBic [89]. Another polarization reconfigurable patch antenna that is operating at 29 GHz has been proposed with LP, LHCP and RHCP radiation modes [90]. The findings demonstrated respective impedance bandwidths of 5.1% and 3.1 % for the CP and LP modes in combination with an AR bandwidth of 1.7%

and a maximum gain of ~8.5 dBi in the LP mode. However, the configurability relies on external stimuli (UV laser pulses) to control the phase change of the Germanium Telluride (GeTe) material, which limits the practicality and poses manufacturing challenges, thereby detracting from its potential implementation. In a more recent study, 4 PIN diodes have been utilized in the design of reconfigurable patch antenna with three polarization modes RCHP, LHCP, and LP operating at 29 GHz with an impedance bandwidth of ~5.4% in all cases [91]. The measured respective gains are 3 dBi and 4dBi in the CP and LP radiations albeit with no data for the AR bandwidths.

On the other hand, a 2×2 mmWave polarization reconfigurable patch antenna array has been reported by utilizing two PIN-diode pairs to switch between dual CP modes with respective impedance and AR bandwidths of 7% and 4% with a radiation efficiency of 51% [92]. Besides, linear and square arrays with 10 and 2×2 T slot elements with respective impedance bandwidths of 3.3% and 10%. Besides, two mechanically switchable CP senses have been achieved over an AR bandwidth of 3% for both arrays [93]. Similarly, a full polarization reconfigurability has been achieved using an 8×12 Butterfly phased array with 4 ports that switch the polarization with the correct amplitude and phase for the excitation signal [94]. The AR and impedance are presented over a frequency range of 27-29 GHz with a simulated total efficiency of 56-60%. Furthermore, a double-folded, polarization-reconfigurable, dual-antenna array has been proposed with a CP switching over a bandwidth of 7% through the activation of a single-pole-double-throw switch when 10 elements are used [95]. In addition, a figure of merit was introduced and used to compare the performance to those in earlier studies. However, in [89]-[95], polarization reconfigurability has been achieved by utilizing substantial number of elements in conjunction with customized feeding networks that naturally increase the cost and complexity compared to a single antenna configuration.

In the presented study three modes of polarization reconfigurability are achieved using a singly fed open-loop antenna that incorporates two PIN diodes only. In addition, the antenna offers impedance and CP bandwidths of 12.9% and 7%, respectively, in combination with a gain of ~8.5 dBi and estimated total efficiency of 79%. Moreover, the proposed configuration avoids the need to utilize UV laser pulses, multi-layer PCB structure or large arrays with complex feeding networks.

It should be noted that the RHCP and LHCP modes have been achieved when a single PIN diode is forward biased while the other is PIN diode reverse biased. On the other hand, when both PIN diodes are under zero-bias condition, the LP mode is achieved with dual narrow impedance bandwidths since the impedance presented by the two unbiased diodes at the input of the antenna is different from that presented using one forward, and one reverse, biased PIN diodes. Therefore, the proposed configuration offers a distinct advantage of offering hybrid reconfigurability by varying polarization and bandwidth without any compromise on the performance. To the best of the authors' knowledge, this is the first attempt to design a mmWave antenna that offers hybrid reconfiguration. It may be worth it to point out that bandwidth reconfigurability received increased interest in recent years since an antenna with bandwidth control could partially perform a filtering task as well as the radiation [96]-[98].

The effectiveness of the proposed antenna design is demonstrated through comprehensive simulation and measurement results. These results showcase promising performance in terms of impedance and axial ratio bandwidths. The outcome of this study highlights the potential usefulness of the proposed CP reconfigurable antenna for mmWave applications, as well as practical implementations in satellite and wireless communications systems.

5.2 Contribution

In light of the challenges mentioned above, we outline the following key contributions of the presented work of this Chapter:

1. Design and Fabrication of a Cost-Effective Polarisation Reconfigurable Planar Loop Antenna: A low-profile, cost-effective circularly polarized single-loop antenna is designed and fabricated specifically at 6 GHz. The proposed design incorporates two gaps to achieve polarisation reconfigurability.

2. Employing a coplanar stripline (CPS) structure featuring a photonic bandgap (PBG) to facilitate biasing of the PIN diodes with no need for lumped RF chokes or capacitors, which eliminates additional losses introduced by these elements, and hence results in a higher efficiency.

3. Generation of Different Circular Polarisation Senses: By biasing the PIN diodes incorporated in the antenna design, LHCP, RHCP, and LP waves can be generated. This capability enables the antenna to produce various types of polarisations, enhancing its versatility and adaptability for different communication needs.

4. Extension to mmWave Frequencies: The design and fabrication process of the planar reconfigurable circular loop antenna is extended to the mmWave frequency range, specifically at 28 GHz. This extension involves the utilization of a different substrate and a different type of PIN diode to ensure compatibility with the higher frequency mmWave systems.

5.3 Chapter Organization

This Chapter contents are organised as follows:

Section 5.4 initiates by introducing the configuration and design principles of the CP reconfigurable loop antenna and the relevant parameters.

This is followed by Sections 5.5 and 5.6 that outline the utilisation of PIN diodes for efficient antenna switching in RF applications and the isolation of RF current from biasing coplanar stripline using a photonic Bandgap Structure. Section 5.7 presents the implementation of different circular polarisation senses by utilising PIN diodes, whereas section 5.8 offers an analysis of the current distribution for circular polarisation over a wavelength effect. It should be noted that a single biasing network has been utilised for the two PIN diodes, which provides further simplicity in the design.

Moving on to Section 5.9, comprehensive details are provided with respect to the prototypes, simulations, fabrication processes, and measurements of the proposed CP reconfigurable loop antenna at 6 GHz. Subsequently, in Section 5.10, we present the prototypes, simulations, fabrication processes, and measurements of the proposed CP reconfigurable loop antenna at 28 GHz. A performance comparison between the proposed configuration and reported counterparts is presented in section 5.11. Finally, Section 5.12 provides a summary and concluding remarks for the chapter.

5.4 Antenna Configuration

Figures 5.1 and 5.2 present the configurations of reconfigurable antennas designed to operate within the frequency range of 6 GHz and 28 GHz. Each of these antennas consists of two concentric loops that are printed on the upper surface of the dielectric substrate, with an equal-sized ground plane positioned beneath substrate.

The outer loop incorporates two gaps that house the PIN diodes, functioning as switches capable of toggling between forward-bias and reverse-bias states to select the desired polarisation. For the 6 GHz antenna, in CST simulation the forward-bias resistance value is set at 5Ω, while the reverse-bias resistance is 20KΩ. Meanwhile, for the 28 GHz antenna, these resistance values were adjusted to 5.2Ω and 15KΩ for forward bias and reverse bias, respectively. In both configurations, an inner loop, featuring a small gap, was employed to optimize the axial ratio bandwidth.

By adjusting the gaps ($\Delta\varphi_1$, $\Delta\varphi_2$) and controlling the PIN diode states, the proposed antenna can electronically switch its polarisation sense between right-hand circular polarisation (RHCP) and left-hand circular polarisation (LHCP) over a wide frequency range.

The antenna is fed through a coplanar waveguide port (CWP) connected to the outer loop at an angle of Φ=0. The feeding strip line width, denoted by the parameter l_2, for both the 6 GHz and 28 GHz antennas has been optimised to achieve a 50Ω impedance match. Detailed configuration parameters for both designs are summarized in Table 5.1.

Table 5.1 Dimensions Parameters of the Proposed Antennas

Symbol	***Quantity***	***6 GHz***	***28 GHz***
R_1	outer loop radius	5.08 mm	1.22mm
R_2	parasitic loop radius	3 mm	0.95 mm
t_1	outer loop width	1.2 mm	0.28 mm
t_2	parasitic loop width	1 mm	0.1 mm
Padl	pads length	26 mm	8.7 mm
Padw	pads width	8.75 mm	3.96 mm
l_2	transmission line width	1.8 mm	0.25 mm
l_3	the gap between the transmission line & pads	2 mm	0.2 mm
a_0	antenna thickness	0.035 mm	0.035 mm
h	The thickness of the substrate	3.2 mm	0.508 mm
t	reflector thickness	0.035 mm	0.035 mm
Subx	substrate length	110 mm	37 mm
Suby	substrate width	110 mm	40 mm
Substrate type		**FR-4**	**RO4003C**
Permittivity (ε_r)		4.3	3.55
loss tangent		0.025	0.0027
$\Delta\varphi_1$	outer loop gap 1	25^{o}	20^{o}
$\Delta\varphi_2$	outer loop gap 2	25^{o}	20^{o}
$\Delta\varphi_3$	parasitic loop gap	5^{o}	18^{o}

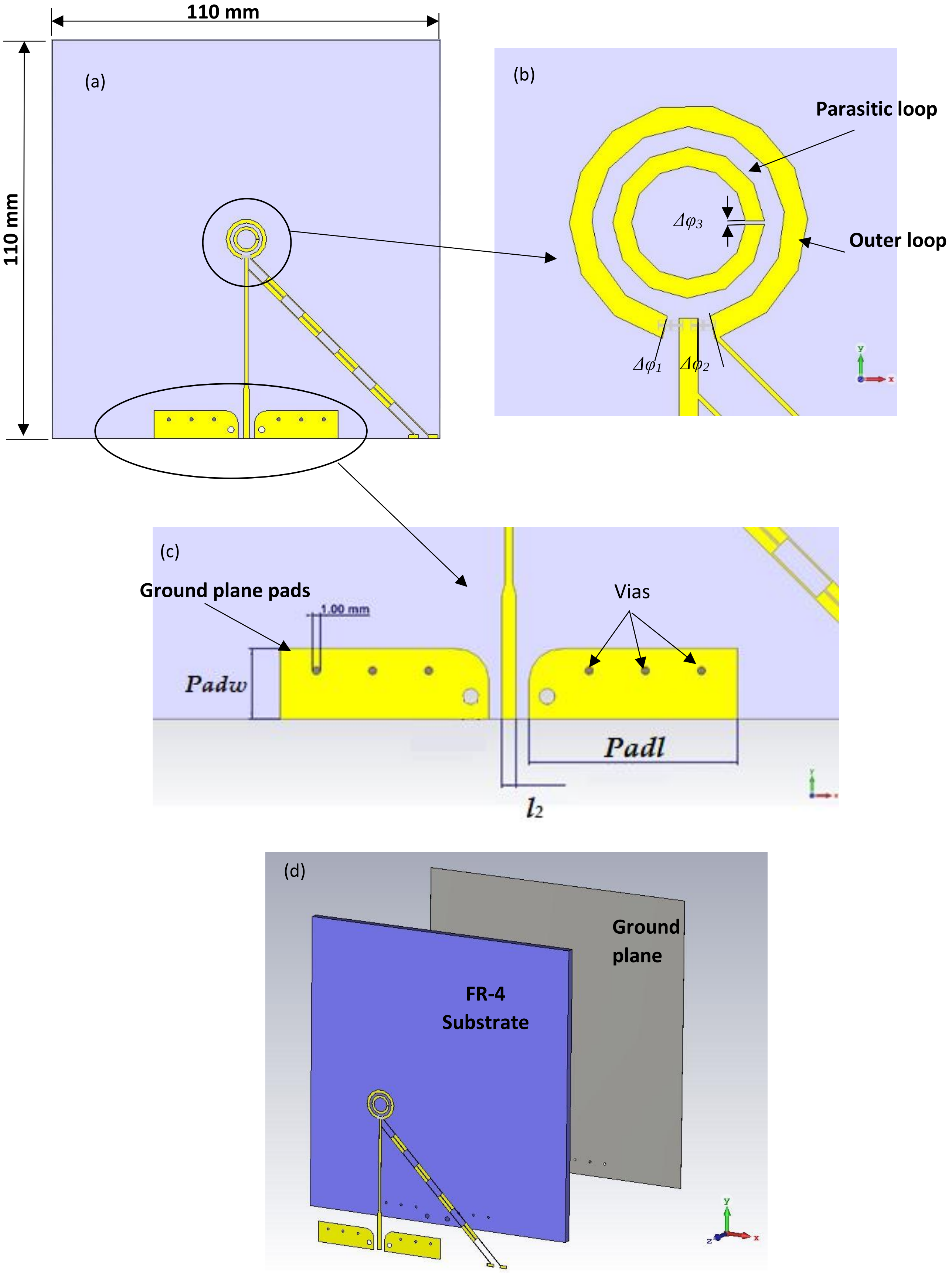

Figure 5.1: The proposed loop antenna at 6 GHz with the integrated two PIN diodes and the corresponding biasing network(a) 2D view. (b) outer and parasitic loops. (c) Ground plane pads. (d) 3D view.

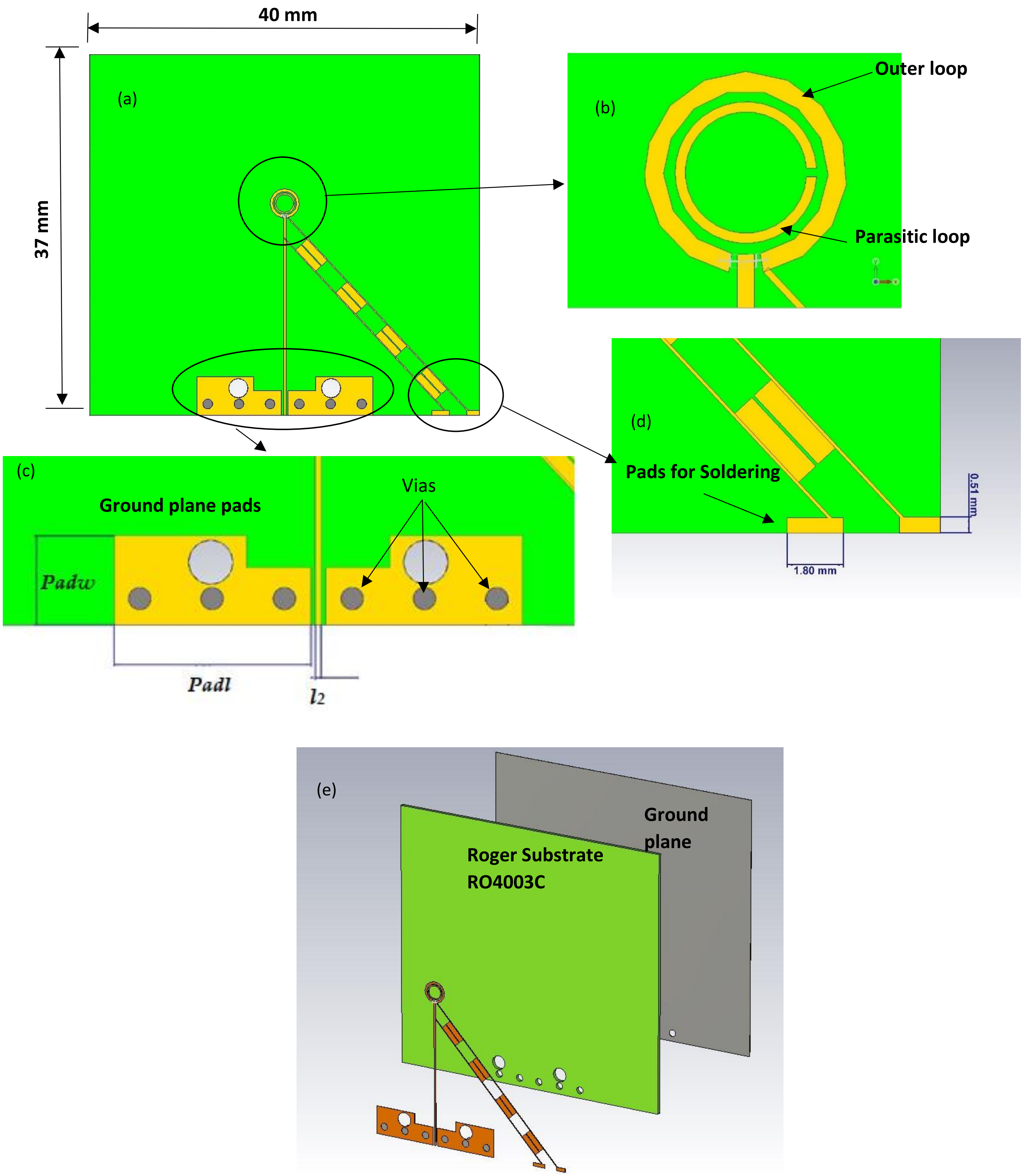

Figure 5.2: The proposed reconfigurable loop antenna at 28 GHz with the integrated two PIN diodes and the corresponding biasing network (a) two-dimensional view. (b) outer and parasitic loops. (c) ground plane pads. (d) Pads for Soldering (e) three-dimensional view.

5.5 PIN Diode

The PIN diode is a versatile semiconductor device for efficient antenna switching in RF applications. The acronym is derived from its construction comprising a P-type semiconductor region, an intrinsic (I) semiconductor region, and an N-type semiconductor region, possesses distinctive electrical characteristics that render it an excellent choice for various switching applications. Its primary advantage lies in its capacity to alter its resistance based on the applied bias voltages, allowing it to seamlessly transition between conducting and non-conducting states.

When incorporated in antennas, the PIN diode functions as a switch, facilitating the antenna's ability to switch between different signal paths. By applying a suitable DC voltage bias, the PIN diode enters a low-resistance state, permitting smooth transmission of RF signals through the diode and toward the antenna. Conversely, reversing the bias voltage causes the PIN diode to transition into a high-resistance state, effectively blocking RF signals from reaching the antenna.

In the proposed designs, two distinct types of PIN diodes have been employed to cater for different frequency requirements. For the 6 GHz antenna, the MA4SPS402 PIN diode has been utilized. On the other hand, the MA4AGFCP910 PIN diode was utilised at 28 GHz, both of which are shown in Figure 5.3. It should be noted that the PIN diodes have been modelled in CST using lumped elements in the equivalent RLC circuits of the forward and revised biased diodes. The dimensional parameters of these PIN diodes and the corresponding RLC equivalent circuit parameters are presented in Table 5.2 and Table 5.3, respectively.

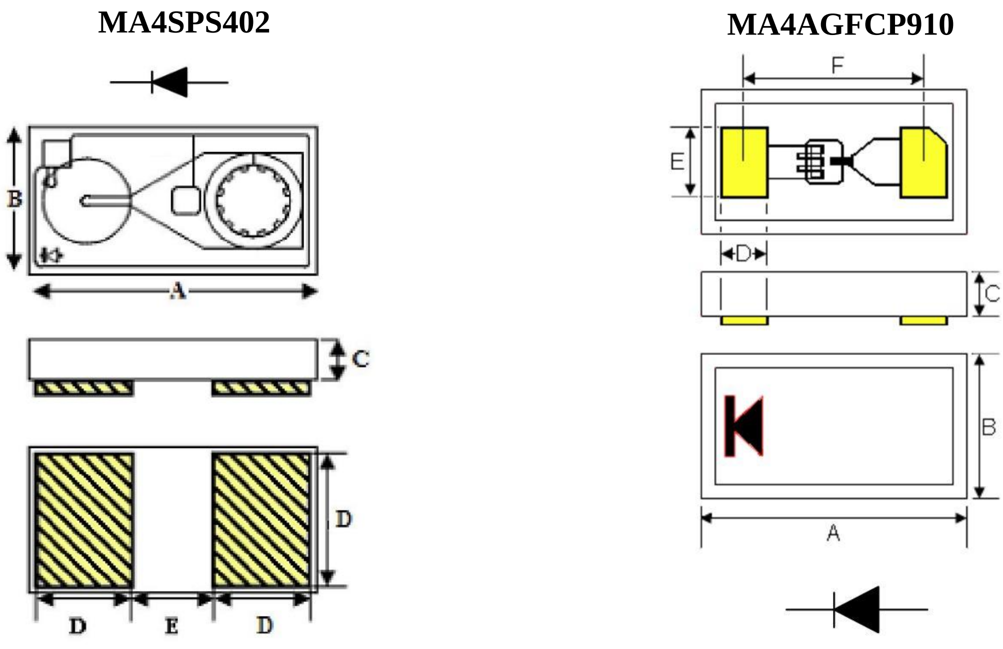

(a)

(b)

Figure 5.3: The PIN diodes for (a) 6 GHz antenna [99] and (b) 28 GHz configuration [100].

Table 5.2 Dimensional Parameters of PIN Diodes.

DIM	A	B	C	D	E	F
6 GHz	1.29 mm	0.533 mm	0.203 mm	0.432 mm	0.406 mm	
28 GHz	0.685 mm	0.368 mm	0.19 mm	0.13 mm	0.185 mm	0.48 mm

Table 5.3 RLC Equivalent Circuit Parameters for PIN Diodes

	6 GHz	28 GHz
PIN Diode type	MA4SPS402	MA4AGFCP910
Total Capacitance C_T	4.5 pF	0.018 pF
Series Resistance R_S	5 Ω	5.2 Ω
Parallel Resistance R_L	20 KΩ	15 KΩ
Total Inductive L_T	4.5 nH	1 nH
Forward Voltage	5 V	1.45 V

5.6 Photonic Bandgap Structure as an RF Choke

Figure 5.4a illustrates the antenna design that incorporates printed strip bias lines, which introduce a negative shunt susceptance (inductive) at the design. To supply the DC bias, a coplanar stripline (CPS) is connected to the antenna element.

The surface current distribution of the antenna with a CPS bias line operating at 6 GHz is displayed in Figure 5.4b. A periodic current distribution is observed in the bias line due to the RF current leakage from the antenna. This current leakage into the bias lines results in unwanted electromagnetic radiation and causes the bias line to function as part of the antenna. Consequently, the antenna's characteristics, such as resonance frequency, input impedance, and radiation pattern, are altered.

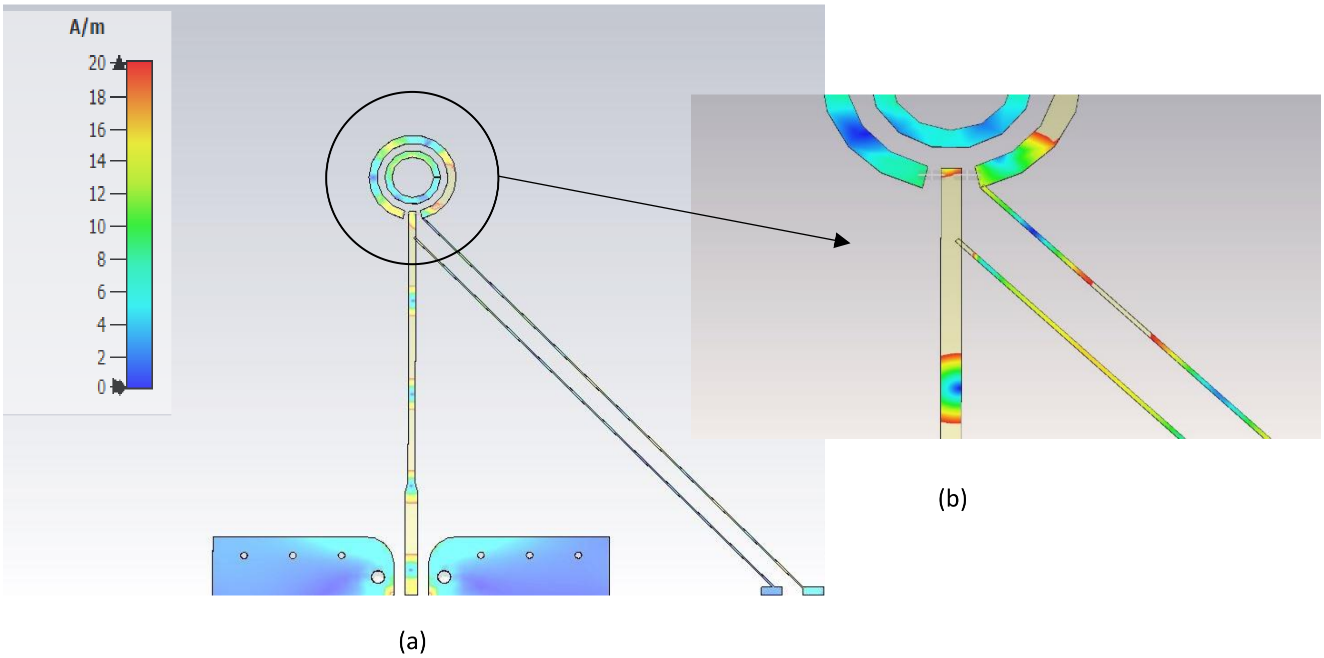

Figure 5.4: Surface current distribution of the proposed antenna with CPS bias line only at 6 GHz.

Figure 5.5: Structure of CPS bias line and PBG.

To address this issue, a new bias line structure is required, i.e. one that not only carries the required DC bias current without an RF current flowing into the bias line. To minimize the RF current flow in the coplanar-stripline, a photonic bandgap (PBG) structure with a periodicity of $\lambda_{eff}/4$ is employed. Figure 5.5 illustrates the PBG structure [101], which consists of a sequence of high and low quarter wavelength transformer sections. The gap width between the high-impedance section CPS line is *X*, the PBG cell length and width are *Y* and *U*, the gap width between the thicker low-impedance PBG cells is *Z*, and the widths of the CPS line are *V*. The design parameters for the CPS bias line and PBG are summarized in Table 5.4.

Table 5.4 Dimensions Parameters for the CPS Bias Line and PBG

Symbol	6 GHz	28 GHz
X	2.68 mm	1.6 mm
Y	7.85 mm	3 mm
Z	0.23 mm	0.1 mm
V	0.23 mm	0.1 mm
U	1.23 mm	0.75 mm
W_b	6.65 mm	1.48 mm
W_a	7.25 mm	2.8 mm
pad_x	3 mm	1.8 mm
pad_y	1.2 mm	0.49 mm

Figure 5.6 showcases the reflection coefficient of the RF choke through the utilization of two waveguide ports positioned at each side of the transmission line, with propagation oriented normally towards each other. This coefficient illustrates the ratio between the reflected power and the input power of the RF choke filter. Notably, the stopband of the proposed choke filter encompasses 28 GHz, where it can be noted that adding the PBG sections effectively cuts off the RF current from flowing across the CPS line, which means the CPS-PBG line serves the purpose as a distributed RF choke.

Figures 5.7a and 5.7b present the surface current distribution of the antennas with a PBG bias line at 6 GHz and 28 GHz, respectively. It is evident that the PBG bias line effectively cuts off the RF current from flowing to the second PBG cell, preventing the undesired leakage. However, some RF current still flows into the first PBG cell, which could potentially impact the antenna's characteristics. To mitigate this effect, the first PBG cell is designed to function as a reflector element in addition to its role as a current isolation mechanism. In this design, the first section of the high-impedance line's near the antenna is operated at a length of less than a quarter-wavelength.

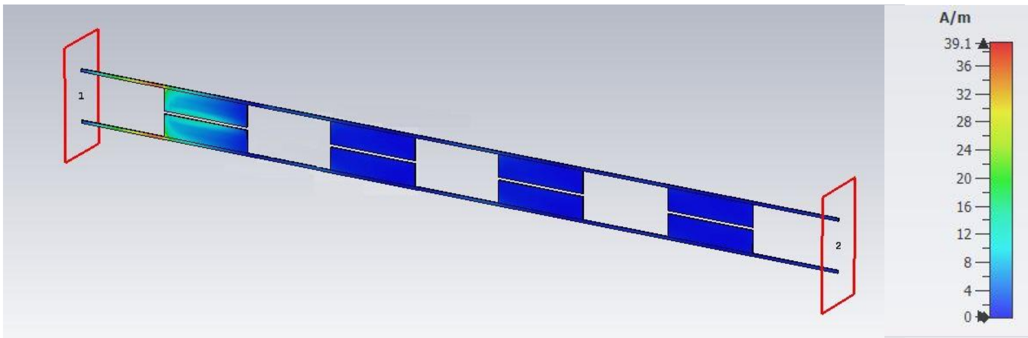

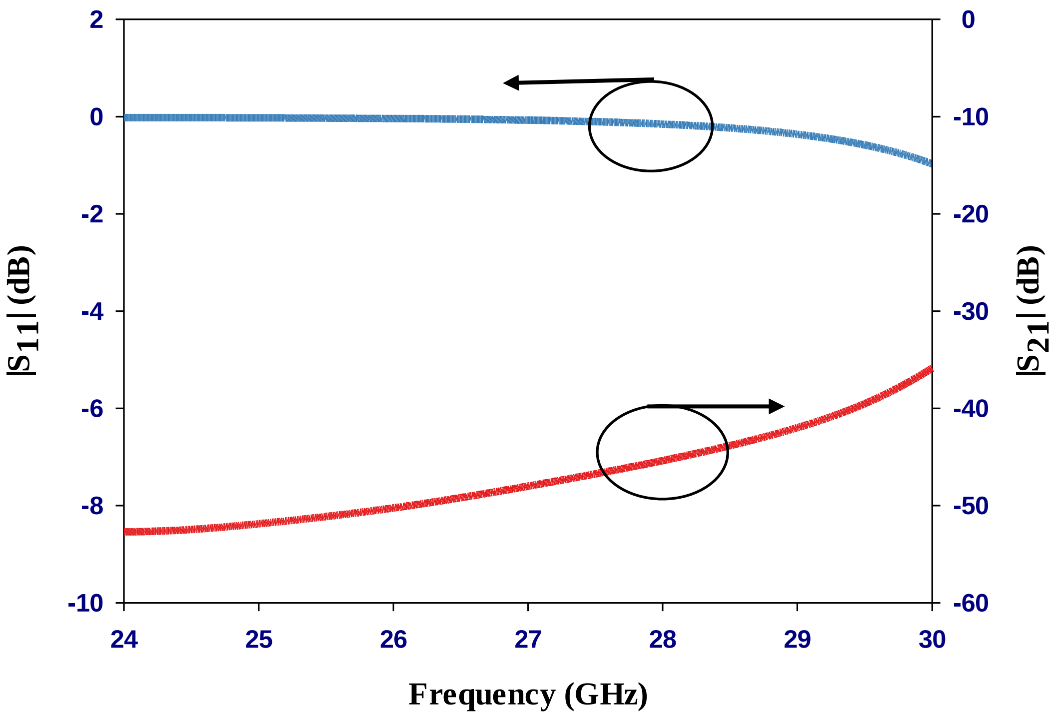

Figure 5.6: illustrates the reflection coefficient of the RF choke in the proposed design.

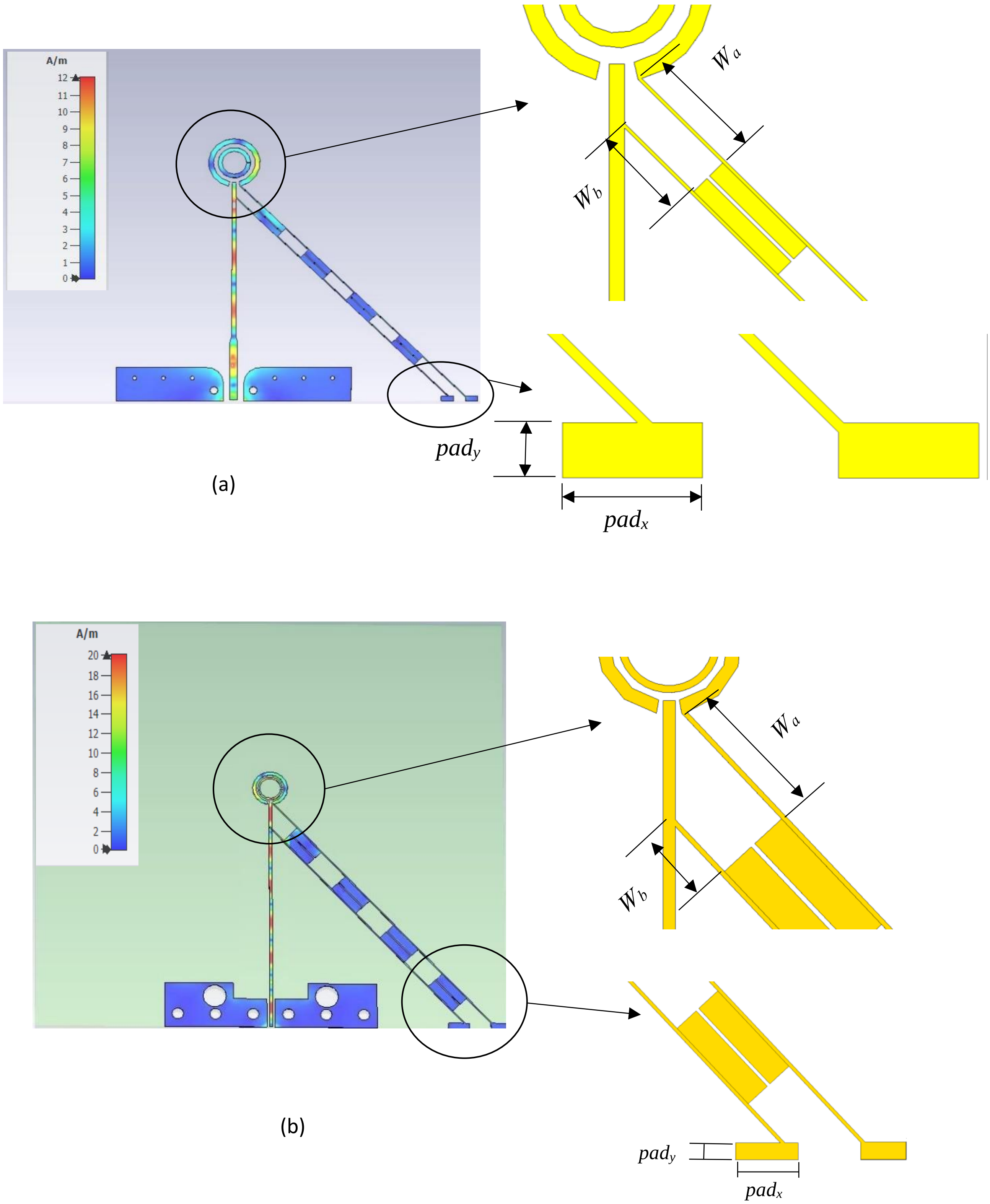

Figure 5.7: Surface current distribution of the proposed antenna with CPS bias line and PBG structure at (a) 6 GHz and (b) 28 GHz.

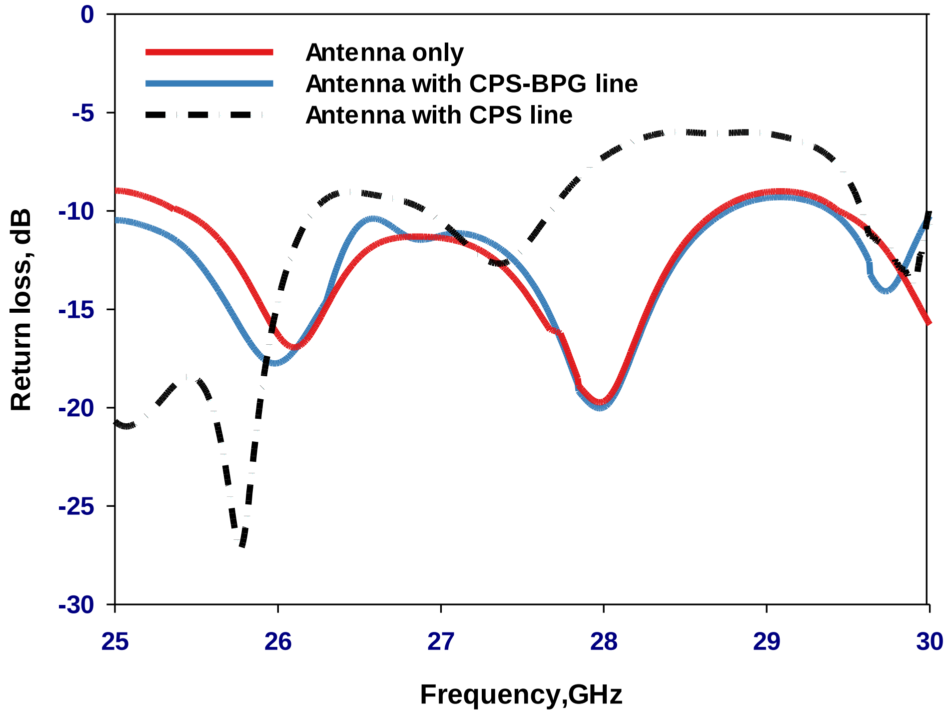

Figure 5.8: Reflection coefficients for various antenna configurations.

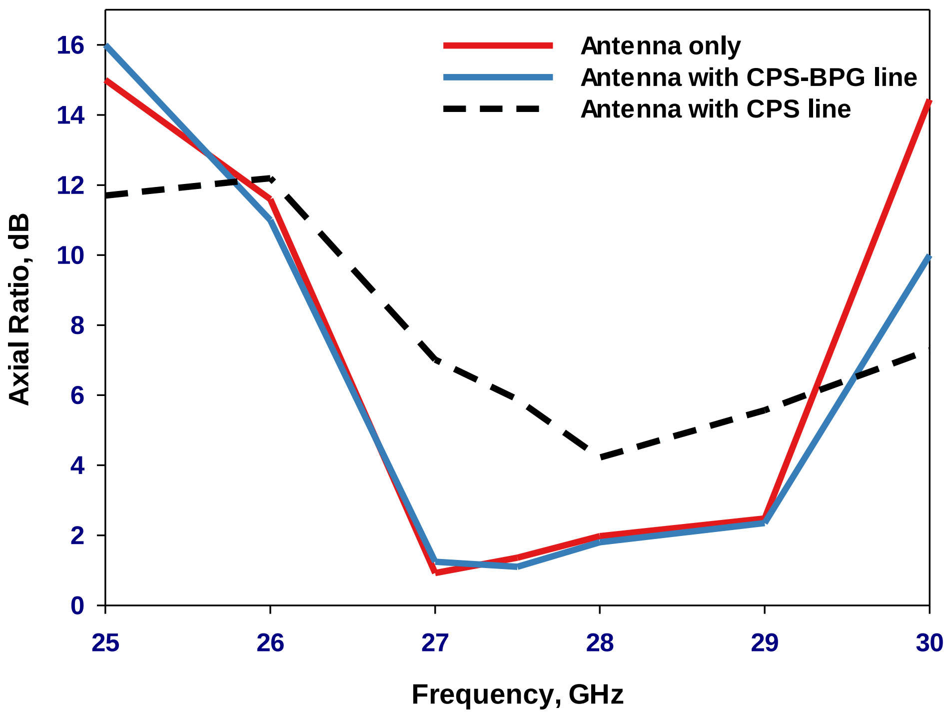

Figure 5.9 Axial ratio for various antenna configurations.

5.7 Realizing Different Polarisations by Utilising Two PIN Diodes

In order to achieve a design that optimizes cost-effectiveness and efficiency while eliminating the need for an additional feeding network to bias the second PIN diode, a modification was introduced by aligning both diodes in the same direction as shown in Figure 5.10. Such arrangement ensures that a single switch and a single biasing circuit are sufficient to achieve reconfigurability, which simplifies the design, improves efficiency, and reduces the required DC power. To achieve different polarisations, three cases have been implemented:

Case A: when the PIN diode 1 is forward biased, it undergoes a state known as the "ON" state. During this state, the diode's resistance decreases significantly, enabling easy flow of current across the gap. As a result, the current passes through the outer loop and reaches the reverse biased PIN diode 2, which is in the "OFF" state. In this state, the diode's resistance increases considerably, effectively blocking the flow of the current. This behaviour resembles that of an open switch, preventing current from flowing through the PIN diode 2.

By implementing this modified design, LHCP can be achieved. This occurs when the current flows clockwise through the outer loop to the PIN diode 2, resulting in the desired polarisation.

Case B: RHCP has been achieved by switching the bias voltage in a manner where PIN diode 2 is forward-biased, while PIN diode 1 is reverse-biased, which changes the current's direction into anticlockwise.

Case C: Linear polarisation has been achieved by utilising unbiased PIN diodes, i.e. in a zero-bias state. Following a commonly used approximation, the equivalent circuits of reverse biased. It should be noted that the proposed antenna offers another advantage of the frequency tunability when both PIN diodes are under zero-bias state.

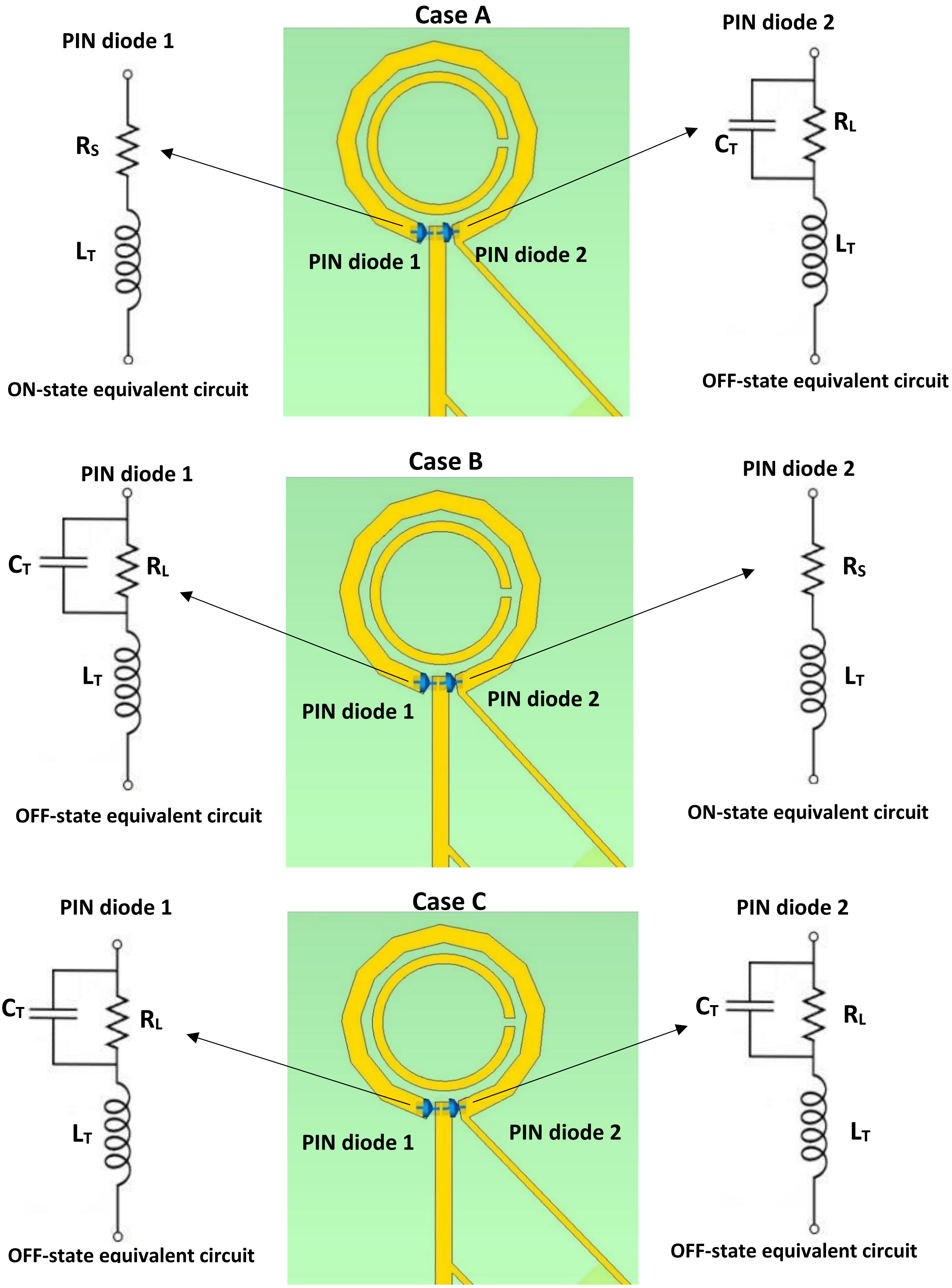

Figure 5.10: Structure for achieving different polarisation by using two PIN diodes.

flow of current when a voltage is applied as demonstrated in Figure 5.11. As a consequence, both gaps of the outer loop remain effectively open, leading to the manifestation of linear polarization.

Overall, this arrangement of diodes simplifies the circuit and eliminates the need for an additional feeding network, thereby optimizing cost-effectiveness and achieving the desired circular polarisations. Table 5.5 illustrates the states of the reconfigurable loop antenna, categorized according to various polarisation states.

Table 5.5 Reconfigurable Loop Antenna States for Different Polarisations States

Case	1st PIN Diode	2nd PIN Diode	Current direction	Polarisation
A	ON	OFF	Clockwise	LHCP
B	OFF	ON	Anti-clockwise	RHCP
C	OFF	OFF	---	LP

5.8 CP Current Distribution Over One Effective Wavelength

Figure 5.12 (a, b) illustrates the current distribution along approximately an effective wavelength of the loop antenna at 6GHz and 28 GHz. In contrast to linear polarisation, where the current's amplitude fluctuates to form a standing wave along the length of the loop, circularly polarized waves exhibit dynamic variations in both magnitude and direction as they propagate. The current's amplitude fluctuates along the loop, gradually decreasing, and adopting a spiral or helical path as it rotates around the direction of propagation. This traveling-wave distribution of the current is responsible for generating the characteristic circular polarisation pattern and the direction, clockwise or anti-clockwise, determines the polarisation sense.

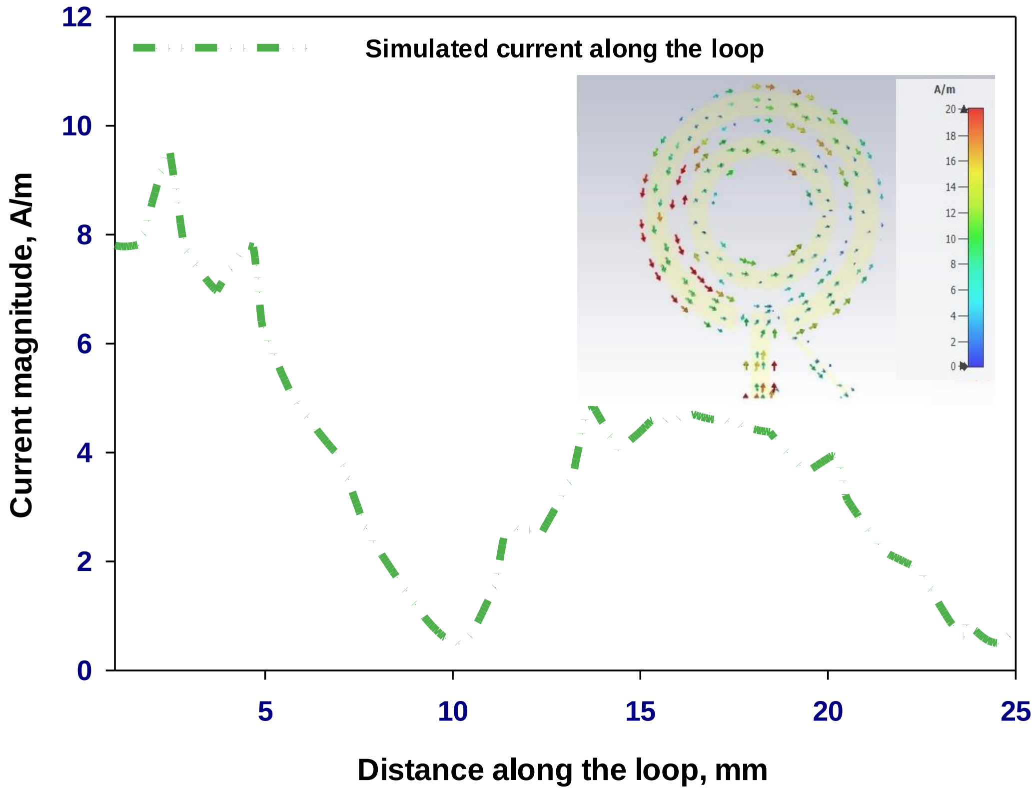

(a)

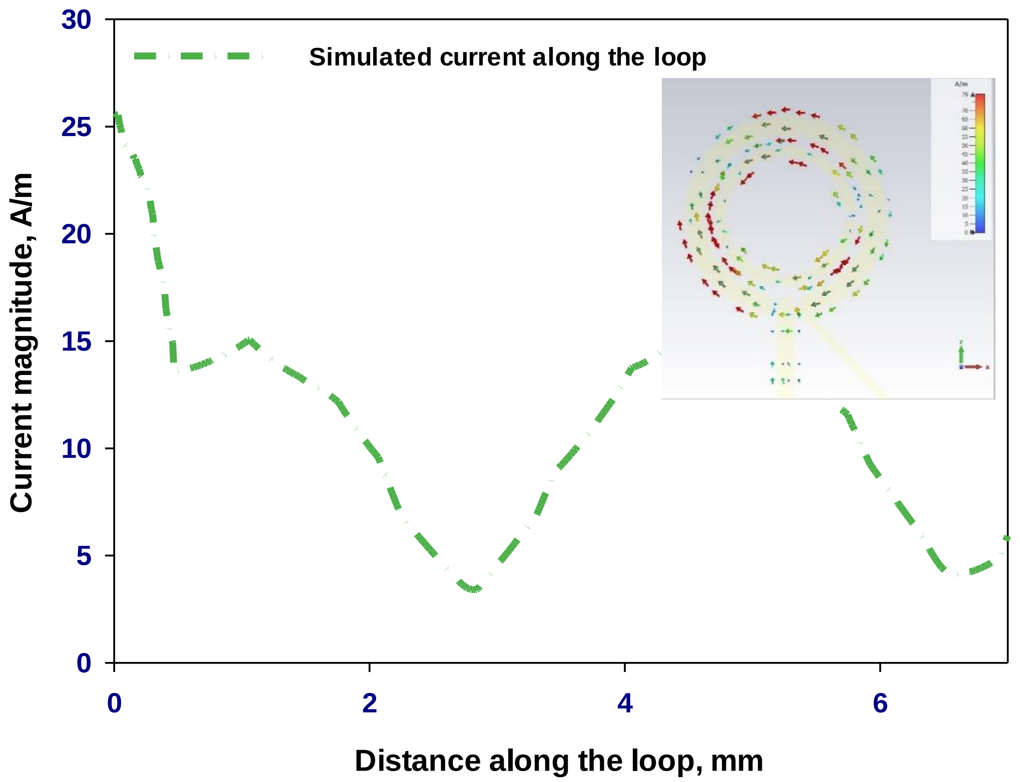

(b)

Figure 5.11: Travelling-wave current distribution along the loop circumference (a) 6 GHz, (b) 28 GHz.

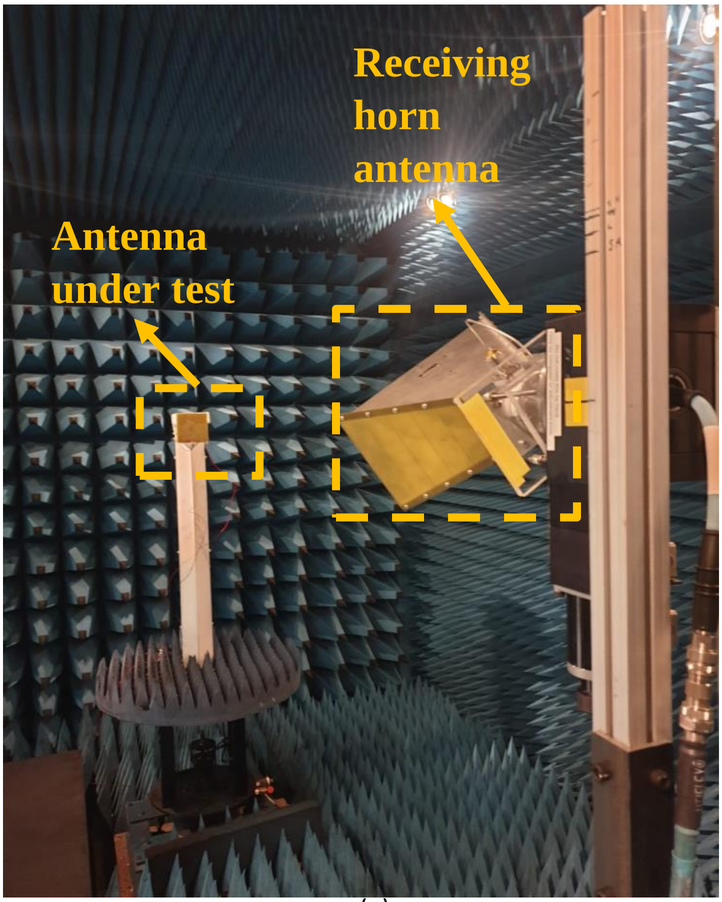

(a)

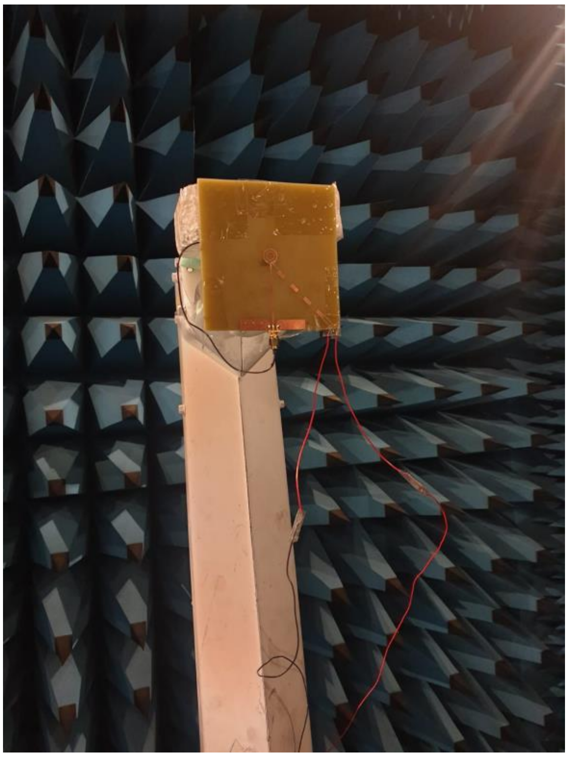

(b)

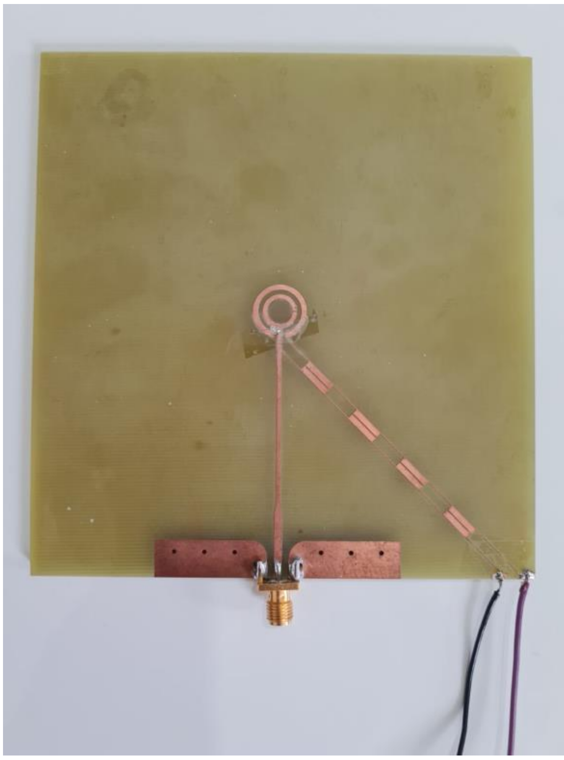

(c)

Figure 5.12: Fabricated prototype of the reconfigurable loop antenna at 6 GHz: (a) antenna under test and (b) measurement setup for verifying radiation pattern (c) top view.

5.9 Fabrication and Measurements at 6 GHz

In the measurement process, depicted in Figure 5.11, photographs demonstrate the 6 GHz reconfigurable loop antenna within the testing environment. The antenna has been fed through an SMA connector, and the S parameters have been gauged utilizing an E5071C vector network analyser connected via a 50 Ω coaxial cable. Precise calibration has been executed employing Agilent's 85052D calibration kit. To assess radiation patterns and gain, an NSI near-field system has been employed.

In Figure 5.13, both the simulated and measured return losses of the proposed antenna are presented. The simulation reveals that when the antenna is configured to operate in the LHCP state, it achieves a 18.2% impedance bandwidth, while in the RHCP state, it attains a 14.7% bandwidth. On the other hand, the measured results show slightly different values, with the LHCP state achieving a 17.6% impedance bandwidth and the RHCP state obtaining a 14% bandwidth. Moreover, the results indicate that the LHCP and RHCP states exhibit nearly symmetrical performance, which is a desirable characteristic for certain applications.

Figure 5.14 presents the simulated and measured axial ratios for both Case A and Case B, indicating the disparity in signal strength between the LHCP and RHCP states of the antenna. For Case A, the simulated 3 dB AR bandwidth is circa 22.8% within the frequency range of 5 to 6.3 GHz. This demonstrates the antenna's capability to maintain its circular polarisation characteristics effectively. On the other hand, the measured 3 dB AR bandwidth for Case A is slightly less, covering the frequency range from 5.1 to 6.2 GHz, with a bandwidth of 19.3%. For Case B, the simulated 3 dB AR bandwidth is ~ 25%, covering the frequency range of 4.9 to 6.35 GHz. Meanwhile, the measured AR is approximately 23.7%, spanning from 5 to 6.3 GHz.

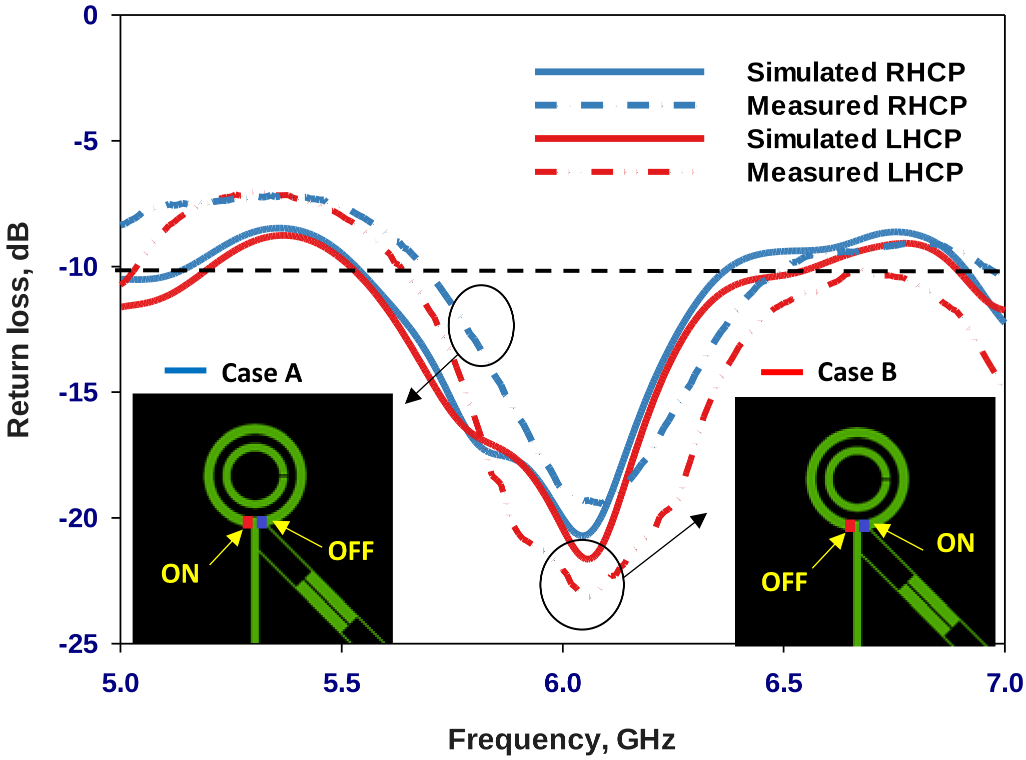

Figure 5.13: Simulated and measured reflection coefficients of the reconfigurable loop antenna.

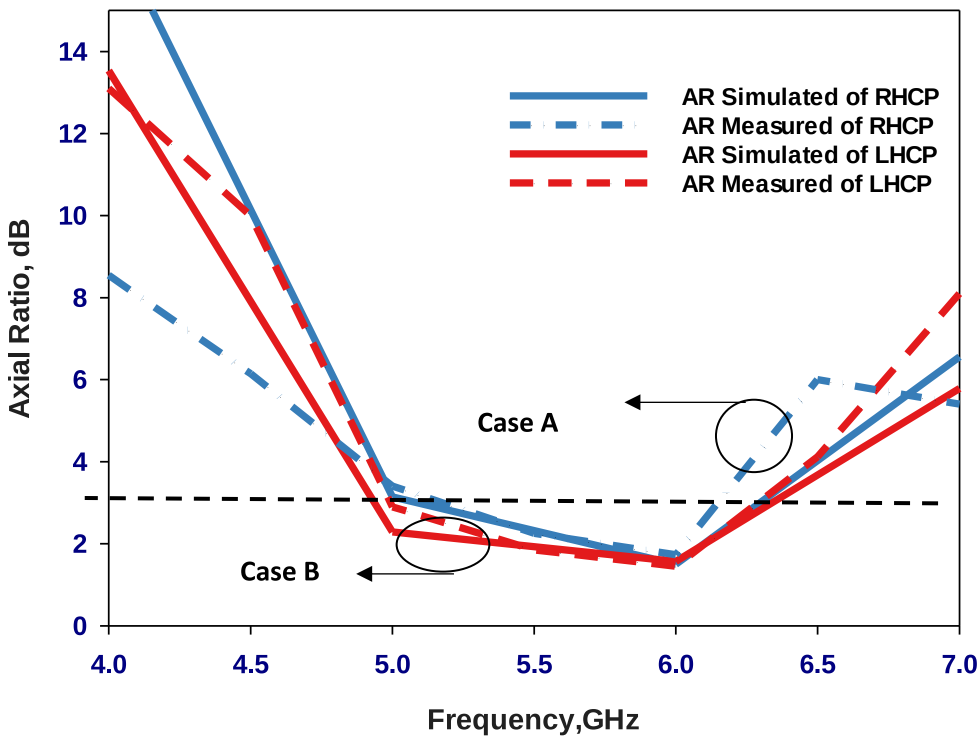

Figure 5.14: Axial Ratio for both circular polarisation senses in the maximum radiation direction.

In Figure 5.15, the simulated and measured realized gains of the proposed antenna are presented. The comparison demonstrates that the measured realised gain closely aligns with the simulated results. In both Case A and Case B, the simulated realized gain is approximately 4.8 dBic.

The simulated total efficiency is depicted in Figure 5.16 for both circular polarisation senses. The total efficiency remains relatively constant at approximately 55%. The lower efficiency is attributed to the use of a lossy FR-4 substrate, which is expected to be enhanced in the mmWave design through the utilization of alternative substrates with lower losses. Finally, Figure 5.17 demonstrates the simulated and measured normalized radiation patterns at 6 GHz in the E-plane (*xz* plane) and H-plane (*yz* plane). The investigation reveals excellent agreement between the simulation and measurement results.

Notably, the broadside mode exhibits the highest gain in the $\theta = 0°$ direction in both cases, with RHCP radiation in Case A and LHCP radiation in Case B. However, it is evident that there is a degradation in the LHCP radiation pattern in Case A and the RHCP radiation pattern in Case B. These findings emphasize the importance of considering polarisation effects in the antenna design, as the circularly polarized radiation patterns exhibit slightly different characteristics in the two cases.

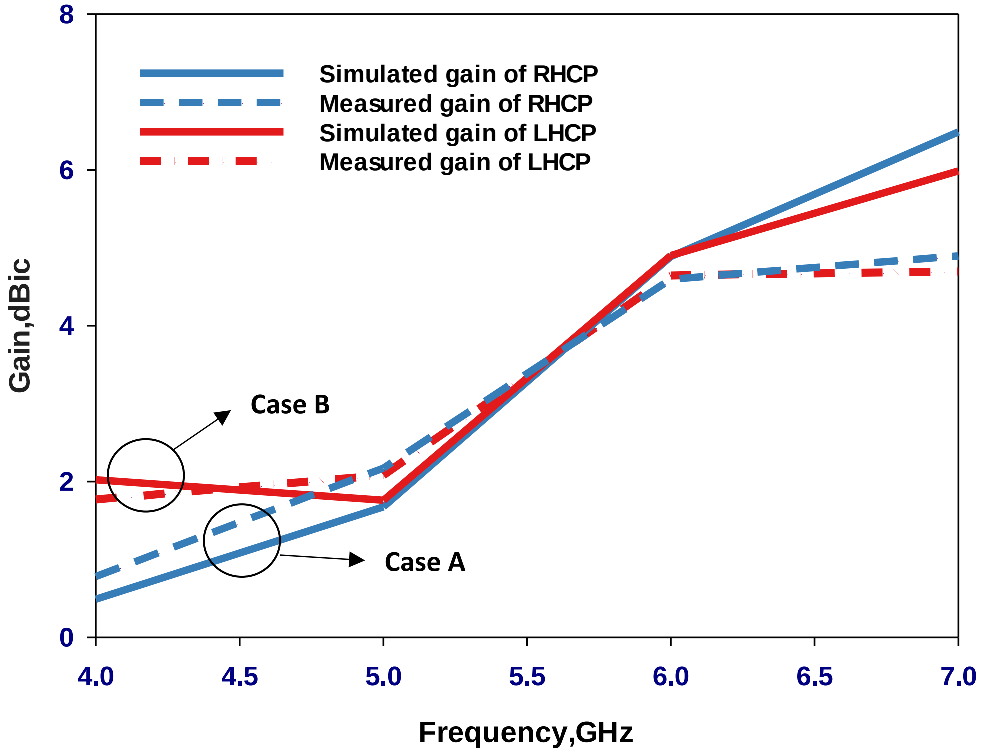

Figure 5.15: Simulated and measured antenna realized gains for Case A and Case B.

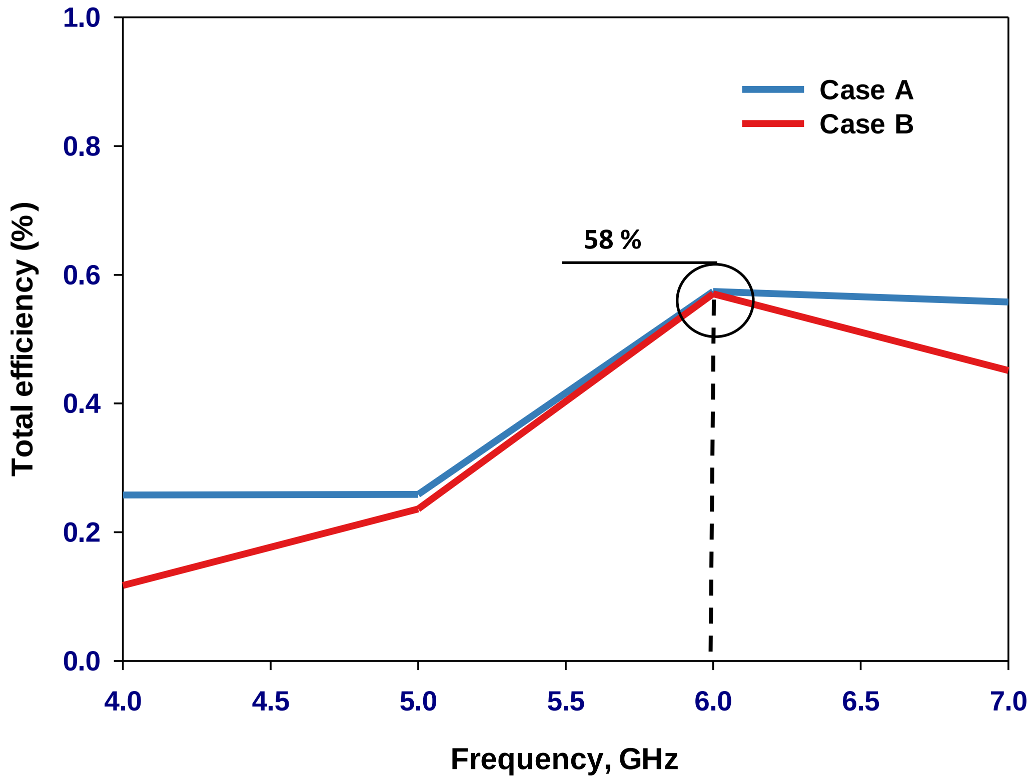

Figure 0-1 Simulated total efficiency for circular polarisation cases at 6 GHz.

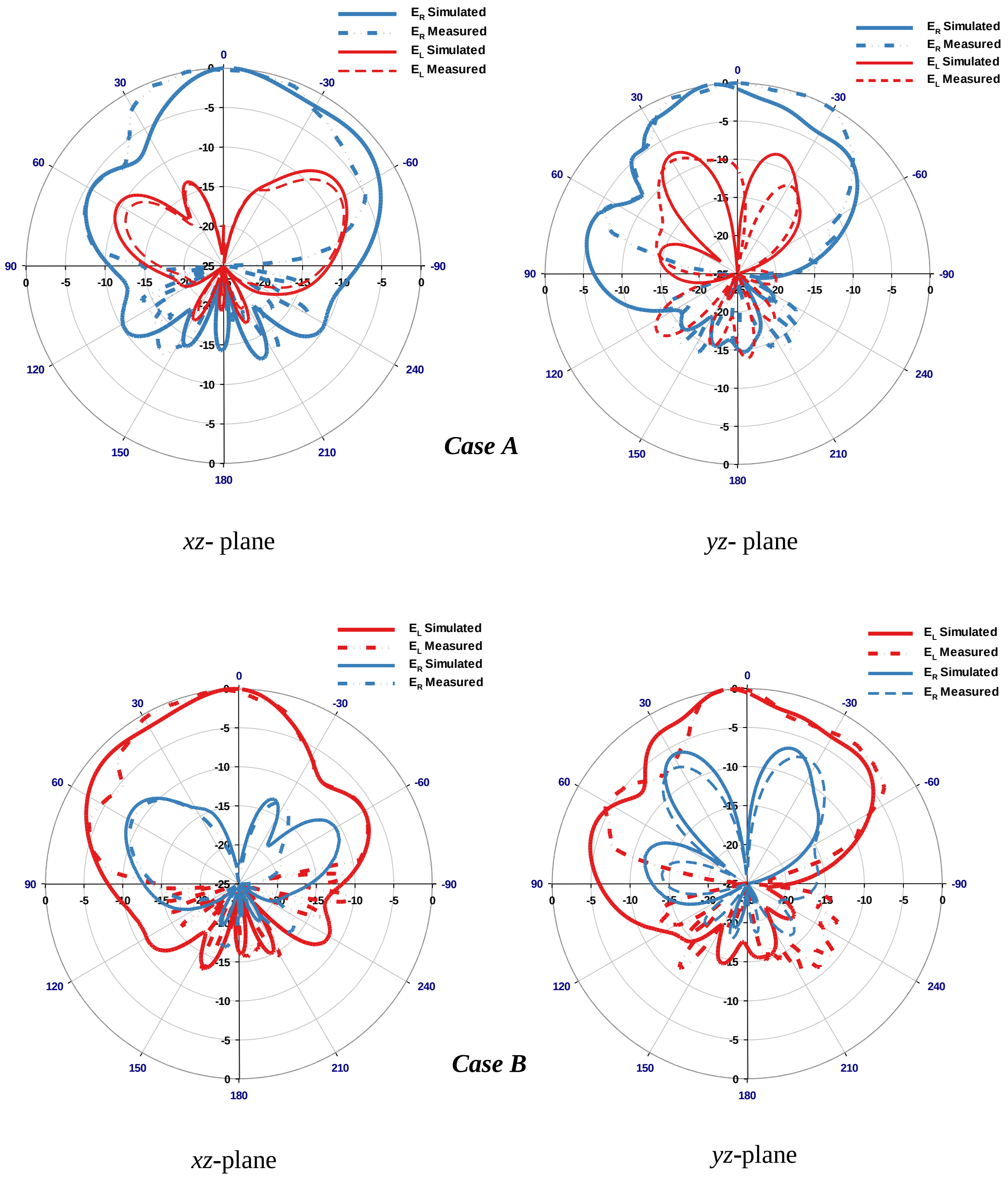

Figure 5.17: The simulated and measured normalized patterns at 6 GHz for the reconfigurable loop antenna equipped with two PIN diodes, depicting two working states: (a) Case A and (b) Case B.

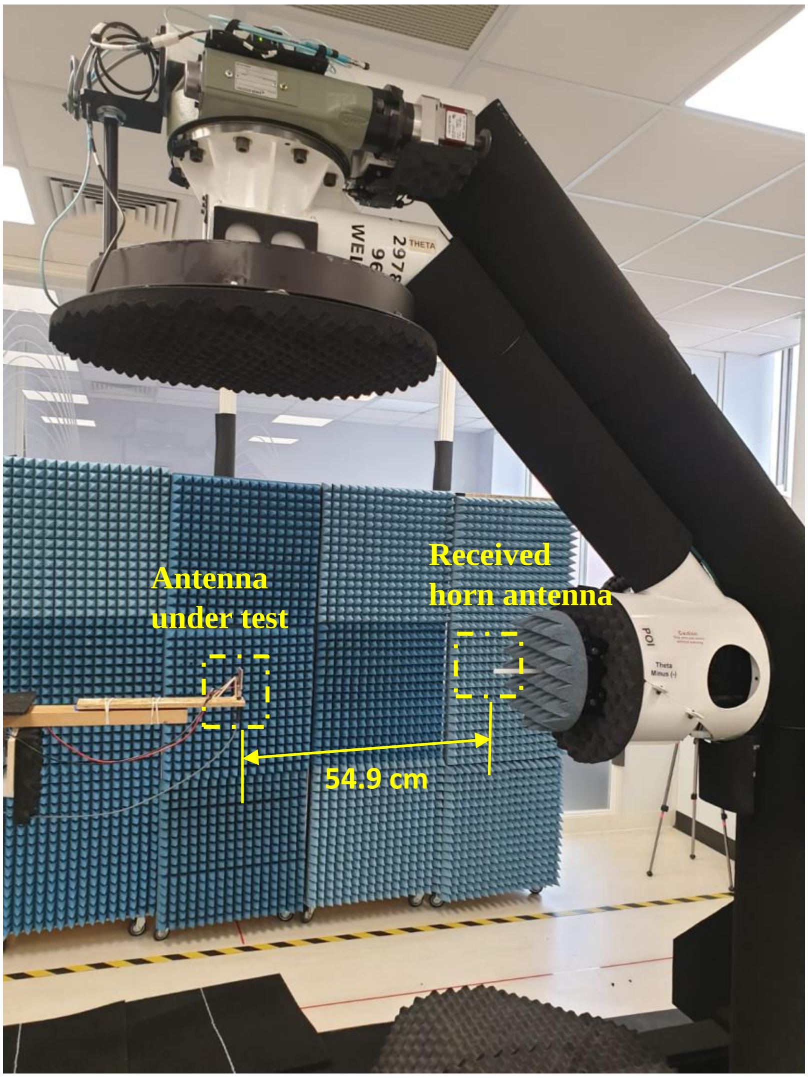

(a)

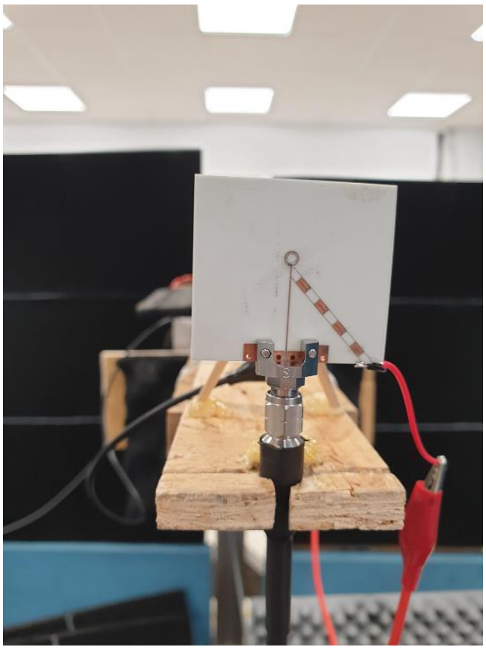

(b)

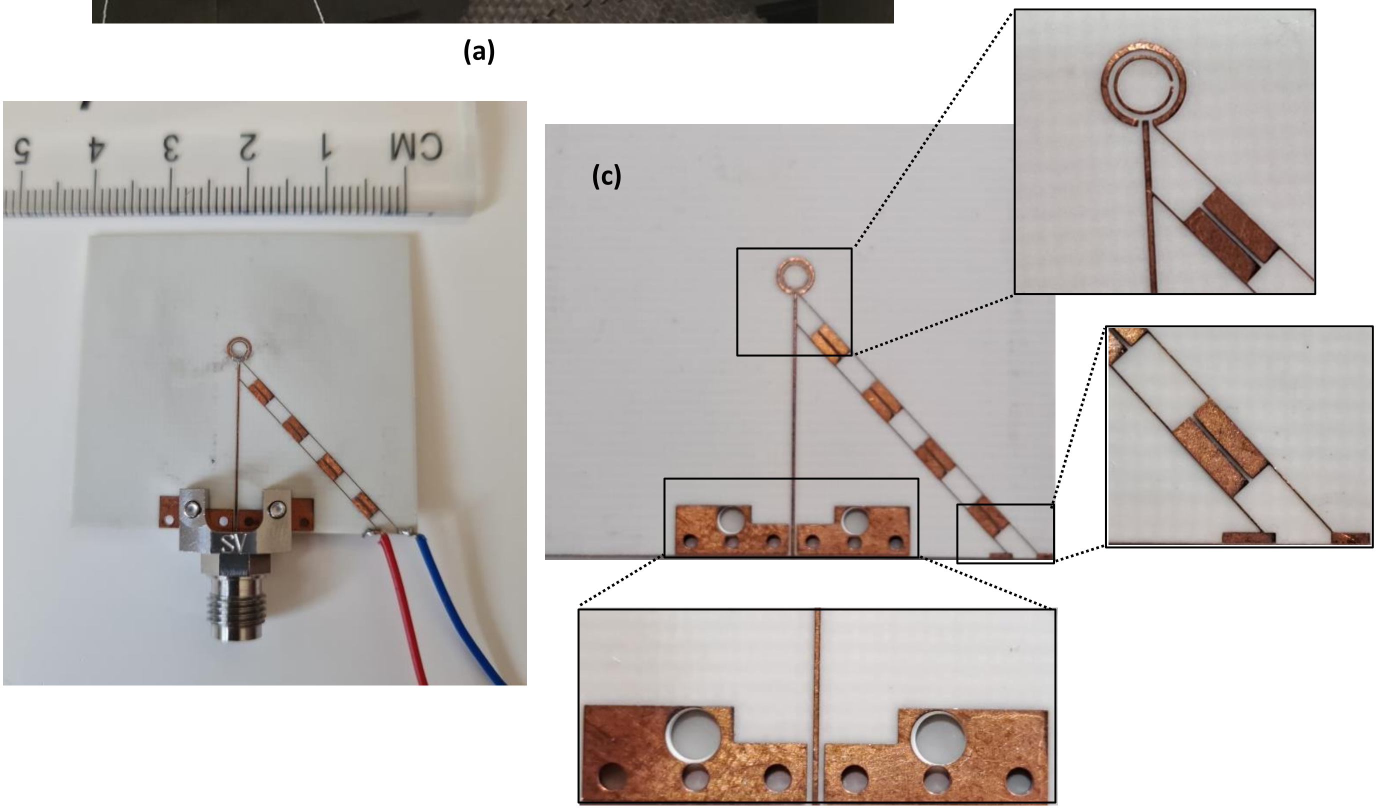

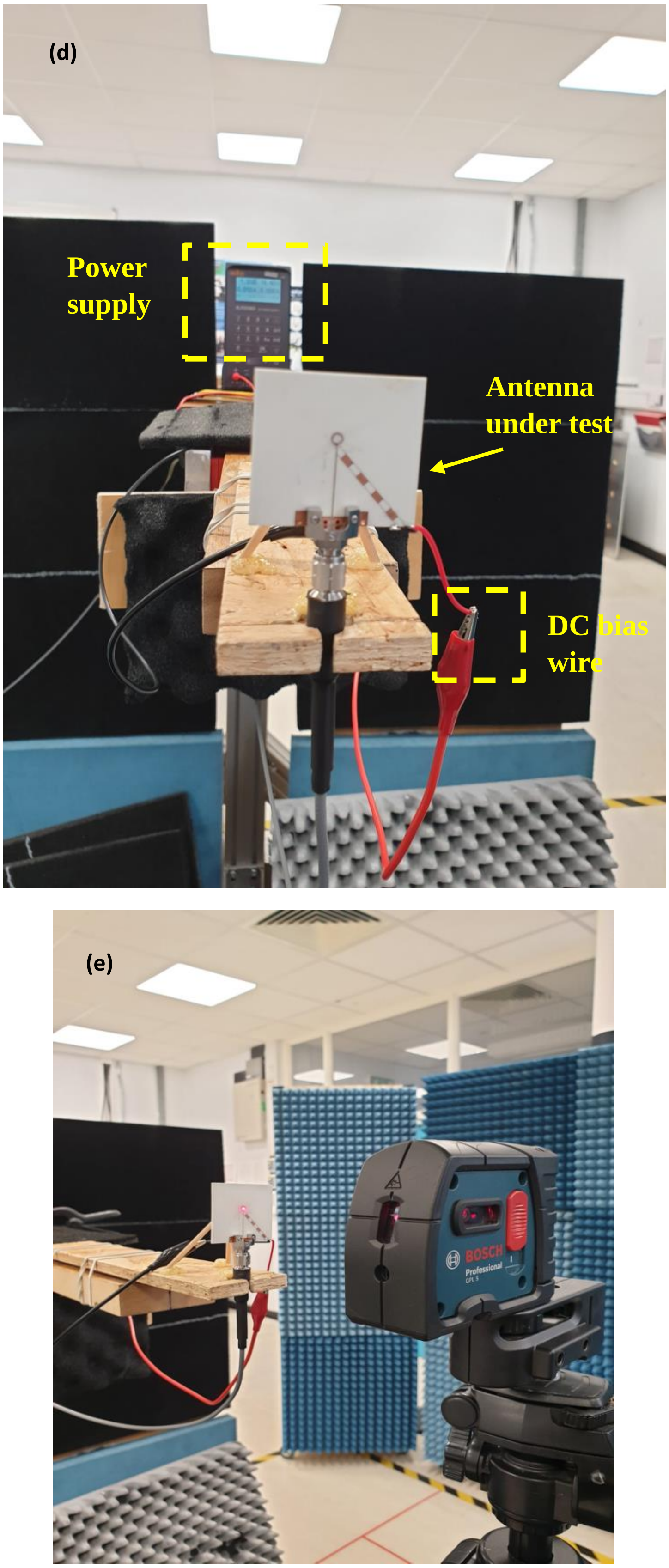

Figure 5.18: showcases the fabricated prototype of the reconfigurable loop antenna at 28 GHz. Panels (a) Far field measurements and (b) provides a top view, while panel (c) Provides a prototype of the reconfigurable loop antenna. Panels (d) Power supply calibration, and panel (e) Antenna alignment.

5.10 Fabrication and Measurements at 28 GHz

A prototype of the antenna has been manufactured by Wrekin [102] as demonstrated in Figure 5.18c, where a 2.4 mm SMA connector has been utilized. The overall antenna size is 40mm×37mm. The vias were created by tiny holes in a printed circuit board (PCB) that are used to establish electrical connections between different layers of the board, and then these holes are plated with gold. The measurements' set-up is illustrated in Figure 5.18a for the mmWave reconfigurable loop antenna within the testing environment. The NSI-MI Technologies system was utilized for the far-field measurements, while the N5245B vector network analyzer (VNA) was used to quantify the return losses [103]. An 85052D kit has been utilized for the measurements of the reflection coefficient. The antenna was positioned at 54.9 cm from the reference horn antenna to measure its radiation pattern. Prior to this measurement, the power supply was calibrated and linked to the antenna through wires to apply bias to the PIN diodes.

Figure 5.19 (a, b) illustrates a compelling comparison between simulated and measured results for reflection coefficients. This analysis delves deeply into the three distinct cases of the proposed antenna with RHCP, LHCP, and LP modes. As shown in Figure 5.19a, the simulation draws out intriguing details. Upon configuring the antenna in Case A, it achieves a 13.3% impedance bandwidth compared to 13.7% in Case B centred at 28 GHz.

What adds credence to these findings is the alignment between measured and simulated −10 dB impedance bandwidths. In case A, the measurements mirror the simulation closely, showcasing a 12.7% impedance bandwidth, and in parallel, case B achieved 11.2% bandwidth - a strong testament to the reliability and consistency of the antenna's performance across these divergent scenarios. Figure 5.19b presents the reflection coefficient when the two PIN diodes are under zero-bias, where it can be noted that matching is achieved over dual narrow bands centered at 26.8 GHz and 29 GHz with considerably narrower bandwidths compared to that in the CP states. Namely, bandwidths of 3.4% and 2.1% have been achieved in the simulation compared to 2.3% and 1.9% in the measurements. These results indicate that in addition to the reconfigurable polarisation, reconfigurable frequency capabilities have also been achieved when utilizing linear polarisation. Therefore, the proposed antenna offers hybrid, or compound, reconfiguration since the frequency and polarisation can be tuned using only two PIN diodes with a single biasing network.

The measure and simulated axial ratios are demonstrated in Figure 5.20 for both cases of LHCP and RHCP. In the scenario of Case A, the simulated 3 dB AR bandwidth covers approximately 8.1% within the frequency range of 26.75 to 29 GHz, effectively achieving RHCP radiation. The measured 3 dB AR bandwidth in Case A ranging from 26.85 to 28.9 GHz, with a bandwidth of circa 7.42% which is in close agreement with simulations.

On the other hand, Case B offers simulated 3 dB AR bandwidth of roughly 7.64%, spanning the frequency band from 26.89 to 29 GHz, while achieving LHCP radiation. Concurrently, the corresponding measurement outcome registers around 5.4%, enveloping frequencies from 26.85 to 28.35 GHz.

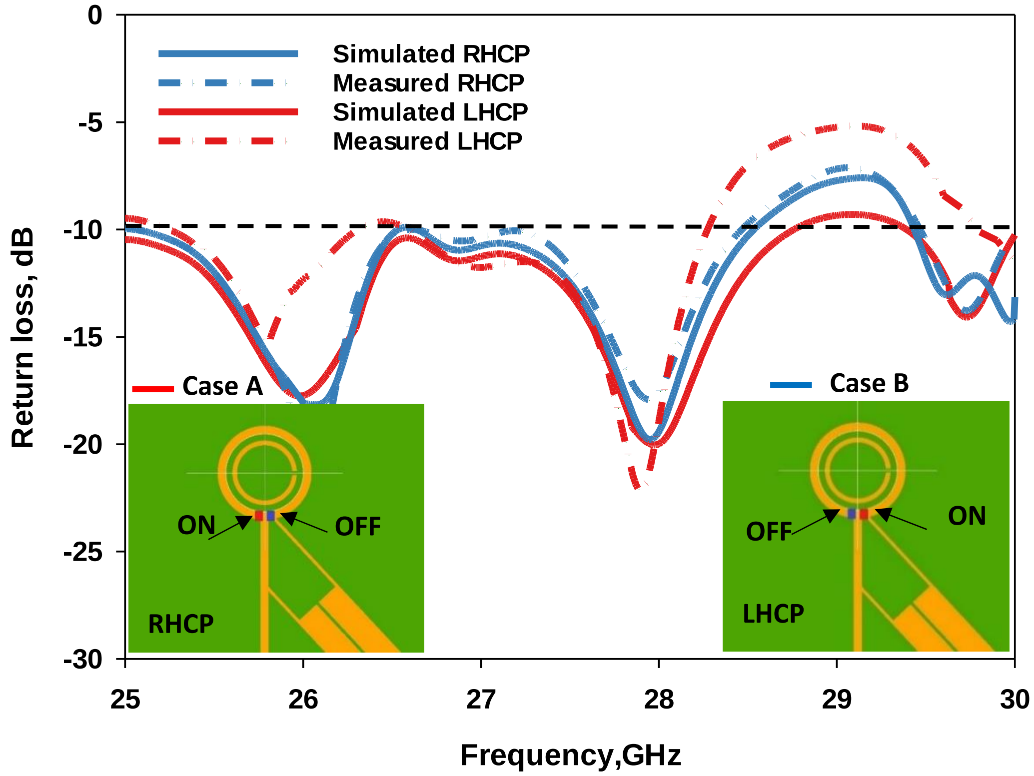

(a)

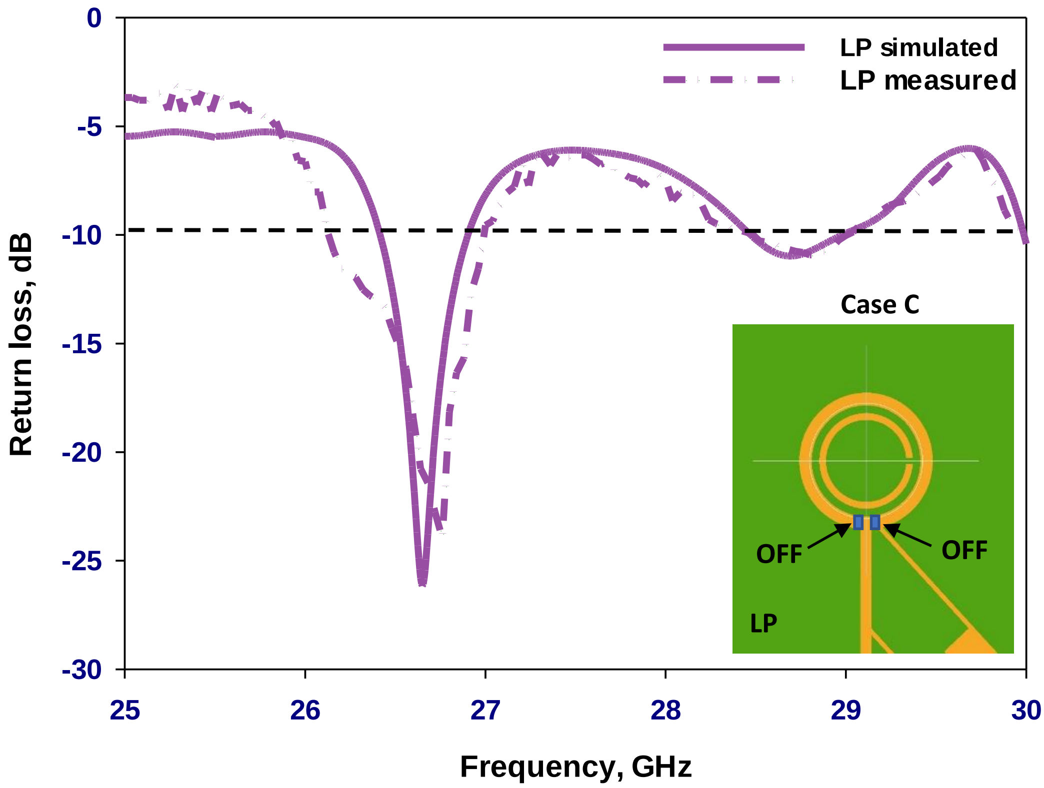

(b)

Figure 5.19: The simulated and measured return losses of the mmWave reconfigurable loop antenna.

The normalized simulated and measured radiation patterns for RHCP and LHCP at 28 GHz in the E-plane (*xz* plane) and H-plane (*yz* plane) are shown in Figure 5.21. The measured radiation patterns mostly follow the simulated counterparts with slight differences due to the measurement errors at the mmWave frequency range. By controlling two cases of the PIN diodes, different main polarisation directions can be switched. Remarkably, in both cases, the maximum radiation pattern is emitted in the broadside direction (at θ = 0°), resulting in RHCP wave in Case A and in LHCP wave in Case B. Nevertheless, a significant deterioration in Case A when LHCP is radiated, and a similar decline in the RHCP radiation pattern in Case B.

Figure 5.22 presents the simulated and measured normalized radiation patterns of the antenna within Case C at 27 GHz in E-plane (*xz* plane) and H-plane (*yz* plane). This configuration enables the radiation of LP at a different operating frequency.

Figure 5.23 illustrates the total efficiency and the gain for both circular polarisation and linear polarisation modes. The simulated total efficiency remains consistent at circa 79% across the desired bandwidth, which demonstrates excellent performance for a reconfigurable antenna operating in the mmWave frequency range [101]. However, when considering Case C, it's worth noting that the total efficiency at 27 GHz exhibits a slight reduction, approximately a 73% decrease in comparison to other cases. This could be attributed to the higher resistances offered by the two unbiased PIN diodes. In addition, the comparison reveals a close correspondence between the measured and simulated realized gains. In both Case A and Case B, the measured and simulated realized gain is circa 7.5 dBic at 28 GHz. In contrast, Case C exhibits a realized gain of approximately 7.6 dBic at 27 GHz.

The improvement in efficiency can be attributed to several factors such as the absence of lumped inductors and capacitors in the biasing network. This is in addition to utilizing a single biasing network for the two diodes instead of the common approach of utilizing a separate biasing network for each diode. This is in addition to employing a lossy Rogers substrate.

However, the PIN diode is associated with losses that have been accounted for in the achieved efficiency of 79% in cases A and B and 72% in case C. The performance comparison in Table 5.6 demonstrates that the proposed mmWave reconfigurable antenna outperforms published counterparts in terms of CP bandwidth, gain and efficiency. It should be noted that the proposed antenna offers another advantage of the frequency tunability when both PIN diodes are under zero-bias states. This has not been demonstrated in Table 5.6 since the comparison is focused on the CP performance of the antenna.

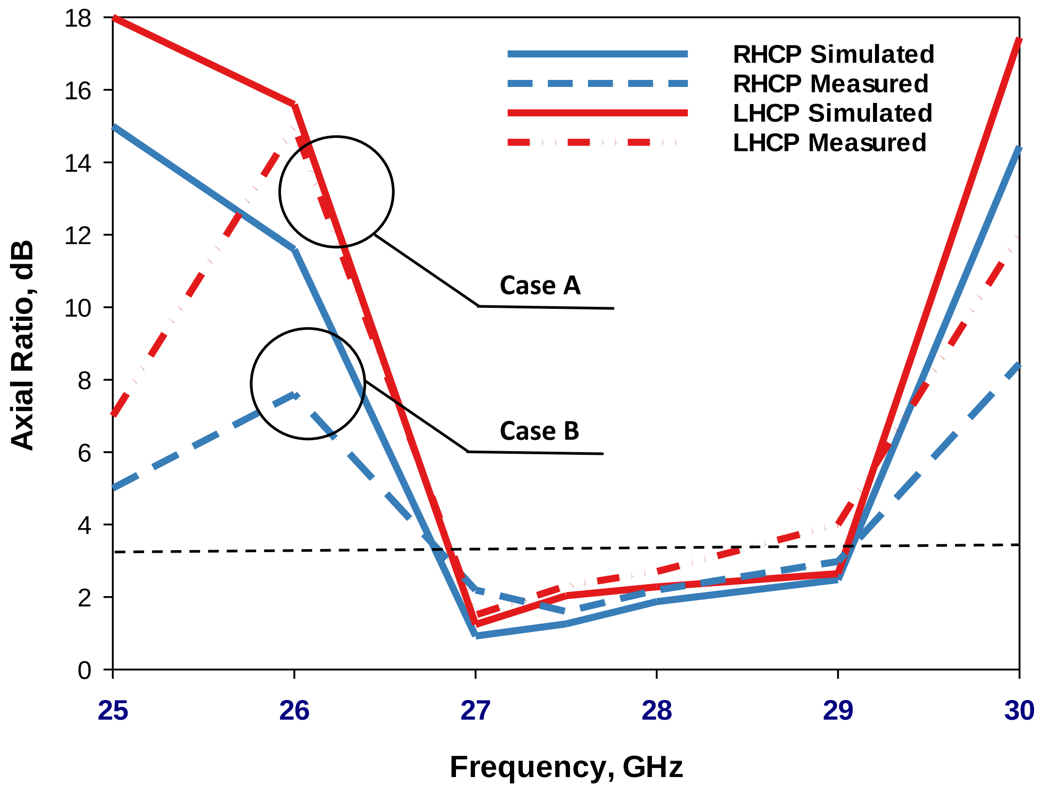

Figure 5.20: Axial Ratio of the mmWave reconfigurable loop antenna for both operational cases.

Case A
xz- plane

Case A
yz- plane

Case B
xz- plane

Case B
yz- plane

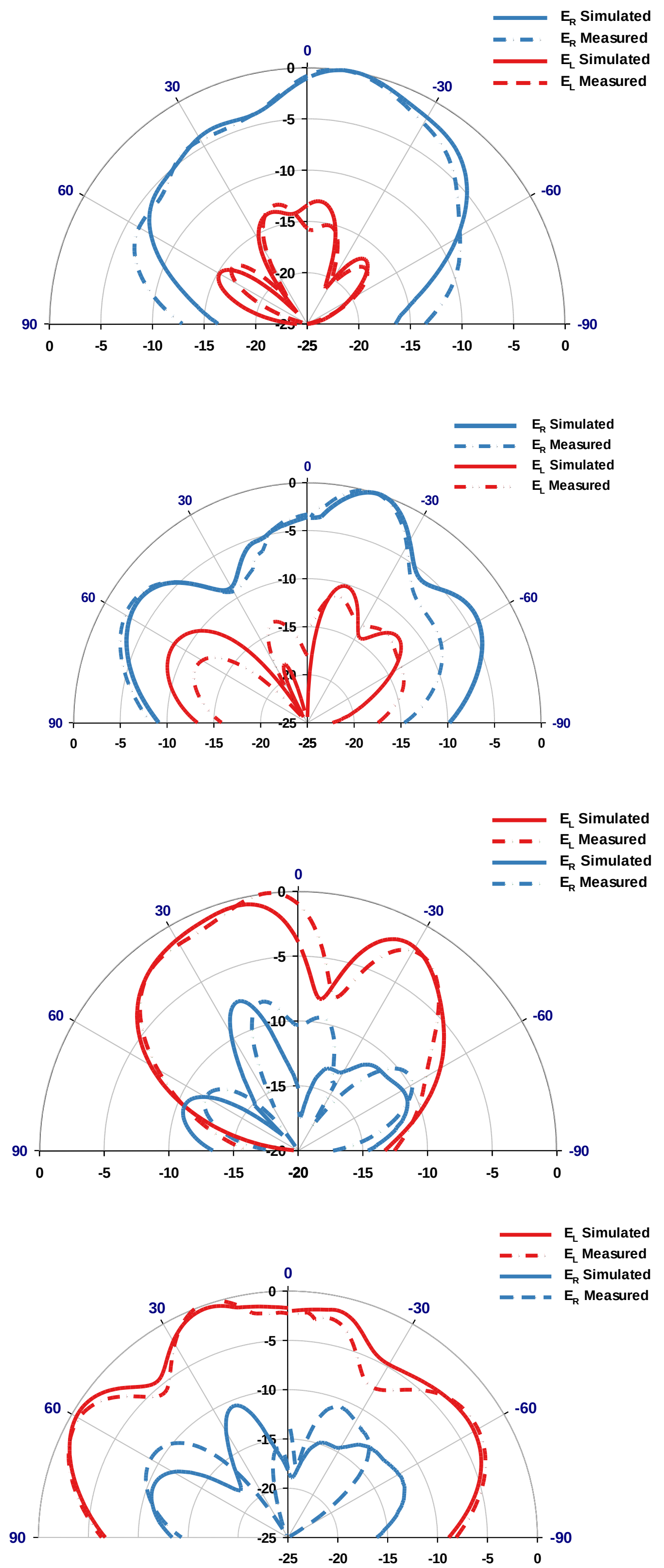

Figure 5.21: Simulated and measured normalized antenna radiation patterns at a frequency of 28 GHz for a mmWave reconfigurable loop antenna: (a) Case A and (b) Case B.

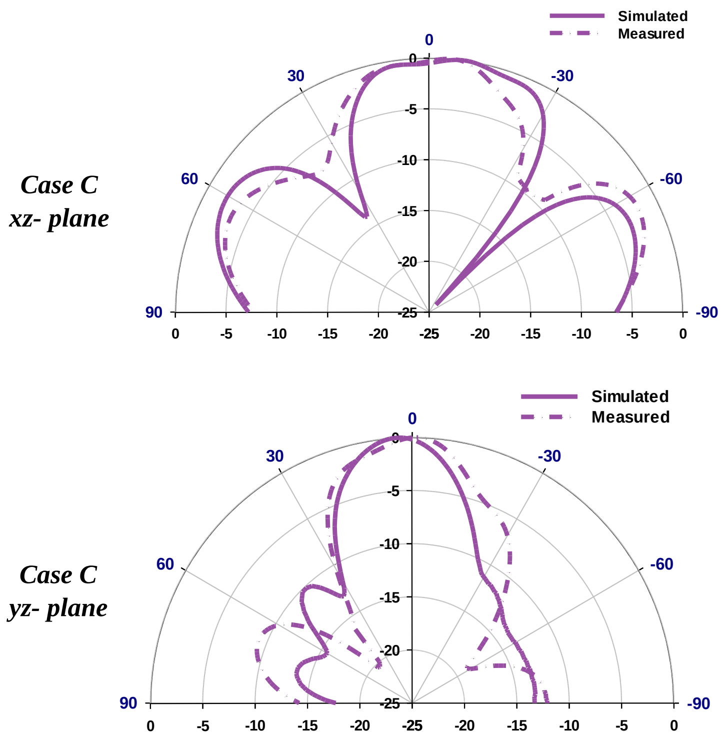

Figure 5.22: Normalized radiation patterns for the reconfigurable antenna in Case C at 27 GHz; (a) ϕ=0°,(b) ϕ=90°.

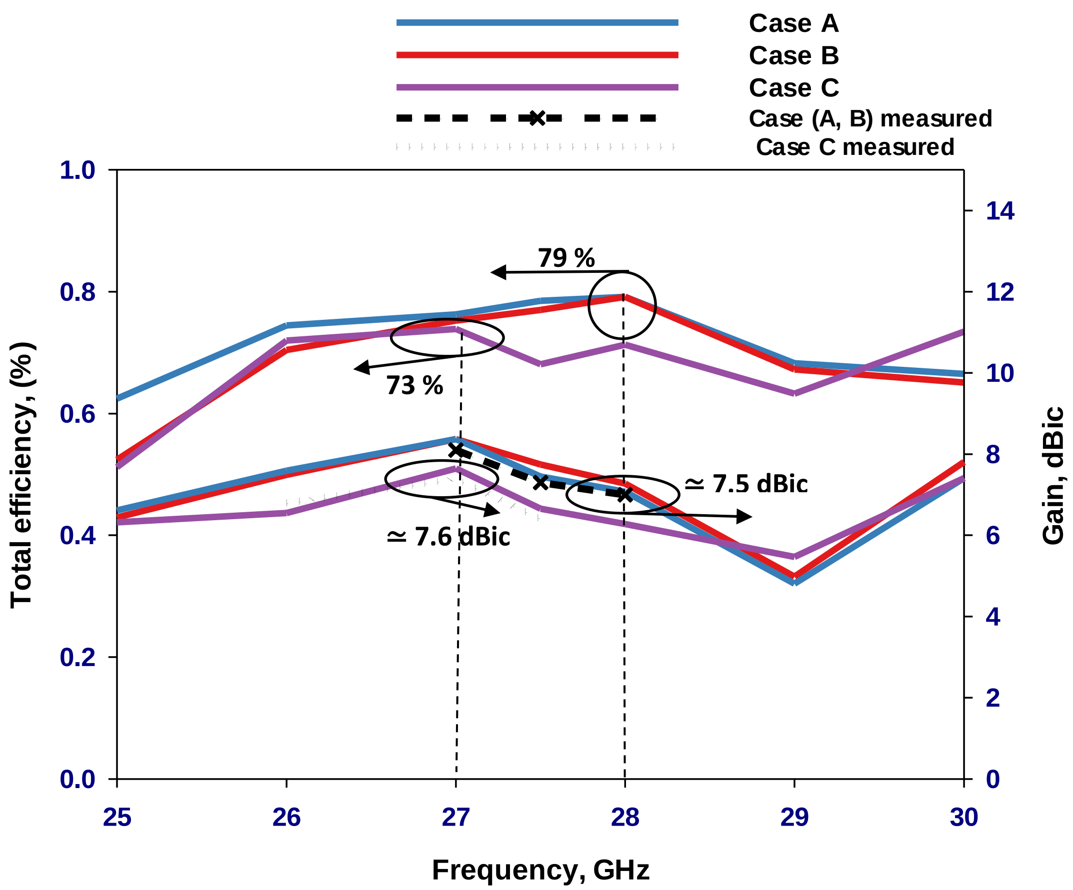

Figure 5.23: Total efficiency for polarization senses of the mmWave reconfigurable loop antenna.

Table 5.6 Performance Comparison Between the Proposed Configuration and Reported Counterparts

Ref.	Working States	Antenna	Elements Number	Switching Method	Frequency GHz	Gain dBci	S11 BW %	AR BW %	η_t %	Size mm2
[89]	LHCP, LP	Patch	1	RF-MEMS	21	3.9	11.8	3	23	12×10
[90]	LHCP, RHCP, LP	Patch	1	Laser pulses	30	6.2	5.1,3.1	1.7	75	12.5×12.5
[91]	LHCP, RHCP, LP	Patch	1	4 PIN diodes	29	3,4	5.4	***	***	10.2×14.1
[92]	LHCP, RHCP	Patch	4	4 PIN diodes	28	6	7	3.5	51	31×34
[93]	LHCP, RHCP	T-Slot	10×1 2×2	Mechanical	29.5 30.5	16 13	3.3 10	3 3	80 80	97.3×18.1 26×26
[94]	LHCP, RHCP, LP	Butterfly	8×12	A ∠φ*	28	22	7	7	60	125×50
[95]	LHCP, RHCP	Patch	10	SPDT**		13.9	17.7	8	75	22.5×61.75
This work	LHCP, RHCP, LP	Loop	1	2 PIN diodes	27/28	7.5	12.9	8	79	37×40

* Switching achieved by adjusting the magnitude and phase of the feeding single to each one of the 4 ports

** Single-Pole-Double Throw Switch

*** Data not provided in the reference

5.11. Performance Comparison

Table 5.6 presents a comparison between the performance of the proposed antenna compared to polarization reconfigurable antenna prototypes that are reported in the literature. From the Table, it is evident that the presented antenna outperforms the single antenna prototypes reported in [89]-[91] in terms of the reported impedance and AR bandwidths, gain, and radiation efficiencies. In addition, the proposed antenna offers three polarization modes compared to two in [95], employs a simple switching mechanism compared to that utilized in [90], and needs only two PIN diodes compared to four in [91]. On the other hand, the studies in [92]-[94] are focused on polarization reconfigurable mmWave arrays, which naturally require a more complex design in terms of feed network and switching mechanisms for many antennas. However, the presented single-loop antenna offers wider impedance and CP bandwidths than those reported in [92]-[94] and a slightly narrower impedance bandwidth compared to [93]. In terms of the polarization modes, the arrays reported in [92]-, [93] offer two polarization states compared to three in the present study. Although full polarization reconfigurability has been achieved in [94], four excitation ports were used, which increases the cost and complexity compared to the case of a singly fed antenna. The radiation efficiency of the presented design is higher than those achieved in [92], [94], [95] and close to that reported in [89]. On the other hand, higher gains have been reported in [92]-[95] due to the considerable number of utilized elements. The overall footprint is larger than that of the radiating element owing to the required length of the CPS-PBG section, which brings benefits to the proposed configuration. According to the figure of merit reported (FOM) in [95], which considers the achieved CP bandwidth, gain, polarization states, and number of antennas. The proposed antenna in this article offers a FOM of 50 compared to 9.75/5.1, 1.44, and 10 in [91], [92], and [93], respectively, which confirms the potential and cost-effectiveness of the proposed antenna. It should be noted that the proposed configuration offers another distinct advantage of hybrid configurations since the bandwidth is also reconfigured from a wider single band in the CP modes to dual-narrower bands in the case of LP radiation.

5.12 Summary

In this Chapter, a novel approach was introduced to design a mmWave antenna with hybrid reconfigurability by employing planar feeding and biasing networks. The proposed design focuses on achieving control over polarisation, enabling seamless transitions between LHCP and RHCP senses along with enabling reconfigurable frequency in the case of LP radiation.

A low-cost 6 GHz loop was designed and measured to prove the proposed concept. This was followed by measuring an antenna's prototype operating at 28 GHz with a close agreement between measurements and simulations.

The core of the presented planar structure features a biasing network that consists of a coplanar strip line integrated with a photonic bandgap circuit. This eliminates the need for traditional lumped elements, leading to enhanced radiation efficiency. Furthermore, the antenna's design has been optimised by aligning the PIN diodes strategically, allowing for the utilization of a single CPS biasing circuit for the two PIN diodes. This contrasts with the conventional approach in the literature, which often necessitates two separate circuits for biasing two PIN diodes. This optimization simplifies the antenna design while improving its overall efficiency, resulting in an effective and streamlined configuration for a hybrid reconfigurable mmWave loop antenna. The proposed antenna outperforms those reported mmWave reconfigurable antennas in terms of CP bandwidth, gain and efficiency as well as the capability of frequency reconfigurability in the case of linear polarisation.

Chapter 6

Multifunctional Reconfigurable mmWave Array Antenna

6.1 Introduction

In light of the relentless pace at which technology advances within the realm of wireless communication systems, antennas, which stand as a fundamental component in contemporary wireless communications, confront ever-mounting demands to achieve heightened performance levels. This is imperative for effectively addressing intricate communication scenarios that encompass challenges like multipath interference and polarisation mismatch. Consequently, the development of multifunctional and intelligent array antennas assumes paramount importance. Amid the various approaches employed to confront this challenge, reconfigurable antennas have emerged as a compelling solution due to their intrinsic flexibility and versatility.

The majority of reported studies on reconfigurable antennas have primarily focused on the modification of a single antenna's parameter. Despite the evident advantages of such antennas, they may prove inadequate in meeting the escalating requirements of high-speed communication systems, such as those used on the Internet of Things and 5G/6G applications. Consequently, there has been an increased emphasis on proposing antennas with the capacity to reconfigure more than one parameter over the past two decades. These antennas can be broadly categorized into two types: hybrid and multifunctional reconfigurable antennas.

The former has been demonstrated in the last Chapter where the bandwidth and polarisation of a mmWave antenna have been configured for the first time. However, a wide band has been achieved for the CP radiation, and a narrower dual-band operation has been achieved for the LP case. Therefore, it cannot be classified as a multifunctional reconfigurable antenna, which is also expected to offer the options of wide-band LP or dual-band CP cases or other operation modes that are difficult to achieve using a single antenna. Meanwhile, the ability to furnish additional radiation modes offers considerable benefits such as increased channel capacity through the polarisation reconfigurability as well as the beam steering, for example. On the other hand, a reconfigurable beam direction of a phased array represents an economical and practical alternative to the high-cost phase shifters and RF chains that are commonly used for beam steering. An antenna array that offers simultaneous polarisation and pattern reconfigurability is known as a multifunctional reconfigurable antenna array (MRAA).

One of the earliest demonstrations of the potential of multifunctional reconfigurable antenna has been reported in [104], where a configuration of Radio Frequency Microelectromechanical Systems (MEMS) integrated antennas has been utilized in a MIMO system with several polarization states that have been achieved at 4.1 GHz and 6.4 GHz. The multifunctional reconfigurability has been achieved using 64 square patches that are inter-connected to each other using 112 MEMS switches. Subsequently, a different study introduced a pattern and frequency reconfigurable annular-ring slot antenna, employing two small PIN diodes on the feeding microstrip line to connect/disconnect stubs for frequency tuning, and incorporating two larger PIN diodes on the annular ring slot to control radiation patterns at 5.2 GHz, 5.8 GHz, and 6.4 GHz [105].

A textile circular patch antenna that is loaded by three varactors to offer frequency and pattern reconfigurability and a wearable textile antenna with frequency and polarisation reconfigurability have been reported [106]. The first antenna switches between broadside and omnidirectional radiation modes over specific frequency ranges, while the second antenna switches the linear polarisation between 0°, 120°, or 240° over a frequency range of 1.9-2.62 GHz. Additionally, a frequency and pattern reconfigurable microstrip antenna has been designed using 6 varactor diodes to achieve a dual-band operation with a broadside pattern at 2.68 GHz and an omnidirectional pattern at 3.5 GHz [107]. In another study, a multifunctional microstrip antenna that offers three linear polarisations, and three main beam directions was demonstrated by utilizing 10 PIN diodes at 11 GHz [108].

Furthermore, a novel multifunctional reconfigurable antenna (MRA) was proposed using a parasitic substrate layer with 5×5 square metallic patches, known as pixels, incorporating 20 MEMS switches for the connection/disconnection of various pixels to achieve reconfigurability of frequency between 9 and 10 GHz with three radiation patterns [109]. However, it was highlighted that the pixeled planar surface requires many switches, which impacts the antenna efficiency and results in a complex fabrication process. A multifunctional reconfigurable pixeled planar antenna was reported by utilizing 144 MEMS switches in a square matrix of 9×9 pixels and tuning the operating frequency within a range of 4-7 GHz with reconfigurable radiation patterns and adjustable linear polarisations at each frequency [110]. Moreover, a frequency and pattern reconfigurable pixeled monopole antenna were reported by utilizing 12 MEMS switches to alter the antenna geometry and achieve operating frequencies of 1.5 GHz, 3.5 GHz, 4.5 GHz, and 5.5 GHz with up to five radiation patterns at each frequency [111]. In a subsequent study, a frequency, pattern, and polarisation reconfigurable antenna were reported by utilizing a single patch antenna in conjunction with a 6×6 parasitic pixel substrate that involved 60 PIN diodes in generating various combinations of pixels albeit with a radiation efficiency of 45% to 55% [112]. Another MRA has been reported using a 4 elements linear patch array, each loaded by a passive substrate of 4×4 pixels [113]. However, for simplicity, perfect short circuits and open circuits were utilised instead of RF switches providing pattern and polarisation reconfigurability in combination with a 13.5 dBi gain. Furthermore, a 3×3 pixels layer with 12 PIN diodes utilised to achieve 9 radiation pattern modes over a frequency range of 2.4-2.5 GHz [114]. Moreover, MRA, which offers six modes of operation has been reported using 60 PIN diodes to achieve a dual-band operation at 2.45 GHz and 5.3 GHz with the option of three radiation patterns in each band [115]. However, the radiation pattern was the only parameter that has been configured in [114] and [115]; therefore, the definition of a multifunctional reconfigurable antenna may not be applicable in these particular cases. On the other hand, it is essential to note that pixel-based antennas involve complex biasing requirements for many switches that are placed above the antenna.

A different approach in designing MRAs has been employed that is based on utilising a liquid metal [116]-[119]. For example, a MRA that offers pattern and linear polarisation reconfigurability has been proposed using a dipole antenna over a frequency range of 1-2.2 GHz [116]. Furthermore, a bent monopole that is based on liquid metal has been proposed for frequency and polarisation reconfigurability, where both LHCP and RHCP radiations have been achieved over a frequency band of 3-5 GHz [117]. Another liquid-metal-based antenna has been reported with both frequency and polarization over a frequency range of 0.5-3.5 GHz [118]. Besides, frequency and polarisation reconfigurability have been achieved using a liquid-metal parasitic over a frequency range of 2-8 GHz by switching a 3D-printed channel between the *x* and *y* polarisation states [119]. Although a liquid-metal-based MRA offers continuous frequency tunability, a longer switching time is expected between various modes. Besides, the required mechanism to inject the liquid metal may be impractical at mmWave frequencies considering the smaller physical dimensions at such frequencies.

Another approach that is based on using multiple ports has been proposed by varying the current distribution along a patch antenna by adjusting the phases of four feeding ports to achieve pattern and polarisation reconfigurability over a frequency range of 4-5 GHz [120].

LHCP and RHCP radiations have been achieved over a main beam scanning range of ±70°. Both single-element and 4×4 element arrays have been considered. However, the utilisation of multiple ports results in an increased size and complexity, with numerous wire connections. This represents a considerable challenge to adapt at mmWave frequencies, owing to the limited physical space to accommodate several SMAs with sufficient de-coupling between them. Furthermore, multifunction digitally controlled reconfigurable antennas have been reported in combinations of multi-port feeding, and PIN diodes have been reported recently [121, 122].

This state of art review of existing literature reveals a notable absence of multifunctional reconfigurable antennas designed for mmWave applications since all the reported MFRA and MFRAA, are focused on antennas operating at lower frequencies with modest radiation efficiencies and complex structures that may be impractical at mmWave frequencies. Therefore, this Chapter is focused on the design, fabrication, and measurements of such an antenna. Building upon the mmWave phased array and reconfigurable antenna designs introduced in Chapters 4 and 5. The novelties of those designs will be combined and enhanced to achieve a multifunctional reconfigurable mmWave array, which has not been reported earlier. The multifunctional reconfigurability can be achieved by utilising a reconfigurable element as well a reconfigurable feed network. The reconfigurable antenna introduced in Chapter 5 will be used as an element from which a multifunctional reconfigurable array will be designed that offers polarisation, pattern, and frequency reconfigurability by utilising PIN diode switches in a simple structure that also offers a high efficiency.

6.2 Contribution

In addressing the aforementioned challenges, this chapter presents significant contributions in the following key areas:

1. *Design and Fabrication of a Cost-Effective Multifunctional Reconfigurable Array Antenna:*

A low-profile, cost-effective 4-element reconfigurable phased array system is designed and fabricated, specifically operating at 27.5 GHz. Within each array element, two strategically designed gaps accommodate PIN diodes, serving as flexible switches. These diodes enable the selection of the desired polarisation by toggling between forward-bias and reverse-bias states, enhancing the adaptability of the antenna system.

2. *Implementation of Corporate Feed Network and Phase Shifters:*

The one-input-four-output feeding network incorporates four transmission line phase shifters, with each section introducing a distinct phase shift. The degree of phase shift is contingent upon the bias applied to the PIN diodes and the length of the corresponding transmission line segment. This innovative approach enhances beam control and array performance.

3. *Utilization of Coplanar Stripline Structure with Photonic Bandgap Elements:*

Only two planar CPS-PBG structures have been utilized; one to switch the polarisation of the 4 elements and another to control the main beam direction. The incorporation of only two represents considerable simplicity and eliminates further efficiency deterioration owing to the absence of lumped RF chokes or capacitors, reducing additional losses associated with these elements. Consequently, the proposed antenna system achieves higher efficiency, providing a more robust and effective solution.

These contributions collectively address challenges in the mmWave antenna design, reconfigurability, and efficiency, offering a comprehensive and innovative framework for the development of advanced phased array systems for 5G and B5G communication systems.

6.3 Chapter Organisation

The organisation of this Chapter unfolds as follows:

Section 6.4 initiates by introducing the configuration and design principles of the mmWave MRAA along with the relevant parameters. Following this, Section 6.5 outlines the utilization of electrical switching at mmWave frequencies. Section 6.6 details the operating mechanism, illustrating the integration of PIN diodes within the proposed array. Proceeding to Section 6.7, comprehensive details are provided concerning the prototypes, simulations, fabrication processes, and measurements of the proposed reconfigurable array antenna at 27.5 GHz. In Section 6.8, a performance comparison between the proposed configuration and reported counterparts is presented. Finally, Section 6.9 delivers a summary and concluding remarks for the chapter.

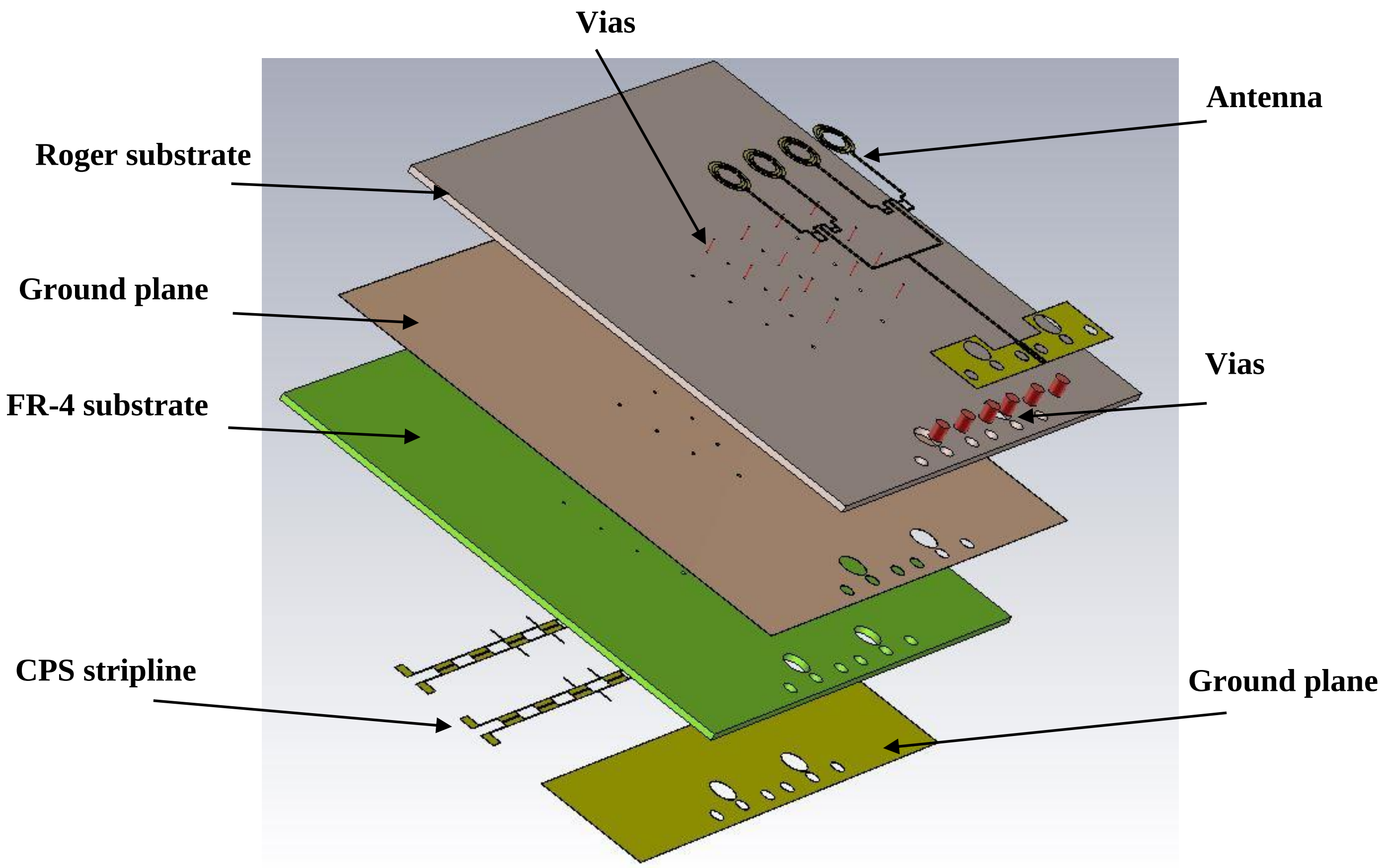

Figure 6.1: The layers of the proposed reconfigurable array.

6.4 Structure of the Multifunction Reconfigurable Array Antenna

6.4.1 Constituent Layers of the Proposed Reconfigurable Array

In this configuration, a total of five layers are utilized, which include the active antenna element, as depicted in Figure 6.1. The second layer comprises Rogers RT/Duroid RO4003C substrate material, featuring a dielectric constant (ε_r) of 3.55 and a loss tangent (tanδ) of 0.0027, with a thickness of 0.508 mm. The choice of Rogers substrate within this design is driven by several distinct advantages, namely, its low dielectric constants, low loss tangents, high efficiency, and ease of manufacturability.

Another substrate employed in this design is the FR-4 material, characterized by respective dielectric constant and thickness of 4.3 and 0.5 mm. This layer primarily functions as an insulator, facilitating the interface between the ground plane layer and CPS-PBG biasing networks. These substrate layers encapsulate a central copper ground plane, serving as a reflective ground plane with a thickness of 0.07 mm. Each substrate possesses dimensions of 37 mm in width and 40 mm in length. Additionally, there is a lower auxiliary ground plane, measuring 40 mm in width and 8.5 mm in length, constructed from copper. This supplementary ground plane assumes a critical role in grounding, particularly when securing the connector in place.

6.4.2 Configuration of Proposed Multifunction CP Antenna Array

Figure 6.2 depicts the configuration of a 1×4 reconfigurable linear antenna array designed to operate at 27.5 GHz, featuring an inter-element spacing of 4.65 mm, approximately equivalent to half the free space wavelength at the operating frequency. Each constituent element within the array exhibits an identical design, characterized by the presence of two concentric loops, with the outer loop serving as the active element. The outer loop for each array element incorporates two gaps that house the PIN diodes, functioning as switches capable of toggling between forward-bias and reverse-bias states to select the desired polarisation senses. The optimization of the outer loop's gaps $(\Delta\Phi_1, \Delta\Phi_2)$ plays a pivotal role in establishing a traveling wave current distribution along the loop. This distribution is indispensable for the generation of diverse circular polarization states. In addition, a reduced gap $(\Delta\Phi_3)$ within the inner loop has been selected to enhance the CP bandwidth of circular polarization.

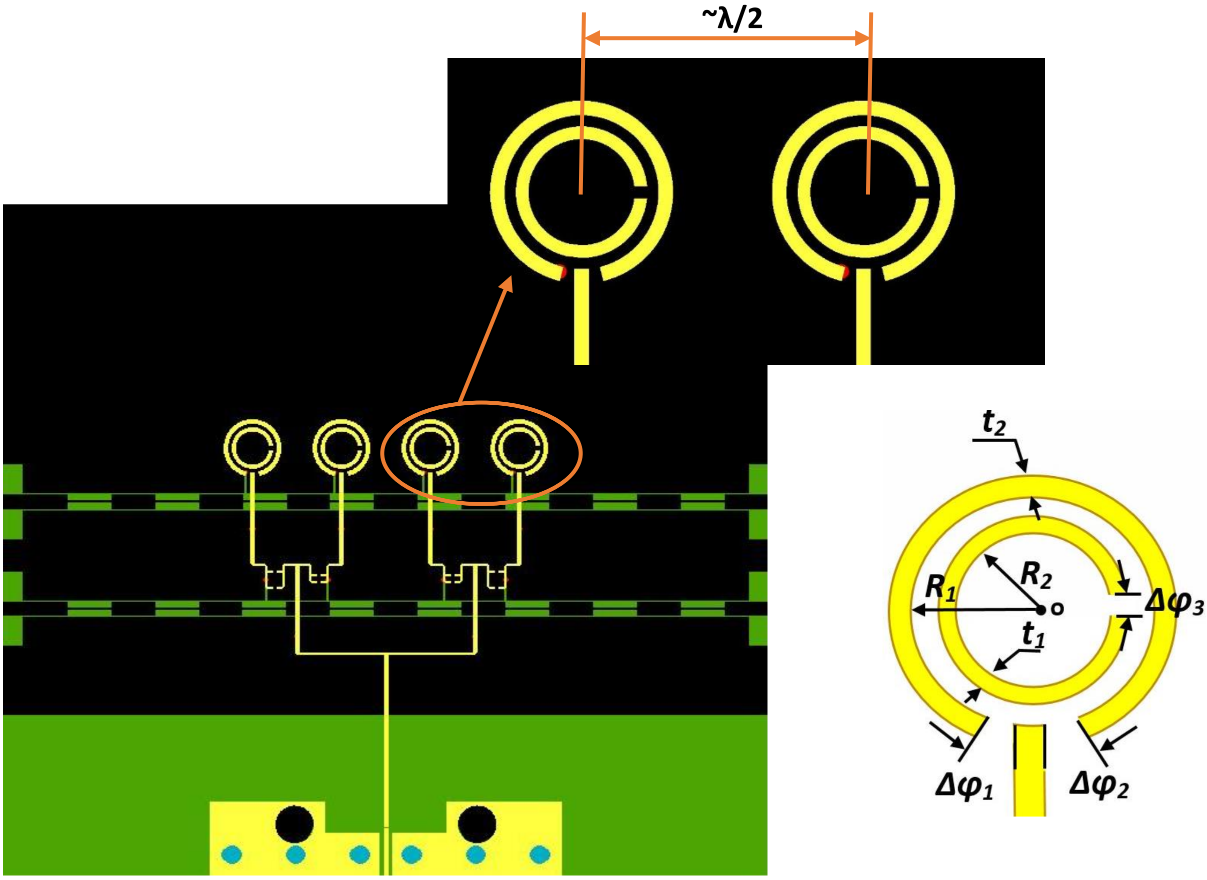

Figure 6.2: The geometry of the proposed wideband CP antenna array.

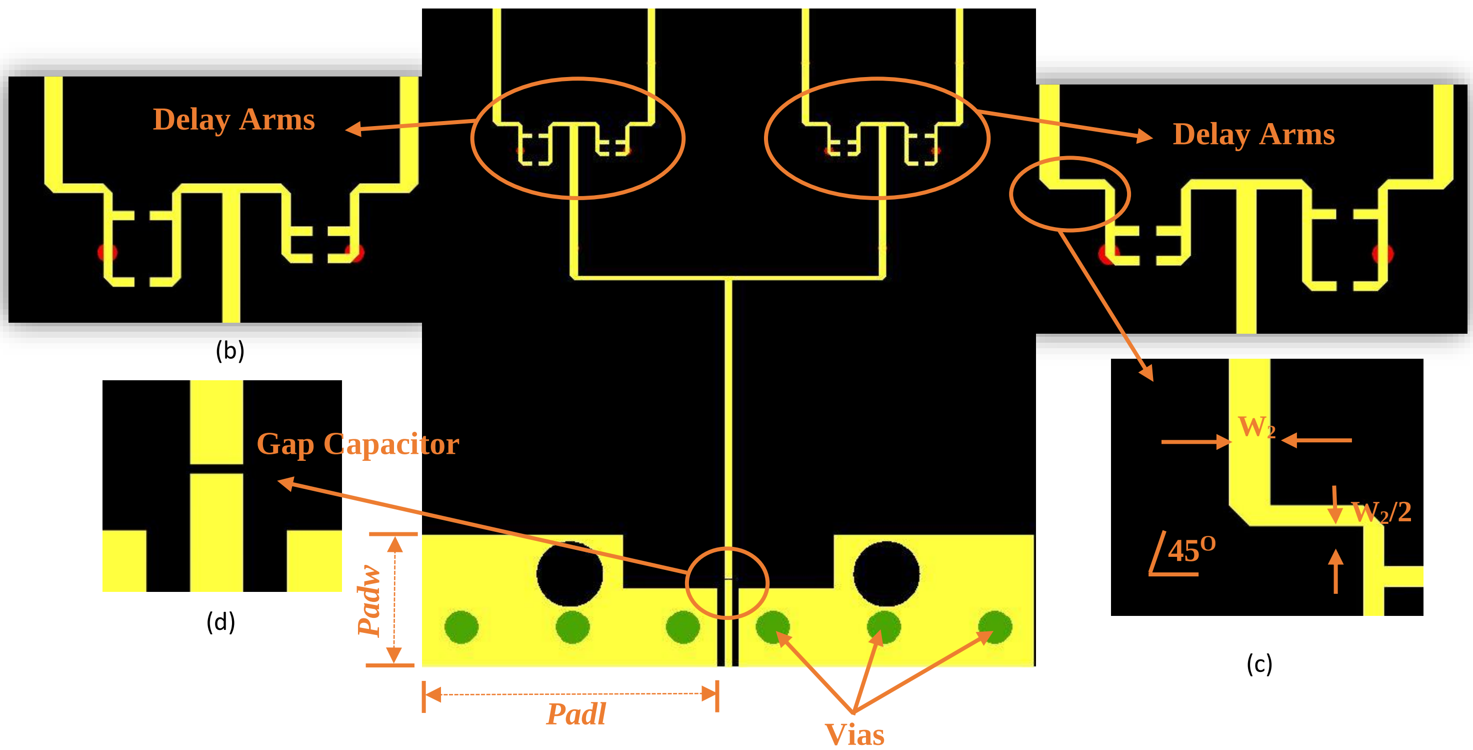

Figure 6.3: Corporate feed network (b) phase shifters of the proposed antenna (c) gap capacitor (d) chamfered corners.

Furthermore, the selection of the loop antenna's radius is critical to ensuring that the circumference approximates one effective wavelength, denoted as λ_{eff}. The inter-element spacing of the antenna array is judiciously chosen to maximize gain and minimize side lobe levels (SLL). The feeding of the antenna arrays is facilitated by a parallel feed network employing microstrip transmission lines with widths of 0.2 mm and 0.25 mm. The configuration parameters for the reconfigurable array are summarized in Table 6.1.

Table 6.1 Dimensions Parameters of the Proposed Design

Symbol	***Quantity***	***27.5 GHz***
R_1	outer loop radius	1.27mm
R_2	parasitic loop radius	0.875 mm
t_1	outer loop width	0.26 mm
t_2	parasitic loop width	0.21 mm
Padl	pads length	8.9 mm
Padw	pads width	3.96 mm
l_2	transmission line width	0.25 mm
l_3	the gap between the transmission line & pads	0.2 mm
a_0	antenna thickness	0.035 mm
h	The thickness of the substrate	0.508 mm
t	reflector thickness	0.07 mm
Subx	substrate length	37 mm
Suby	substrate width	40 mm
Substrate type		**RO4003C**
Permittivity (ε_r)		3.55
loss tangent		0.0027
$\Delta\varphi_1$	outer loop gap 1	20^{o}
$\Delta\varphi_2$	outer loop gap 2	20^{o}
$\Delta\varphi_3$	parasitic loop gap	18^{o}

6.4.3 Corporate Feed Network Connected to Phase Shifters of the Proposed Array

Figure 6.3a introduces a one-input-four-output feeding network, which features the integration of four transmission line phase shifters. Within this network, each section is responsible for introducing a distinct phase shift as depicted in Figure 6.3b. This phase shift is contingent upon the specific bias applied to the PIN diode and the length of the corresponding transmission line segment. This method harnesses transmission lines to achieve the requisite phase shift, thereby constituting what is recognized as a "true-time delay". This approach is particularly advantageous in the context of phased arrays with parallel feeding, as it enhances the system's bandwidth. True-time delay is especially well-suited for broad-spectrum applications, as it maintains the stability of the primary beam direction across a spectrum of frequencies.

In essence, the concept of true-time delay encompasses the integration of delay sections along the transmission lines within the feed network. These delay sections align with the precise phase shifts needed. By adjusting the time delay for each individual element, it becomes possible to manage the aggregate phase shift across the array, enabling precise control of beam steering. To enhance matching and elevate the array's performance, a design enhancement is introduced, featuring the implementation of 45° chamfered corners on the transmission lines, as depicted in Figure 6.3c. Additionally, Figure 6.3d highlights the presence of a gap capacitor, devised through microstrip line patterning, yielding a modest capacitance of approximately 0.1 pF. This component serves the crucial function of stopping the direct current (DC) flowing to the network analyser. The integration of vias into the design yields several benefits, encompassing improved grounding, mitigation of surface waves, and the expansion of bandwidth, thereby enhancing overall each possessing a radius of 1 mm and situated at 4 mm intervals, center to center.

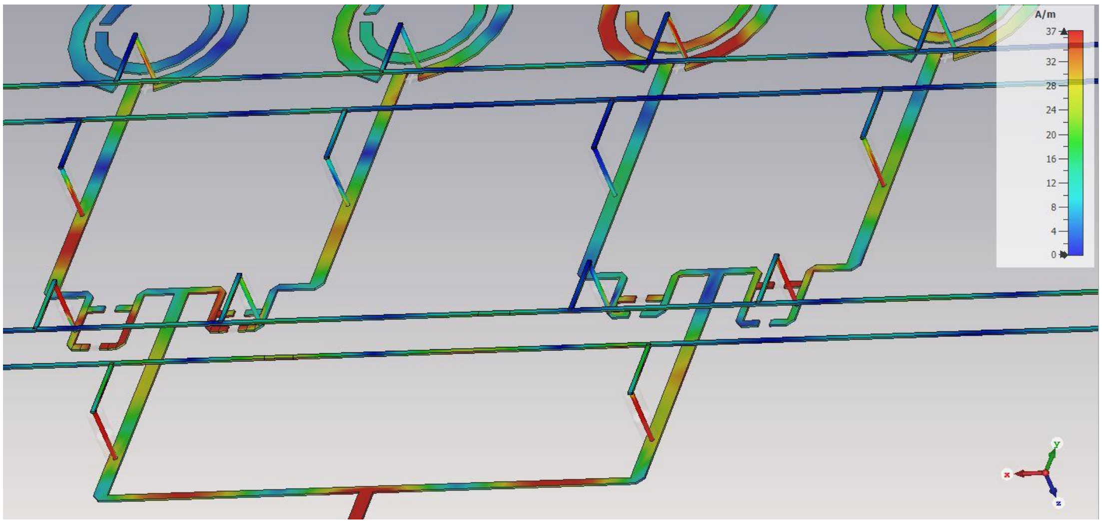

Figure 6.4: Surface current distribution of the proposed array with CPS bias line only at 27.5 GHz.

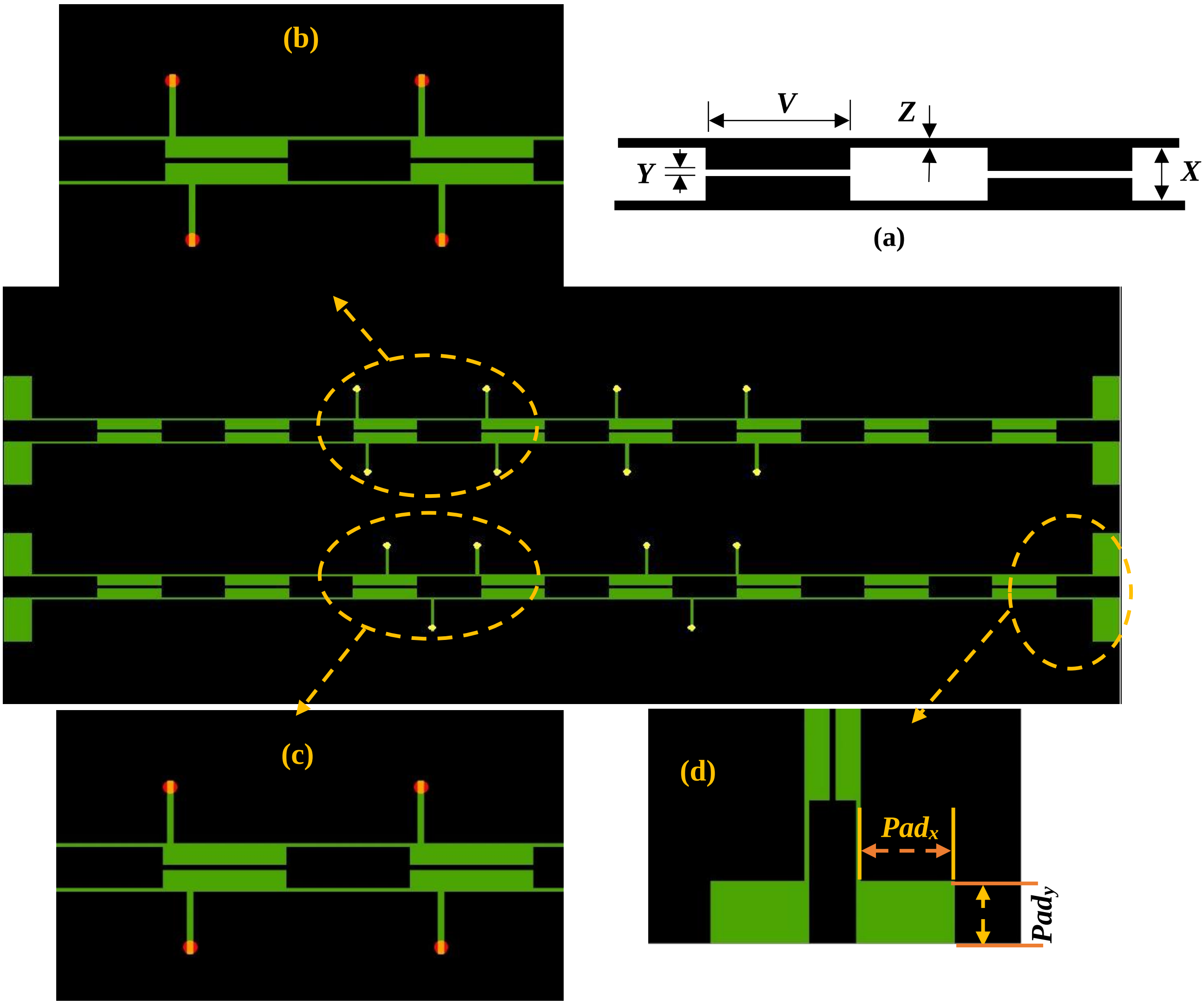

Figure 6.5: (a) Structure of CPS bias line and PBG (b) CPS connected to outer loops (c) CPS connected to phase shifters (d) solder pad.

6.4.4 Innovative RF Choke Design Using Coplanar Stripline and Photonic Bandgap Structure

In Figure 6.4, the integration of printed strip bias lines is presented, which introduces a negative shunt susceptance (inductive) as part of the design. For the provisioning of DC bias, a coplanar stripline is connected to the antenna element via vias that establish a connection between the CPS and an array. The current distribution along the bias line leads to undesirable RF current leakage into the antenna, turning the bias line into an unintended component of the antenna system. Consequently, the antenna's key characteristics, including resonance frequency, input impedance, and radiation pattern, are affected.

To mitigate this issue, the development of a novel bias line structure is imperative one that effectively carries the requisite DC bias current while preventing the unwanted flow of RF current. To curtail RF current propagation within the coplanar stripline, a PBG structure featuring a $0.25\lambda_{eff}$ periodicity is deployed. Figure 6.5 illustrates this PBG structure, which comprises a series of high and low quarter-wavelength transformer sections. It should be noted that the existence of antennas, feeding, and biasing networks on the same substrate surface represents a challenging task and complications that can avoided by moving the biasing network to another substrate, FR4 in this case, which is positioned at the other side of the shared ground plane surface. However, the connections of the biasing networks to the diodes have been implemented by utilising metallised vias. Such an arrangement provides an optimum isolation between the biasing network and the antenna. In addition, the chosen alignment of the diodes facilitated the utilization of only two biasing networks for the 16 PIN diodes.

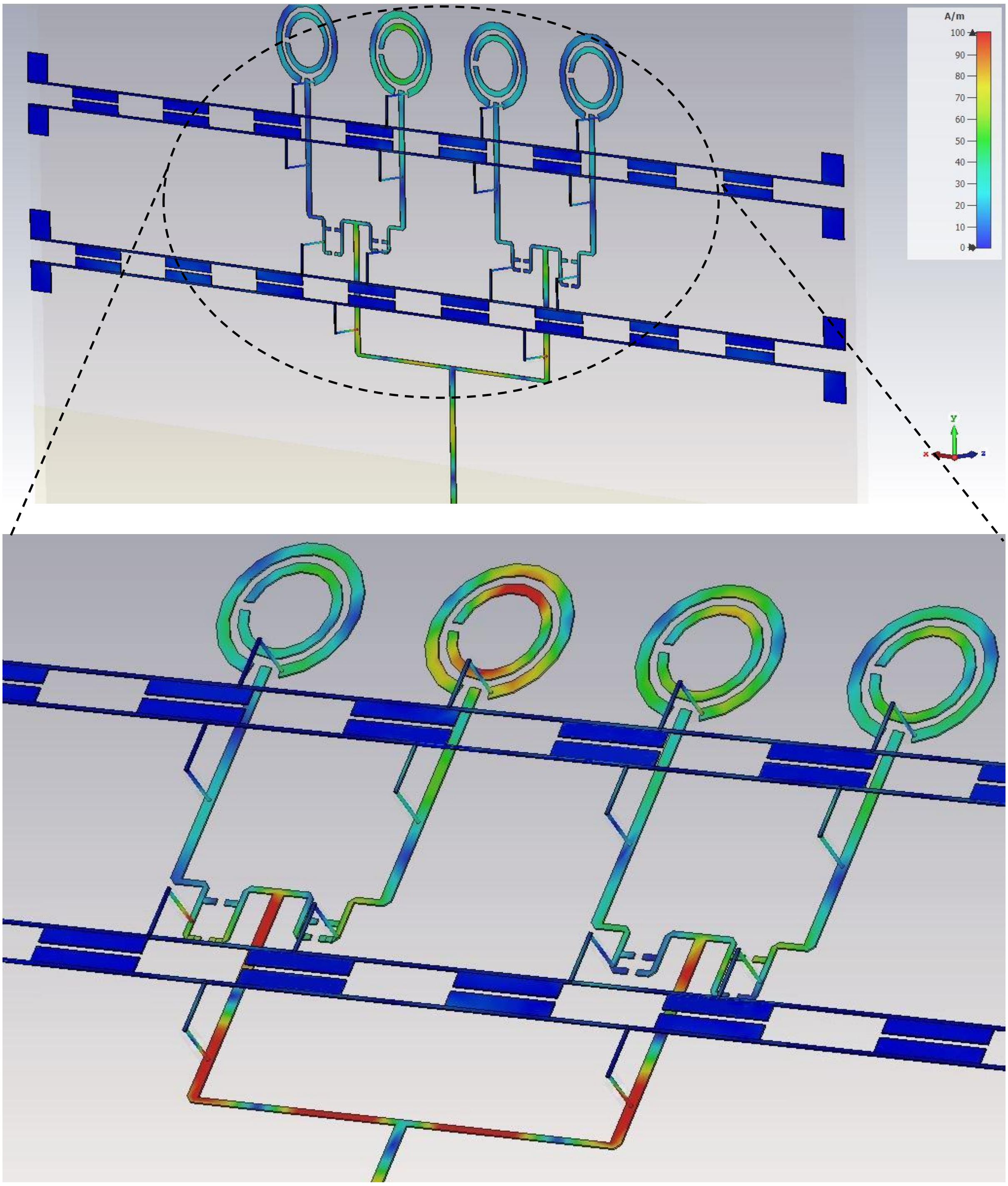

Figure 6.6: Surface current distribution of the proposed antenna with CPS bias line and PBG structure at 27.5 GHz

In the proposed design, a total of fourteen vias have been thoughtfully incorporated to establish connections between the CPS and the PIN diodes placed on the array configuration. This strategy stems from the unique approach employed in positioning the PIN diodes within the outer loop gaps. As a result, eight vias which means 2 vias per loop are dedicated to the precise control of polarisation senses. In addition, the placement strategy of the PIN diodes on the phase shifters minimizes the vias count as well, with only six vias serving the purpose of beam steering within a range of ±25 °. Hence, the utilization of only two CPS networks in the proposed design results in cost savings, lower losses, and a simplified design structure. Improve matching has been accomplished by adding strip lines between the antenna and the CPS-BPG structure, as illustrated in Figures 6.5 b and c.

The gap width between the high-impedance section CPS line is defined as X, the PBG cell length is V, the gap width between the thicker low-impedance PBG cells is Y, and the widths of the CPS line are Z. Due to the relatively small size of the CPS line, especially in the mm-wave frequencies designs, two solder pads have been employed as shown in Figure 6.5d. The design parameters for the CPS bias line and PBG are summarized in Table 6.2. Figure 6.6 presents the surface current distribution of the antenna with a PBG bias line at 27 GHz. It is evident that the PBG bias line effectively cuts off the RF current from flowing to the second PBG cell, preventing the undesired current leakage.

Table 6.2 Dimensions Parameters for the CPS Bias Line and PBG

Symbol	**28 GHz**
V	2.29 mm
X	0.76 mm
Y	0.1 mm
Z	0.1 mm
pad_x	1.8 mm
pad_y	1 mm

6.5 Electrical Switching at mmWave Frequencies

Table 6.3 presents a concise performance comparison of prevalent electrical switching mechanisms employed in the mmWave frequency range. These mechanisms encompass PIN diodes, RF MEMS, and Radio Frequency Field-Effect Transistors (RF FETs) [123]. Among these alternatives, PIN diodes offer notable advantages relative to other switching methods, which include cost-effectiveness, reduced switching times, and a higher supply voltage threshold. Consequently, PIN diodes emerge as the predominant choice for electrical switching in the mmWave frequency range. A PIN diode, an exemplar of this technology, is characterized by an intrinsic semiconductor region ("I") positioned between a p-type ("P") and an n-type ("N") semiconductor region. In RF circuitry, a PIN diode serves as a variable resistor. Figure 6.7 illustrates the equivalent circuit of a PIN diode when it functions in both the ON and OFF states. The MA4AGFCP910 PIN diode is used within the proposed array operating at 27.5 GHz. It is worth noting that these PIN diodes have been meticulously modeled in CST, utilizing lumped elements in the equivalent RLC circuits of the forward-biased and reverse-biased diodes. The dimensional characteristics of these PIN diodes, along with the corresponding RLC equivalent circuit parameters, are comprehensively detailed in Table 6.4.

Table 6.3 Comparative Analysis of Electrical Switching Mechanisms in the Millimeter-Wave Frequency Range [123]

Parameter	**PIN-diode**	**RF MEMS**	**FET**
Voltage (V)	±1-5	20-80	3-5
Current (mA)	3-20	0	0
Power consumption (mW)	5-100	0.05-0.1	0.05-0.1
Switching time	1-100 ns	1-300 µs	1-100 ns
Isolation	Medium	High	Low
Loss	0.3-1.2	0.05-0.2	0.4-2.5
Power handling (W)	<10	<1	<10

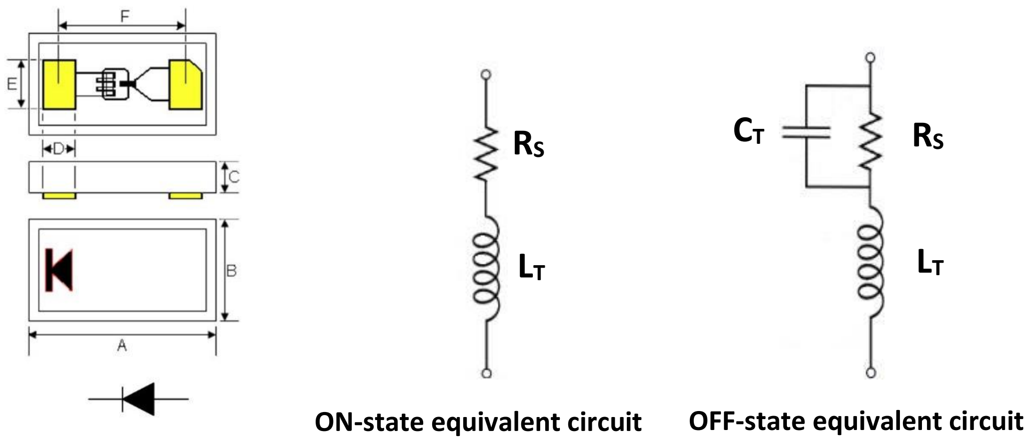

Figure 6.7: The PIN diode configuration for 28 GHz antenna [100].

Table 6.4 RLC equivalent Circuit Parameters for PIN Diodes and its Dimensions

PIN Diode	**Total Capacitance C_T**	**Series Resistance R_S**	**Parallel Resistance R_L**	**Total Inductive L_T**	**Forward Voltage**	
MA4AGFCP910	0.018 pF	5.2 Ω	15 KΩ	1 nH	1.45 V	
		Dimensions				
Frequency	**A**	**B**	**C**	**D**	**E**	**F**
28 GHz	0.685 mm	0.368 mm	0.19 mm	0.13 mm	0.185 mm	0.48 mm

Table 6.5 Switch Configuration for Desired Modes of Operation (1=ON,0=OFF), and Ө is the Mian Beam Direction.

Cases	**Modes**	**θ**	**D_1**	**D_2**	**D_3**	**D_4**	**D_5**	**D_6**	**D_7**	**D_8**	**D_9**	**D_{10}**	**D_{11}**	**D_{12}**	**D_{13}**	**D_{14}**	**D_{15}**	**D_{16}**
1	**LHCP**	**-25**	1	0	1	0	1	0	1	0	0	1	0	1	1	0	1	0
2	**LHCP**	**+25**	1	0	1	0	1	0	1	0	1	0	1	0	0	1	0	1
3	**RHCP**	**-25**	0	1	0	1	0	1	0	1	0	1	0	1	1	0	1	0
4	**RHCP**	**+25**	0	1	0	1	0	1	0	1	1	0	1	0	0	1	0	1
5	**LP**	**-25**	0	0	0	0	0	0	0	0	0	1	0	1	1	0	1	0
6	**LP**	**+25**	0	0	0	0	0	0	0	0	1	0	1	0	0	1	0	1

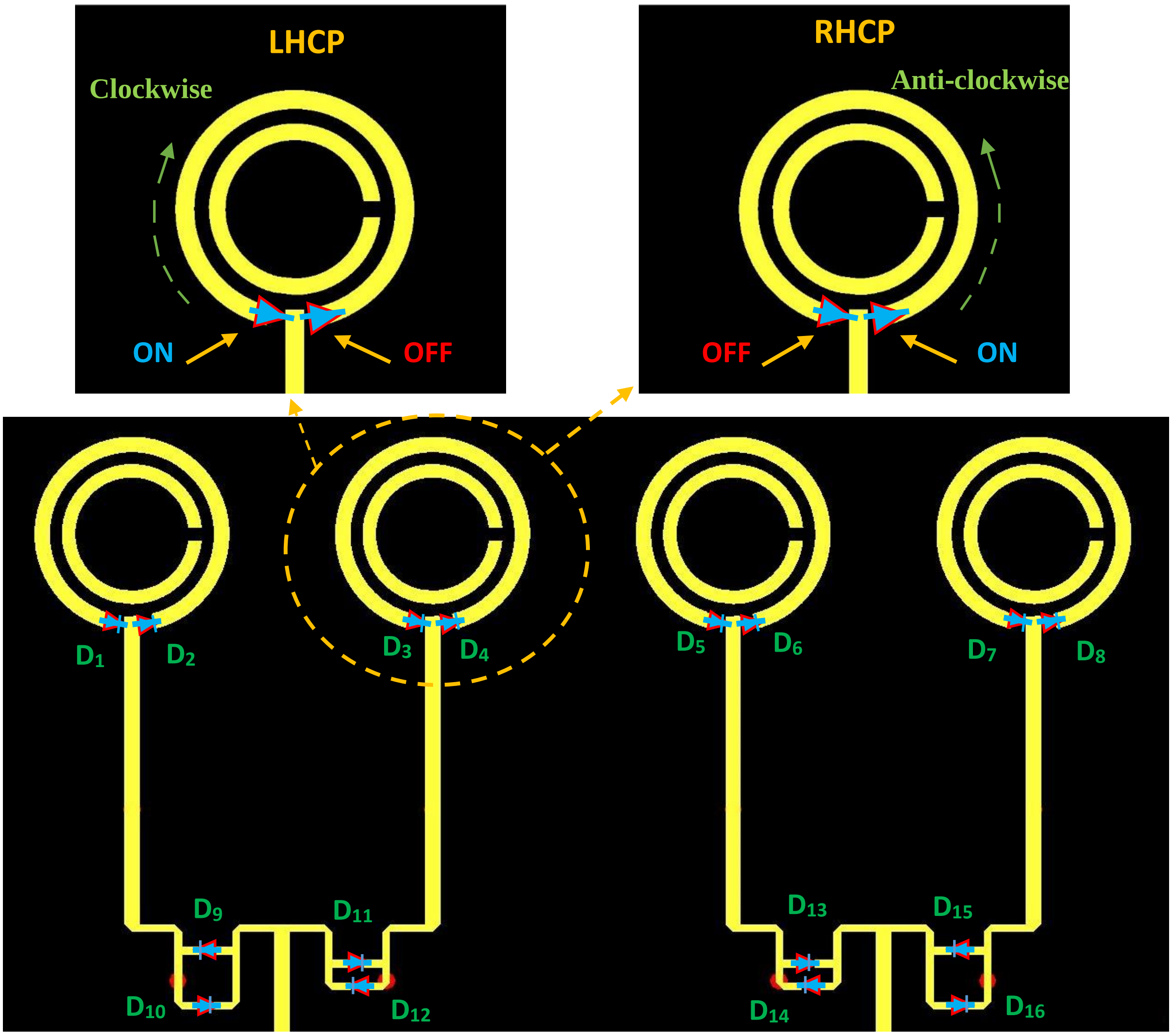

Figure 6.8: demonstrates the incorporation of PIN diodes into the proposed array.

6.6 Operating Mechanism

Figure 6.8 illustrates the integration of PIN diodes within the proposed array, where each of the sixteen PIN diode switches is numbered to designate their respective statuses across various operational modes. Comprehensive details regarding the switch configurations and their corresponding operational modes are presented in Table 6.5.

When a direct current (DC) is applied to the CPS lines, strategically positioned vias facilitate the current's path reaching the PIN diodes, enabling the application of forward and reverse bias as required. Six distinct polarisation cases, each associated with a different beam steering direction, are attainable based on the status of the PIN diodes. Notably, the case of the PIN diodes, specifically from D_1 to D_8, positioned on each outer loop of the array, is meticulously controlled to effect changes in polarization. Meanwhile, the PIN diodes fixed on the transmission lines, specifically D_9 to D_{16}, are leveraged to enable precise beam steering within a range of ±25°. The control of antenna radiation patterns is achieved by implementing forward and reverse biasing of PIN diodes. To steer the beam towards an angle of +25°, the following PIN diodes are engaged in the ON state: D_9, D_{11}, D_{14}, and D_{16}, while simultaneously switching D_{10}, D_{12}, D_{13}, and D_{16} to the OFF state.

Conversely, to redirect the beam towards a negative angle of -25°, a complementary configuration is applied. This entails biasing D_{10}, D_{12}, D_{13}, and D_{16} in the forward state, while D_9, D_{11}, D_{14}, and D_{16} are subjected to a reverse bias. This level of control enables the array to achieve precise beam steering in multiple directions, enhancing its versatility and adaptability. In the context of polarization, three cases are attainable: LHCP, RHCP, and Linear Polarization (LP). LHCP configuration is realized by placing D_1, D_3, D_5, and D_7 in forward bias states, while concurrently holding D_2, D_4, D_6, and D_8 in reverse bias.

Conversely, to achieve RHCP, the PIN diode cases are inverted, with D_2, D_4, D_6, and D_8 in forward bias and D_1, D_3, D_5, and D_7 in reverse bias. Lastly, for LP, PIN diodes from D_1 to D_8 are set to a zero-bias, or unbiased, state effectively holding them in a neutral position, and allowing the antenna to operate without imparting circular polarization. This precise control over polarization cases empowers the array to adapt to various communication scenarios and requirements.

6.7 Fabrication and Measurements

This segment showcases the fabrication and measurement results of this Chapter. Specifically, one prototype of the suggested reconfigurable CP 4-element circular loop array using PIN diodes is fabricated and tested to verify the design. The measurements have been conducted using the E5071C mmWave vector network analyser and the National mmWave Measurement

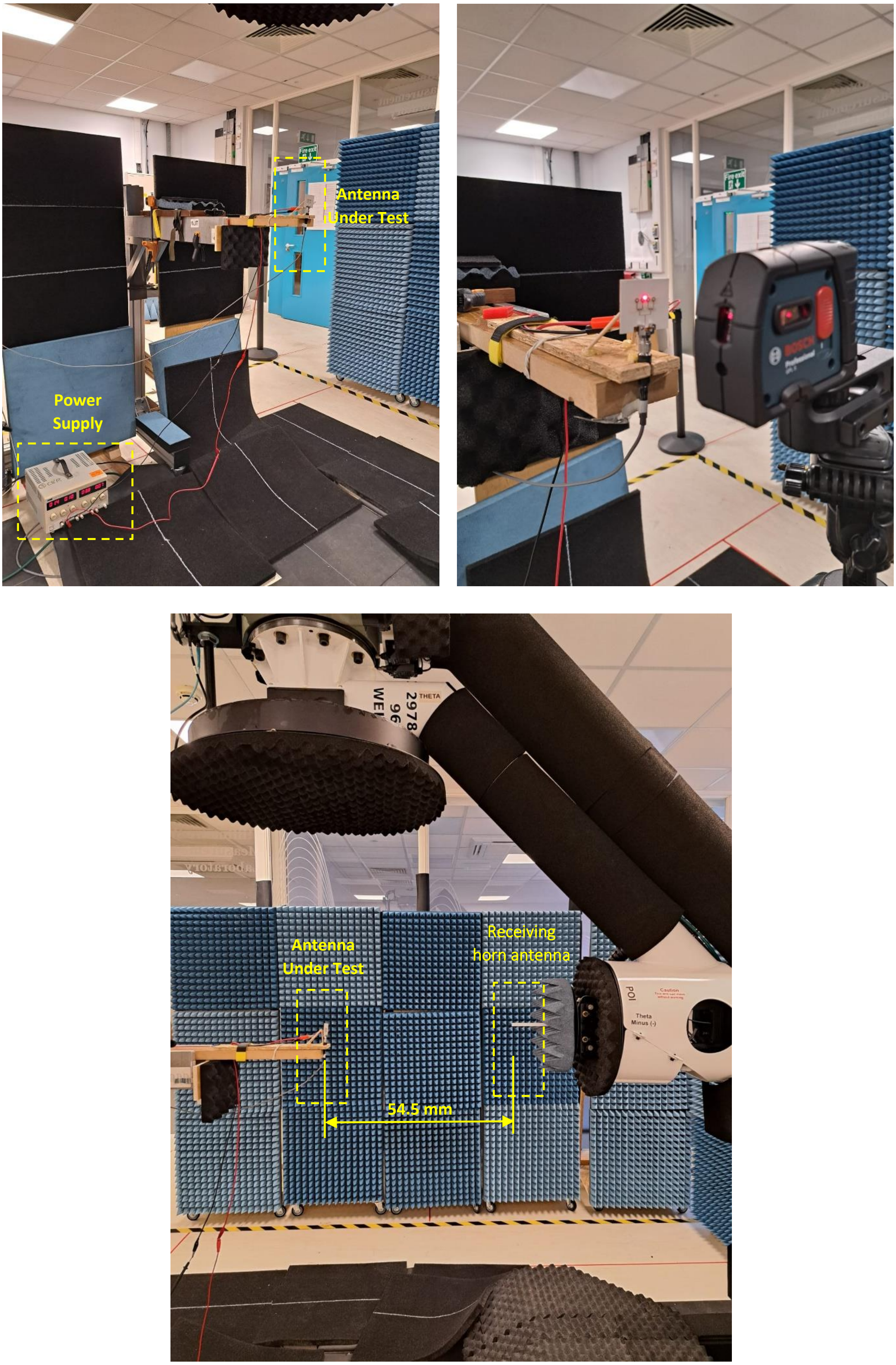
Antenna
Under Test
Power
Supply
Antenna
Under Test
Receiving
horn antenna
54.5 mm

(a)

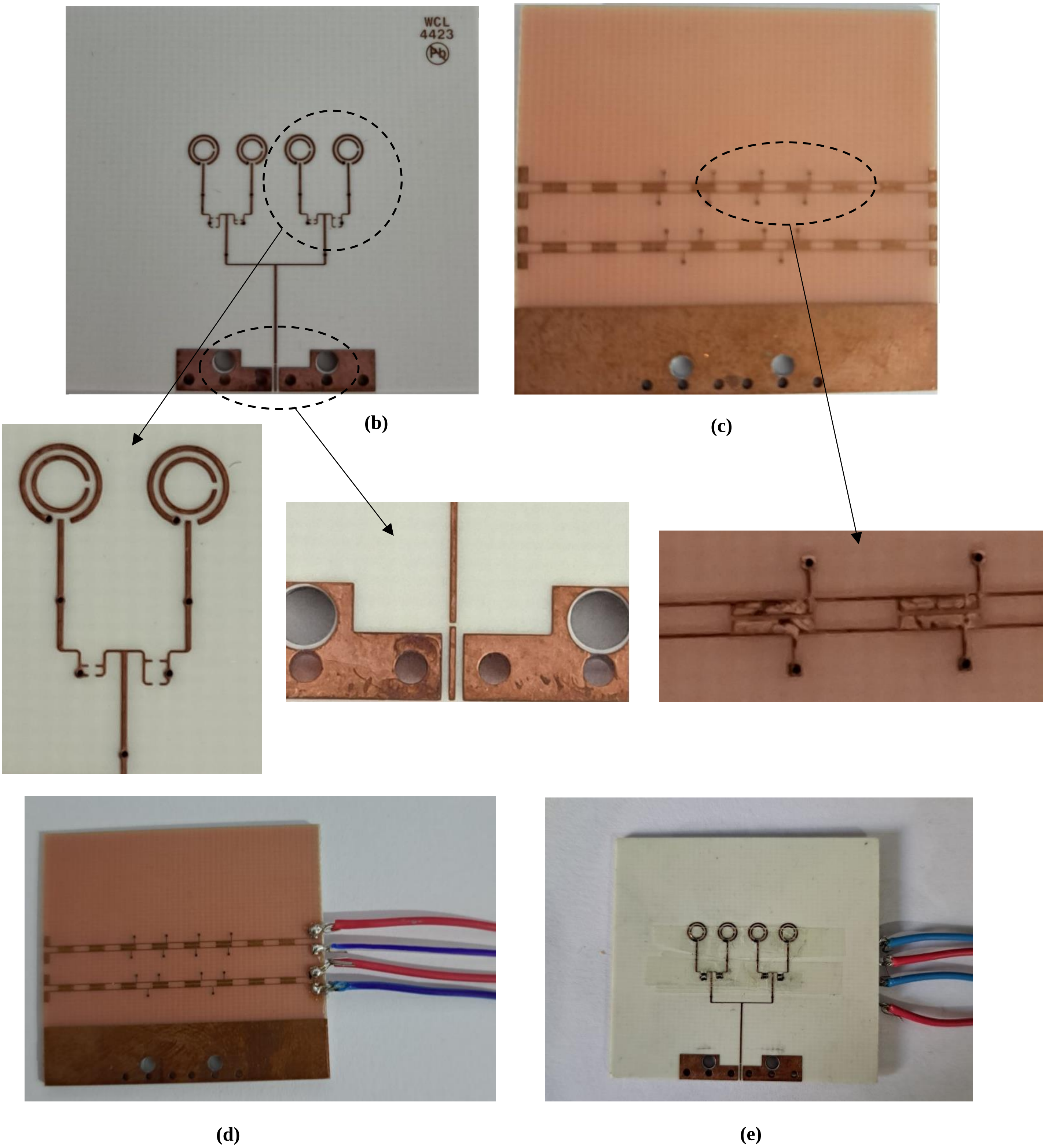

Figure 6.9: Fabricated prototype of the reconfigurable array antenna at 27.5 GHz: (a) antenna under test and (b) top view (c) bottom view (d) Soldered the wires to the solder pads. (e) Proposed antenna with PIN diodes.

Facility (NmmMF). The reflection coefficient was measured using a 2.4 mm SMA connector and an N5245B vector network analyser (VNA). Figure 6.9 presents photographs of a reconfigurable array antenna in the NmmMF during the measurement process. The phased array needs to maintain good impedance matching at all beam steering angles.

Simulations and measurements were conducted to verify the simulations, focusing on return losses at beam steering angles of -25° and +25° and considering three different polarisation senses (LHCP, RHCP, and LP). The comparisons of these results are illustrated in Figures 6.10 and 6.11, revealing good agreement between simulations and measurements. Additionally, the findings highlight consistently good impedance matching across all beam steering angles.

In the first scenario, the simulation indicates that configuring the antenna to operate in the LHCP case results in percentage impedance bandwidths of approximately 9.96% and 9.1% for the evaluated beam steering angles (-25° and +25°) respectively. The corresponding measured results show bandwidths of around 6.8% and 6.75%. In the second scenario, when RHCP cases are considered for the same beam steering angles, the simulated antenna array exhibits percentage impedance bandwidths of approximately 8.6% and 8.4%, while the measured results show bandwidths of around 5.9% and 5.7% respectively.

Furthermore, the results indicate that LHCP and RHCP cases demonstrate nearly symmetrical performance, a desirable characteristic for specific applications. On the other hand, differences between measurement and simulations can be attributed to the assembly of the PIN diodes using silver paint as well as experimental errors. Overall, these findings underscore the reliability of the simulations, highlight impedance matching effectiveness, and suggest potential applications for LHCP and RHCP cases.

In Figure 6.11, the achieved reflection coefficient in the LP case is depicted under the scenario where the PIN diodes of the loops are under zero bias, and the beam steering angles are the same (-25° and +25°). Notably, the figure reveals successful matching over a narrow band centered at 26 GHz, with bandwidths considerably narrower compared to those in the CP cases. Specifically, the simulation demonstrates bandwidths of 3.28% and 3.5%, while the

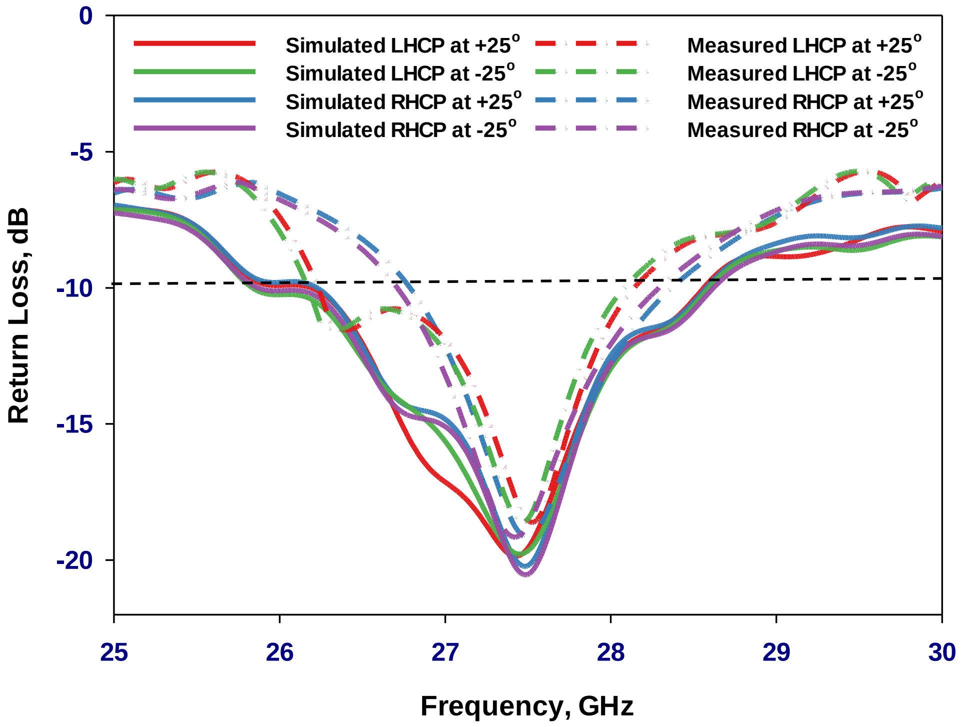

Figure 6.10: Return losses as a function of frequency across various CP senses and beam steering angles.

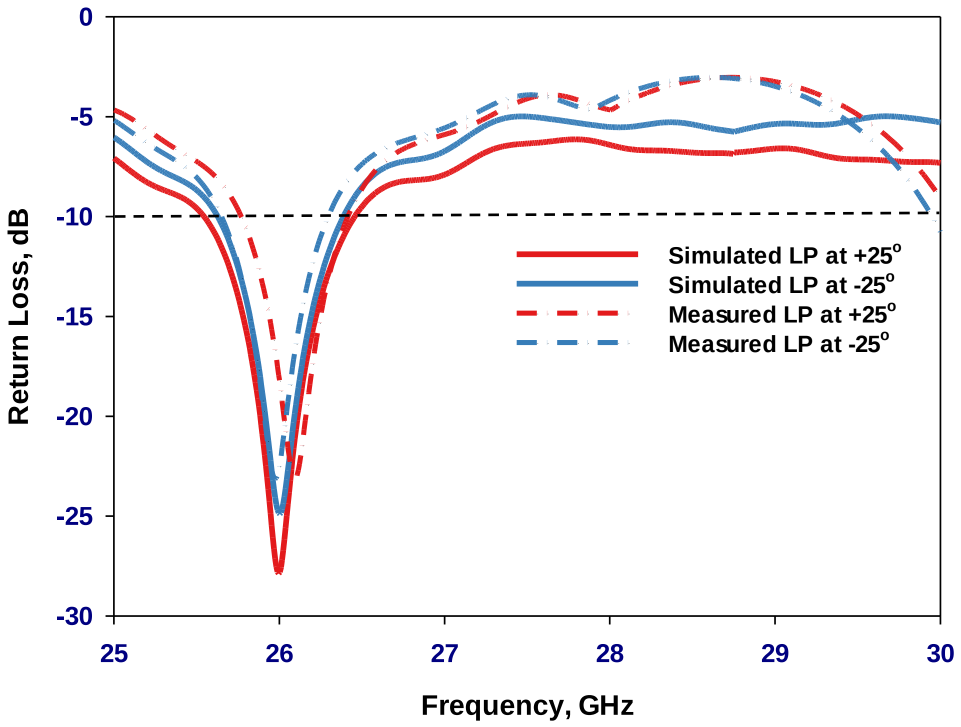

Figure 6.11: Return losses of the mmWave reconfigurable array antenna operating in the LP case.

measurements show slightly narrow bandwidths at 2.46% and 2.42%. These findings suggest that, in addition to achieving reconfigurable polarization and beam steering, the antenna also possesses reconfigurable frequency capabilities when utilizing linear polarization. Therefore, the proposed antenna introduces a multifunctional, or compound, reconfiguration as it enables the tuning of frequency, polarisation, and radiation patterns using 16 PIN diodes and two biasing networks only, offering a versatile solution for various applications.

Figures 6.12a and 6.12b showcase the measured and simulated axial ratios for both LHCP and RHCP cases at beam steering angles of -25° and +25°. In the LHCP scenario, the simulated 3 dB axial ratio bandwidths cover approximately 8.7% and 8.1% within beam steering angles of -25° and +25°, respectively. The measured 3 dB AR bandwidth in the same LHCP scenario registers around 6.1% and 6.3%, demonstrating close agreement with simulations. Conversely, in the RHCP scenario, the simulated 3 dB AR bandwidths are roughly 8.2% and 8.5% within beam steering angles of -25° and +25°, respectively. Correspondingly, the measured outcomes show bandwidths of approximately 6.2% and 6.1%, all centered at 27.5 GHz.

Furthermore, Figures 6.13a and 6.13b illuminate the 3 dB axial ratio (AR) beamwidths for the LHCP and RHCP configurations at beam steering angles of -25° and +25°, showcasing a commendable convergence between measured results and simulations at the pivotal frequency of 27.5 GHz. In the LHCP scenario, when the main beam is directed at -25°, the experiment yielded a measured AR beamwidth spanning from (-26° to 14°), harmonizing closely with the simulated range of (-28° to 15°). Similarly, with the main beam steered to +25°, the measured AR beamwidth extended from (-12° to 26°), aligning seamlessly with the simulated range of (-7° to 29°).

Switching to the RHCP scenario, when the main beam position at -25°, the measured AR beamwidth unfolded from (-26° to 15°), aligning effectively with the simulated range of (-30°

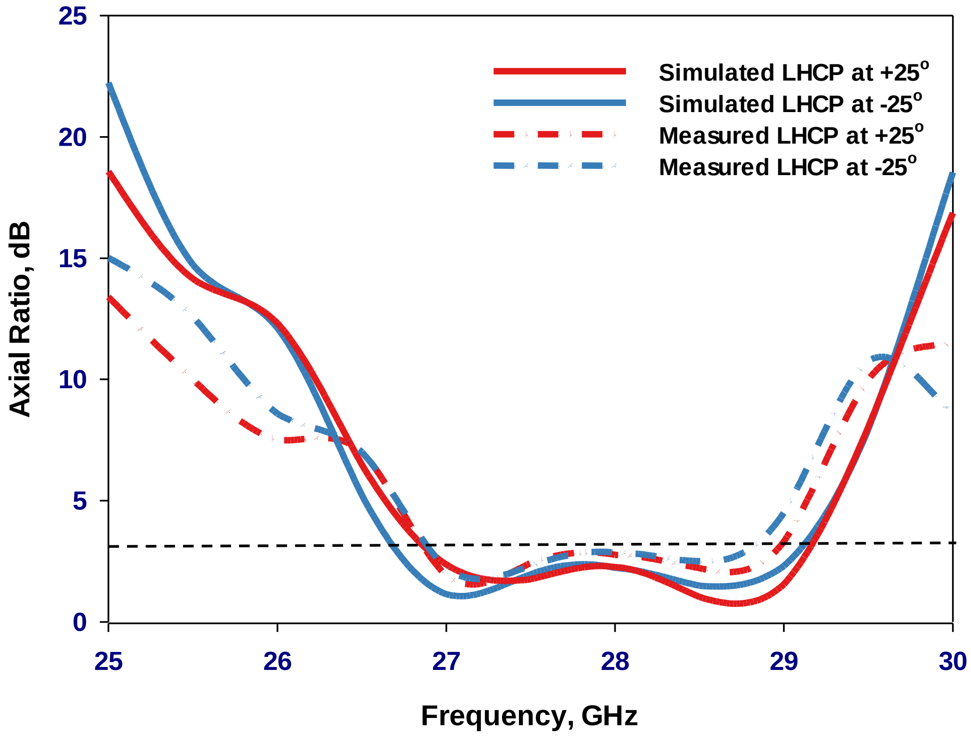

(a)

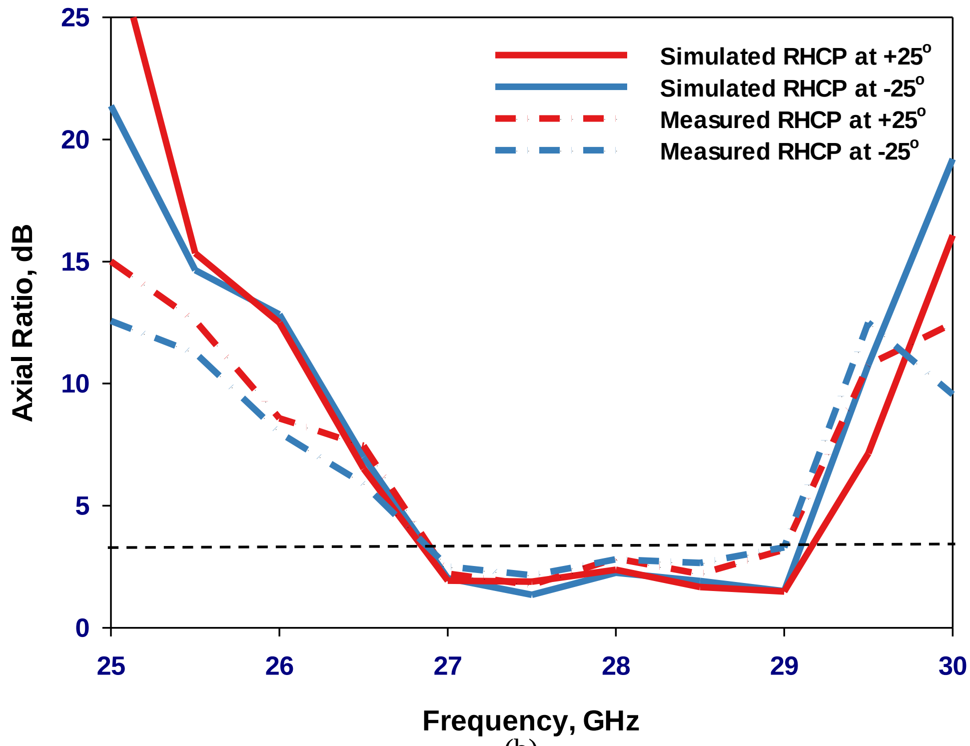

(b)

Figure 6.12: Axial Ratio for both circular polarisation senses and beam steering angles in the maximum radiation direction (a) LHCP (b) RHCP.

to 18°). Finally, with the main beam pointed at +25°, the measured AR beamwidth spanned from (-11° to 26°), in striking accord with the simulated range of (-13° to 27°). This striking alignment between experimental findings and simulations not only attests to the precision of our methodology but also underscores the substantive contribution of this research to the field.

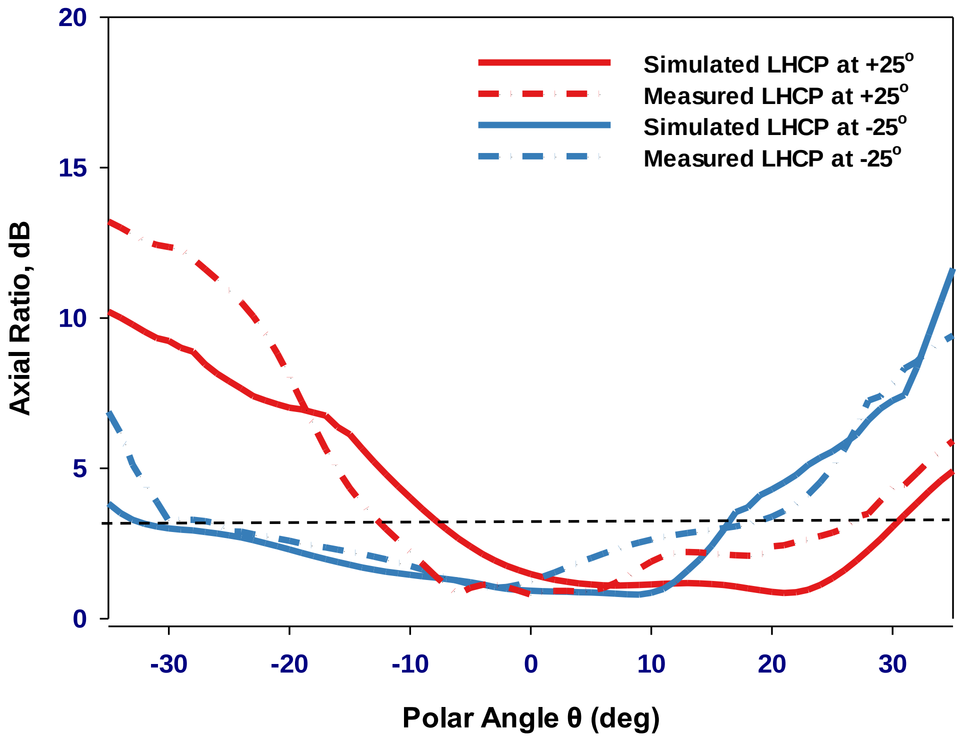

(a)

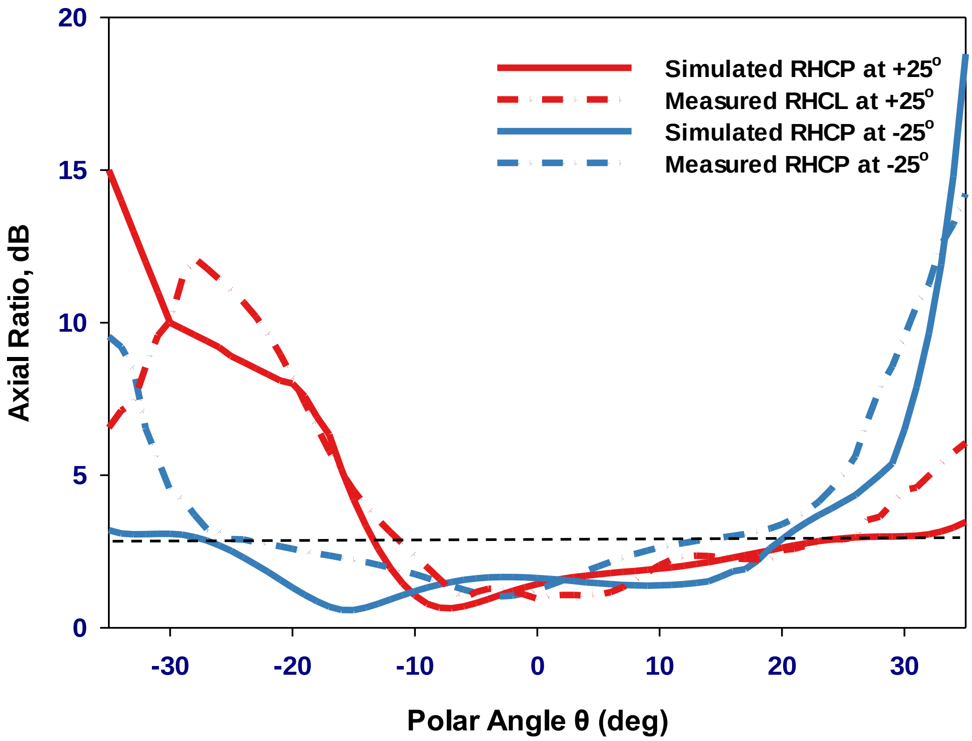

(b)

Figure 6.13: AR as a function of polar angle θ at 27.5 GHz for two polarisation senses: (a) LHCP and (b) RHCP.

Figure 6.14 and Figure 6.15 illustrate the normalized simulated and measured radiation patterns of the E_L and E_R components at the ϕ=0° principal plane, corresponding to LHCP and RHCP cases achieved by the reconfigurable array with two beam steering angles (-25° and +25°). The results reveal a substantial alignment between experimental measurements and simulated data, albeit with minor discrepancies attributed to measurement errors in the mmWave frequency range. In some cases, E_L is stronger than E_R by more than 20 dB in the main beam direction, which corresponds to an LHCP sense. Conversely, when the E_R component exceeds the strength of E_L, it signifies an RHCP. However, the difference between E_L & E_R is reduced as the elevation angle is shifted from ±25°, which indicates the degradation of the circular polarization level. By controlling all cases of the PIN diodes, different main beam polarisation and steering can be switched.

Figure 6.16 presents the normalized radiation patterns at 26 GHz in the E-plane (*xz* plane) of the antenna when the PIN diodes on the loop antennas are under zero bias with a close agreement between simulated and measured results. This configuration enables the radiation of LP wave at varying operating frequencies and two distinct beam steering angles of +25° and -25°. Overall, the proposed array has successfully achieved six distinct cases, incorporating reconfigurable frequency, reconfigurable polarization, and reconfigurable beam steering functionalities.

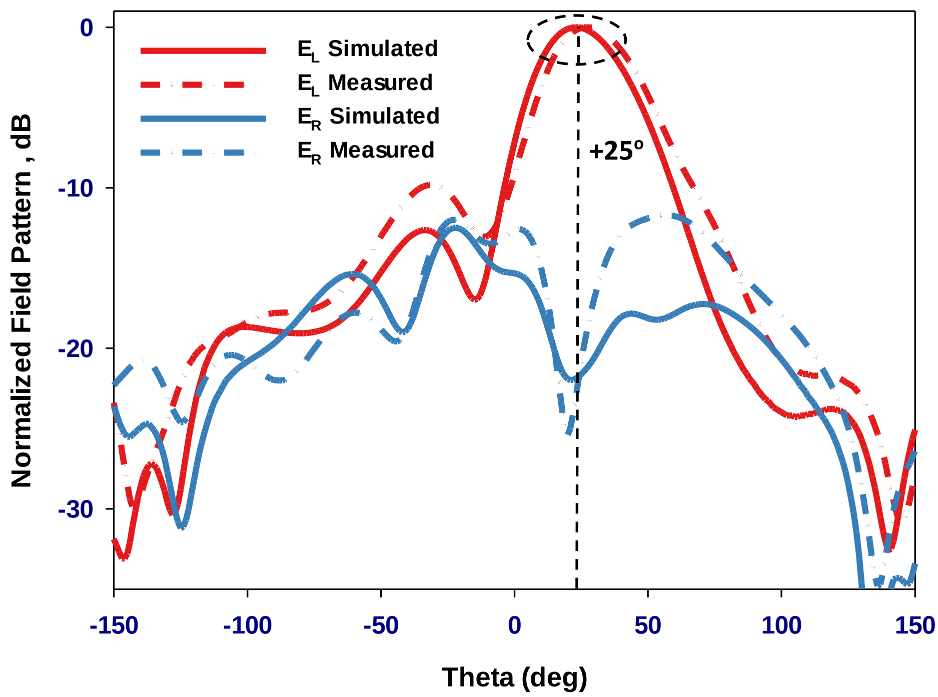

(a)

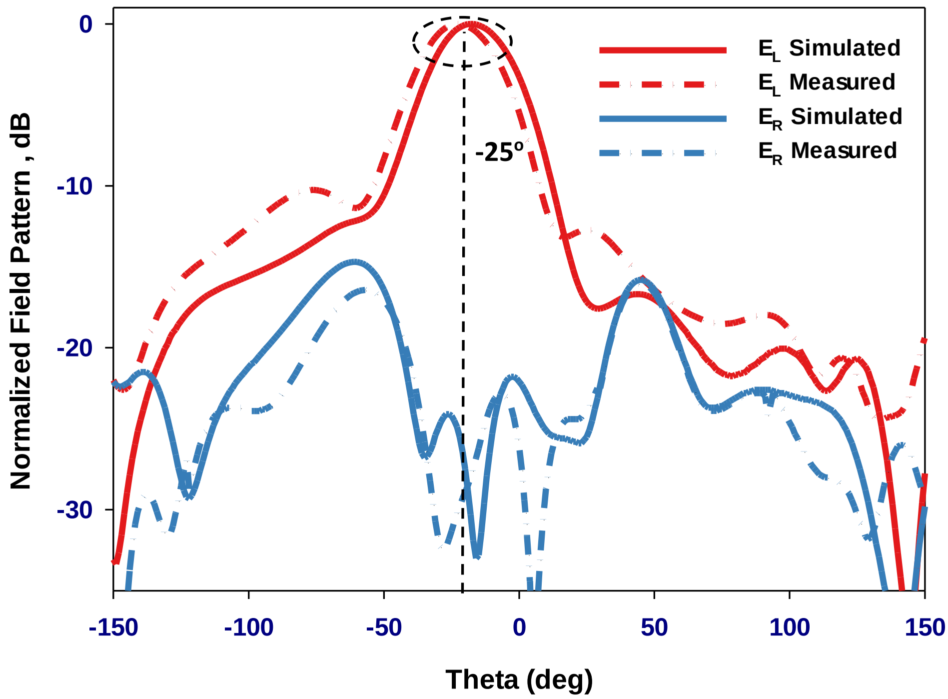

(b)

Figure 6.14: E_L & E_R radiation patterns (a) Beam steering angle of +25° (b) Beam steering angle of -25°

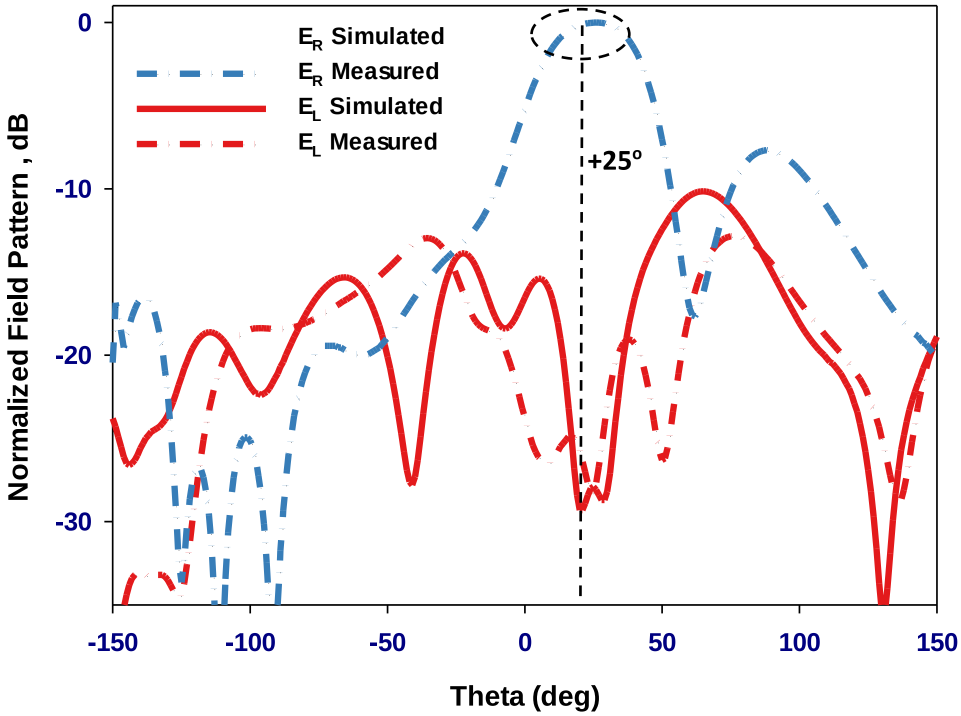

(a)

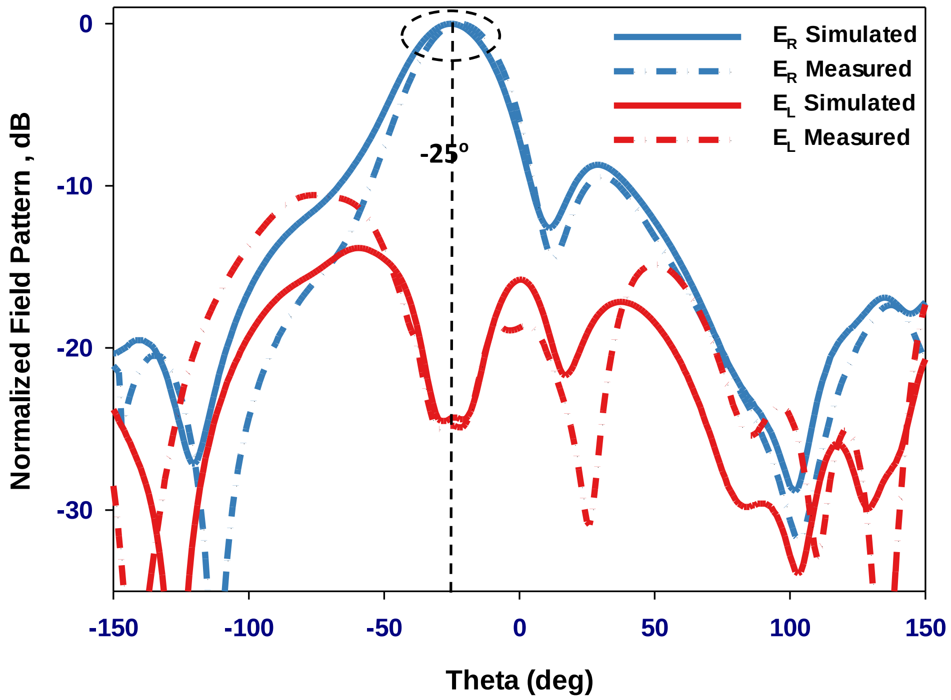

(b)

Figure 6.15: E_L & E_R radiation patterns (a) Beam steering angle of +25° (b) Beam steering angle of -25°

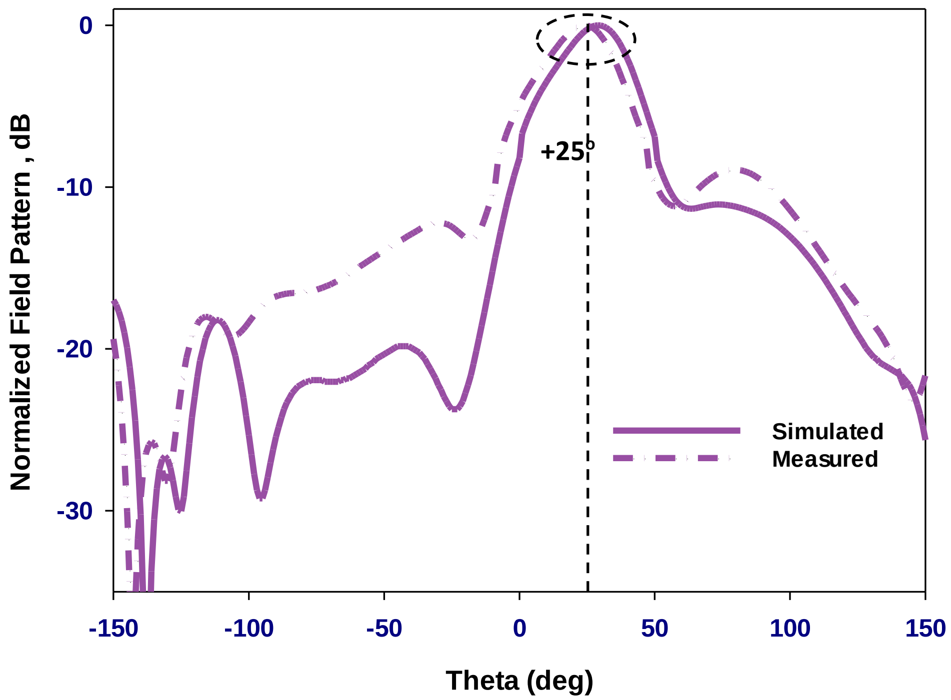

(a)

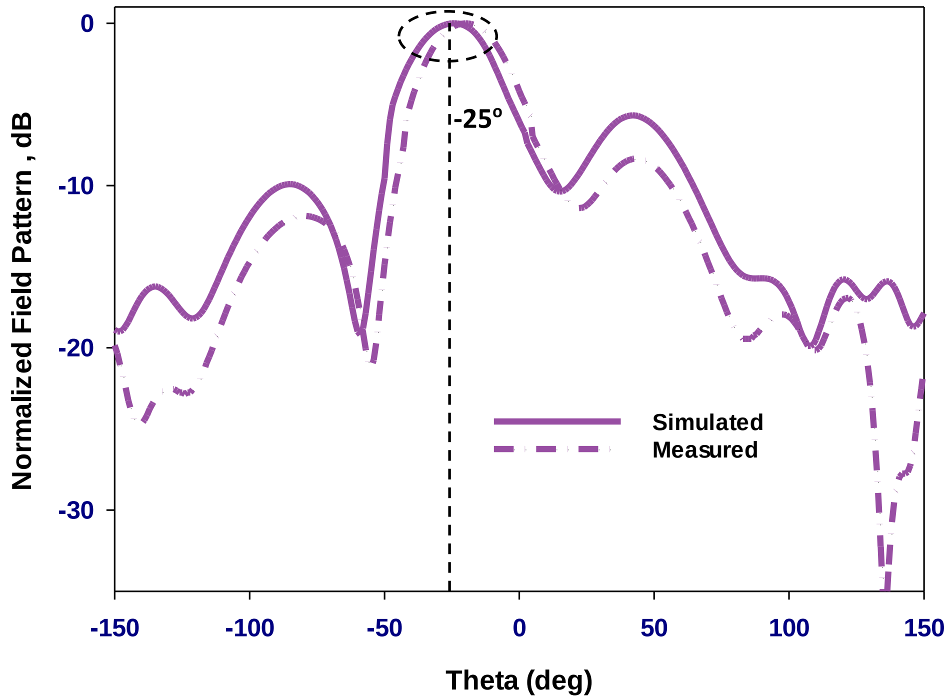

(b)

Figure 6.16: Normalised radiation patterns (a) Beam steering angle of +25° (b) Beam steering angle of -25°

Figure 6.17 illustrates the maximum realised gains for both circular polarization and linear polarization modes across all cases as the main beam is steered to angles of (-25° and +25°). From these results, it can be observed that for Cases 1 to 4, which correspond to CP radiation, the simulated realized gain is circa 10.3 dBic at 27.5 GHz, while Cases 5 and 6, which correspond to LP case, the antenna exhibits a slightly lower realized gain of approximately 9.1 dBi at 26 GHz. This agrees with the measurements and can be explained as a result of the different loading impedances offered to the antenna by biased diodes in cases -4 and unbiased diodes in cases 5-6, which could alter the current distribution and reduce the efficiency.

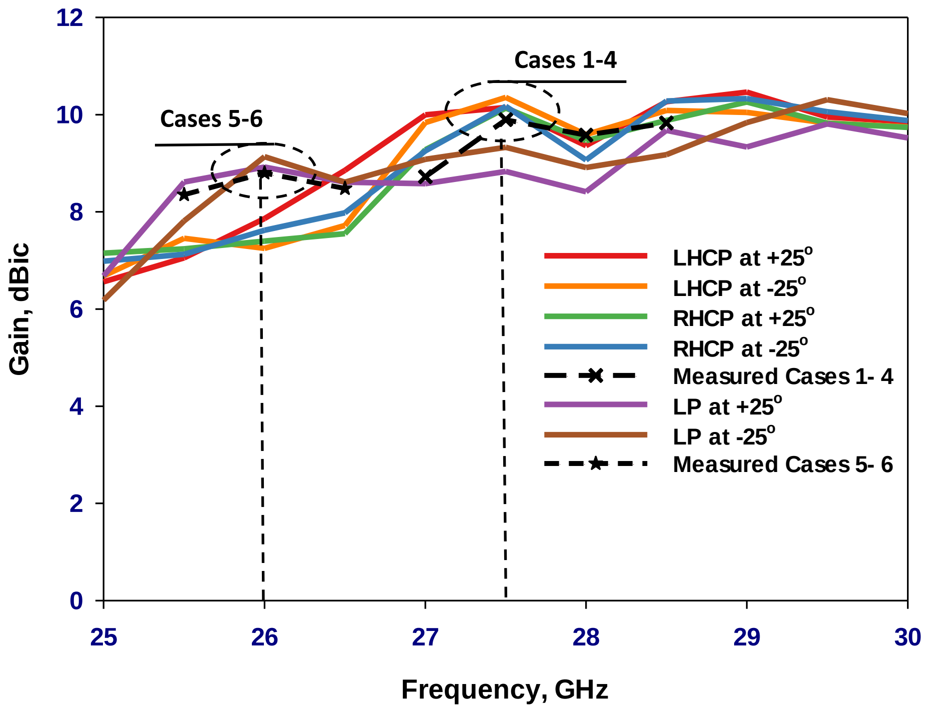

Figure 6.17: Realised gains for different polarisations and different main beam directions of the mmWave MRAA.

Significantly, the simulated total efficiency remains consistently high across various scenarios. It reaches approximately 73% for cases 1 to 4 and 64% for cases 5 to 6, aligning with the desired bandwidth as illustrated in Figure 6.18. The lower efficiency in the LP case could be attributed to the higher resistance offered by the unbiased PIN diodes. This finding emphasizes the remarkable performance of the multifunctional reconfigurable antenna within the mmWave frequency range.

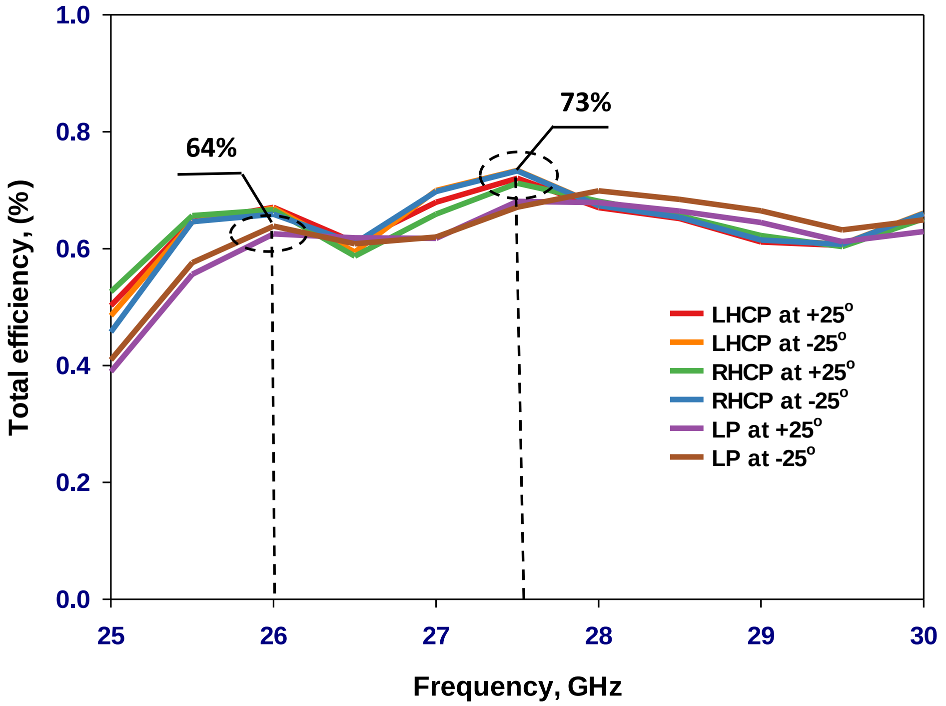

Figure 6.18: Total efficiency for different polarisations of the proposed mmWave MRAA.

6.8 Performance Comparison

A comparison between the performance of the proposed antenna and those reported in the literature is presented in Table 6. However, the comparison has been made with counterparts that operate at lower frequencies as no mmWave multifunctional reconfigurable array is available in the literature, which emphasises the significance of the findings of the presented study.

The first that can be observed from Table 6.6 is that there are only two reported MRAA configurations that offer reconfigurability of the three key parameters, frequency, pattern, and polarisation [114], [116] albeit with a higher number of operating modes compared to 6 in this study. However, this is more than compensator for by the simpler proposed design in this work that utilises only 16 PIN diodes compared to 144 and 60 in these references. This is in addition to the mmWave operation, higher gain, and wider bandwidth.

TABLE 6.6: COMPARISON OF THE PROPOSED ANTENNA PERFORMANCE AGAINST REPORTED MFRA PROTOTYPES.

Ref.	Freq. GHz	Antenna	Switches	S_{11} BW%	AR BW%	Gain dBi	η%	Reconfigurability
[104]	4.1, 6.4	MIMO	112*	3	___	____	___	Polarisation &Freq.
[105]	5.2, 6.4	Slot	4⁑	___	NA	___	80	Pattern, Frequency
[106]	1.4-2.8 2.0-2.5 1.9-2.6	PA	3**	___	NA	-0.7 6.5 3.8	42 95 65	Frequency &Pattern Freq. & Polarisation
[107]	2.68,3.5	PA	6**	___	NA	7.5 5	94 76	Frequency & Pattern
[108]	11	PA	10⁑	___	NA	8,7. 2, 7.4	___	Pattern & Polarisation
[109]	10	Pixel	20*	5	NA	____	___	Frequency & Pattern
[110]	4.5, 7	81 PAs	144*	1.5-4	NA	3.47	46	Pattern, Frequency & Polarisation
[111]	2.5	PA-Pixel	12*	~16	NA	6	70	Frequency & Pattern
[112]	2.7	PA-Pixel	60⁑	2.8	___	4	50	Pattern, Frequency & Polarisation
[113]	5.4-5.6	4 PAs-Pixel	24⁑⁑	3	1.8	13.5	___	Pattern& Polarisation
[114]	2.4	PA-Pixel	12⁑	4	NA	6.5	___	Pattern
[115]	2.45,5.3	PA-Pixel	60⁑	__	NA	6.9, 8.2	___	Pattern
[116]	0.8-3	Crossed dipole	Liquid Metal	__	___	0.3- 1.7	41- 70	Frequency & Polarisation
[117]	1.5	Dipole	Liquid Metal	__	NA	2.12	95	Pattern& Polarisation
[118]	3-5	Monopole	Liquid Metal	40	37.5/48.8	2.2	__	Frequency & Polarisation
[119]	2-7	Microstrip	Liquid Metal	5.9	narrow	5.9	90	Frequency & Polarisation
[120]	4-5	PA, 4×4 PA	Multi-ports	22	__	__	75	Pattern& Polarisation
[121]	1.3- 2.19	PA, 4×4 PA	Digital, 4-ports, 4⁑	2	NA	15.5	54- 59	Frequency & Polarisation
[122]	2.5	1×4 DR	Digital,32⁑, Metasurface	12.5	2.4	9	60%	Pattern& Polarisation
This work	28	1×4 Loop	16⁑	13	8	10	73%	Pattern, Frequency & Polarisation

∗ MEMS, ⁑ PIN diodes, ∗∗ Varactors, ⁑⁑ Hard wired, PA Patch Antenna

In addition, the suitability of the reported designs to work in the mmWave frequencies is questionable due to the complexities introduced by the excessive number of switches and/or parasitic substrates [104], [109], [110], [112], [113], [115], utilizing metal liquids [116]-[119], multiple ports [120],[121], and the utilisation of DR elements that are associated with the assembly and bonding complexities [122]. Furthermore, CP radiation has only been reported in 8 studies, mostly with narrower AR bandwidths [104], [112],[113], [116], [118], [119], [120], and [122].

The proposed configuration represents the first attempt to demonstrate the potential of a multifunctional reconfigurable array for millimeter frequencies, which makes it most suitable for 5G and B5G systems. Furthermore, the design also offers distinctive advantages such as simplicity and improved performance in terms of bandwidth, gain, and efficiency.

6.9 Summary

This Chapter presented a comprehensive literature review of reconfigurable multifunction antennas. This is followed by introducing a novel design of such arrays that is suitable for mmWave frequency applications, where special attention has been paid to designing an efficient biasing network for the 16 PIN diodes. It should be noted that only two biasing networks have been utilised compared to many more in the literature. A prototype has been fabricated and measured with excellent agreement between measured and simulated results. The measured results confirm the potential of the proposed MRAA when reconfigurability is needed for the key antenna parameters such as pattern, polarisation, and frequency.

Chapter 7

An Investigation of On-chip Circularly Polarized Circular Loop Antenna Fabricated on 350µm Thick 4H-SiC and GaAs Substrates in the Q/V Band.

7.1. Introduction

Global mobile data traffic has increased significantly in recent years. It is expected that data traffic will continue to strain the capacity of communication networks in the future [124]. An analysis of current statistics from the International Telecommunication Union (ITU) shows that global mobile data traffic will increase to 607 exabytes (EB) per month by 2025 [125]. The exponential increase of the 5G throughput requirement drives the spectrum used for the front haul from the conventional microwave band to the mmWave spectrum. It has been the consensus that the Q/V-band offers many advantages over the lower frequency bands. The Q-V band holds considerable potential that has yet to be harnessed for commercial systems. This frequency range encompasses a significant portion of the spectrum designated for satellite services, presenting promising prospects for future applications [126, 127]. One of the reasons for the growing enthusiasm for communications and existing communication systems that utilize higher frequencies. The main obstacle in utilizing these bands is the increased propagation loss in terms of the attenuation caused by rain and the path loss [128]. Therefore, to overcome the limitations of mmWave signal propagation, the commonly used linearly polarized elements are replaced by circularly polarized counterparts [129, 130]. Circular polarization radiation is used in several applications such as global positioning systems (GPS), satellite communications, RFID systems, ground radar, and wireless local area networks [131]. To meet the requirements of specific applications, CP antennas can be realized by generating orthogonal modes using perturbation techniques [132]. On the other hand, loop antenna has received much attention as it offers several advantages such as simple design and fabrication, low-cost implementation, and ease of implementation. As a result, it has been employed in many wireless applications [133].

The employment of on-chip antennas offers significant advantages in the development of highly integrated transceiver systems by utilizing complementary metal–oxide–semiconductor (CMOS) technology. For example, antenna with artificial magnetic conductor (AMC)-based wide-slot squared design has been seamlessly integrated at 60-GHz [134]. In simulations, this integrated antenna exhibited a gain of approximately -2.1 dBi. Consequently, the concept of antenna-on-chip holds promise as a viable alternative to conventional metal interconnects for connecting chips on a printed circuit board (PCB), especially when dealing with extremely wide bandwidths and sub-terahertz carrier frequencies, where traditional metal leads become impractical.

In another study, a vertical-type loop design with two wire bonds of varying sizes has been introduced for 50 GHz operation using a Silicon substrate [135]. These wire bonds originate from the ends of a differential line and culminate at a shorted-metal pattern. The antenna is linearly polarized with a circa 8% return losses' bandwidth, along with a total efficiency of 24% and a gain of -2 dBi. In addition, the utilization of two wire bonds of differing sizes and complex feeding structures can result in a relatively large and intricate antenna configuration. Furthermore, the fabrication process may pose challenges, particularly when dealing with small dimensions such as a 10 µm slot width and 100 µm metal line width, demanding advanced manufacturing techniques to achieve precise dimensions at this scale. Furthermore, three on-chip antenna prototypes were designed and compared using a high-resistivity Silicon substrate operating at the V-band [136]. These antennas: loop, slot, and dipole, were tested with measured boresight gains of 3.7dBi, 3.8dBi, and 3.9dBi, with corresponding radiation efficiencies of 79%, 83%, and 82%, respectively. The results highlight the effectiveness of using high-resistivity substrates to enhance the gain and efficiency of on-chip antennas significantly. This demonstrated the potential of on-chip antennas as a promising technology for highly integrated mmWave applications.

Other studies consider GaAs substrates due to higher resistivity and lower losses compared to Si substrates. For example, an on-chip antenna of a half-wavelength dipole radiating element and two tilted and slotted dipole elements was designed, using GaAs substrate, to operate in the V-band frequency range, i.e. at 60 GHz, and the results demonstrated a gain of circa 3.6 dBi [136]. A multilayer patch antenna that is integrated with a V-band MMIC transmitter has been fabricated on a 100 μm thin GaAs wafer and measured with a maximum gain of ~2dBi at 57 GHz [137]. Furthermore, a 94-GHz log-periodic planar antenna has been reported, where a lapping process was utilized to reduce the substrate thickness to 100 μm for efficiency improvement purposes with an achieved gain of 4.8 dBi [138].

Most reported studies on the on-chip antenna are based on utilizing Si or GaAs wafers as substrates. However, such materials suffer from relatively high dielectric losses, which deteriorate the antenna's radiation efficiency at higher frequencies [139-141]. Besides, the higher dielectric constants of 12 and 12.94 for Si and GaAs substrates, respectively, may result in a stronger surface wave excitation for a given wafer thickness. On the other hand, 4H-SiC offers lower dielectric losses compared to Si and GaAs substrates as well as a distinctive advantage of the capability to work in harsh environments such as high temperature and high power [142], which make it most suitable for the design of conventional antennas and antenna sensors that operate in such conditions. Despite the considerable reported studies on the potential of 4H-SiC-based devices, only two studies are available on the design of 4H-SiC-based antennas [143, 144]. A patch antenna has been fabricated on a 4H-SiC substrate operating at 10 GHz with a narrow impedance bandwidth and gain of 2 dBi [143]. On the other hand, a simulations-based study was reported in [144] to demonstrate the potential of a mmWave dielectric resonate antenna on a 4H-SiC substrate.

This paper presents the design and comprehensive measurements of a circularly polarized on-chip loop antenna that is fabricated on a 4H-SiC substrate to operate at the Q/V frequency bands. This design delivers commendable performance characteristics in terms of both return losses and axial ratio bandwidths. In addition, for comparison purposes, two different substrates have been considered, namely 4H-SiC and GaAs. The performance of the single loop antenna on each substrate has been thoroughly examined, focusing on key parameters such as return losses, circular polarization, gain, and radiation efficiency. Furthermore, 4 elements 4H-SiC-based array has been designed and measured with a high gain of 9.5 dBic. In the proposed array design, a parallel feed network has been implemented, which plays a crucial role in optimizing the antenna's performance. Different circular polarizations by changing the position of the gaps in the loop antenna. This capability enables the antenna to produce various types of circular polarization, enhancing its versatility and adaptability for different communication needs. The simulations were conducted using the Computer Systems Technology (CST) Microwave Studio software. A close agreement has been achieved between simulations and measurements. This research contributes to the development and understanding of on-chip loop antennas for Q/V band frequencies, showcasing their potential applications in various wireless communication and sensing systems.

7.2 Contribution

1. Designed and fabricated an on-chip circularly polarized (CP) single-loop antenna specifically tailored for the Q/V band frequency range, utilizing two distinct substrates: GaAs and 4H-SiC. The proposed antenna design incorporates two concentric loops, with the outer loop serving as the active element and the inner loop enhancing the CP bandwidth. This design delivers commendable performance characteristics in terms of both return losses and axial ratio bandwidths.

2. Generation of Different Circular Polarizations using GaAs antennas: By changing the position of the gaps in the antenna design, LHCP and RHCP circular polarizations can be generated. This capability enables the antenna to produce various types of circular polarization, enhancing its versatility and adaptability for different communication needs.

3. A 4-element open loop array antenna using the 4H-SiC substrate. In the proposed design, a parallel feed network has been implemented, which plays a crucial role in optimizing the antenna's performance. In addition, the proposed design offers a high gain of 9.5 dBic, particularly in the broadsight direction. This enhancement in gain underscores the antenna's effectiveness in transmitting and receiving signals.

The chapter is organized as follows; Section 7.3 introduces the configuration and design principles of a circularly polarized. The measurements of an on-chip antenna on a GaAs substrate is presented in Section 7.4 with detailed investigation of the CP radiation options. This GaAs-based prototype will be used as reference against which the performance of a 4H-SiC-based antenna will be compared in Section 7.5 through fabrication and measurement. In Section 7.6, we outline the methodology for the proposed on-chip array antenna design using a 4H-SiC substrate and covers the prototype development, simulation, fabrication, and measurement of the proposed antenna array. The paper is concluded in Section 7.7

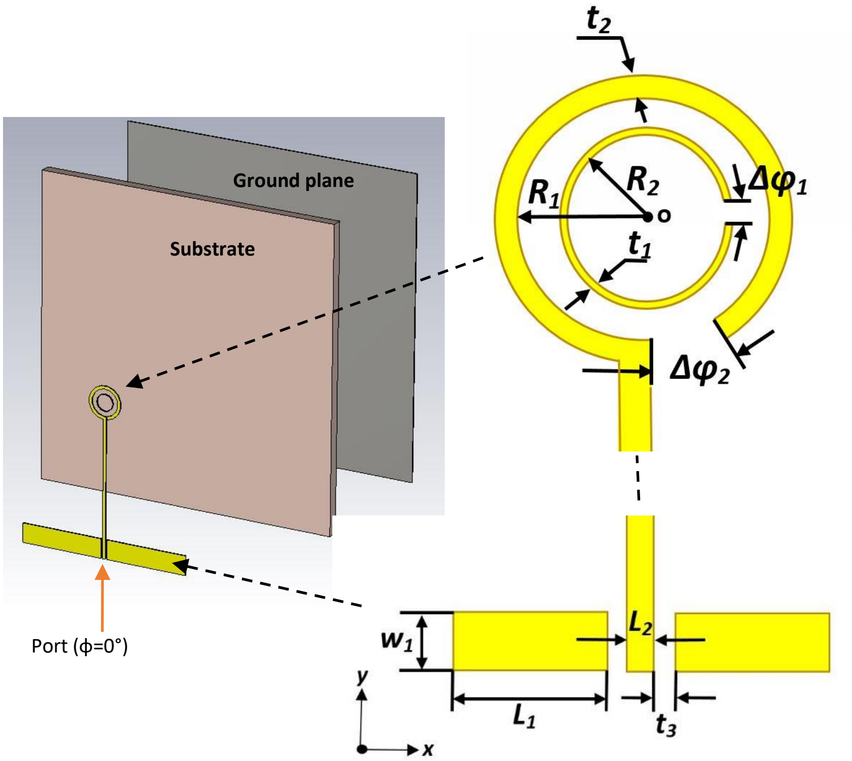

Figure 7.1: Geometry of the on-chip circular loop.

7.3 Q/V- Band Circularly Polarastion Antenna Design and Configuration

This section presents the proposed single antenna on different substrates as well as the on-chip configurations.

7.3.1 Design of Circular Polarisation Single Element

This section presents the proposed single antenna on different substrates. For the design of a single element, three layers are used including the actual antenna, substrate, GaAs or 4H-SiC, as well and a copper ground plane ground plane with a size of 10 mm × 10 mm. Figure 7.1 depicts the configuration of the utilized CP antenna element. The printed circular loop and substrate are positioned above a square copper plate, which functions as a reflector. This proposed antenna comprises two concentric loops, with the outer loop serving as the active element. To achieve the CP radiation, the outer loop's circumference needs to be approximately one effective wavelength. With the aid of Equations (1), (2), and (3), the circumference of the outer can be calculated [20], i.e.,

$$\varepsilon_{eff} = (\varepsilon_r + 1)/2. \tag{7.1}$$

$$\lambda_{eff} = \lambda_0/\sqrt{(\varepsilon_{eff})}. \tag{7.2}$$

$$2\pi R_1 \simeq \lambda_{eff} \tag{7.3}$$

where ε_{eff} is the effective permittivity, λ_{eff} is the effective wavelength, and λ_0 is the free-space wavelength.

The optimization of the outer loop gap, denoted as $\Delta\varphi_2$, is carried out to establish a current distribution that supports traveling waves along the loop, a critical factor for achieving circular polarization. Furthermore, the inner loop is designed with a smaller gap to enhance the CP bandwidth. Due to the shorter wavelengths at high frequencies, which results in a small antenna size, a coplanar waveguide probe with ground-signal-ground (GSG) contact geometry has been used for measurements as shown in Figure 7.2. The center-to-center spacing of the probe tips is 150µm. The width of the feed line, l_2, has been chosen as 100µm. The distance between the feed line and the grounded rectangular pads, l_3, has been optimized to 50µm for optimum 50Ω matching. The antenna has been designed for operating frequencies ranging between 40 and 44 GHz. By adjusting the width and the positions of the two-loop gaps (φ_1, φ_2), the required axial ratio (AR) can be achieved.

The antenna has been designed using CST and the optimized geometrical parameters for the circularly polarized loop antenna are listed in Table 7.1.

Table 7.1 Used Parameters of the Antennas (all dimensions in mm)

Symbol	***Quantity***	***GaAs***	***4H-SiC***
ε_r	relative permittivity	12.94	10.2
$\tan\delta$	loss tangent	0.006	0.00003
R_1	outer loop radius	0.441	0.55
R_2	parasitic loop radius	0.266	0.34
t_1	outer loop width	0.1	
t_2	parasitic loop width	0.014	0.02
l_1	pads length	2.69	3.18
l_2	transmission line width	0.1	
l_3	gap between the transmission line & pads	0.05	
w_1	pads width	0.574	0.85
w_2	length between the pads & outer loop	3.886	
a_0	antenna thickness	0.035	
h	thickness of the substrate	0.35	
$0.t$	reflector thickness	0.035	
$\Delta\varphi_1$	parasitic loop gap	5°	
$\Delta\varphi_2$	outer loop gap	10°	

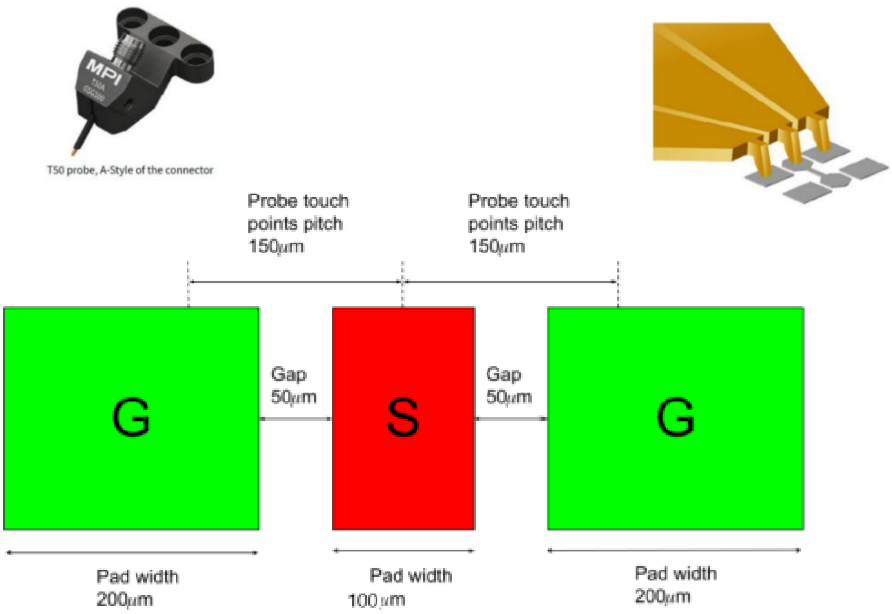

Figure 7.2: RF probes and landing pad dimensions.

7.4 GaAs-Based Antennas with Different Polarization Senses

Figure 7.3 (a, b) provides an illustrative depiction of two on-chip GaAs antennas in operation, functioning at a frequency of 44 GHz. These antennas exhibit two different types of polarization, a phenomenon that is accomplished through the strategic placement of gaps. It is worth noting that a one-wavelength loop antenna inherently radiates a linearly polarized wave. However, the introduction of a gap within a circular loop antenna induces a traveling-wave current, leading to the generation of circularly polarized radiation.

As shown in Figure 7.3a when the gaps $\Delta\varphi_1$ and $\Delta\varphi_2$ for the outer and parasitic loop are positioned on the right side of the antenna structure, it fosters the formation of a traveling wave current, circulating in a clockwise direction, ultimately resulting in the Left-Hand Circularly Polarized (LHCP) wave in the far-field region. Conversely, in the antenna configuration portrayed in Figure 7.3b, when the gaps of $\Delta\varphi_1$ and $\Delta\varphi_2$ for the outer and parasitic loop are situated on the left side, it facilitates the generation of a Right-Hand Circularly Polarized (RHCP) wave. This duality in polarization characteristics demonstrates the versatility and controllability of GaAs antennas, opening up opportunities for various applications in wireless communication and antenna engineering.

Figure 7.4 presents the simulation current distribution along the loop at circa one wavelength, utilizing LHCP and RHCP at the operating frequency of 44 GHz. In contrast to linear polarization, where the current maintains a constant amplitude throughout the ring's length, circularly polarized waves exhibit dynamic alterations in both strength and orientation as they advance across their wavelength. As the current progresses along the loop, its amplitude undergoes gradual fluctuations, diminishing while adopting a spiral or helical trajectory as it revolves around the propagation direction. This current rotation is responsible for generating the characteristic circular polarization pattern. Figure 7.5 (a, b) shows the outcomes of CST simulations that depict how current flows within a loop antenna when it operates in both LHCP and RHCP modes. These simulations help in understanding the antenna's behavior and performance under different polarization conditions.

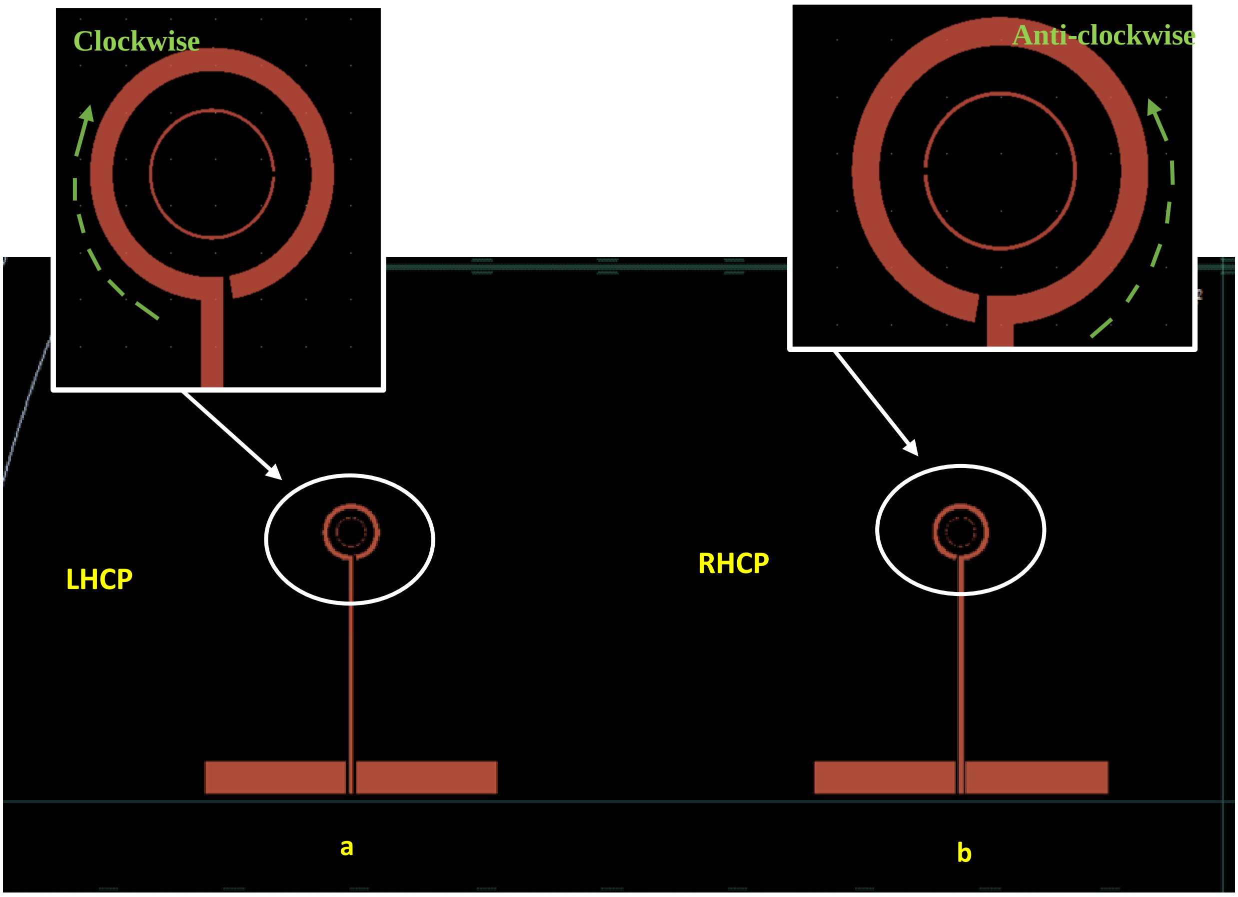

Figure 7.3: The configuration of various polarization modes for a GaAs antenna operating at 44 GHz.

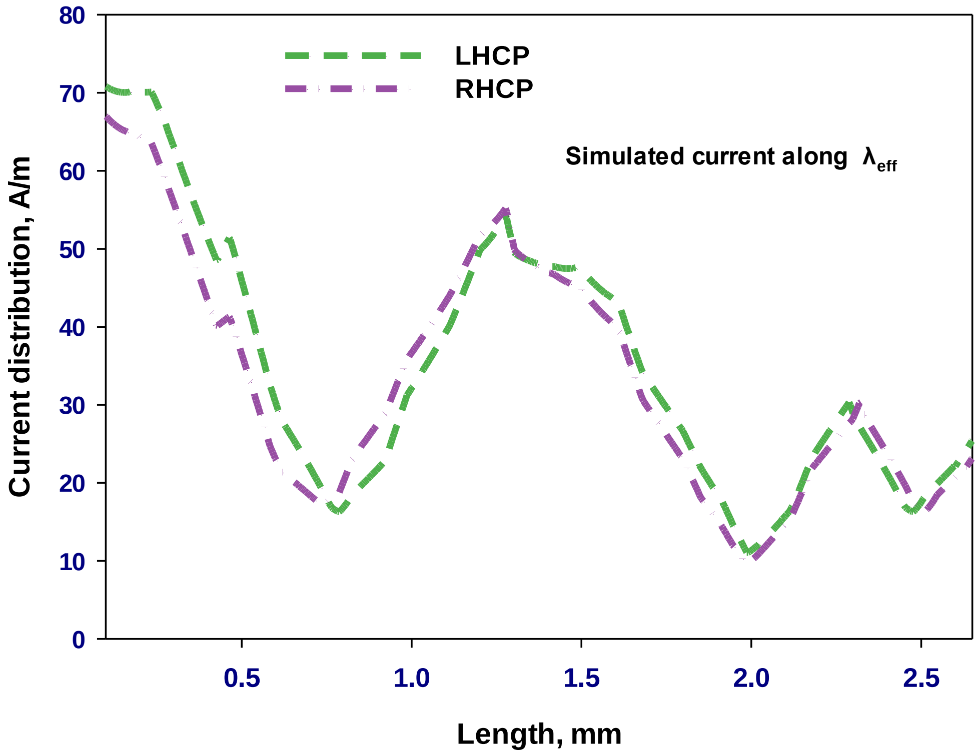

Figure 7.4: depicts the current distribution of a GaAs antenna at 44 GHz, showcasing both LHCP and RHCP.

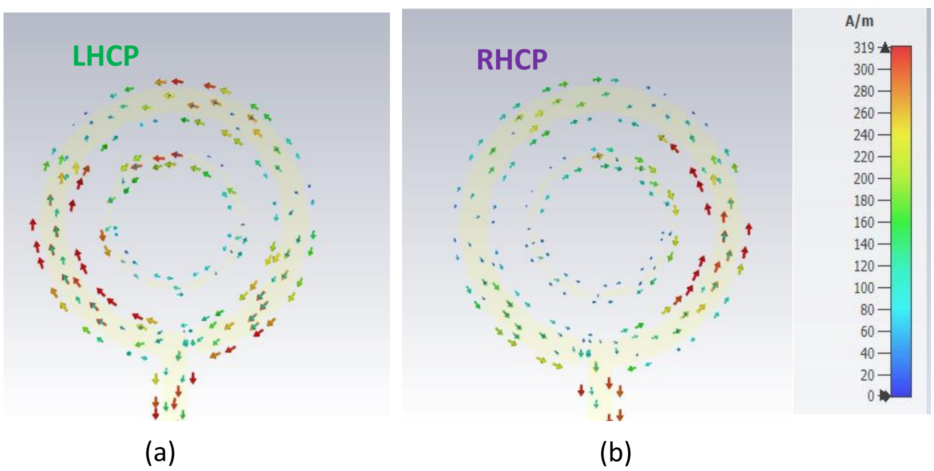

Figure 7.5: Simulated current distribution at 44 GHz, depicting (a) LHCP and (b) RHCP.

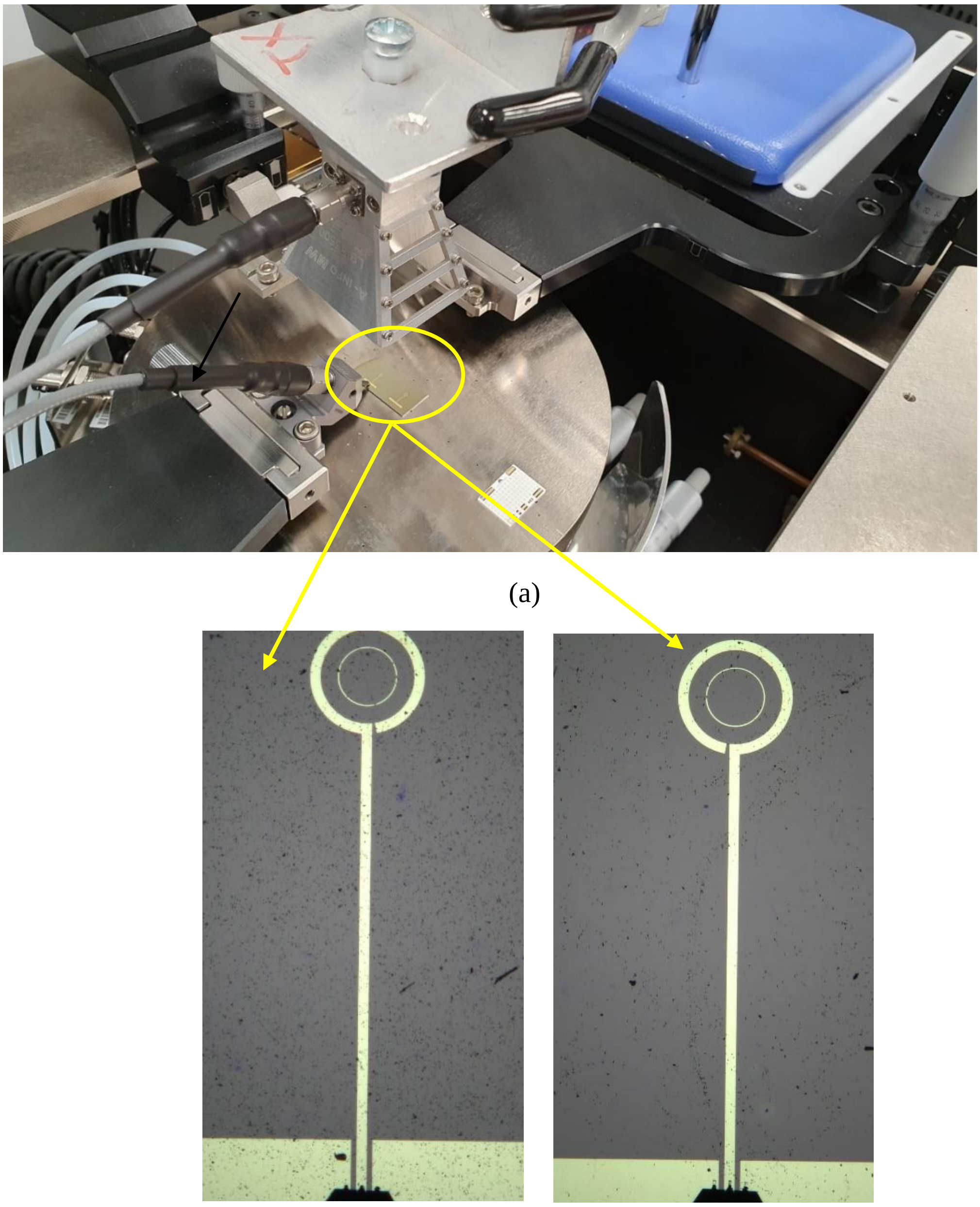

(a)

(b) (c)

Figure 7.6: The fabricated prototype of the on-chip GaAs antenna at 44 GHz (a) Antenna under test, (b) LHCP antenna, and (c) RHCP antennas.

7.5 Assessment of GaAs Antennas through Fabrication and Measurements

To manufacture the antenna, a 350 μm thick substrate is chosen. Thanks to a photolithography process with only one mask for the antenna metallization, we can obtain accurate and small dimensions of the gaps and the transmission lines. A 40/400 nm of Ti/Au is deposited for the antenna metallization and the ground plane. Between the antenna and the substrate, there is a silicon dioxide layer of 1 μm.

Figure 7.6 presents the fabricated prototype of the on-chip GaAs antennas under test for different polarisation LHCP and RHCP operating at 44 GHz.

As depicted in Figure 7.7, there is a notable concurrence between the experimental reflection coefficients and their simulated counterparts. The measured outcomes demonstrate an impedance bandwidth of 3.68% for the LHCP state and a 3.7% bandwidth for the RHCP state. It is worth noting that the simulated S11 bandwidths for both LHCP and RHCP are approximately 3.6%, affirming the consistency between experimental and simulated results.

Figure 7.8 displays the measured and simulated Axial Ratio (AR) for the LHCP and RHCP states, demonstrating an agreement between the measured and simulated AR bandwidths. In evaluating the bandwidth characteristics of CP antennas, the overlapping bandwidth between impedance bandwidth and AR bandwidth is typically considered. When comparing Figures 7.7 and 7.8, it becomes evident that the measured overlapped bandwidth for RHCP and LHCP states is approximately 2.75% and 2.8%, respectively, while the simulation results indicate a bandwidth of around 3.2% for RHCP and 3.4% for LHCP states.

At the same Figure 7.8, the simulated realized gain of the GaAs antenna proposed for operation at 44 GHz is displayed. It is noteworthy that the simulated realized gain is consistent at circa 4.6 dBic for both polarizations, LHCP and RHCP.

Figure 7.9 showcases the normalized radiation patterns at 44 GHz in the E-plane for GaAs antennas, with both LHCP and RHCP polarizations. The presented investigation reveals excellent agreement between the simulation and measurement results at the operating frequency. Notably, the broadside mode exhibits the highest gain in the $\theta = 0°$ direction in both cases, with RHCP and LHCP.

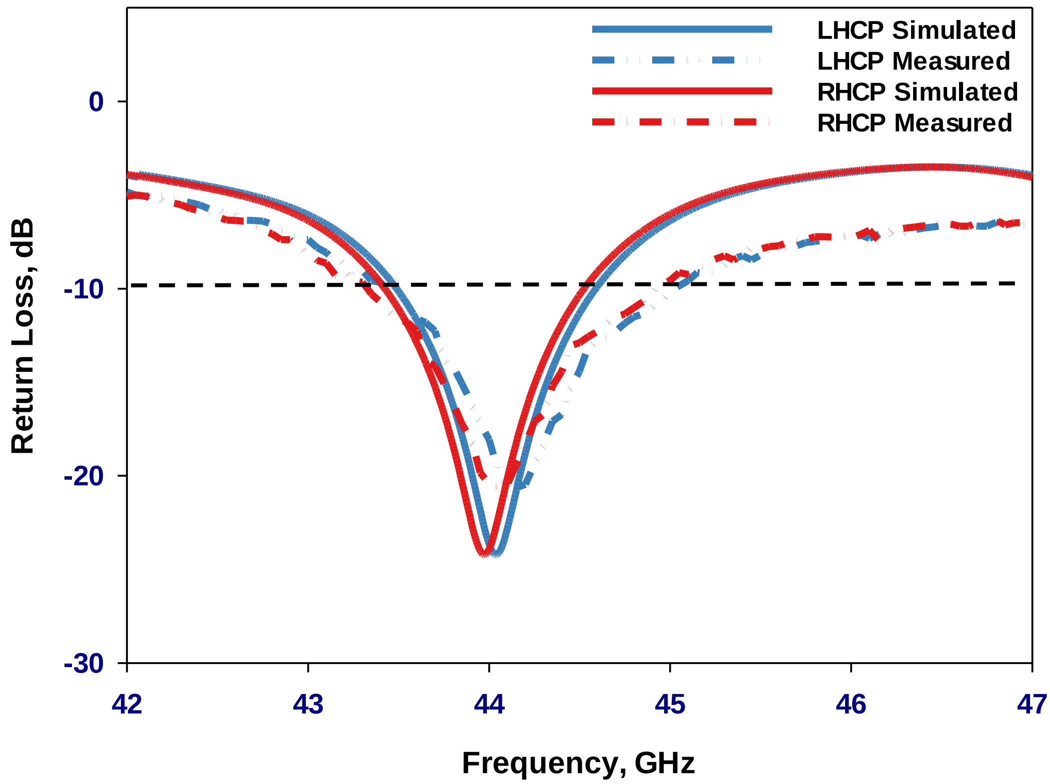

Figure 7.7: Reflection coefficients of the on-chip antenna on GaAs substrate.

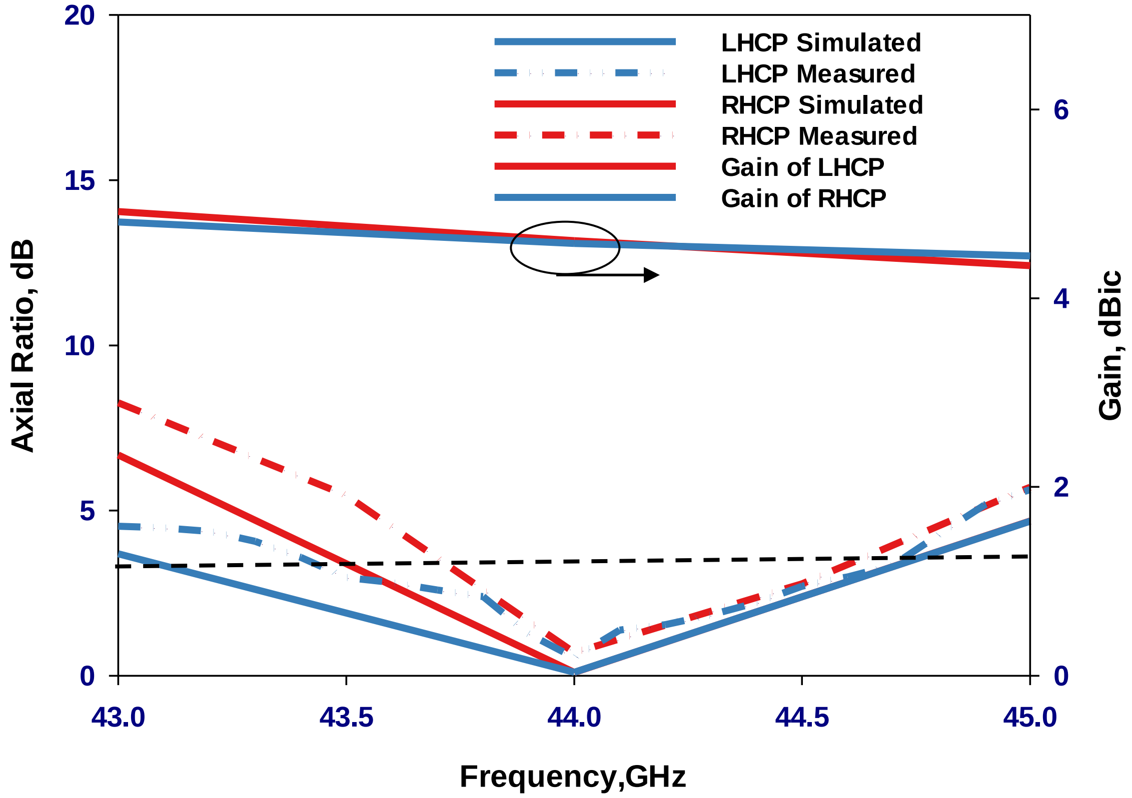

Figure 7.8: Axial ratio and gain for both circular polarization senses in the main beam direction.

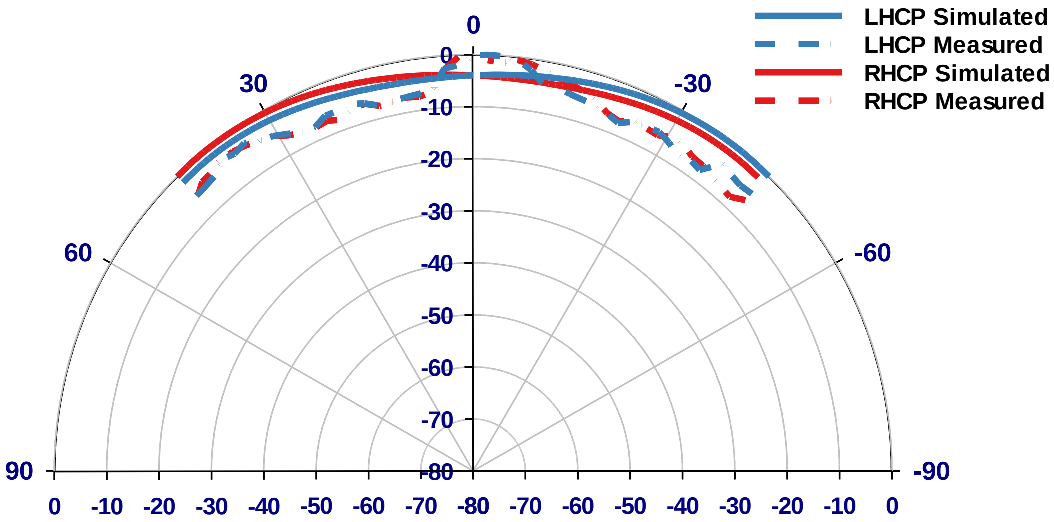

Figure 7.9: Normalized Radiation Patterns for GaAs Antennas at 44 GHz in E-Plane with LHCP and RHCP Polarizations.

7.6 Performances of 4H-SiC Based Antenna

Images of the measurement process are depicted in Figure 7.10 and illustrate the single loop antenna within the testing environment using two substrates GaAs and 4H-SiC.

Figure 7.11 presents a comparison between the measured and simulated return losses for the proposed single element when fabricated on 4H-SiC and GaAs substrates. The results show that the antennas on 4H-SIC and GaAs substrates exhibit measured S_{11} bandwidths of approximately 3.5% and 3.6%, respectively, which agree closely with the simulations. These bandwidths extend over frequency bands of 39.4-40.8 GHz for 4H-SiC-based antenna and 43.35-44.93 GHz for the GaAs-based counterpart, which correspond to respective bandwidths of 3.68% and 2.5% It should be noted that different frequencies bands have been achieved to the different electrical thicknesses of the GaAs and 4H-SiC. Moreover, the physical dimensions of each loop antenna were determined using the effective wavelengths, which are based on the approximation of equation (7.1). It is noteworthy that Figure 7.11 also presents the radiation efficiencies, where it can be observed that for the GaAs-based configuration offers a radiation efficiency of 78%, which is notably lower than that of ~96% for the 4H-SiC-based antenna. This clearly demonstrates the lower dielectric losses of the 4H-SiC substrate, which results in higher radiation efficiency.

Figure 7.12 illustrates the measured and simulated axial ratio as well as the simulated gain of the proposed antenna. The results reveal that the measured AR bandwidth for 4H-SiC and GaAs substrates are 4.75% and 2.8%, respectively. In comparison, the respective simulated AR bandwidths are 4.75% and 3.4% for the 4H-SiC-based and GaAs-based antennas. Additionally, a narrower bandwidth is achieved when a GaAs substrate is utilized, which can be attributed to the higher dielectric constant of this substrate. Furthermore, the simulated single antenna's gains for 4H-SiC and GaAs configurations are ~6.5 dBic and 4.6 dBic, respectively.

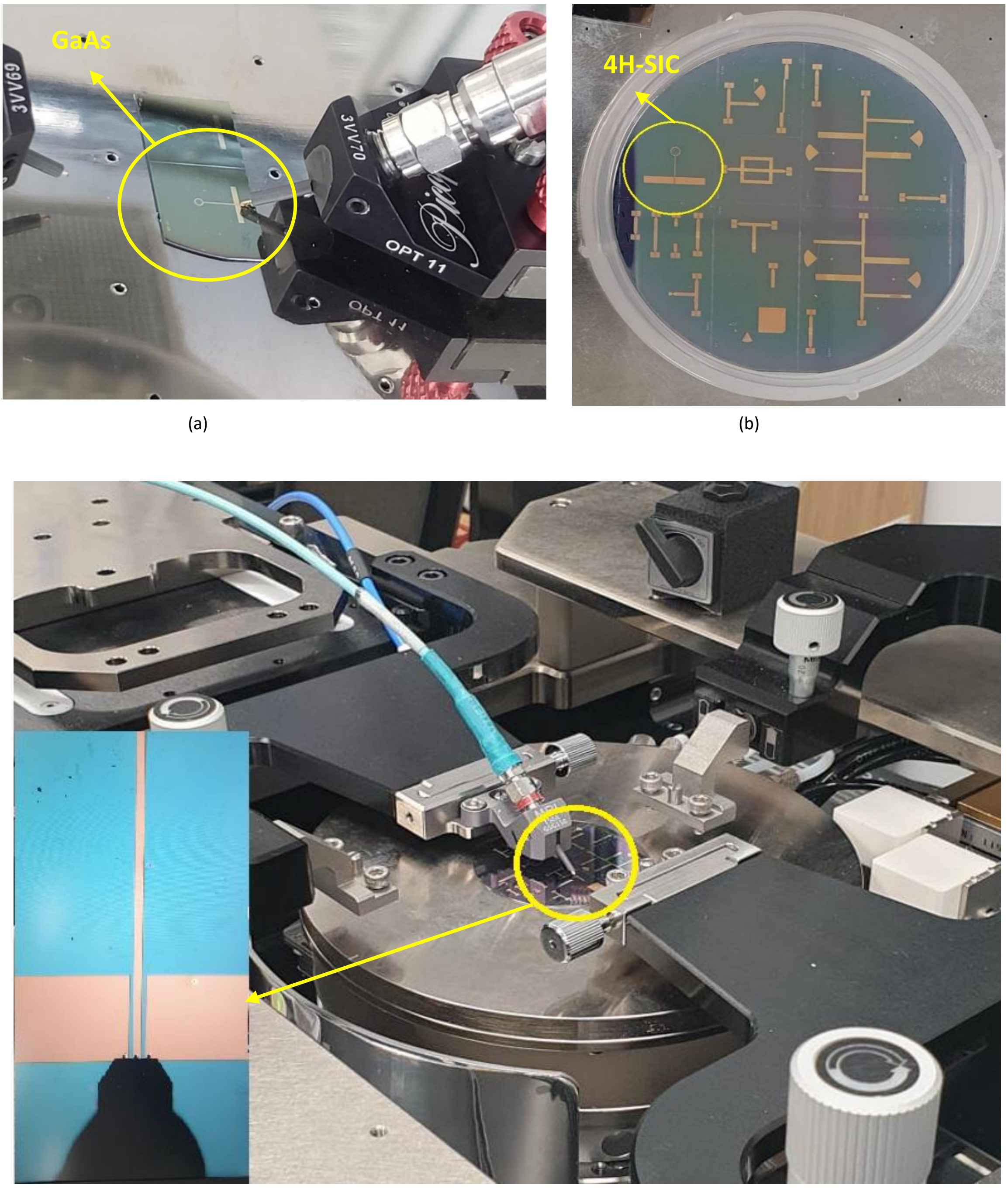

(c)

Figure 7.10: The single loop antenna within the testing environment (a) On GaAs substrate, (b) On 4H-SIC substrate, and (c) antenna under test using an RF wafer probe.

Once more, the highest broadside gain has been achieved by utilizing the 4H-SiC substrate and is in line with the higher radiation efficiency, which is attributed to the lower loss tangent and weaker surface waves created by the substrate with lower permittivity.

Figures 7.13a and 7.13b presents the measured and simulated radiation patterns for the proposed antenna within the principal plane, $\phi = 0°$, at 40 GHz and 44 GHz, corresponding to 4H-SiC and GaAs substrates, respectively. Furthermore, the simulation results reveal the generation of a left-hand circularly polarized wave (LHCP) since E_L is larger than E_R as demonstrated in Figure 7.13(c, d). This observation also signifies that the traveling wave current circulates counterclockwise along the surface of the loop.

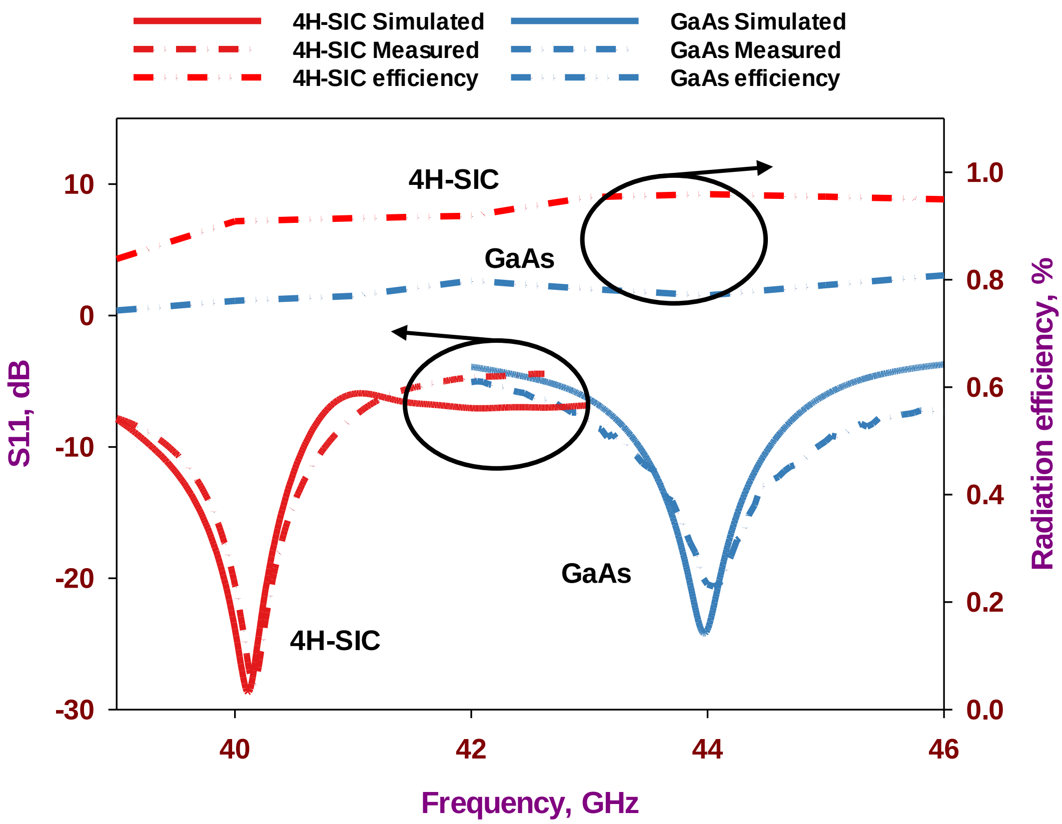

Figure 7.11: Return losses and radiation efficiencies of the two on-chip antenna configurations.

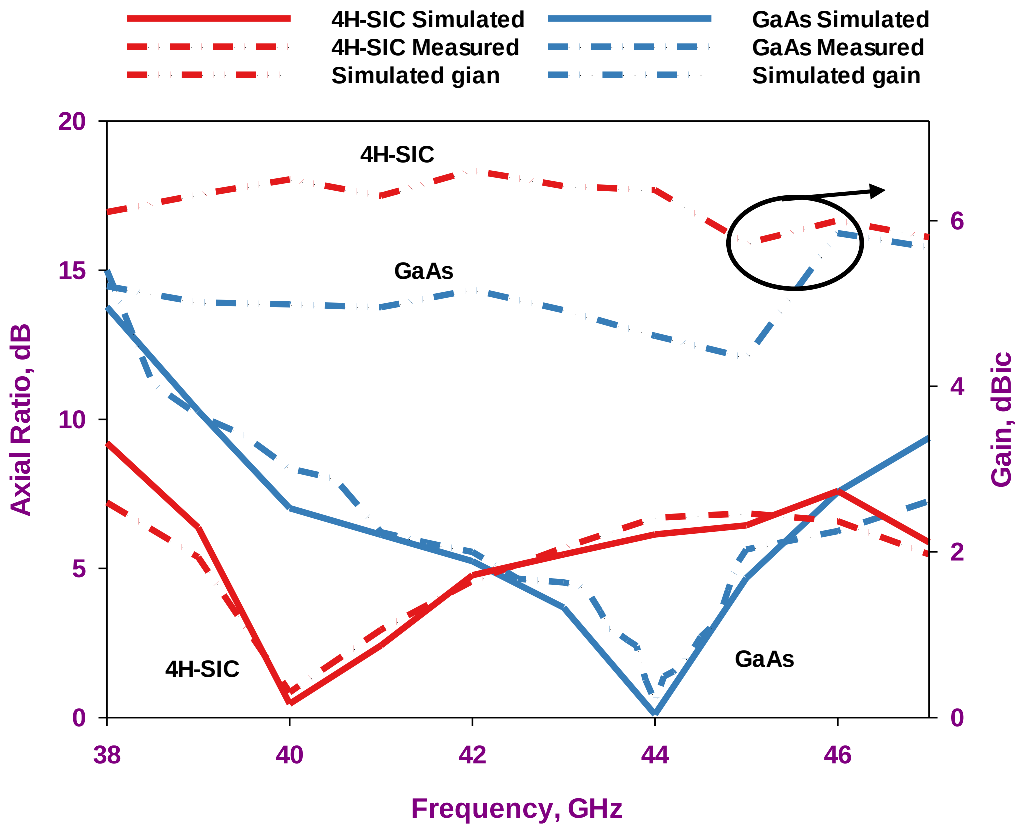

Figure 7.12: Gain and the axial ratio of the two on-chip antenna configurations.

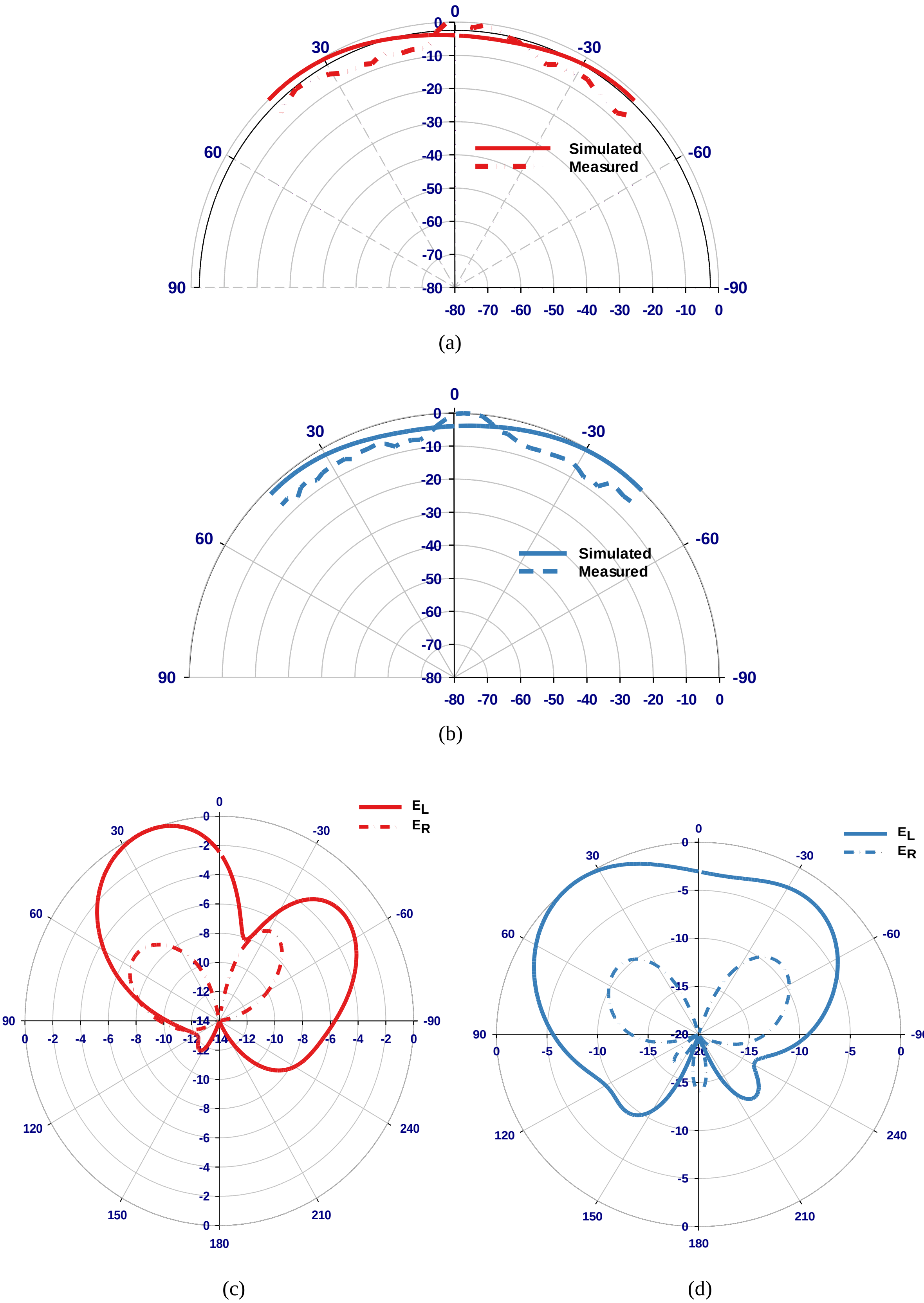

Figure 7.13: Simulated and measured radiation patterns at ϕ=0° for on-chip antennas on two substrates: (a) GaAs, (b) 4H-SiC, (c) simulated EL & ER radiation patterns for the 4H-SiC antenna, and (d) simulated EL & ER radiation patterns for the GaAs antenna.

7.7 Design of A 4-Element Circularly Polarisation Antenna Array using 4H-SiC

Following the successful testing of a single on-chip CP antenna, the investigations have been extended to design a 4-element on-chip antenna array employing the 4H-SiC substrate with dimensions of 10×10mm×35μm. Building upon the performance insights gained from an individual antenna, we proceed to design 1×4 uniform linear antenna arrays with a precise spacing of 1.9 mm between adjacent elements, which is approximately equivalent to $\lambda_o/2$ at 43 GHz.

The antenna spacing is chosen to achieve maximum gain and minimum side lobe levels (SLL). The antenna arrays are fed using uniform-length feeding lines for all elements with a 0.1 mm wide microstrip transmission line as presented in Figure 7.14. This design choice ensures uniform signal amplitudes and phases across all elements, resulting in constructive interference and the formation of a robust main beam directed at θ=0°.

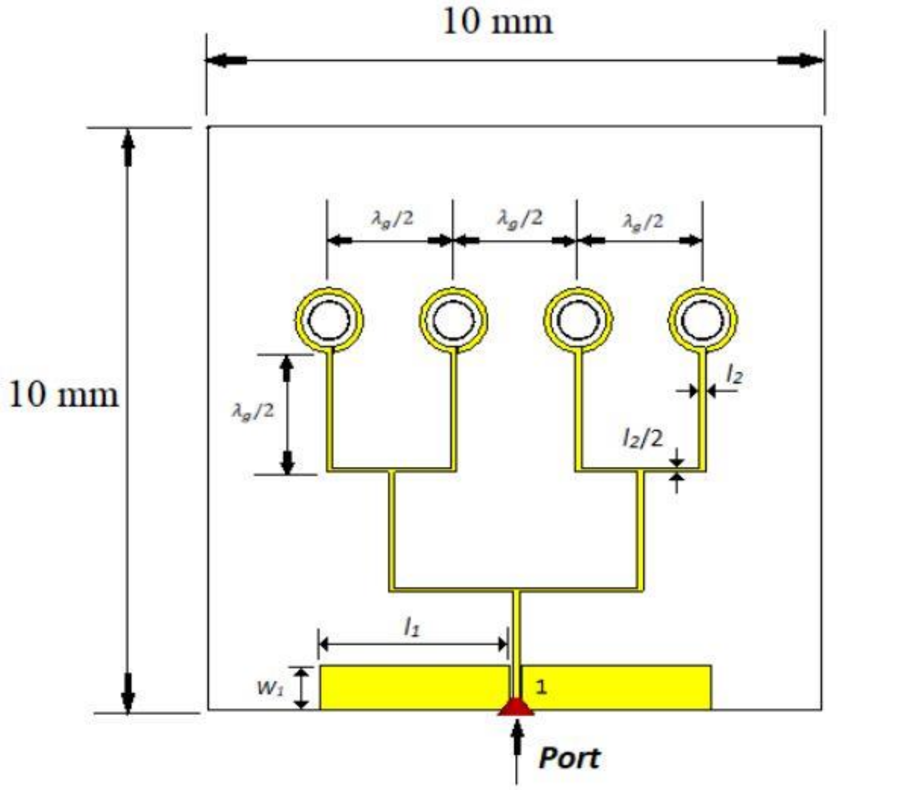

Figure 7.14: The proposed configuration of on-chip antenna array using 4H-SIC substrate.

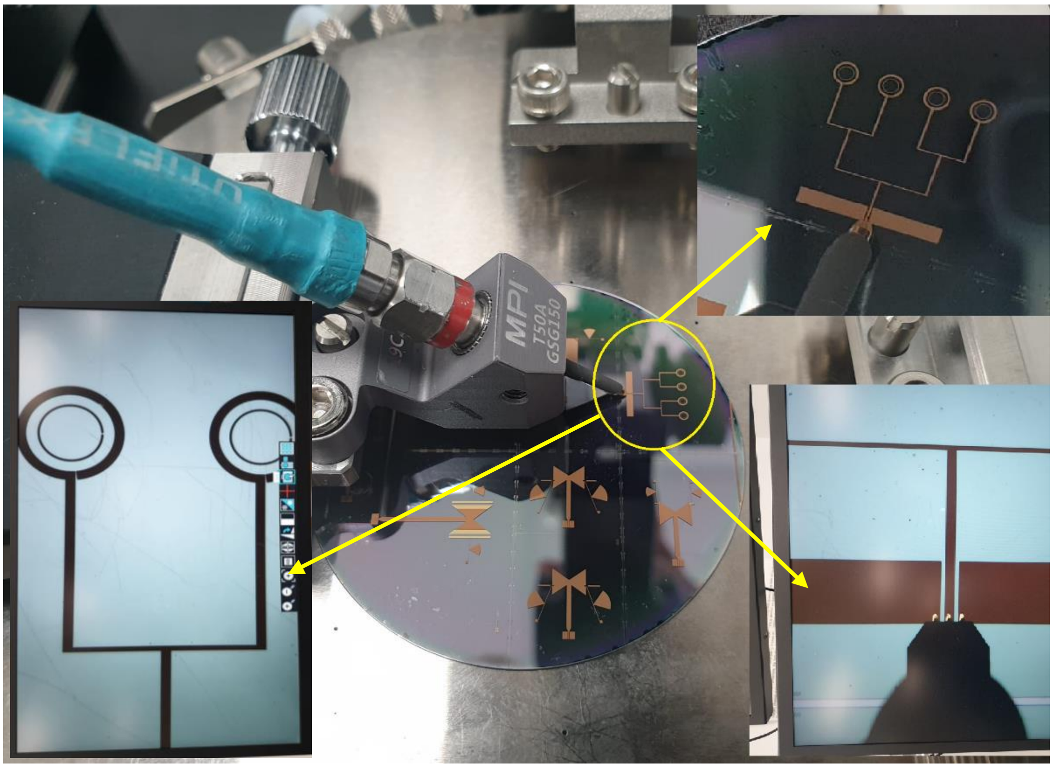

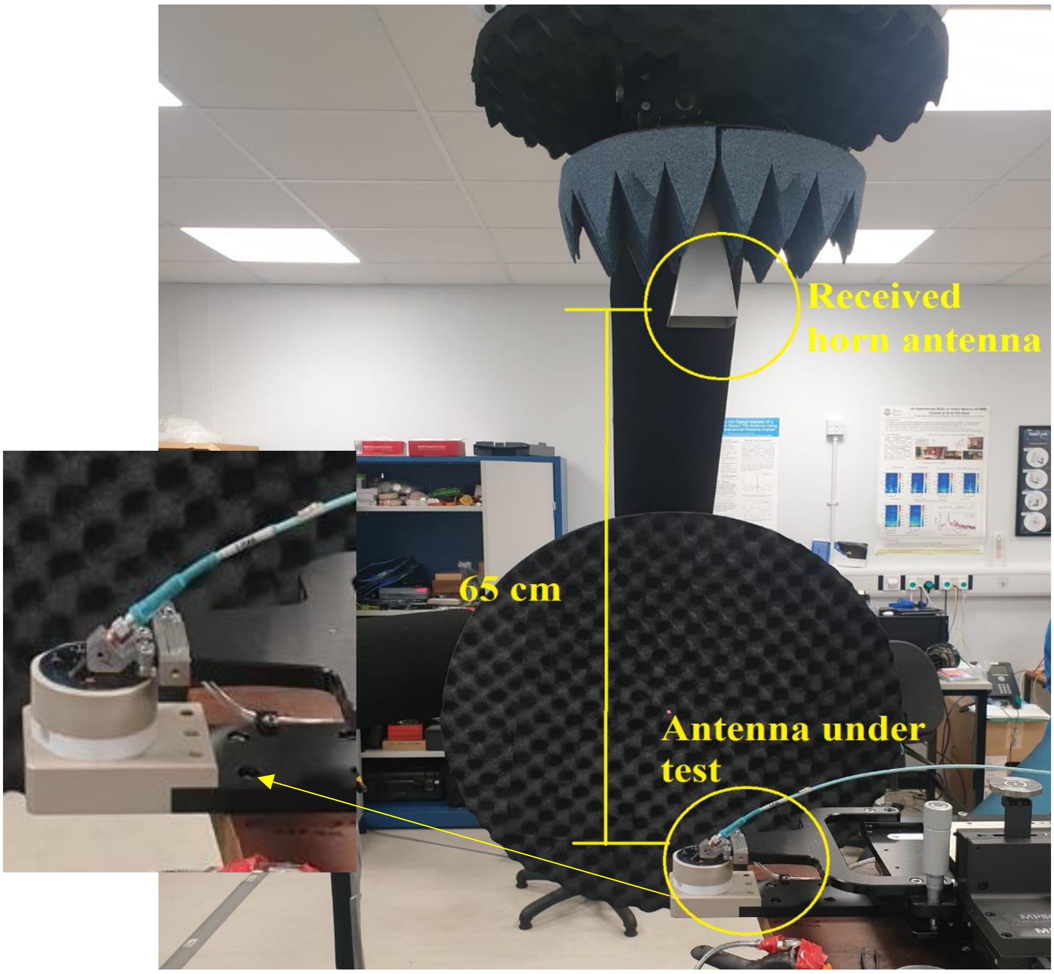

Figure 7.15: Photographs of the array antennas in the spherical measurement lab.

7.8 Fabrication and Measurements of On-Chip Array

Figure 7.15 presents the measurement settings of the Q/V band circularly polarized antenna within the testing environment.

Figure 7.16 presents the simulated and measured return losses as well as the simulated total efficiency of the 4H-SiC antenna array. These results show that the antenna array boasts simulated and measured impedance bandwidths of approximately 4.4% and 4.6%, respectively. The array impedance bandwidth is slightly wider than that of a single antenna due to mutual coupling between elements. Furthermore, total efficiency has reached approximately 92%.

The simulated and measured axial ratio and gain of the proposed arrays are presented in Figure 7.17. The simulated 3dB AR bandwidths are approximately 4%, which is in close agreement with the measured results of 3.9% centered at 43 GHz. In addition, , the achieved simulated gain is 9.7 dBic. It is worth noting that the 4H-SiC array exhibits a 3 dB gain advantage compared to the single element. It is important to emphasize that the relationship between the number of elements and the gain is not strictly linear. The addition of more antenna elements may not yield a commensurate increase in gain, primarily because the radiation pattern may not significantly narrow for each additional element.

Furthermore, another critical consideration for achieving only a marginal 3 dB gain enhancement in the array is the limitation imposed by the constrained ground plane size, which matches that of the single-element antenna. Expanding the ground plane dimensions presents itself as a viable strategy for augmenting antenna gain.

Figure 7.18 depicts the E_L & E_R radiation patterns at both $\phi=0^o$ and $\phi=90^o$ at 43 GHz. Notably, there is close agreement between the measured and simulated results. In this case, the electric field component E_L surpasses E_R in strength, indicating the generation of a left-hand circularly polarized (LHCP) wave. For instance, E_L is greater than E_R by more than 15 dB in the case of broadside radiation.

Table 7.2 presents a comparative analysis between the suggested antenna and prior investigations [141-146]. It is evident from this table that the suggested antenna exhibits superior characteristics, including increased gain, heightened efficiency, and circular polarization utilization in contrast to earlier antenna designs relying on linear polarization (LP).

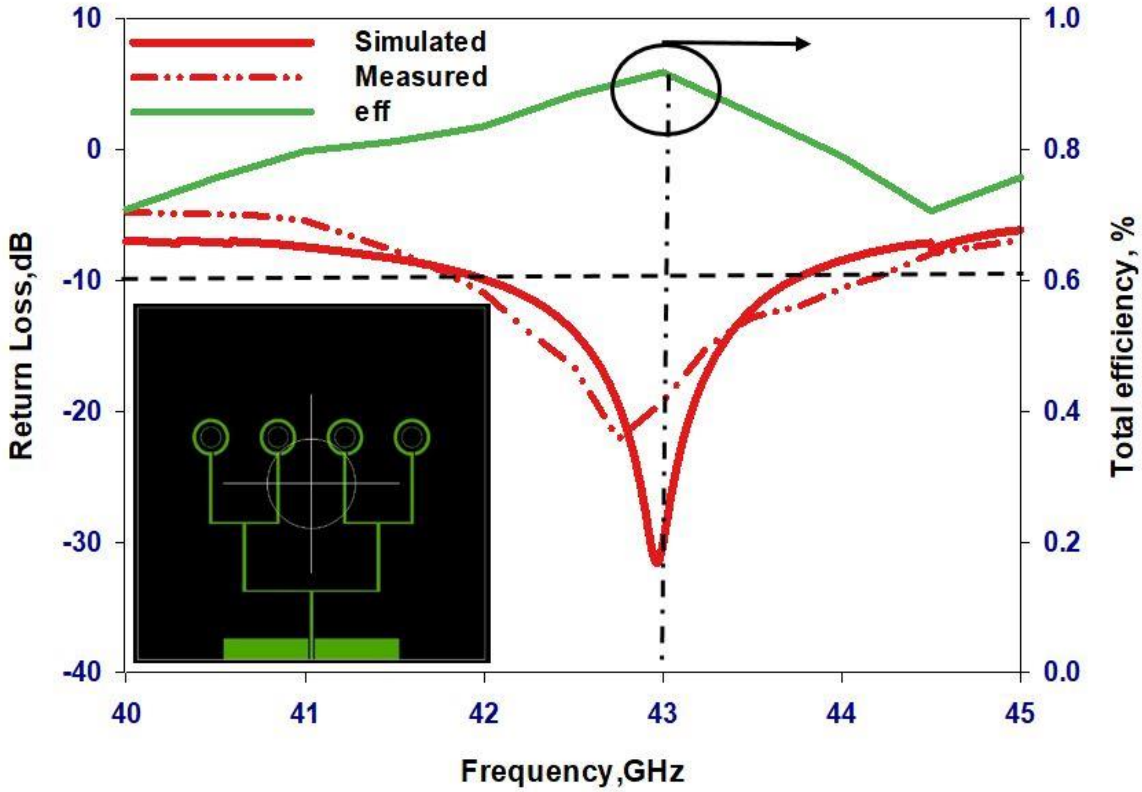

Figure 7.16: Reflection coefficients and total efficiency of the on-chip array using 4H-SIC substrate.

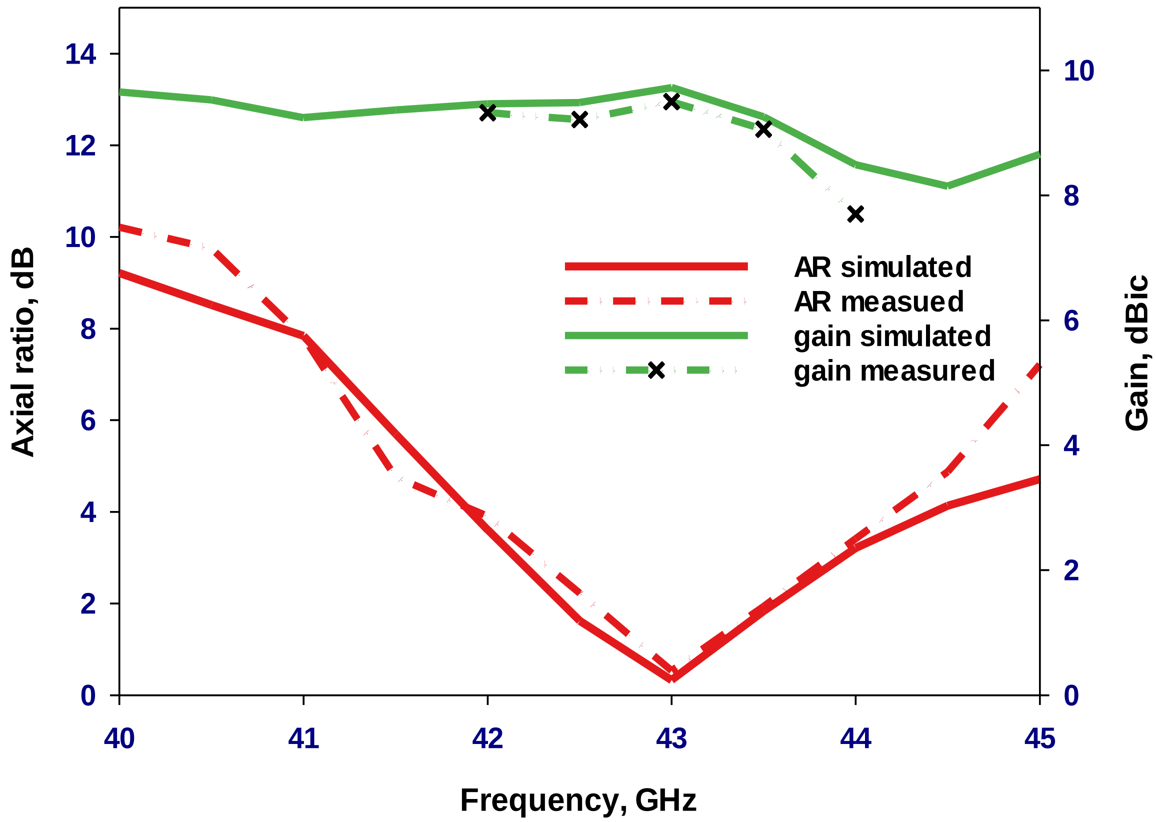

Figure 7.17: Axial ratio and gain of the on-chip array antenna using 4H-SiC substrate.

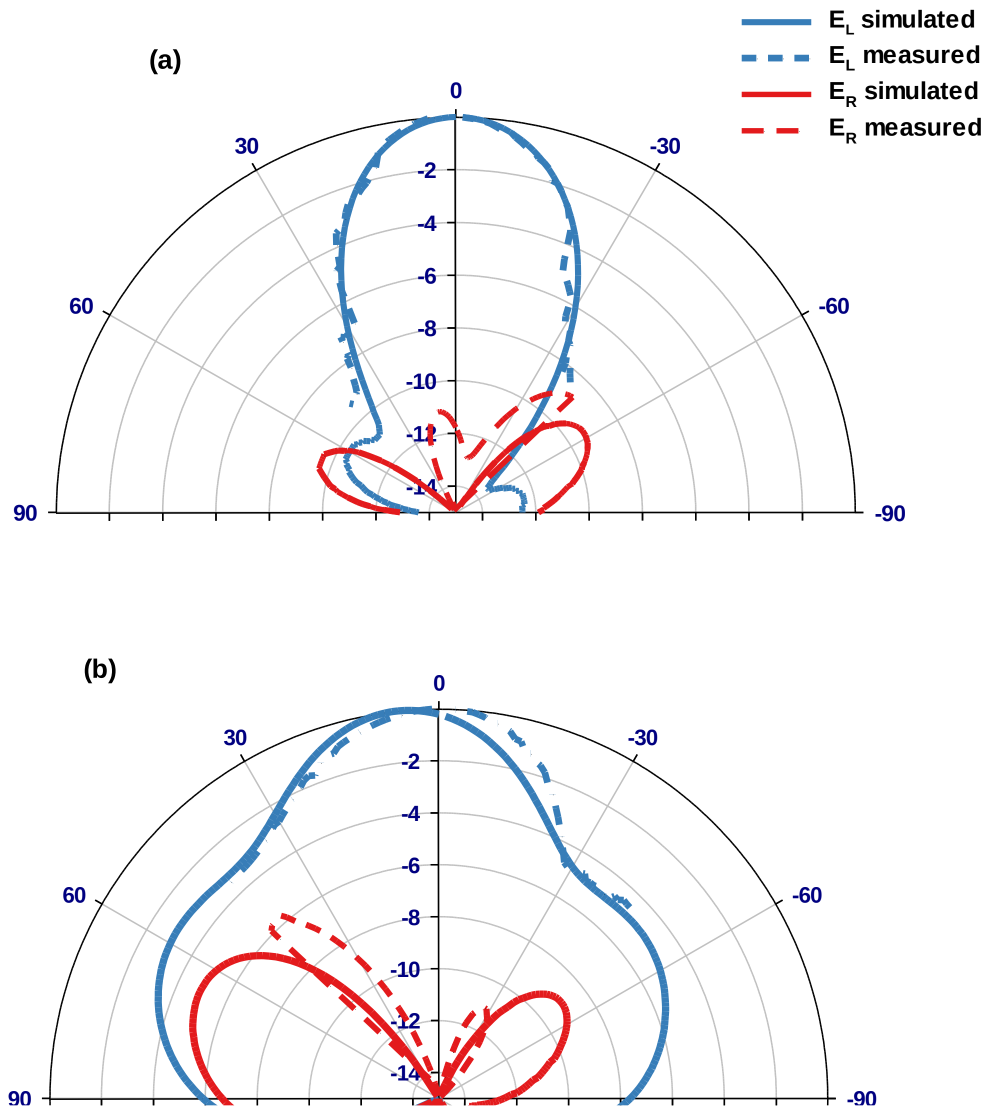

Figure 7.18: The radiation patterns of EL & ER; at ϕ=00, and ϕ=900 for on-chip array printed on 4H-SiC substrate.

Table 7.2 Performance Comparison of the V-band on-chip Antenna Designs

Ref.	Type of Antenna	Number of elements	Substrate	Operating Frequency GHz	S_{11} bandwidth	Polarisation	AR Bandwidth	Peak gain	Efficiency
[135]	Vertical-Type wire loop antenna	1	Silicon	50	⸙8%	LP	**	-2 dBi	24%
[136]	Loop Slot dipole	1	Silicon	70	⸙ ~ 8.5%	LP	**	3.7dBi, 3.8dBi 3.9 dBi	79% 83% 82%
[137]	Slot	1	Silicon	60	**	LP	**	-2.1 dBi	**
[138]	Dipole based	1	GaAs	61	⸙11.6%	LP	**	3.6 dBi	**
[139]	Patch	1	GaAs	57, 59	**	LP	**	-1.5 dBi, ~1dBi	33%,21%
[140]	Log periodic	1	GaAs	94	12.5%	LP	**	4.8dBic	**
This work	Open-Loop	1	GaAs	44	3.6%	CP	3.4%	4.6 dBic	78%
This work	Open-Loop	1	4H-SiC	40	3.5%	CP	4.75%	6.5 dBic	95%
This work	Open-Loop	1×4	4H-SiC	43	4.6%	CP	4%	9.7 dBic	92%

** The values were not supplied.
⸙ The exact values were not supplied, and the data were obtained by extrapolating the given information.

6.9 Summary

It is well-known that the performance of the on-chip loop antennas operating at high frequencies can deteriorate owing to dielectric and surface wave losses. Consequently, the selection of an appropriate substrate with the right dielectric constant and loss tangent plays a crucial role in achieving optimal antenna performance. In a comparative study, two different dielectric substrates have been utilized for a CP circular loop antenna operating within the Q/V frequency band. The potential of designing and fabricating an on-chip mmWave antenna on a 4H-SiC has been demonstrated for the first time. The results demonstrate that an on-chip antenna fabricated on a 4H-SiC substrate, with lower dielectric constant and loss tangent, offers the highest gain, reaching 6.5 dBic, and a high efficiency of circa 95% for the single antenna configuration. As a result, a CP array antenna employing a 4H-SiC substrate in the Q/V band was successfully fabricated and measured. The results are highly promising, with the on-chip antenna array exhibiting an impressive gain of approximately 9.7 dBic combined with a commendable efficiency of 92%. Furthermore, the antenna array achieves left-hand circular polarization and offers an axial ratio bandwidth of circa 4%. The achieved results demonstrate an excellent agreement between simulations and measurements. Besides, the results also indicate that particularly good impedance matching is achieved.

Chapter 8

Conclusion and Future Work

8.1 Conclusion of the Thesis

In today's era, wireless communications are essential, seamlessly integrating with daily life where connectivity, internet access, audio-visual communication, and data transfer have become indispensable. The antenna, situated at the core of any communication system, serves as a vital frontier element, facilitating the transceiving of communication signals through electromagnetic radiation. Traditionally, antenna design focuses on optimizing performance for fixed frequency, radiation, and polarization characteristics. However, with the surge in engagement with man-machine devices over the last few decades, the concept of antenna design, particularly array antennas, has undergone significant transformation.

Phased array technology emerges as a key player in this evolutionary shift, presenting advantages like precise beamforming, adaptive steering, and interference mitigation. This technology adeptly addresses modern wireless communication systems' dynamic needs and challenges. However, as environments change and the demand for adaptability in frequency, radiation pattern, and polarization becomes crucial for efficient communication, the limitations of fixed-performance antennas become apparent.

In response, the antenna reconfiguration concept has gained prominence, opening doors to new possibilities. The adoption of reconfigurable phased array technology in wireless communication is a strategic move that significantly enhances reliability, efficiency, and adaptability. This evolution aligns with and effectively meets the constantly evolving demands of contemporary communication systems. This study addressed a number of the needs mentioned above with the main contributions summarised as below.

Initially, the development of a wideband CP circular loop antenna in the 6 GHz band demonstrated remarkable achievements, with an augmented AR bandwidth exceeding 33%. The integration of a parasitic loop played a pivotal role in expanding the AR bandwidth, resulting in left-hand circular polarization radiation. The antenna's structural simplicity, flexibility in the CP sense, and the utilization of coplanar waveguide (CWP) feeding position it as a promising candidate for diverse wireless communication applications, especially at mmWave frequencies. Hence, it becomes imperative to progress to the next phase in designing the antenna at mmWave frequencies for 5G and B5G communication systems.

A cost-effective, low-profile, single-loop circularly polarized antenna is designed and fabricated to validate the earlier work, but at the mmWave frequency range. The subsequent investigation introduced a 4-elements phased array of circular loop antennas designed for CP radiation. By manipulating the lengths of the transmission line phase shifters, efficient beam steering within ±25^{o} was achieved, demonstrating LHCP radiation at 27.5 GHz with a peak gain of approximately 11 dBic and a radiation efficiency exceeding 85%. The simplicity and cost-effectiveness of the proposed phased array configuration were highlighted, making it an attractive option for practical implementations in satellite and wireless communication systems. Therefore, it becomes feasible to undertake the development of this design further to address the challenge of developing the first multifunctional reconfigurable array antenna that operates in the millimetre-wave frequency range.

As a first step in meeting this challenge, the thesis introduced a novel approach for a mmWave antenna with hybrid reconfigurability, utilizing planar biasing feeding networks. The design achieved control over polarization, enabling seamless transitions between LHCP and

RHCP senses, along with reconfigurable bandwidth in the case of linear polarisation. The optimised design, featuring strategically aligned PIN diodes and a coplanar strip line integrated with photonic bandgap sections, exhibited enhanced radiation efficiency. The proposed antenna introduced good results in terms of CP bandwidth, gain, and efficiency, while also showcasing the capability of bandwidth reconfigurability for linear polarisation.

A multifunctional reconfigurable mmWave array, capable of modifying both its polarization and pattern, has been designed and fabricated, marking a significant advancement in antenna technology. This is based on utilising the polarisation reconfigurable antennas in combination with a pattern reconfigurability that has been achieved through an enhanced design of the feed network. The use of 16 PIN diodes as flexible switches and their strategic placement within the loops and phase shifter gaps allowed precise control over polarisation and beam steering. The comprehensive approach using coplanar stripline lines demonstrated the adaptability and versatility of the mmWave array, making a substantial contribution to the field of reconfigurable antenna technology. The design successfully achieved polarization control, enabling smooth transitions between LHCP and RHCP, as well as achieving reconfigurable frequency in the case of linear polarisation. Additionally, the design demonstrated efficient beam steering within a range of ±25 degrees. It total, the multifunctional reconfigurable array offers six operation modes in the form of three polarisation states at each of the two main beam directions.

Finally, in a comparative investigation, two distinct dielectric substrates (GaAs and 4H-SIC) were employed for a circularly polarised loop antenna designed to operate within the Q/V frequency band. Notably, this study marks the first instance of designing and fabricating an on-chip millimeter-wave antenna on a 4H-SiC substrate. The results demonstrate that an on-chip antenna fabricated on a 4H-SiC substrate, characterized by lower dielectric constant and loss tangent, exhibits the highest gain at 6.5 dBic and an impressive efficiency of approximately

95.5% in the single antenna configuration compared to GaAs substrate. Consequently, a CP array antenna, utilising a 4H-SiC substrate in the Q/V band, was successfully manufactured and assessed. The outcomes are promising, as the on-chip antenna array showcases a notable gain of around 9.7 dBic coupled with commendable efficiency at 92%. Moreover, the antenna array achieves left-hand circular polarisation and provides an axial ratio bandwidth of about 4%. Therefore, the attained outcomes pave the path for further advancements in the fabrication of on-chip antennas, particularly in the context of emerging technologies like 6G.

8.2 Future Work

While this thesis has explored various aspects of phased array antennas, hybrid and multifunctional reconfigurable antennas, and on-chip antennas, introducing novel designs, there are still avenues to be further explored and continued in this line of research. The ongoing exploration of this research domain presents promising opportunities. Some suggested areas for further investigation include:

Exploring the potential of achieving beam steering in two planes using a square array. Typically, a phased array enables beam steering in a singular plane, such as $\phi=0°$ or $\phi=90°$, contingent upon the array axis. The inquiry arises as to whether employing a square array configuration could extend this capability to facilitate beam steering in two distinct planes. This investigation is crucial for advancing our understanding of phased array systems and unlocking additional dimensions of control over beam steering mechanisms.

In addition, the fabrication and testing of an on-chip multifunctional reconfigurable array represents another timely topic that need to be explored further. The primary objective is to increase the number of elements within the array, specifically catering to 60 GHz communication systems. This proposed array will incorporate diodes and switches, all fabricated on the same chip. The rationale behind this integration is to mitigate the challenges associated with the manual connection of diodes and switches, a task particularly demanding at the 60 GHz frequency range. The envisioned research aims to streamline the integration process, enhance efficiency, and contribute to the development of more practical and seamless 60 GHz communication systems.

Although it's improbable to decrease the number of PIN diodes per element, there is a potential avenue for optimisation in the feed network. It might be feasible to minimize the number of PIN diodes in the feed network while still achieving the necessary phase shift. One approach to accomplish this is through the utilisation of digital techniques, allowing for the adjustment of progressive phase shifts between elements. For instance, employing 4 bits could provide us with 16 possible phases, offering a means to achieve the desired adjustments in a more streamlined manner. Furthermore, another possible direction is to use a pixel substrate to steer the beam, which has been explored in many studies already. However, it would be most suitable to have such substrate in the same plane as the antenna to reduce the complexity and have a fully planar structure. However, it is expected that more PIN diodes may be needed to achieve a wider beam steering range, which will impact the radiation efficiency However, both of these suggestions are associated with overheads such as the digital control unit in the first approach and the need for optimisation algorithm in the second suggestion to decide on which diodes need to be ON for a given beam direction. In addition, a more sophisticated switching mechanism is needed.

References

[1] Niu, Y., Li, Y., Jin, D., Su, L. and Vasilakos, A., 2015. “A survey of millimeter wave communications (mmWave) for 5G: opportunities and challenges. ” Wireless Networks, 21(8), pp.2657-2676.

[2] Singh, S. and Chawla, M., 2017. “A Review on Millimeter Wave Communication and Effects on 5G Systems. ” IARJSET, 4(7), pp.28-33.

[3] Ghosh, S. and Sen, D., 2019. “An Inclusive Survey on Array Antenna Design for Millimeter-Wave Communications. ” IEEE Communications Magazine, 7, pp.83137-83161.

[4] X. Wang et al., “Millimeter Wave Communication: A Comprehensive Survey, ” IEEE Communications Surveys & Tutorials, vol. 20, no. 3, pp. 1616-1653, thirdquarter 2018, doi: 10.1109/COMST.2018.2844322.

[5] M. M. Abdin, W. Joel, D. Johnson and T. M. Weller, “A system and technology perspective on future 5G mm-wave communication systems, ” 2017 IEEE 18th Wireless and Microwave Technology Conference (WAMICON), Cocoa Beach, FL, 2017, pp. 1-6, doi: 10.1109/WAMICON.2017.8023879.

[6] S. Hur, T. Kim, D. J. Love, J. V. Krogmeier, T. A. Thomas and A. Ghosh, “Millimeter Wave Beamforming for Wireless Backhaul and Access in Small Cell Networks, ” IEEE Transactions on Communications, vol. 61, no. 10, pp. 4391-4403, October 2013, doi: 10.1109/TCOMM.2013.090513.120848.

[7] Wang, J., Weitzen, J., Bayat, O., Sevindik, V. and Li, M., 2019. “Interference coordination for millimeter wave communications in 5G networks for performance optimization. EURASIP Journal on Wireless Communications and Networking, 2019(1).

[8] Reil, M. and Lloyd, G., 2016. “Millimeter-Wave Beamforming: Antenna Array Design Choices & Characterization.” [online] Cdn.rohde-schwarz.com. Available at: <https://cdn.rohde-schwarz.com/pws/dl_downloads/dl_application/application_notes/1ma276/1MA276_2e_Beamform_mmW_AntArr.pdf> [Accessed 27 July 2020].

[9] A. Shaikh and M. J. Kaur, “Comprehensive Survey of Massive MIMO for 5G Communications, ” 2019 Advances in Science and Engineering Technology International Conferences (ASET), Dubai, United Arab Emirates, 2019, pp. 1-5, doi: 10.1109/ICASET.2019.8714426.

[10] Zhang, J., Ge, X., Li, Q., Guizani, M. and Zhang, Y., 2017. “5G Millimeter-Wave Antenna Array: Design and Challenges. ” IEEE Wireless Communications, 24(2), pp.106-112.

[11] G. Misra, A. Agarwal, S. Misra and K. Agarwal, “Device to device millimeter wave communication in 5G wireless cellular networks (A next generation promising wireless cellular technology), ” 2016 International Conference on Signal Processing, Communication, Power and Embedded System (SCOPES), Paralakhemundi, 2016, pp. 89-93, doi: 10.1109/SCOPES.2016.7955587.

[12] S. Hur, T. Kim, D. J. Love, J. V. Krogmeier, T. A. Thomas and A. Ghosh, “Millimeter Wave Beamforming for Wireless Backhaul and Access in Small Cell Networks, ” IEEE Transactions on Communications, vol. 61, no. 10, pp. 4391-4403, October 2013, doi: 10.1109/TCOMM.2013.090513.120848

[13] Naqvi, A. and Lim, S., 2018. “Review of Recent Phased Arrays for Millimeter-Wave Wireless Communication. Sensors, ” 18(10), p.3194.

[14] Zhang, Y., Pang, L., Liang, X., Liu, X., Chen, R. and Li, J., 2014. Propagation characteristics of circularly and linearly polarized electromagnetic waves in urban macrocell scenario. IEEE Transactions on Vehicular Technology, 64(1), pp.209-222.

[15] Abdul Matin, M., 2017. “Modern Antenna Systems ” 1st ed. North South University, Bangladesh: InTech, pp.130-143.

[16] Bevelacqua, P., 2015. “Wave Polarization and Antenna Polarization ”. [online] Antenna-theory.com. Available at: <http://www.antenna-theory.com/basics/polarization.php> [Accessed 28 July 2020].

[17] RongLin Li, G. DeJean, J. Laskar and M. M. Tentzeris, “Investigation of circularly polarized loop antennas with a parasitic element for bandwidth enhancement, ” IEEE Transactions on Antennas and Propagation, vol. 53, no. 12, pp. 3930-3939, Dec. 2005, doi: 10.1109/TAP.2005.859917.

[18] Sahal, M., & Tiwari, V. N. (2016). “Review of circular polarization techniques for design of microstrip patch antenna ”. In Proceedings of the international conference on recent cognizance in wireless communication & image processing: ICRCWIP-2014, New Delhi, India (pp. 663–669).

[19] Chaudhary, R.K.; Kumar, R.; Chowdhury, R. Circularly Polarized Dielectric Resonator Antennas; Artech House: Norwood, MA, USA, 2021. [Google Scholar]

[20] Balanis, C., 2005. “Antenna Theory (ANALYSIS AND DESIGN). ” 3rd ed. Hoboken, New Jersey, pp.231-371.

[21] McKinley, A., 2018. “The Analytical Foundations of Loop Antennas And Nano-Scaled Rings. ” 1st ed. London: Springer Nature Singapore, pp.107-119.

[22] Edwards, T.C. and Steer, M.B. (2016) Foundations for Microstrip Circuit Design. Chichester, West Sussex, United Kingdom: John Wiley & Sons Inc.

[23] IEEE Standard for Definitions of Terms for Antennas: IEEE Std 145-2013 (Revision of IEEE Std 145-1993), IEEE Standard, 2014.

[24] J. T. Bernhard, "Reconfigurable Antennas," Synthesis Lectures on Antennas, vol. 2, no. 1, pp. 1-66, 2007.

[25] R. L. Haupt and M. Lanagan, "Reconfigurable antennas," IEEE Antennas and Propagation Magazine, vol. 55, no. 1, pp. 49-61, 2013.

[26] N. Haider, D. Caratelli, and A. G. Yarovoy, "Recent Developments in Reconfigurable and Multiband Antenna Technology," International Journal of Antennas and Propagation, Art. no. 869170, vol. 2013, pp. 1-14, 2013.

[27] J. Costantine, Y. Tawk, S. E. Barbin, and C. G. Christodoulou, "Reconfigurable antennas: Design and applications," Proceedings of the IEEE, vol. 103, no. 3, pp. 424-437, 2015.

[28] C. G. Christodoulou, Y. Tawk, S. A. Lane, and S. R. Erwin, "Reconfigurable antennas for wireless and space applications," Proceedings of the IEEE, vol. 100, no. 7, pp. 2250-2261, 2012.

[29] B. Y. Toh, R. Cahill, and V. F. Fusco, "Understanding and measuring circular polarization," IEEE Transactions on Education, vol. 46, pp. 313-318, 2003.

[30] S. Gregson, J. McCormick, and C. Parini, Principles of planar near-field antenna measurements vol. 53: IET, 2007.

[31] Gao, S., Luo, Q. and Zhu, F., 2014. “Circularly Polarized Antennas. ” 1st ed. Chennai, India, pp.1-28.

[32] RongLin Li, G. DeJean, J. Laskar and M. M. Tentzeris, "Investigation of circularly polarized loop antennas with a parasitic element for bandwidth enhancement," in IEEE Transactions on Antennas and Propagation, vol. 53, no. 12, pp. 3930-3939, Dec. 2005, doi: 10.1109/TAP.2005.859917.

[33] A. Hassan, F. Elhefnawi, A. Z. Elsherbeni, M. Hendi and S. Elramly, “Compact dual circularly-polarized microstrip antennas, ” 2010 IEEE Antennas and Propagation Society International Symposium, Toronto, ON, 2010, pp. 1-4, doi: 10.1109/APS.2010.5560927.

[34] Rong-Lin Li, Fusco, V. and Nakano, H., 2003. “Circularly polarized open-loop antenna”. IEEE Transactions on Antennas and Propagation, 51(9), pp.2475-2477.

[35] R. L. Li, J. Laskar and M. M. Tentzeris, “Wideband probe-fed circularly polarised circular loop antenna ”. IEEE in Electronics Letters, vol. 41, no. 18, pp. 997-999, 1 Sept. 2005, doi: 10.1049/el:20052315.

[36] Zhang, L., Gao, S., Luo, Q., Young, P. and Li, Q., 2017. “Wideband Loop Antenna with Electronically Switchable Circular Polarization. ” IEEE Antennas and Wireless Propagation Letters, 16, pp.242-245.

[37] RongLin Li, G. DeJean, J. Laskar and M. M. Tentzeris, “Investigation of circularly polarized loop antennas with a parasitic element for bandwidth enhancement, ” IEEE Transactions on Antennas and Propagation, vol. 53, no. 12, pp. 3930-3939, Dec. 2005, doi: 10.1109/TAP.2005.859917.

[38] Sahal, M., & Tiwari, V. N. (2016). “Review of circular polarization techniques for design of microstrip patch antenna ”. In Proceedings of the international conference on recent cognizance in wireless communication & image processing: ICRCWIP-2014, New Delhi, India (pp. 663–669).

[39] Y. Ojiro, T. Hiraguri and K. Hirasawa, "A monopole-fed circularly polarized loop antenna," IEEE Antennas and Propagation Society International Symposium. 1998 Digest. Antennas: Gateways to the Global Network. Held in conjunction with: USNC/URSI National Radio Science Meeting (Cat. No.98CH36, Atlanta, GA, USA, 1998, pp. 810-813 vol.2, doi: 10.1109/APS.1998.702062.

[40] Nakano, H., Yoshida, H., and Wu, Y.: ‘C-figured loop antennas’, Electron. Lett., 1995, 31, (9), pp. 693–694

[41] M. Alsabah et al., "6G wireless communications networks: a comprehensive survey," IEEE Access, vol. 9, pp. 148191-148243, 2021, doi: 10.1109/ACCESS.2021.3124812.

[42] X. Wang, L. Kong, F. Kong, F. Qiu, M. Xia, S. Arnon, and G. Chen, ‘‘Millimeter wave communication: A comprehensive survey,’’ IEEE Commun. Surveys Tuts., vol. 20, no. 3, pp. 1616–1653, 3rd Quart., 2018 doi: 10.1109/COMST.2018.2844322.

[43] Jacob, M., Pujol, X., Mestres, X. Key aspects of the propagation in 5G millimeter-wave bands. J. of App. Phys., 125(21), 215102, 2019.

[44] O. Kramer, T. Djerafi, and K. Wu, “Very small footprint 60 GHz stacked yagi antenna array,” IEEE Trans. Antennas Propag., vol. 59, no. 9, pp. 3204–3210, Sept. 2011.

[45] X. Bai, S. W. Qu, S. Yang, J. Hu, and Z. P. Nie, “Millimeter-wave circularly polarized tapered-elliptical cavity antenna with wide axial-ratio beamwidth,” IEEE Trans. Antennas Propag., vol. 64, no. 2, pp. 811–814, Feb. 2016.

[46] H. Vettikalladi, O. Lafond, and M. Himdi, “High-efficient and high-gain superstrate antenna for 60-GHz indoor communication,” IEEE Antennas Wireless Propag. Lett., vol. 8, no. , pp. 1422–1425, 2009.

[47] M. Imbert, A. Papió, F. De Flaviis, L. Jofre, and J. Romeu, “Design and performance evaluation of a dielectric flat lens antenna for millimeter-wave applications,” IEEE Antennas Wireless Propag. Lett., vol. 14, no. , pp. 342–345, 2015.

[48] H. Kaouach, “Design and characterization of circularly polarized discrete lens antennas in 60-GHz band,” IEEE Antennas Wireless Propag. Lett., vol. 15, no. , pp. 1200–1203, 2016.

[49] T. Seki, N. Honma, K. Nishikawa, and K. Tsunekawa, “A 60-GHz multilayer parasitic microstrip array antenna on LTCC substrate for system-on-package,” IEEE Microw. and Wireless Component Lett., vol. 15, no. 5, pp. 339–341, 2005.

[50] Y. Li and K. M. Luk, “60-GHz substrate integrated waveguide fed cavity-backed aperture-coupled microstrip patch antenna arrays,” IEEE Trans. Antennas Propag., vol. 63, no. 3, pp. 1075–1085, March 2015.

[51] Y. Li and K. M. Luk, "A 60-GHz wideband circularly polarized aperture-coupled magneto-electric dipole antenna array," IEEE Trans. Antennas Propag., vol. 64, no. 4, pp. 1325–1333, April 2016.

[52] J. Wu, Y. J. Cheng, and Y. Fan, "Millimeter-wave wideband high-efficiency circularly polarized planar array antenna," IEEE Trans. Antennas Propag., vol. 64, no. 2, pp. 535–542, Feb. 2016.

[53] A. D. Nesic and D. A. Nesic, "Printed planar 8 × 8 array antenna with circular polarization for millimeter-wave application," IEEE Antennas Wireless Propag. Lett., vol. 11, no. , pp. 744–747, 2012.

[54] C. Liu, Y. X. Guo, X. Bao, and S. Q. Xiao, "60-GHz LTCC integrated circularly polarized helical antenna array," IEEE Trans. Antennas Propag., vol. 60, no. 3, pp. 1329–1335, March 2012.

[55] Y. Li, Z. N. Chen, X. Qing, Z. Zhang, J. Xu, and Z. Feng, "Axial ratio bandwidth enhancement of 60-GHz substrate integrated waveguide-fed circularly polarized LTCC antenna array," IEEE Trans. Antennas Propag., vol. 60, no. 10, pp. 4619–4626, Oct. 2012.

[56] W. Zhang, Y. P. Zhang, M. Sun, C. Luxey, D. Titz, and F. Ferrero, "A 60-GHz circularly-polarized array antenna-in-package in LTCC technology," *IEEE Trans. Antennas Propag*, vol. 61, no. 12, pp. 6228–6232, 2013.

[57] H. Sun, Y. X. Guo, and Z. Wang, "60-GHz circularly polarized U-slot patch antenna array on LTCC," IEEE Trans. Antennas Propag., vol. 61, no. 1, pp. 430–435, Jan. 2013.

[58] Q. Wu, H. Wang, C. Yu, and W. Hong, "Low-profile circularly polarized cavity-backed antennas using SIW techniques," IEEE Trans. Antennas Propag., vol. 64, no. 7, pp. 2832–2839, July 2016.

[59] D. F. Guan, C. Ding, Z. P. Qian, Y. S. Zhang, Y. J. Guo, and K. Gong, "Broadband high-gain SIW cavity-backed circular-polarized array antenna," IEEE Trans. Antennas Propag., vol. 64, no. 4, pp. 1493–1497, April 2016.

[60] H. Zhang, S. Yang, Y. Chen, J. Guo, and Z. Nie, ''Wideband dual-polarized linear array of tightly coupled elements,'' IEEE Trans. Antennas Propag., vol. 66, no. 1, pp. 476–480, Jan. 2018.

[61] Naqvi, A. and Lim, S., 2018. "Review of Recent Phased Arrays for Millimeter-Wave Wireless Communication. Sensors, " 18 (10), p.3194.

[62] Y. -L. Yao, F. -S. Zhang and F. Zhang, "A New approach to design circularly polarized beam-steering antenna arrays without phase shift circuits," IEEE Trans. Antennas Propagat., vol. 66, no. 5, pp. 2354-2364, May 2018, doi: 10.1109/TAP.2018.2811839

[63] R. Movahedinia, A. -R. Sebak, M. R. Chaharmir, M. Ranjbar Nikkhah and A. A. Kishk, "X-band circularly polarized electronically steerable parasitic array radiator of DRA," IEEE Trans. on Antennas and Propagat., vol. 66, no. 2, pp. 721-728, Feb. 2018, doi: 10.1109/TAP.2017.2780895.

[64] R. Hong, J. Shi, D. Guan, W. Cao, and Z. Qian, ''Wideband and low-loss beam-scanning circularly polarized antenna based on air-filled SIW,'' IEEE Antennas Wireless Propag. Lett., vol. 20, no. 7, pp. 1254–1258, Jul. 2021.

[65] P. Liu, Y. Li and Z. Zhang, "Circularly polarized 2 bit reconfigurable beam-steering antenna array," IEEE Trans. Antennas Propagat., vol. 68, no. 3, pp. 2416-2421, March 2020, doi: 10.1109/TAP.2019.2939669.

[66] H. Scott and V. Fusco, "Polarization agile circular wire loop antenna," IEEE Antennas Wireless Propag. Lett., vol. 1, pp. 64–66, 2002.

[67] Carrasco, E., & De Flaviis, F.," Loop antenna arrays and patch antennas: A comparative study on linear and dual linear polarizations," IEEE Antennas Wireless Propag. Lett., 16, 2862-2865, 2017.

[68] A. Narbudowicz, X. Bao, and M. J. Ammann, "Dual circularly-polarized patch antenna using even and odd feed-line modes," IEEE Trans. Antennas Propag., vol. 61, no. 9, pp. 4828–4831, Sep. 2013.

[69] R. Movahedinia, A. -R. Sebak, M. R. Chaharmir, M. Ranjbar Nikkhah and A. A. Kishk, "X -Band Circularly Polarized Electronically Steerable Parasitic Array Radiator of DRA," IEEE Trans. Antennas Propag., vol. 66, no. 2, pp. 721-728, Feb. 2018, doi: 10.1109/TAP.2017.2780895.

[70] P. Liu, Y. Li and Z. Zhang, "Circularly polarized 2 bit reconfigurable beam-steering antenna array," IEEE Trans. Antennas Propag., vol. 68, no. 3, pp. 2416-2421, March 2020, doi: 10.1109/TAP.2019.2939669.

[71] H. Al-Saedi et al., "An integrated circularly polarized transmitter active phased-array antenna for emerging ka-band satellite mobile terminals," *IEEE Trans. Antennas Propagat.* vol. 67, no. 8, pp. 5344-5352, Aug. 2019, doi: 10.1109/TAP.2019.2913745.

[72] Nadeem, I., et al. (2022). A comprehensive survey on 'Circular polarized antennas' for existing and emerging wireless communication technologies. Journal of Physics D: Applied Physics, 55, 033002.

[73] B. Strassner and K. Chang, "5.8-GHz circularly polarized dual-rhombicloop traveling-wave rectifying antenna for low power-density wireless power transmission applications," IEEE Trans. Microw. Theory Tech., vol. 51, no. 5, pp. 1548–1553, May 2003.

[74] L. Zhang, S. Gao, Q. Luo, P. R. Young and Q. Li, "wideband loop antenna with electronically switchable circular polarization," *IEEE Antennas and Wireless Propag. Lett.*, vol. 16, pp. 242-245, 2017, doi: 10.1109/LAWP.2016.2570859.

[75] P. Delos, B. Broughton, and J. Kraft, "Phased array antenna patterns—Part 1: linear array beam characteristics and array factor," IEEE Antennas Propag. Mag., vol. 54, no. 2, 2020.

[76] Stutzman, W. L., & Thiele, G. A. (2012). Antenna Theory and Design, 3rd Edition. Hoboken, NJ: John Wiley & Sons.

[77] UKRI National Millimetre Wave Facility. Available online: https://www.sheffield.ac.uk/mm-wave/ (accessed on 22 January 2023).

[78] Bernhard, J. T., Reconfigurable Antennas, Synthesis Lectures on Antennas, 2007, 2, pp. 1-66.

[79] Haupt, R. L; Lanagan, M. Reconfigurable antennas, IEEE Antennas and Propagat. Mag., 2013, 55, pp. 49-61.

[80] Hussain, M.; Awan, W.A.; Alzaidi, M.S.; Hussain, N.; Ali, E.M.; Falcone, F. Metamaterials and Their Application in the Performance Enhancement of Reconfigurable Antennas: A Review. Micromachines, 2023, 14, 349.

[81] Bari, I.; Iqbal, J.; Ali, H.; Rauf, A.; Bilal, M.; Jan, N.; Illahi, U.; Arif, M.; Khan, M.A.; Ghoniem, R.M. Bandwidth Enhancement and Generation of CP of Yagi-Uda-Shape Feed on a Rectangular DRA for 5G Applications. Micromachines 2022, 13, 1913. https://doi.org/10.3390/mi13111913.

[82] Wang, K.X.; Wong, H. A wideband millimeter-wave circularly polarized antenna with 3-D printed polarizer, IEEE Trans. Antennas Propag., 2017, 65, pp. 1038-1046.

[83] Akbari, S.G.M.; Farahani ,M.; Sebak, A.R.; Denidni, T.A. Analytic study on CP enhancement of millimeter wave DR and patch subarray antennas, Int. J. RF Microw. Comput. Aided Eng., 2017, 27, p. e21053.

[84] Asaadi, M.;Sebak, A; High-gain low-profile circularly polarized slotted SIW cavity antenna for MMW applications, IEEE Antennas and Wireless Propagat. Lett., 2017, 16, pp. 752-755.

[85] Bisharat, D.J.; S. Liao, S.; Xue, Q. High gain and low cost differentially fed circularly polarized planar aperture antenna for broadband millimeter-wave applications, IEEE Trans. Antennas Propag., 2016, 64, pp. 33-42.

[86] Park, S. J.; Park, S.O. LHCP and RHCP Substrate integrated waveguide antenna arrays for millimeter-wave applications, IEEE Antennas and Wireless Propag. Lett., 2017, 16, pp. 601-604.

[87] Cheng, Y. J.; Hong, W.; Wu, K. Millimeter-wave half mode substrate integrated waveguide frequency scanning antenna with Quadri-polarization, IEEE Trans. on Antennas Propag., 2010, 58, pp. 1848-1855.

[88] Guntupalli, A.B.; Wu, K. Frequency-steered directive beam with dual circular polarization and two-dimensional scan capability for millimeter- wave imaging and sensing systems, WAMICON 2014, Tampa, FL, USA, 2014, pp. 1-3.

[89] Jung, T. J.; Hyeon, I.J. ; Baek, C.W.; Lim, S. Circular/linear polarization reconfigurable antenna on simplified RF-MEMS packaging platform in K-Band, IEEE Trans. Antennas Propagat., 2012, 60, pp. 5039-5045.

[90] Valdes, J. L.; Huitema, L.; Arnaud, E.; Passerieux, D.; Crunteanu, A. A polarization reconfigurable patch antenna in the millimeter-waves domain using optical control of phase change materials, IEEE Open J. Antennas and Propag., 2020, 1, pp. 224-232.

[91] Alreshaid, A.T.; Cui, Y.; Bahr, R.; Sharawi, M. S.; Tentzeris, M.M. A compact millimeter wave polarization reconfigurable double patch antenna, IEEE Int. Symp. Antennas Propagat. and USNC-URSI Rad. Science Meeting, Portland, OR, USA, 2023, pp. 1865-186.

[92] Al Abbas, E.; Nguyen-Trong, N.; Mobashsher, A.T.; Abbosh, A.M. Polarization-reconfigurable antenna array for millimeter-wave 5G, IEEE Access, 2019, 7, pp. 131214-131220.

[93] Ferrando-Rocher, M.; Herranz-Herruzo, J.I.; Valero-Nogueira, A.; Bernardo-Clemente, B. Switchable T-Slot for dual-circularly-polarized slot-array antennas in Ka-band," IEEE Antennas Wireless Propagat. Lett., 2021, 20, pp. 1953-1957.

[94] Mishra, G.; Sharma, S.K. A multifunctional full-polarization reconfigurable 28 GHz staggered butterfly 1-D beam steering antenna, IEEE Trans. Antennas Propagat., 2021, 69, pp. 6468-6479.

[95] Jabri, A.; Asadallah, F.; Tawk, Y.; Costantine, J. A millimeter-wave polarization-reconfigurable double-folded antenna array, IEEE Antennas Wireless Propagat. Lett., 2023, 22, pp. 2060-2064.

[96] Cummings, N.P. Active Antenna Bandwidth Control Using Reconfigurable Antenna Elements. Ph.D. Thesis, Virginia Tech, Bradley Department of Electrical and Computer Engineering, Blacksburg, VA, USA, 2003

[97] Zainud-Deen, S.H.; Malhat, H.A.E.A.; El-Shalaby, N.A.A.S.; Gaber, S.M. Circular polarization bandwidth reconfigurable high gain planar plasma helical antenna, IEEE Trans. Plasma Science, 2019, 47, pp. 4274-4280

[98] Zang, Y.; Li, W., Ma, J.; Yang, J.; Xiong, W. A new bandwidth reconfigurable antenna, 2022, J. Phys. Conf. Ser. 2384 012035

[99] MA4SPS402 - Mouser Electronics. Available at: https://www.mouser.co.uk/datasheet/2/249/MA4SPS402-335177.pdf (Accessed: 19 October 2023).

[100] MA4AGFCP910 - Mouser Electronics. Available at: https://www.mouser.com/datasheet/2/249/MA4AGP907_FCP910-838114.pdf (Accessed: 19 October 2023).

[101] Duffy, S. M., Verghese, S.; McIntosh, K. A.; Jackson,A.; Gossard, A. C.; Matsuura, S. Accurate modeling of dual dipole and slot elements used with photomixers for coherent terahertz output power, IEEE Trans. Microw. Theory Tech., 49, 2001, pp. 1032–1038.

[102] "Wrekin Circuits Ltd. Available online: https://www.wrekin-circuits.co.uk/. (accessed on 03 October 2023).

[103] UKRI National Millimeter Wave Facility. Available online: https://www.sheffield.ac.uk/mm-wave/ (accessed on 03 October 2023).

[104] B. A. Cetiner, H. Jafarkhani, Jiang-Yuan Qian, Hui Jae Yoo, A. Grau and F. De Flaviis, "Multifunctional reconfigurable MEMS integrated antennas for adaptive MIMO systems," in IEEE Communications Magazine, vol. 42, no. 12, pp. 62-70, Dec. 2004, doi: 10.1109/MCOM.2004.1367557.

[105] Symeon Nikolaou et al., "Pattern and frequency reconfigurable annular slot antenna using PIN diodes," in IEEE Transactions on Antennas and Propagation, vol. 54, no. 2, pp. 439-448, Feb. 2006, doi: 10.1109/TAP.2005.863398.

[106] A. Grau Besoli and F. De Flaviis, "A Multifunctional Reconfigurable Pixeled Antenna Using MEMS Technology on Printed Circuit Board," in IEEE Transactions on Antennas and Propagation, vol. 59, no. 12, pp. 4413-4424, Dec. 2011, doi: 10.1109/TAP.2011.2165470.

[107] Q. H. Dang, S. J. Chen, N. Nguyen-Trong and C. Fumeaux, "Multifunctional Reconfigurable Wearable Textile Antennas Using Coplanar Reconfiguration Modules," in IEEE Transactions on Antennas and Propagation, vol. 71, no. 5, pp. 3806-3815, May 2023, doi: 10.1109/TAP.2023.3242459.

[108] N. Nguyen-Trong, L. Hall and C. Fumeaux, "A Frequency and Pattern-Reconfigurable Center-Shorted Microstrip Antenna," in IEEE Antennas and Wireless Propagation Letters, vol. 15, pp. 1955-1958, 2016, doi: 10.1109/LAWP.2016.2544943.

[109] P. -Y. Qin, S. -L. Chen and Y. J. Guo, "A compound reconfigurable microstrip antenna with agile polarizations and steerable beams," *2017 International Symposium on Antennas and Propagation (ISAP)*, Phuket, Thailand, 2017, pp. 1-2, doi: 10.1109/ISANP.2017.8228879.

[110] D. Rodrigo, Y. Damgaci, M. Unlu, B. A. Cetiner, J. Romeu and L. Jofre, "Antenna Reconfigurability based on a Novel parasitic pixel layer," Proceedings of the 5th European Conference on Antennas and Propagation (EUCAP), Rome, Italy, 2011, pp. 3497-3500.

[111] D. Rodrigo and L. Jofre, "Frequency and Radiation Pattern Reconfigurability of a Multi-Size Pixel Antenna," in IEEE Transactions on Antennas and Propagation, vol. 60, no. 5, pp. 2219-2225, May 2012, doi: 10.1109/TAP.2012.2189739.

[112] D. Rodrigo, B. A. Cetiner and L. Jofre, "Frequency, Radiation Pattern and Polarization Reconfigurable Antenna Using a Parasitic Pixel Layer," in IEEE Transactions on Antennas and Propagation, vol. 62, no. 6, pp. 3422-3427, June 2014, doi: 10.1109/TAP.2014.2314464.

[113] Z. Li, E. Ahmed, A. M. Eltawil and B. A. Cetiner, "A Beam-Steering Reconfigurable Antenna for WLAN Applications," in IEEE Transactions on Antennas and Propagation, vol. 63, no. 1, pp. 24-32, Jan. 2015, doi: 10.1109/TAP.2014.2367500.

[114] J. Pu, B. Zhang, Y. Zhou, K. Huang, T. Zhang and J. Yang, "Notice of Violation: A Dual-Band Beam Steering Multifunctional Reconfigurable Antenna Optimized by Non-Dominated Sorting Genetic Algorithm (NSGA-II) for Wi-Fi 6 Applications," in IEEE Transactions on Antennas and Propagation, doi: 10.1109/TAP.2022.3209180.

[115] M. Wang, M. R. Khan, M. D. Dickey and J. J. Adams, "A Compound Frequency- and Polarization-Reconfigurable Crossed Dipole Using Multidirectional Spreading of Liquid Metal," in IEEE Antennas and Wireless Propagation Letters, vol. 16, pp. 79-82, 2017, doi: 10.1109/LAWP.2016.2556983.

[116] G. B. Zhang, R. C. Gough, M. R. Moorefield, K. J. Cho, A. T. Ohta and W. A. Shiroma, "A Liquid-Metal Polarization-Pattern-Reconfigurable Dipole Antenna," in *IEEE Antennas and Wireless Propagation Letters*, vol. 17, no. 1, pp. 50-53, Jan. 2018, doi: 10.1109/LAWP.2017.2773076.

[117] X. H. Wang, H. W. Pan, L. Z. Wang, X. W. Shi and Y. Xu, "A Simple Frequency- and Polarization-Reconfigurable Bent Monopole Antenna Based on Liquid Metal," in IEEE Antennas and Wireless Propagation Letters, vol. 22, no. 5, pp. 950-954, May 2023, doi: 10.1109/LAWP.2022.3225213.

[118] V. T. Bharambe, J. Ma, M. D. Dickey and J. J. Adams, "Planar, Multifunctional 3D Printed Antennas Using Liquid Metal Parasitics," in IEEE Access, vol. 7, pp. 134245-134255, 2019, doi: 10.1109/ACCESS.2019.2942058.

[119] G. Yang, Q. Cheng, J. Li, S. Zhang, S. Gao and X. Chen, "A Multifunctional Array System Based on Adjustable-Phase Antenna for Wireless Communications," in IEEE Transactions on Antennas and Propagation, vol. 71, no. 5, pp. 4552-4557, May 2023, doi: 10.1109/TAP.2023.3243987.

[120] J. Wu, X. Lu, W. Wang, J. Han, G. Xu and Z. Huang, "Design of a Compact Polarization-Agile and Frequency-Tailored Array Antenna with Digital-Controllable Radiation Beams," in *IEEE Transactions on Antennas and Propagation*, vol. 70, no. 2, pp. 813-822, Feb. 2022, doi: 10.1109/TAP.2021.3111325.

[121] Zhan Wang, Yuandan Dong, "Phase and Polarization Digitally Modulated Array Using Reconfigurable DR Element: Proposal, Design, and Verification", IEEE Transactions on Antennas and Propagation, vol.71, no.5, pp.4102-4114, 2023.

[122] Edwards, T.C. and Steer, M.B. (2016) Foundations for Microstrip Circuit Design. Chichester, West Sussex, United Kingdom: John Wiley & Sons Inc.

[123] N. O. Parchin, H. J. Basherlou, Y. I. Al-Yasir, A. M. Abdulkhaleq, and R. A. Abd-Alhameed, ‘‘Reconfigurable antennas: Switching techniques— A survey,’’ Electronics, vol. 9, no. 2, p. 336, Feb. 2020.

[124] Z. Xiao et al.,A survey on millimeter-wave beamforming enabled UAV communications and networking, IEEE Comms. Surveys & Tutorials, 2022, 24, pp. 557-610

[125] Abdul-Hadi, A.; Abdulrazzaq Naser, M.; Alsabah, M.; Abdulhussain, S., Mahmmod, B. Performance evaluation of frequency division duplex (FDD) massive multiple input multiple output (MIMO) under different correlation models. PeerJ Computer Science, 2022, 8, p.e1017.

[126] Sacchi, C.; Rossi,T. ; Murroni, M.; Ruggieri, M. Extremely high frequency (EHF) bands for future broadcast satellite services: Opportunities and challenges. IEEE Trans. on Broadcasting, 2019, 65, pp.609-626.

[127] Rossi, T.; De Sanctis, M.; Maggio, F.; Codispoti, G.; Parca, G. Q/V-band satellite communication experiments on channel estimation with Alphasat Aldo Paraboni P/L, Proc. IEEE Aerospace Conf., Big Sky, MT, USA, 2015, pp. 1-11

[128] Li, R.L.; DeJean, G.; Laskar, J.; Tentzeris, M.M. Investigation of circularly polarized loop antennas with a parasitic element for bandwidth enhancement, IEEE Trans. Antennas and Propagat., 2005, 53, pp. 3930-3939

[129] Asfour, R.; Khamas, S.; Bal, E.A., Performance evaluation of a millimeter-wave phased array antenna using circularly polarized elements. Int. Scholarly and Scientific Res. & Innovat., 2021, 15, pp. 398-401

[130] H. Morishita, K. Hirasawa, and T. Nagao, “Circularly polarized wire antenna with a dual rhombic loop,” Proc. Inst. Elect. Eng. Microw. Antennas Propag., pt. H, vol. 145, no. 3, pp. 219–224, Jun. 1998..

[131] Zhang, L.; Gao, S.; Luo, Q.; Young, P.R.; Li, Q. Wideband loop antenna with electronically switchable circular polarization IEEE Antennas Wireless Propagat. Lett., 2017, 16, pp. 242-245.

[132] Bharathi, A.A.; Merugu, L. A wideband circularly polarized end-fire microstrip antenna, IEEE 18th India Council Int. Conf. (INDICON), India, 2021, pp. 1-6.

[133] M. Sumi, K. Hirasawa, and S. Shi, “Two rectangular loops fed in series for broad-band circular polarization and impedance matching,” IEEE Trans. Antennas Propag., vol. 52, no. 2, pp. 551–554, Feb. 2004.

[134] D. Kim, R. Willmot and D. Peroulis, "A high-efficiency low-cost wire-bond loop antenna for CMOS wafers, IEEE Antennas and Propagat. Soc. Int. Symp., North Charleston, USA, 2009, pp. 1-4.

[135] Kang, K. et al. A 60-GHz OOK receiver with an on-chip antenna in 90 nm CMOS, IEEE J. Solid-State Circ., 2010, 45, pp. 1720-1731.

[136] Li, S. et al. Performance of V-Band on-chip antennas in global foundries 45nm CMOS SOI process for mm-wave 5G applications, IEEE/MTT-S Int. Microwave Symp., Philadelphia, USA, 2018, pp. 1593-1596,

[137] Chen, I.-S. ; Chiou, H.-K.; Chen, N.-W. V-Band on-chip dipole-based antenna, IEEE Trans. Antennas and Propagat., 2009, 57, pp. 2853-2861.

[138] Passiopoulos, .;, Nam, S.; Georgiou, A. Ashtiani, A.E.; Robertson, I.D.; Grindrod, E.A. V-band single chip, direct carrier BPSK modulation transmitter with integrated patch antenna, IEEE MTT-S Int. Microwave Symp. Digest, 1998, 1, 305–308.

[139] Baek, Y.-H.; Truong, L.H.; Park, S.-W.; Lee, S.-J.; Chae, Y.-S.; Rhee, E.-H.; Park, H.-C.; Rhee J.-K. 94-GHz log-periodic antenna on GaAs substrate using air-bridge structure, IEEE Antennas Wireless Propagat. Lett., 2009, 8, pp. 909–911.

[140] Singh, H.; Mandal, S.K. Current trends and future perspective of designing on-chip antennas, Int. J. Microwave and Wireless Tech., 2023, 15, pp. 535–545.

[141] Sedlačková, K.; Zat'ko, B.; Šagátová, A.; Nečas, V.; Boháček, P.; Sekáčová, M. Comparison of semi-insulating GaAs and 4H-SiC-based semiconductor detectors covered by LiF film for thermal neutron detection. Appl. Surf. Sci. 2018, 461, 242–248.

[142] Chaturvedi, A. Review of semiconductor materials for monolithic microwave millimeter wave integrated circuits. Mater. Today Proc. 2020, 37, pp. 1567–1570.

[143] Karacolak, T.; Thirumalai, R.V.K.G.; Merrett, J.N.; Koshka, Y.; Topsakal, E. Silicon Carbide (SiC) antennas for high-temperature and high-power applications, IEEE Antennas and Wireless Propagat. Lett., 2013, 12, pp. 409-412,

[144] Dasari, S. A. ; Williamson, T. G.; Ghalichechian, N. Silicon Carbide Slot Dielectric Resonator Antenna for High Temperature and Power Applications, IEEE Int. Symp. Antennas Propagat. and USNC-URSI Radio Science Meeting (USNC-URSI), 2023, Portland, OR, USA, 2023, pp. 1887-1888.